Development of the Aprotic Lithium-Oxygen Battery System

by

Brian Adams

A thesis
presented to the University of Waterloo
in fulfillment of the
thesis requirement for the degree of
Doctor of Philosophy
in
Chemistry

Waterloo, Ontario, Canada, 2015

AUTHOR'S DECLARATION

I hereby declare that I am the sole author of this thesis. This is a true copy of the thesis, including any required final revisions, as accepted by my examiners.

I understand that my thesis may be made electronically available to the public.

_____

Brian Adams

ABSTRACT

With the increasing importance of electrified transport, the need for high energy density storage is also increasing. Possible candidates include Li-O_2 batteries, which are the subject of rapidly increasing focus worldwide despite being in their infancy of understanding. This excitement owes to the high energy density of Li-O_2 (up to 2-3 kWh kg^{-1}), theoretically much higher compared to that of other rechargeable systems, and the open "semi-fuel" cell battery configuration that uses oxygen as the positive electrode material. To bring aprotic Li-O_2 batteries closer to practical reality, and to attain suitable power delivery, understanding of the underlying chemistry based on the reversible reaction of $O_2 + Li \leftrightarrow Li_2O_2$ is essential. In this thesis, the precise reactions (including side reactions) which occur during both discharge and charge are studied in detail. Light is shed on the true effect of heterogeneous electrocatalysis in this system. A trend is identified between the observed overpotential during charge and the stability of the electrode material to oxidation by lithium peroxide. Additionally, plausible mechanistic pathways for the decomposition of glyme electrolyte solvent molecules by superoxide attack are proposed along with the synthesis and characterization of a solvent with enhanced stability.

In Chapter 3 of this thesis, a fundamental understanding of the discharge process in the battery (the oxygen reduction reaction or ORR) is presented. The effect of current density on the morphology and chemical nature of the discharge product (namely toroidal and thin-film morphologies of Li_2O_2) is discussed along with the related charging performance. Evidence from diffraction, electrochemical, FESEM and STEM measurements shows that slower current densities favor aggregation of lithium peroxide

nanocrystallites nucleated *via* solution dismutase on the surface of the electrode; whereas fast rates deposit quasi-amorphous thin films. The latter provide a lower overpotential on charge due to their nature and close contact with the conductive electrode surface, albeit at the expense of lower discharge capacity.

The charge reaction (oxygen evolution or OER) was studied using *operando* X-ray diffraction, online electrochemical mass spectrometry, and scanning electron microscopy and the results are discussed in Chapter 4. Both electrochemically deposited Li_2O_2 (E-Li_2O_2) and commercial crystalline Li_2O_2 powder (C-Li_2O_2) were analyzed. For electrochemically formed Li_2O_2 a two-stage oxidation is proposed. At low potentials this involves the decay of amorphous Li_2O_2, whereas at higher potentials, crystalline Li_2O_2 is decomposed via a small actively transforming fraction that evolves oxygen via a Li deficient solid-solution reaction. This preferentially starts with the smallest crystallites. For bulk crystalline Li_2O_2 with an isotropic crystallite shape and larger crystallite dimensions, we propose a single stage oxidation on the basis of the XRD data. The observation of sub-stoichiometric $Li_{2-x}O_2$ at the early stage of oxidation and the gradual decreasing average crystallite size suggests a small active fraction that also evolves oxygen via a Li deficient solid solution reaction. However, in this case the oxidation process gradually consumes the larger C-Li_2O_2 crystallites.

Recently, there has been a transition from fully carbonaceous positive electrodes for the aprotic lithium oxygen battery to alternative materials and the use of redox mediator additives, in an attempt to lower the large electrochemical overpotentials associated with the charge reaction. However, the stabilizing or catalytic effect of these materials can become complicated due to the presence of major side-reactions observed during

dis(charge). In Chapter 5, the charge reaction is isolated from the discharge by utilizing electrodes prefilled with commercial lithium peroxide with a crystallite size of about 200 - 800 nm. Using a combination of STEM, on-line mass spectrometry, XPS, and electrochemical methods to probe the nature of surface films on carbon and conductive Ti-based nanoparticles, it is shown that oxygen evolution from lithium peroxide is strongly dependent on their surface properties. Insulating TiO_2 surface layers on TiC and TiN - even as thin as 3 nm – can completely inhibit the charge reaction under these conditions. On the other hand, TiC which lacks this oxide film readily facilitates oxidation of the bulk Li_2O_2 crystallites, at a much lower overpotential relative to carbon. Since most materials suffer from oxidation to some degree, precise control of the surface chemistry at the nanoscale becomes of upmost importance.

The role that "electrocatalysts" play in the aprotic Li-O_2 battery and the mechanism(s) by which they function has been under much scrutiny. In Chapter 6, a lead ruthenium oxide with a pyrochlore structure proved to be a paramount catalyst for the oxygen reduction and evolution reactions (particularly OER) in alkaline aqueous media. This material was then utilized as a model catalyst for these same reactions in non-aqueous media with Li^+ cations present. It was found that, relative to carbon, the pyrochlore does have significant electrocatalytic properties, namely a lowering of the charging voltage. The main cause of this voltage shift is the ability of the metal oxide to completely oxidize side-products which are formed during discharge, by reaction between the superoxide (O_2^- /LiO_2) intermediate and the electrolyte solvent (tetraethylene glycol dimethyl ether, TEGDME). Carbon is unable to oxidize these side-products below the voltage at which

electrolyte oxidation occurs. This further helps to explain the nature of "electrocatalysis" in the Li-O_2 battery.

In Chapter 7, a new lithium-ether-derived chelate ionic liquid was synthesized to serve as an electrolyte for the Li-O_2 battery that is stable to metallic lithium, and whose ethereal framework is much more inherently stable to superoxide-initiated hydrogen abstraction than the simple glyme, dimethoxyethane (DME). Reactions of chemically generated superoxide with this electrolyte show that virtually no decomposition products such as lithium formate are generated. When employed in a Li-O_2 battery, a ten-fold decrease in CO_2 evolution is evident on charge by comparison to DME and greatly enhanced cycling stability was observed with TiC as a cathode support. A mechanism is proposed to account for the lowered reactivity, offering new insight into the stability of organic electrolytes in Li-O_2 batteries. This approach to electrolyte design can be extended to other organic systems to provide a platform for the design of advanced electrolyte systems.

ACKNOWLEDGEMENTS

I would like to extend my appreciation to my supervisor, Professor Linda F. Nazar, for her guidance throughout the course of this research project. Additionally, I am happy to have had the opportunity to work with all other members of the research group, past and present, who have lent me their assistance and expertise. Thanks also to my committee members, Drs. Holger Kleinke, Eric Prouzet, and Jacek Lipkowski, for taking the time to discuss my research and provide suggestions throughout the duration of my PhD studies.

The TEM imaging and EELS analysis in Chapter 3 was done at Hydro Quebec by Dr. Michel Trudeau and Dr. Karim Zaghib. This contribution enhanced the publication and I thank you both for this.

The *operando* XRD studies described in Chapter 4 were performed at TU Delft, located in Delft, Netherlands by Dr. Marnix Wagemaker and Dr. Swapna Ganapathy. This was an exciting and successful collaboration and I greatly appreciate the opportunity and experience of travelling to the Netherlands and Germany to assist.

The electrochemical studies done on the lead ruthenium oxide pyrochlore could not have been done without the material. Thank you, Dr. Sihyoung Oh, for preparing this material in its mesoporous form.

The STEM images of TiC nanoparticles in Chapter 6 were acquired and provided by Dr. Layla Medhi at the Pacific Northwest National Laboratory. I appreciate the communication and help in figuring out the conundrum of the TiC surface layers.

The online electrochemical mass spectrometry work throughout this thesis was performed by Robert Black at the University of Waterloo or Dr. Erik J. Berg at the Paul

Scherrer Institute in Villigen, Switzerland. Although these were very difficult experiments to conduct, I enjoyed the teamwork between the three of us which eventually paid off.

I extend my gratitude to Prof. Graham Murphy, who although was not on my PhD committee, assisted me with the many questions and challenges relating to organic chemistry. I feel as though I gained an understanding of a whole new field of chemistry which was not in my original interest.

Lastly, I wish to thank all of my family and friends from the bottom of my heart for their continuous support and encouragement. I could not have done it without all of you.

TABLE OF CONTENTS

LIST OF FIGURES

LIST OF TABLES

GLOSSARY

2NM4	Tetraethylene glycol di(trimethylsilyl) ether
BET	Brunauer-Emmett-Teller
CH_3CO_2Li	Lithium acetate
CO_2	Carbon dioxide
CV	Cyclic voltammetry
DFT	Density functional theory
DMA	Dimethylacetamide
DMDMB	2,3-dimethoxy-2,3-dimethylbutane
DME	1,2-dimethoxyethane
DMF	Dimethylformamide
DMSO	Dimethylsulfoxide
EASA	Electroactive surface area
EDS	Energy dispersive X-ray spectroscopy
EIS	Electrochemical impedance spectroscopy
Fc	Ferrocene
Fc^+	Ferrocenium
Fc/Fc^+	Ferrocene/ferrocenium couple
FTIR	Fourier transform infrared spectroscopy
GDE	Gas diffusion electrode
GDL	Gas diffusion layer
H_2O	Water
HCO_2Li	Lithium formate

HF	Hartree Fock
IUPAC	International Union of Pure and Applied Chemistry
Li_2O_2	Lithium peroxide
Li_2CO_3	Lithium carbonate
$LiNO_3$	Lithium nitrate
Li-O_2	Lithium oxygen
LiO_2	Lithium superoxide
$LiPF_6$	Lithium hexafluorophosphate
LiTFSI	Lithium bis(trifluoromethanesulfonyl)imide
LSV	Linear sweep voltammetry
MeCN	Acetonitrile
MS	Mass spectrometry
NMP	*N*-Methyl-2-pyrrolidone
NMR	Nuclear magnetic resonance spectroscopy
NO	Nitric oxide
O_2^-	Superoxide anion
O_2^{2-}	Peroxide anion
OEMS	Online electrochemical mass spectrometry
OER	Oxygen evolution reaction
ORR	Oxygen reduction reaction
OCV	Open circuit voltage
PC	Propylene carbonate
PRO	Lead ruthenium oxide

PTFE	Polytetrafluoroethylene
PVdF	Polyvinylidene fluoride
PXRD	Powder X-ray diffraction
RDE	Rotating disk electrode
RRDE	Rotating ring disk electrode
SA	Surface area
SAED	Selected area electron diffraction
SEM	Scanning electron microscope
STEM	Scanning transmission electron microscope
TBA^+	Tetrabutylammonium cation
TBAP	Tetrabutylammonium perchlorate
$TBAPF_6$	Tetrabutylammonium hexafluorophosphate
TBATFSI	Tetrabutylammonium bis(trifluoromethylsulfonyl)imide
TEGDME	Tetraethylene glycol dimethyl ether
TiC	Titanium carbide
TiN	Titanium nitride
TiO_2	Titanium dioxide
Triglyme	Triethylene glycol dimethyl ether
TEM	Transmission electron microscope
$TFSI^-$	Bis(trifluoromethylsulfonyl)imide anion
TGA	Thermogravimetric analysis
XPS	X-ray photoelectron spectroscopy
XRD	X-ray difraction

Chapter 1

Introduction

1.1 Overview of Lithium-Oxygen Batteries

Our global society is becoming increasingly energy dependent: projections are that our energy demands will easily double within the next 15 years as nations around the world strive for a common level of development and infrastructure. This poses problems as we approach an age of diminishing petroleum resources. More worryingly, oil, coal and natural gas have been extensively used to power automobiles, power plants and factories, causing a dramatic build-up of greenhouse gases in the atmosphere. While a transition from combustion engine powered automobiles to electric vehicles will not solve all of these problems, it is nonetheless an important goal that will help us sustain our standard of living and minimize urban pollution without sacrificing the environment. Such a transition is underway with a more widespread incursion of hybrid electric vehicles into the marketplace, and plug-in hybrid vehicles starting to make their mark in the last two years. However, no currently developed battery chemistries meet the energy storage requirements for pure electric vehicles that make them highly palatable to consumers. Enthusiastic adoption of electrified transport is very dependent on developing higher energy density storage batteries to extend the comfortable driving range and reduce costs, thus making electric vehicles – and hybrid electric vehicles - more practical.

Battery chemistries that do not operate on the basis of intercalation chemistry, such as lithium-sulfur and lithium-oxygen, are amongst those which offer the best possibility of

achieving such goals. Lithium-oxygen ($Li-O_2$) or lithium-air (Li-air) batteries were proposed in the 1970s for automotive transportation, and yet they began to receive worldwide attention just this decade. [1,2,3,4] The excitement mostly owes to the high energy density of $Li-O_2$ (up to 2-3 kWh kg^{-1}), which is theoretically much higher compared to that of other rechargeable systems; and its open cell configuration that uses oxygen as the reactant at the positive electrode (cathode), so that only the product (and conductive cathode support) is housed on board.[5-11] Coupled with the higher efficiency of electric propulsion systems, which have efficiency (battery-to-wheels) of approximately 90 % compared to 12.6 % tank-to-wheel efficiency for gasoline powered vehicles, the $Li-O_2$ battery system could offer driving ranges that approach that of gasoline powered automobiles.[12]

There are currently four types of $Li-O_2$ batteries under investigation, designated by the type of electrolyte used. All make use of a lithium metal anode and a porous oxygen diffusion cathode with lithium salts dissolved in (i) non-aqueous aprotic solvents, (ii) aqueous solvents, (iii) hybrid non-aqueous/aqueous solvents, or (iv) solid-state electrolytes. The chemistry at the oxygen cathode differs depending on the electrolyte. The reactions in the aqueous and hybrid systems are identical, since the cathode is exposed to aqueous electrolyte in both, and although not as widely studied, the solid-state type $Li-O_2$ battery functions similarly to the non-aqueous system. The work in this thesis is limited to the non-aqueous aprotic type of $Li-O_2$ battery and it should be assumed that the literature discussed herein refer specifically to this type.

In practice, the system presents many challenges, however, noted ever since a rechargeable non-aqueous Li-air battery was introduced 15 years ago.[13] On discharge, oxygen from the atmosphere is reduced at the cathode, and combines with Li to form Li_2O_2 (the oxygen reduction reaction or ORR): $Li + O_2 \leftrightarrow Li_2O_2$ (**Figure 1.1**). The peroxide is stored within the voids of a porous carbon black (or other lightweight inert, conductive material) that acts as a membrane and support. On charge, the lithium peroxide is converted back to Li and O_2 (oxygen evolution reaction; OER). A report based on online electrochemical mass spectroscopy (OEMS) showing that O_2 is indeed released by oxidation of Li_2O_2,[14] recently confirmed by in-depth studies,[15] re-kindled the interest in Li-O_2 chemistry. Carbons act as ORR catalysts,[7, 16] but they are not as effective for OER.[8,15,12,17] This is a major challenge in the rechargeable Li-air cell, the need being to reduce the substantial polarization on charge exhibited by most cells.[13] Although this is less of an issue at low discharge capacities,[18] it is a problem at the high discharge capacities that could fulfill the promise for the Li-O_2 cell.

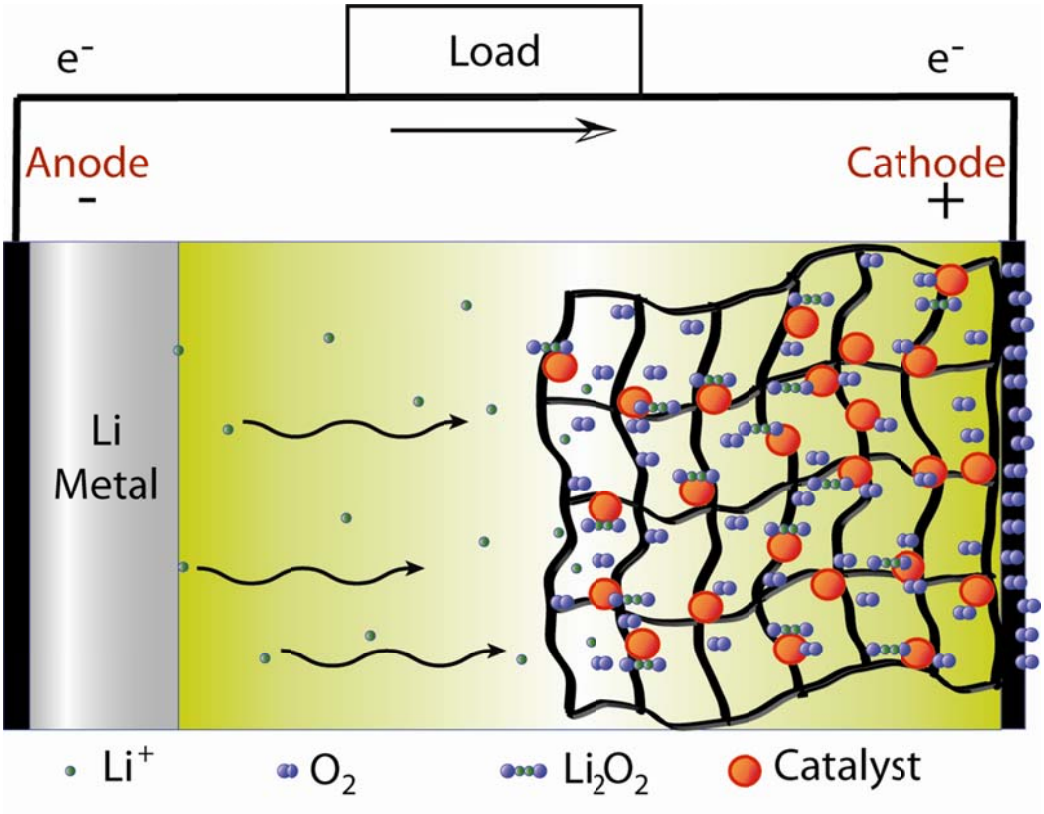

Figure 1.1 Systematic operation of the non-aqueous Li-O_2 cell during discharge.[1] The porous cathode is exposed to a source of oxygen and the spontaneous reaction of $2Li + O_2 \rightarrow Li_2O_2$ occurs, accompanied by flow of electrons in the external circuit. The reverse occurs on charge.

Furthermore, the processes are usually more complex than as described. The first ORR step is thought to be a one electron reduction that forms the highly reactive intermediate lithium superoxide, LiO_2.[7,17,19] This radical reacts with many electrolytes such as propylene carbonate to prohibit the formation of Li_2O_2;[20] and detailed elucidation of the mechanism reveals the formation of lithium alkylcarbonates and Li_2CO_3.[21] OEMS studies have further identified the critical role of the electrolyte, highlighting the

unsuitability of alkyl carbonates.[15] Many previously published reports of both ORR and OER reactions on Li-air catalyzed systems are affected by this factor, since ORR coupled with electrolyte decomposition affects the discharge product. Although catalyzed oxidation takes place on charge, high polarization and the release of CO_2 (not O_2) are the outcome. Many metal oxide catalysts have been examined for ORR and OER, however, the nature of catalytic reactivity for OER from *lithium peroxide* is thus somewhat unclear.

In short, the exploration of the Li-O_2 cell is at its initial stages and extensive research must occur before this type of battery can be commercially utilized. There are several well-defined challenges with the Li-O_2 battery which need to be addressed, in addition to acquiring a much better understanding of the chemistry. Suitable electrolytes and cathodes must be developed that can resist decomposition at high oxidation potentials, and minimize reactivity with intermediates formed on cell discharge/charge. Secondly, the use of electrocatalysts in the cathode needs to be studied to determine their ability to lower the overpotentials for charge and discharge reactions and enhance cycle life.[14] Cleverly structured porous oxygen cathodes must be designed which can optimize the transport of all reactants to the active catalyst/carbon surfaces. Also, air-breathing membranes must be developed that allow O_2 to pass through while preventing ingress of H_2O, CO_2, and other environmental contaminants which limit the lifetime of the Li-O_2 batteries.[9] Finally, the lithium metal anode must be protected to prevent reaction with trace amounts of H_2O and O_2, and inhibit dendrite formation upon charge.[22]

1.2 ORR and OER Reactions in Non-Aqueous Media

The possible reactions in the non-aqueous Li-O_2 cell which occur at the cathode via a series of oxygen reduction processes are described below: [8,13,19]

$$O_2 + Li^+ + e^- \rightarrow LiO_2 \quad (1\text{-}1)$$

$$2LiO_2 \rightarrow Li_2O_2 + O_2 \quad \text{(Chemical Process)} \quad (1\text{-}2)$$

$$LiO_2 + Li^+ + e^- \rightarrow Li_2O_2 \quad (1\text{-}3)$$

$$Li_2O_2 + 2Li^+ + 2e^- \rightarrow 2Li_2O \quad (1\text{-}4)$$

Theoretically speaking, Li_2O_2 ($E° = 2.96$ V) and Li_2O ($E° = 2.91$ V) are both possible discharge products of the Li-O_2 cell, but Li_2O_2 is the reaction product observed in practice for voltage cut-offs above 2.0V.[17,23,24] This product can be decomposed electrochemically ($Li_2O_2 \rightarrow 2Li^+ + 2e^- + O_2$), allowing for rechargeability of the non-aqueous Li-O_2 cell. However, as will be detailed in this thesis, the reactivity of other components of the Li-O_2 cell – namely, the electrolyte and cathode support - directly impact both the oxygen reduction reaction (ORR) and oxygen evolution reaction (OER).

The oxygen evolution reaction is of great importance for industrial and practical applications including water electrolysis, metal electrowinning, and secondary metal air batteries. Electrocatalysts are required to overcome the high overpotential associated with this reaction in both alkaline and acidic electrolytes. The fundamental electrochemistry of OER in aqueous solutions differs immensely from that in the non-aqueous Li-O_2 cell. In aqueous solutions, the source of oxygen to be evolved is the solvent itself (water). The

complete oxidation of water occurs via a four-electron transfer in both alkaline and acid media, respectively:

$$4OH^- \rightarrow O_2 + 2H_2O + 4e^- \quad (1\text{-}5)$$

$$2H_2O \rightarrow O_2 + 4H^+ + 4e^- \quad (1\text{-}6)$$

On the other hand, in the non-aqueous Li-O_2 cell, OER refers to the electrochemical decomposition of solid lithium oxide products formed during discharge of the cell and could be either a four or two electron process, or one that has as its first step, the formation of "a superoxide-like species":

$$2Li_2O \rightarrow O_2 + 4Li^+ + 4e^- \quad (1\text{-}7)$$

$$Li_2O_2 \rightarrow O_2 + 2Li^+ + 2e^- \quad (1\text{-}8)$$

$$Li_2O_2 \rightarrow Li_{2-x}O_2 + xLi^+ + xe^- \quad (1\text{-}9)$$

Li_2O has very rarely been observed however,[17] with the main discharge product in a Li-O_2 cell being Li_2O_2,[24] which can be electrochemically decomposed. Reaction 1-8 (or 1-9) remains challenging and the exact mechanism is still up for debate, although it is most likely dependent on both solvent and the morphology of the solid Li_2O_2. Compared to the ORR process, OER for the Li-O_2 cell has been studied much less intensively.

The mechanisms of the Li-O_2 discharge and charge reactions were elucidated in acetonitrile on a gold electrode.[25] It was found that the discharge process occurs through an "ECC" mechanism, with the initial electrochemical step ($O_2 + e^- \rightarrow O_2^{\cdot -}$) being followed by two chemical steps ($O_2^{\cdot -} + Li^+ \rightarrow LiO_2$ and $2LiO_2 \rightarrow Li_2O_2 + O_2$). The charge reaction was suggested to occur *via* direct electrochemical oxidation of Li_2O_2 (equation 1-

8), because any formation of superoxide (reaction 1-9) would be expected to decompose the propylene carbonate electrolyte that was used. No decomposition was detected. In acetonitrile, the oxidation of LiO_2 occurs at approximately 3.5 V and Li_2O_2 at around 3.75 V vs. Li/Li^+, so LiO_2 is not expected to be an intermediate in the oxidation process of Li_2O_2, since it would be unstable at the higher potential. In contrast, first-principles calculations have determined that decomposition starts with Li removal to form a superoxide, and that the kinetic rate of OER is highly dependent on surface orientation.[26] Based on this, a lithium deficient species could be an intermediate of the OER process, following reaction (1-9).

Although these studies provide a step forward, a more complete understanding of the reaction mechanisms of ORR and OER is still necessary. Since the Li-O_2 chemistry involves multiple phases (solid, gas, and liquid), controlling the precipitation of the discharge product(s) requires knowledge of the solubility of the O_2^-/LiO_2 intermediate. Additionally, it needs to be determined whether a surface or solution mediated pathway is dominant.

1.3 ORR/OER Catalysis and Materials Selection

The ultimate goal of investigations into the ORR process is to determine how to effectively increase the overall power and energy densities of the Li-O_2 cell. This could be accomplished through improvement of the discharge capacity, as well as increasing the discharge rate (ORR kinetics) without suffering a large overpotential.[27] Thus, one of the most important factors to increase the capacity is tailoring the porous cathode membrane. In theory, the capacity of the Li-O_2 cell is determined by the quantity of Li_2O_2 that is able

to be accumulated on or within the porous cathode structure, with the blockage of available surface area, catalytic sites for ORR, and/or open pores decreasing the capacity.[28] Computational studies have also shown that oxygen diffusion through the cathode assembly (in solution) and the accumulation of Li_2O_2 during discharge plays a large role in both increasing the discharge capacity as well as lowering the overpotential associated with ORR.[29] Li_2O_2 coverage will influence the increase of interfacial resistance of the cathode interior because it is an insulator by nature. Its deposition as a solid product on the cathode surface gives rise to electronic resistance that exacerbates any oxygen transport issues arising due to pore occlusion.[30,31] It was determined from these studies that Li_2O_2 passivation limits the accumulation on the cathode surface to tens of nanometers, occupying a volume fraction of the porous electrode of only a few percent before it ultimately terminates the discharge process.[29] If such homogeneous thin-film coverage of the cathode surface with Li_2O_2 occurs, this would greatly decrease the catalytic activity of the carbon and limit the supply of reactants (Li^+/O_2); furthermore, the subsequent high impedance of the cathode would require an even higher overpotential. This is obviously not an ideal situation to obtain maximum discharge capacity. Therefore, carefully designed cathode structure and architecture are critical in order to maximize the total pore volume while minimizing the ORR limitations caused by Li_2O_2 deposition by controlling the precipitation.

The effect that the cathode has on ORR has been described above: pore volume/dimensions and the electrochemically active surface area are major factors in overall discharge capacity, and the surface defects and functional groups facilitate the

growth of Li_2O_2, acting as active sites towards Li_2O_2 production and aiding in the ORR process. The role or the necessity of a co-catalyst in ORR is less clear. An increase in current density on discharge creates an increase in the discharge overpotential that is logarithmic with respect to the current, and not linear as would be the case of an ohmic IR drop due to internal cell resistances caused by Li_2O_2 accumulation.[32] Hence, the observed overpotential must also be related to kinetic activation barriers, implying that a more effective catalyst is necessary to minimize the discharge overpotential at high current rates and achieve respectable power density.[12] The vast majority of catalysts which have been examined for non-aqueous ORR in the Li-O_2 cell have been modelled after those which are highly active for ORR in aqueous solutions.[6,33] Metal oxides,[34] and even transition metal macrocycles like CoPc used in the very first Li-O_2 cell,[13] are widely known to have high activity for the reduction of oxygen in either acidic or alkaline aqueous media. They are used in primary (or secondary) metal-air batteries and fuel cells.[35] The use of metal-free catalysts via the modification of carbon by nitrogen doping is another promising avenue.[36,37,38] While it makes sense that these are also good candidates for ORR in non-aqueous media, it remains unclear whether they function in the same manner. There are studies which suggest that the discharge potential is similar in the presence and absence of a "catalyst".[8] Another discrepancy is observed in the case of pure carbon, which shows little catalytic activity for ORR in aqueous media,[38] but has significant activity in organic aprotic solvents.[39,40] Lu *et al.*[8] suggest that the high activity of the carbon present in Li-O_2 cathodes dominates the ORR kinetics, given that it is usually present in larger quantities than the electrocatalyst of interest.

Previous studies that investigated the role of Li-O_2 catalysts have demonstrated their importance for improved Li-O_2 performance in terms of discharge capacity, and reducing the overpotential. Since most of these studies were performed in carbonate-based electrolytes, where – unfortunately - OER catalysis (and cyclability) is dominated by the oxidation of the decomposition products, some of the proposed mechanisms explaining improved electrochemical performance need to be revisited. Nonetheless, the reduction of oxygen to form LiO_2 is the same regardless of the electrolyte, suggesting that catalysts could have vital roles to play by generating active sites for oxygen reduction, and affecting the strength of LiO_2 binding and the morphology of the peroxide. The underlying concepts provide useful information when designing a catalyst for use in new electrolyte systems: for example, the idea of catalyst morphology. As demonstrated by Debart *et al.*,[6] the performance of a metal-oxide catalyst in a Li-O_2 cell is directly influenced by its morphology. Nanomaterials are prime candidates for ORR catalysts in a Li-O_2 cell due to their larger surface area compared to their bulk counterparts. The uniform distribution of catalysts on the cathode surface to maximize the interaction between active materials and catalytic sites, as well as improved electrical connection between catalyst sites and the current collector, have been proven to be pivotal in improving ORR of the Li-O_2 cell.[41,42] Inherent catalytic activity is paramount though. AuPt alloys have been reported to be successful bi-functional catalysts that target both the ORR and OER of a Li-O_2 cell,[43] although more recent reports suggest that Pt strongly promotes electrolyte decomposition on charge.[18] From a practical point of view, cost and availability are also important factors. The development of bi-functional catalysts is a key area that will gain future ground once other pressing issues, such as finding a suitable electrolyte, are resolved.

The role of an ORR catalyst in a Li-O_2 cell, while still important, is less so compared to that of an OER catalyst owing to the very poor abilities of carbon to conduct OER. Without effective removal of the peroxide on the oxidation cycle, clogging of the active ORR sites occurs and discharge – and hence reversible capacity – is curtailed. While it is somewhat unclear whether or not catalysts can assist in lowering the overpotential associated with this reaction, the morphology of the Li_2O_2 formed during discharge most definitely plays an important role in its subsequent oxidation during charge. Direct contact of solid Li_2O_2 and a catalyst particle (or carbon) must be made since Li_2O_2 has been reported to have zero solubility in organic electrolytes.[44] The morphology and surface coverage of the catalyst is also critical to ensure contact. The focus on developing such catalysts should be on nanoscale materials with high surface area and uniform dispersion on the carbon support surface to maximize electrocatalytic area and mass activity.

Following the preliminary studies and controversial debate over the effect of catalysts,[18,45] and mainly due to the apparent high activity of carbon for ORR, a trend in the literature appeared to fabricate oxygen electrodes using only carbonaceous materials which were free of metal and metal oxide catalysts.[23,24,46,47] These had the benefits of being inexpensive, lightweight and having high capacities. The performance of new carbon based materials - aside from commercially available carbon black - has proven to be very successful when used in conjunction with a stable electrolyte, however. Mitchell *et al.* have used carbon nano-fibers as a free standing cathode structure, eliminating the need for a binder.[23] This electrode design demonstrates an exceptionally high discharge capacity of 7,200 mAh g_c^{-1}, the result of deposition of characteristic Li_2O_2 large "toroids"

on the carbon surface. The toroidal morphology of the Li_2O_2 is very interesting, because it gives rise to very non-uniform surface coverage. Nor is the size of the product within the tens of nanometer size limitation for which ORR termination was theoretically determined to occur.[29,12] At the time of that report, this was the highest capacity reported, and it was suggested that the inhomogeneous surface coverage reduces the surface resistance, allowing for more complete discharge. Other recent studies have turned to a graphene as a different lightweight, conductive and catalytically active surface. With respect to aprotic electrolyte Li-O_2 cells, two reports have been published recently which studied catalyst-free graphene as the positive electrode. Yoo *et al.* focused on the cycling capabilities of graphene (in a carbonate based electrolyte)[48], while Xiao *et al.* utilized a hierarchical porous graphene in a *primary* (*i.e.* non-recharged) Li-O_2 cell, to obtain an extremely high discharge capacity of 15,000 mAh g_c^{-1}.[24] Of interest in this report is that the ORR product, confirmed to be Li_2O_2, takes on a completely different morphology compared to the toroids reported by Mitchell *et al.* discussed above.[23] The deposited Li_2O_2 appears to be small nanometer sized particles that are isolated from one another. This is intriguing owing to the fact that the ultra-high capacity is obtained with no visible blockage of pores as occurred for the toroid structures once maximum discharge was reached.[23] These structures, much like the toroids, do not show uniform surface passivation that was predicted to be a limiting factor for ORR.[29] The proposed explanation for this observation is supported through DFT calculations, which reveal that the degree of Li_2O_2 formation is dependent on surface defects present on the graphene. Li_2O_2 is more strongly bound to defect sites and surface functional groups compared to that of defect free graphene sites. This is a key reason for both the high discharge as well as the small Li_2O_2 particle

formation.[24] The specific nature of the graphene surface/Li_2O_2 interaction also gives rise to limited aggregation among Li_2O_2 particles as a result of this being energetically unfavourable. The result experimentally demonstrates that the binding of Li_2O_2 to the cathode surface directly impacts not only the total discharge capacity but also affects the deposited product morphology. Furthermore, the binding energy is dependent upon both the fraction of defects on the graphene surface, as well as the surface functional groups. The lack of surface passivation and no observable pore occlusion demonstrates that the presence of surface defects and functional groups aid in overcoming the transport and conductivity issues that are associated with complete Li_2O_2 surface coverage. Through the restriction of Li_2O_2 production to defect sites and limitation of their agglomeration size to within a few nanometers (to essentially maintain surface Li_2O_2 and not bulk), the cathode surface will maintain its high electrical conductivity,[49] utilize more surface area, and better permit oxygen diffusion to the surface. Utilization of a tailored carbon material that allows one to modulate the morphology of the discharge product has significant implications for increased ORR performance as well as improved OER performance: smaller, better dispersed Li_2O_2 should ultimately lead to superior cycling stability, although cell charging was not examined in the study. Hence, the amount of control that the cathode provides over the Li-O_2 ORR reaction is quite clear. Exploring the role of surface defects for Li-O_2 ORR is an important direction for future research, for it is clear that these defect sites and surface groups are key components for Li_2O_2 nucleation. Intriguingly, recent reports suggest that the surface of lithium peroxide possesses metallic conductivity owing to the reduced coordination of oxygen atoms in the outer Li_2O_2

region.[39] Future studies focusing on fine tuning the parameters associated with Li_2O_2 morphology and passivation will be a major contribution to Li-O_2 developments.

However, since these studies of carbonaceous electrodes, carbon was found to suffer from instability related to oxidation at high voltages and in the presence of the O_2^-/LiO_2 and Li_2O_2. [50, 51] More recently, carbon-free electrodes have been under examination.[52,53,54,55,56] In the work of Lu *et al.*,[57] the carbon used as a support was passivated by Al_2O_3 and the surface was decorated with Pd nanoparticles to drastically lower the overpotential on charge relative to a pure carbon electrode. Also, in the work of Peng *et al.*,[58] a nanoporous gold electrode was used in conjunction with a DMSO electrolyte to obtain 100 cycles with reversible capacity. Since all reactions occur at the surface of any given electrode material (carbon, catalyst, or non-carbon support), an understanding of the surface chemistry is required to design stable and active oxygen electrodes.

1.4 Influence of Electrolyte on the Performance of the Li-O_2 Battery

The choice of organic solvent is perhaps the most important factor in the performance and development of non-aqueous Li-O_2 cells. A good electrolyte should possess the following qualities: good stability against O_2^- attack; a wide potential window to withstand both high oxidation potentials and be stable to reaction with metallic lithium; low viscosity; low volatility; and high oxygen solubility. Reaction with the highly reactive radical species (O_2^-, LiO_2) to form decomposition products is especially problematic for alkylcarbonate electrolytes. They are highly subject to nucleophilic attack of the superoxide radical (O_2^-),[59] the initial product formed from the oxygen reduction reaction

(ORR) upon discharge. Their instability was made apparent by Mizuno *et al.*[20] and Freunberger *et al.*,[21] who demonstrated that the cycling performance associated with Li-O_2 cells utilizing carbonate based electrolytes were primarily due to oxidation of the decomposition products of the electrolyte on charge, and not Li_2O_2 (**Figure 1.2**). Experimental studies using chemically generated superoxide to probe its reactivity with different solvents confirm the high reactivity of propylene carbonate, and indicate that ethers such as TEGDME are relatively stable.[60] This is also supported by theoretical studies using DFT that show that ethers are more stable to the oxygen reduction products;[61,62] however, behavior in an actual cell, especially on charge at high potential in the presence of lithium peroxide, may be different and more investigation is necessary. The importance of electrolyte stability cannot be overstated, since this governs the nature of both the ORR and OER processes. This is currently the most challenging hurdle that must be overcome before any other component of the Li-O_2 cell (catalyst, cathode etc.) can be properly evaluated.

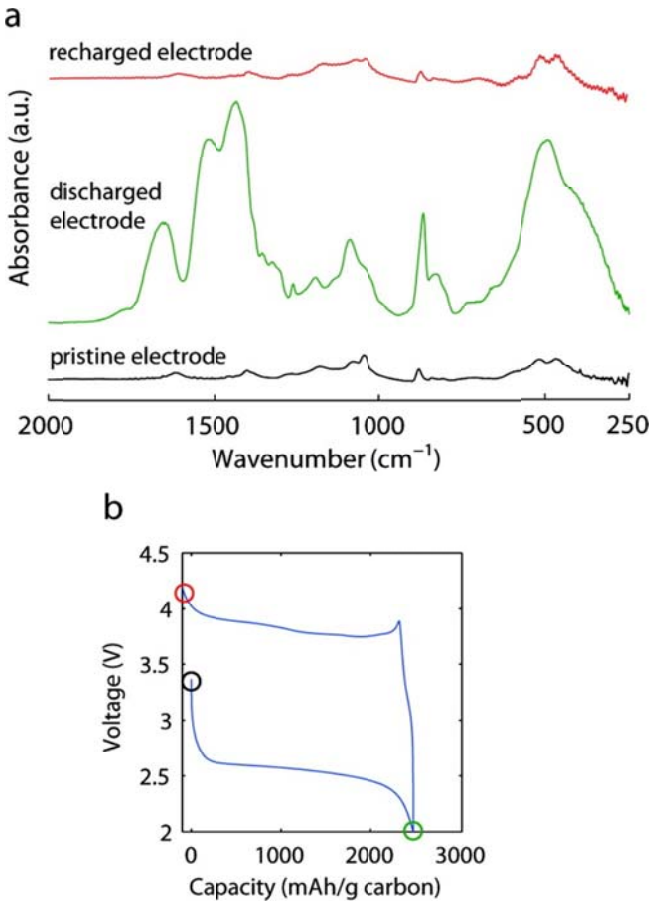

Figure 1.2 (a) FTIR spectra of a pristine electrode (Super P/α-MnO_2/Kynar) and after the first discharge, then charge in 1 M $LiPF_6$ in PC under O_2. (b) Variation of voltage as cell is discharged then charged. The FTIR data in (a) show the spectra from the pristine electrode and the electrode after one cycle are identical, indicating that the products of electrolyte decomposition that are formed on discharge (namely $C_3H_6(OCO_2Li)_2$, Li_2CO_3, HCO_2Li and CH_3CO_2Li) are oxidized on charging to 4.2 V as shown in the electrochemical curve in (b). [21]

As discussed above, it has been shown that ether-based electrolytes form Li_2O_2 upon discharge.[15] 1,2-dimethoxyethane (DME) and tetraethylene glycol dimethyl ether (TEGDME) have both been used successfully as solvents to form the desired Li_2O_2 product during discharge.[4,15,17,18,23,24] While TEGDME is far more stable to $O_2^{\cdot-}$ attack than carbonate-based electrolytes, Freunberger *et al.*[63] have observed some decomposition which results in a combination of Li_2CO_3, HCO_2Li, CH_3CO_2Li, polyethers/esters, CO_2, and H_2O in addition to Li_2O_2. The amount of Li_2O_2 formed on the first discharge diminishes after repeated cycling in favour of greater electrolyte decomposition. A recent study that compared PC:DME and DME as solvents suggests that although catalysts aid in lowering the charging overpotential when PC:DME is used as the solvent, the overpotential is identical among the chosen catalysts when DME alone is the solvent.[18] **Figure 1.3** displays the major results from this study. The use of online electrochemical mass spectroscopy (OEMS) coupled to galvanostatic cycling of the Li-O_2 cells proved to be a very powerful tool to analyze gas evolution during charging. Their work verified that of Lu *et al*.[43], showing that when PC:DME was used as the electrolyte solvent, Au (and Pt) catalyze ORR and Pt catalyzes OER. However, it also shows that large amounts of CO_2 are produced from the oxidation of lithium alkyl carbonates. In DME, only Pt shows catalytic activity for ORR, yet it decomposes the electrolyte upon charge. This suggests that Li_2CO_3 oxidation can be catalyzed, yet Li_2O_2 oxidation cannot. It is possible however, that carbon itself is better at catalyzing the OER from Li_2O_2 than the chosen catalysts of their study.

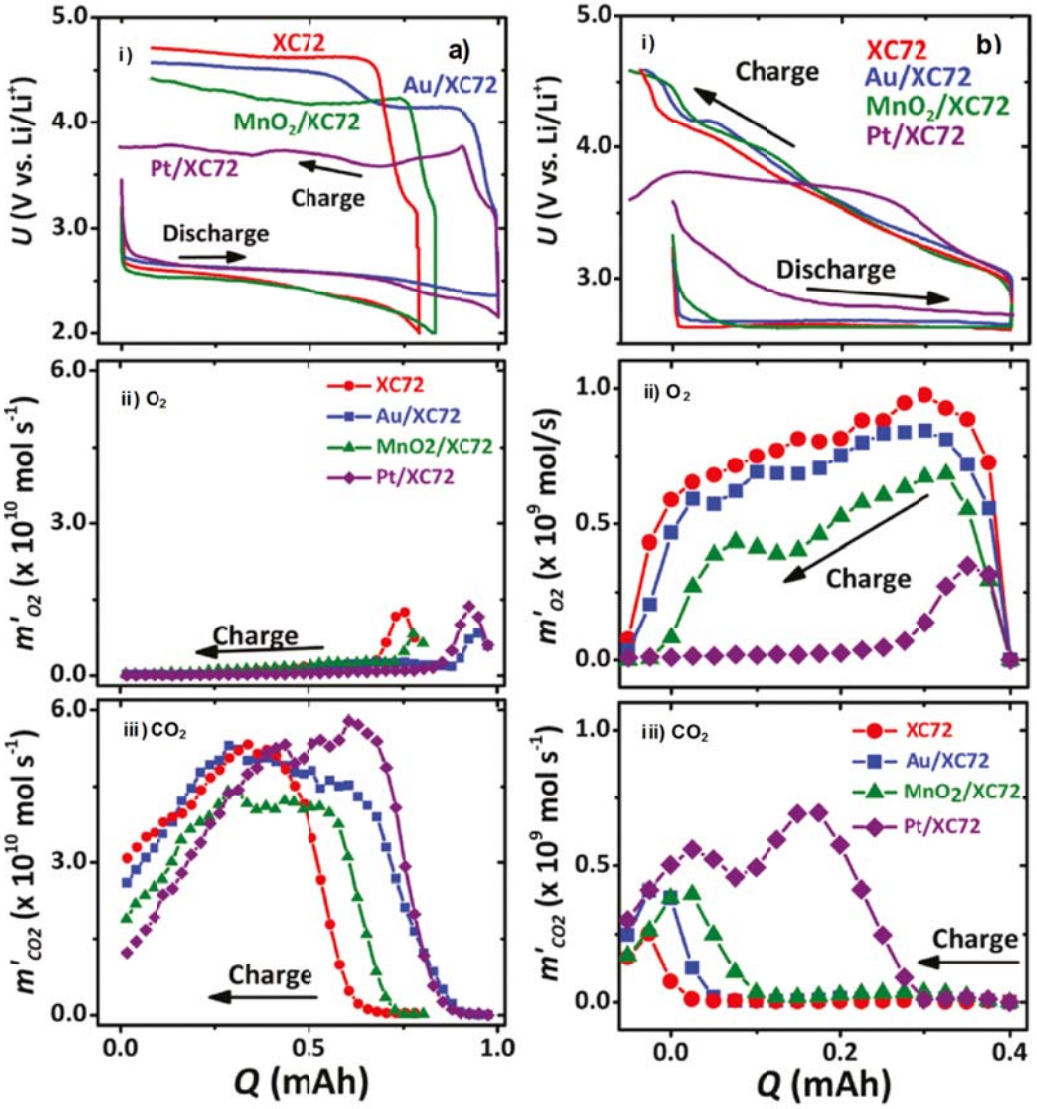

Figure 1.3 Gas evolution from cells employing a) 1PC:1DME and b) DME. i) Discharge-charge voltage curves, and corresponding ii) O_2 and iii) CO_2 evolution during charging of cells using various cathode catalysts. m'_i is the molar generation of species "i", U is cell output voltage, and Q is cell charge.[18]

Apart from electrolyte decomposition, a few defining electrolyte properties have a very large impact on the ORR process. Solvents that possess characteristics of high oxygen solubility as well as low viscosity are optimal. Electrolytes with these characteristics show increased discharge capacity due to a higher concentration of oxygen in solution, as well as improved ORR kinetics due to improved oxygen diffusion. [5,64] While these studies were performed in carbonate based electrolytes, the knowledge gained from these studies still applies to new electrolytes being investigated today. The applicability of ionic liquids, for example, is under investigation. To date, their high viscosity and poor oxygen diffusion has been shown to negatively affect the ORR process.[65] However, other important factors for Li-O_2 cells, such as hydrophobicity (to prevent water from reaching the Li-metal anode) and low volatility to prevent evaporation, are properties of ionic liquids that makes them appealing.[66,67]

One specific area of electrolyte properties that deserves recognition is the concept of Hard Soft Acid Base theory.[68] O'Laoire *et al.* explored various electrolyte systems to determine the effect that the donor number (DN, solvent basicity) and acceptor number (AN, solvent acidity) of solvents had on the Li-O_2 discharge product.[17] The coordination strength of solvent molecules to the Li^+ ions is dependent on the DN of the solvent. The Li^+ ion, being a hard Lewis acid, exhibits modified properties based on the solvent's coordination strength. The Li^+ ion will have a high affinity for the strong basic products of oxygen reduction O_2^{2-} and O^{2-}, and hence under normal circumstances with a low DN solvent (where the Li^+ still exhibits hard acid character), the stable reduction products are Li_2O_2 and Li_2O. Production of O_2^-, a soft base, will either disproportionate to O_2^{2-} and O_2,

or undergo a direct second reduction step to O_2^{2-} in a low DN number solvent to increase stability.[19] Hence, a solvent with a low DN and weak coordination for Li^+ will favour the production of Li_2O_2. High DN solvents modulate the acidity of Li^+ to give it the characteristics of a weak acid, resulting in the formation of stable Li^+[solvent]--O_2^- complexes due to the stable nature of O_2^- in high DN solutions. The consequence of this is that Li_2O_2 is not the favoured end product of O_2 reduction in the presence of the Li^+ cation. In the presence of other species, as in the case of alkylcarbonate electrolyte decomposition, Li^+ preferentially reacts with the more weakly basic CO_3^{2-} ions in solution as opposed to O_2^-, resulting in the multitude of Li-carbonate discharge products that are observed.[5,6,17] Based on this principle, O'Laiore *et al.* have defined TEGDME, a relatively low DN solvent, as a useable Li-O_2 electrolyte.[4] Thus, the use of HSAB theory can be utilized in a Li-O_2 system as a control medium, for modulation of the Li^+ ion acidity within solution can lead to affinity for different types of discharge products during ORR. Successful implementation of this theory can be used for future investigation of different electrolytes, and should be a prime consideration for optimization of the Li-O_2 cell.

Related to the theory above, the addition of water has been used to promote a solution mediated process by solubilizing the O_2^- intermediate.[69,70] The effect of water, however, has been also proven to be detrimental due to high reactivity of the formed HO_2.[71,72] Beyond the glyme electrolyte, high donor number solvents such as amides have been examined. Giordiani *et al.*,[73,74,75] have studied a lithium nitrate salt in dimethyl acetamide ($LiNO_3$/DMA) electrolyte. DMA is unstable in the presence of metallic lithium, yet the group claims it is stable against attack by superoxide. In this case the lithium nitrate acts to

passivate the lithium negative electrode through a synergistic mechanism with oxygen in the electrolyte. However, the work by Chen *et al.*[76] clearly shows that while amides, including DMA and dimethylformamide (DMF), are more stable than the family of glymes and ethers, they are still subject to superoxide attack. The products formed during discharge are Li_2O_2, Li_2CO_3, HCO_2Li, CH_3CO_2Li, NO, H_2O, and CO_2. Of these, mainly the lithium carbonate accumulates in the electrode with cycling. Overall, the authors suggest that the stability of amides (mainly DMF) towards reduced oxygen species is insufficient for their use in aprotic Li-O_2 batteries. Currently, the use of dimethylsulfoxide (DMSO) as a solvent is under much scrutiny. The Bruce group[58,77] has used DMSO in conjunction with non-carbonaceous electrodes (Au and TiC) to provide 100 cycles in both cases with no capacity fade. Xu *et al.* also attest to its stability,[78] and Trahan *et al.* [79] prove that its high donor number aids in stabilizing the $1e^-$ reduction product (O_2^-/LiO_2). On the other hand, with the extensive combination of fourier-transform infrared spectroscopy (FTIR), nuclear magnetic resonance spectroscopy (NMR), energy dispersive X-ray spectroscopy (EDS), X-ray photoelectron spectroscopy (XPS), mass spectrometry (MS) and X-ray diffraction (XRD) techniques, DMSO was proven to decompose in the Li-O_2 battery by two separate groups of researchers.[80,81] The decomposition products include LiOH, dimethylsulfone, Li_2SO_3, and Li_2SO_4. These conflicting results will be discussed again in chapters 5 and 7 of this thesis.

1.5 Summary

In the non-aqueous Li-O_2 system, most initial research has employed carbonate-based electrolytes. Because of the preponderance of using carbonate-based electrolytes, the published studies on OER catalysts to date have mostly only proven that the oxidation of *Li_2CO_3* is catalytically sensitive. The Li_2CO_3 precipitates on the surface of porous positive electrodes or within its pores, and little or no Li_2O_2 is observed. The oxidation of Li_2CO_3 to Li^+, CO_2, and O_2, occurs theoretically at 4 V,[82] which is slightly lower than the potential observed in most studies. It is hopefully now universally recognized that these electrolytes decompose in the presence of the superoxide radical, the initial ORR product. They should no longer be used in research on non-aqueous Li-O_2 cells. Although ether based electrolytes such as DME and TEGDME appear to be relatively stable in the presence of superoxide on discharge, their electrochemical behavior remains to be thoroughly investigated. The search is on for new electrolytes which are fully stable on cycling. Additionally, investigations on the stability of carbonaceous electrodes and the development of carbon-free electrode materials are paramount. To clarify the use of terms "carbonaceous", "non-carbonaceous" and "carbon-free" in this thesis; these are used to distinguish between electrodes in which the active component is pure carbon and those which are not. Titanium carbide, for example, is considered as a non-carbonaceous or carbon-free material. Knowledge of the precise ORR and OER pathways in non-aqueous solvents containing Li^+ salts is also of importance. Conflicting views on the solubility limits of the discharge intermediate, superoxide need to be addressed to determine the reaction mechanisms (surface vs. solution mediated processes) and control the discharge product. Additionally, understanding the effect that the morphology and chemical nature

of the discharge product(s) has on the charge performance, and thus cycleability, will be highly beneficial in the development of the aprotic Li-O_2 battery.

1.6 Scope of this Thesis

Chapter 1 is a general introduction of pertinent research that has been undertaken in the past few years on the non-aqueous Li-O_2 battery. This chapter was reproduced in part with permission from R. Black, B. Adams and L. F. Nazar, *Adv. Energ. Mater.* **2012**, *2*, 801–815; Copyright 2012: WILEY-VCH Verlag GmbH & Co. KGaA, Weinheim. Chapter 2 is an overview of the research methods and techniques that were used in this thesis. Chapter 3 contains the results of a study on the dependence of current density on lithium peroxide formation in the Li-O_2 battery and its effect on charge. The work has been published elsewhere: B. D. Adams, C. Radtke, R. Black, M. L. Trudeau, K. Zaghib, and L. F. Nazar, *Energy Environ. Sci.*, **2013**, *6*, 1772–1778; Copyright 2013: The Royal Society of Chemistry. In chapter 4, the pathway of the oxygen evolution reaction from solid Li_2O_2 is revealed with the aid of operando X-ray diffraction and scanning electron microscopy. This work has been previously published: S. Ganapathy, B. D. Adams, G. Stenou, M. S. Anastasaki, K. Goubitz, X.-F. Miao, L. F. Nazar, and M. Wagemaker, J. Am. Chem. Soc. **2014**, *136*, 16335–16344; Copyright 2014: American Chemical Society. In chapter 5, the nature and role of surface films on positive electrode materials for Li-O_2 batteries is examined. This work is published elsewhere: B. D. Adams, R. Black, C. Radtke, Z. Williams, B. L. Mehdi, N. D. Browning, and L. F. Nazar, *ACS Nano*, **2014**, *8*, 12483–12493; Copyright 2014: American Chemical Society. Chapter 6 compares the oxygen reduction and evolution reactions in an alkaline aqueous electrolyte to aprotic non-aqueous

electrolyte and examines the electrocatalytic effect of two different electrode materials for these reactions in Li^+-containing non-aqueous media. This work has been published elsewhere: S. H. Oh, B. D. Adams, B. Lee, and L. F. Nazar, *Chem. Mater.* **2015**, *27*, 2322–2331; Copyright 2015: American Chemical Society. Chapter 7 describes the synthesis and study of a new chelate ionic liquid electrolyte which demonstrates enhanced stability in the Li-O_2 battery. This work has been published previously: B. D. Adams, R. Black, Z. Williams, R. Fernandes , M. Cuisinier, E. J. Berg, P. Novak, G. K. Murphy, and L. F. Nazar, *Adv. Energy Mater.* **2015**, 5, 1400867; Copyright 2015: WILEY-VCH Verlag GmbH & Co. KGaA, Weinheim. Chapter 8 concludes and summarizes this entire thesis.

Chapter 2

Experimental Methods and Theory

2.1 Chemicals and Materials

The following is a list of all chemicals and materials used throughout this thesis: tetraethylene glycol dimethyl ether (99%, Aldrich), 1,2-dimethoxyethane (99.5% anhydrous, Sigma-Aldrich), acetonitrile (anhydrous HPLC Grade, 99.8%, Caledon or 99.8%, Sigma-Aldrich), lithium hexafluorophosphate (Novolyte), tetrabutylammonium hexafluorophosphate (for electrochemical analysis, >99.0%, Fluka), lithium bis(trifluoromethanesulfonyl) imide (Novolyte), silver perchlorate (97% anhydrous, Aldrich), ferrocene (98%, Aldrich), lithium peroxide (90%, Sigma-Aldrich), Triton X100 (Laboratory Grade, Sigma), propylene carbonate (anhydrous, 99.7%, Sigma-Aldrich), *N*-Methyl-2-pyrrolidone (≥99%, Sigma-Aldrich), Nafion® perfluorinated resin solution (DE521, 5 wt.% mixture in lower aliphatic alcohols and water, Aldrich), tetrabutylammonium perchlorate (≥99%, Fluka), polytetrafluoroethane (free-flowing powder, 1 μm particle size, Aldrich), polytetrafluoroethane (60 wt.% dispersion in H_2O, Sigma-Aldrich), tetrabutylammonium bis(trifluoromethanesulfonyl) imide (for electronic purposes, ≥99.0%, Fluka), molecular sieves (4A, Sigma-Aldrich), titanium mesh (100 mesh, Alfa Aesar), stainless steel mesh (100 mesh, 316 grade), titanium nitride (nanopowder <20 nm, >97%, Nanostructured and Amorphous Materials), titanium dioxide (anatase nanopowder, <200nm, 99.7%, Aldrich), glass fiber filter without binder (AP4004705, Millipore), lithium (foil ribbon, 0.75 mm thickness, 99.9%, Aldrich), oxygen

(99.995%, Linde or 99.999%, Praxair), Toray carbon paper (TGP-H-030, Fuel Cell Store), potassium hydroxide (semi-conductor grade, 99.99%, Sigma-Aldrich), ^{13}C carbon (99%, Aldrich), lithium hydroxide hydrate (>98%, Alfa Aesar), argon (99.999%, Praxair), Vulcan XC72 (Cabot Corp.), 2-propanol (anhydrous, 99.5%, Sigma-Aldrich), TiC-A (titanium (IV) carbide nanopowder, <200 nm, 95%, Aldrich), TiC-B (titanium carbide nanopowder, <25 nm, 99+%, US Research Nanomaterials), lithium carbonate (99.997%, Aldrich), lithium hydroxide (anhydrous, 98%, Alfa Aesar), sodium formate (99.0%, Sigma-Aldrich), sodium thiosulfate (97%, BDH Laboratory Supplies), ammonium heptamolybdate tetrahydrate (99.98%, Sigma-Aldrich), potassium iodide (anhydrous, 99%, Sigma-Aldrich), sodium phosphate monobasic dihydrate (≥99.0%, Sigma), sodium phosphate dibasic (>99.0%, Sigma-Aldrich), activated carbon (Kuraray Chemical), carbon paper (Spectracarb), P50 carbon paper (Fuel Cell Store), hexadecyl-trimethylammonium chloride (Fluka), ruthenium(III)nitrosyl nitrate (1.53 wt.% Ru solution, Sigma-Aldrich), lead subacetate (ACS grade, Fischer Scientific), sodium hydroxide (≥97.0%, Sigma-Aldrich), sodium hypochlorite (reagent grade, available chlorine 10-15%, Sigma-Aldrich), cobalt nitrate hexahydrate (98%, Sigma-Aldrich), nickel nitrate hexahydrate (≥97%, Sigma-Aldrich), glycine (≥98%, Alfa Aesar), chloroplatinic acid hexahydrate (99.9%, Alfa Aesar), hydrochloric acid (37%, Sigma-Aldrich), sodium borohydride (powder, ≥98.0%, Aldrich), dimethylsulfoxide (dried, ≥99.9%, ≤0.03% water, Sigma-Aldrich), tetrahydrofuran (>99%, Caledon), sodium hydride (50 wt.% in mineral oil, J.T. Baker), iodomethane (99%, Sigma-Aldrich), deuterium oxide (99.9% D, Aldrich), deuterated chloroform (99.8% D, Cambridge Isotope Laboratories), potassium superoxide (Sigma-Aldrich), 18-crown-6 (99%, Sigma-Aldrich), pinacol (98%, Aldrich), triethylamine

(≥99%, Sigma-Aldrich), tetraethylene glycol (99%, Alfa Aesar), chlorotrimethylsilane (≥99.0%, Sigma-Aldrich), lithium fluoride (99.98%, Sigma-Aldrich).

2.2 Purification Techniques

Tetraethylene glycol dimethyl ether was vacuum distilled over metallic sodium, and all solvents dried over molecular sieves (4A, Sigma-Aldrich) prior to use. The molecular sieves were always activated prior to use by heating at 250 °C under vacuum for 24 hours. The water content of the solvents was ensured to be <1 ppm by the Karl Fischer titration method with a C30 Coulometer (Mettler Toledo) or an 831 KF Coulometer (Brinkman, Metrohm).

The tetrabutylammonium hexafluorophosphate, tetrabutylammonium bis(trifluoromethanesulfonyl) imide, lithium hexafluorophosphate, and silver perchlorate were dried at 110 °C for 24 hours. Lithium bis(trifluoromethanesulfonyl) imide was dried at 120 °C under vacuum for at least four days. The ferrocene was purified by sublimation at 110 °C.

In Chapter 7, the water content of dried DMDMB was below detection limit of the instrument (<1 ppm) and $[(DMDMB)_2Li]TFSI$ was <10 ppm. The slightly higher water content of the $[(DMDMB)_2Li]TFSI$ electrolyte was the result of the large quantities of the LiTFSI salt, although rigorous drying of the salt was undertaken prior to preparation of the electrolyte.

2.3 Electrochemical Methods

2.3.1 Electrochemical Cells

2.3.1.1 Three-Electrode System

All three-electrode studies were performed in an Argon-filled glovebox, with the exception of the aqueous studies in Chapter 6. The gas-tight cell design (**Figure 2.1**) consisted of a four-neck round-bottom flask. One neck was fitted with a gas-flow stopper which supplied and vented gas from tanks outside the glovebox. This gas flow system was controlled with valves located on the glovebox exterior. The electrodes were placed in the other flask openings. The vertical flask opening was used for the working electrode in all cases and allowed for the shaft of the rotating (ring) disk electrode system to be used. The modulated speed rotator (AFMSRCE, Pine Instruments) was also contained in the glovebox. Experiments were controlled with a VMP3 potentiostat and EC-Lab® software (Bio-Logic Science Instruments). In the case where the rotating ring disk electrode was used, two separate channels were used on the potentiostat with shared counter and reference electrodes.

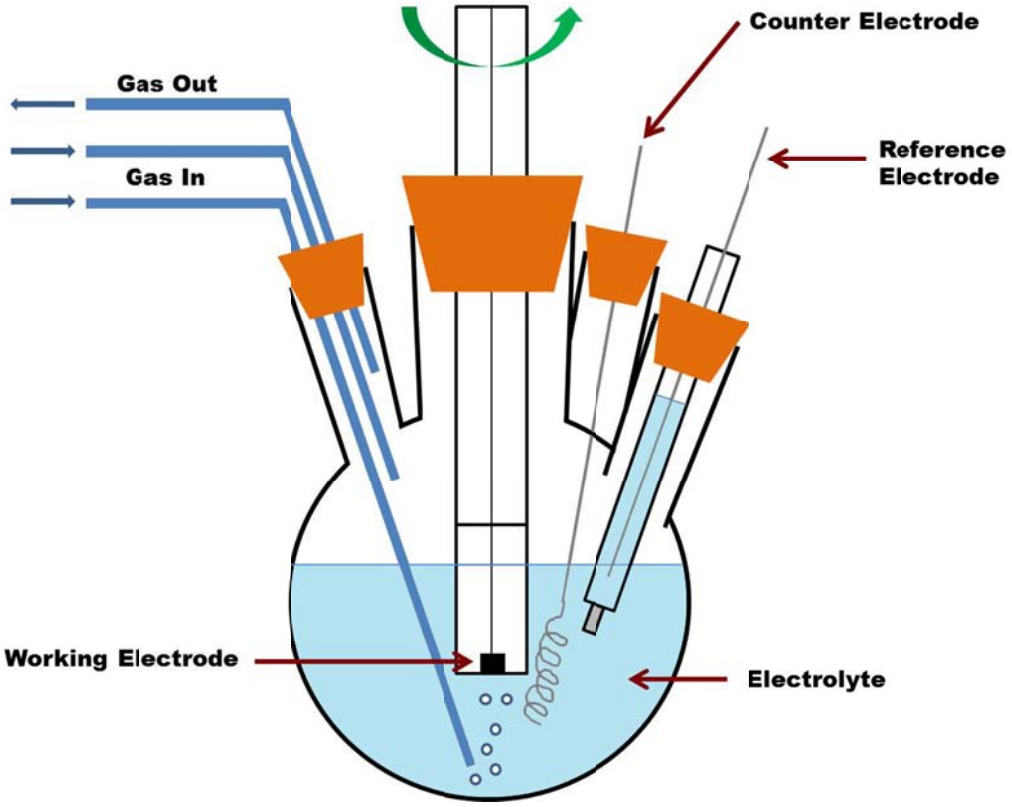

Figure 2.1 The schematic diagram of a gas-flow-enabled three-electrode cell used in the studies in this thesis. The working electrode pictured is a rotating disk electrode, however, the glassy carbon disk was also used without rotation in some cases, or alternatively, a rotating ring disk electrode or different working electrodes were substituted.

2.3.1.2 Two-Electrode System

Non-aqueous Li–O_2 cells were prepared using a modified Swagelok™ design. A 1 M LiTFSI (Novolyte) in dry, distilled TEGDME (<1 ppm H_2O) electrolyte was used in all studies with the exception of Chapter 7 where the $[(DMDMB)_2Li]TFSI$ and $[(DME)_2Li]TFSI$ electrolytes were used. Cells were assembled in an argon filled glovebox with a lithium metal anode, porous separators (millipore glass fiber), and a gas diffusion

electrode as the cathode (**Figure 2.2**). Electrolyte (50 µL – 200 µL) was added to the separator during cell assembly. In the case of the cells which were discharged, O_2 (99.999%, Praxair) was introduced through a quick connect gas line system with Swagelok™ fittings and metal tubing. An excess volume of O_2 was stored in a headspace (an aluminum tube above the cathode) at a pressure of 1.5 atm. For all Li_2O_2-loaded electrodes, galvanostatic charging was performed under an argon atmosphere. The cells were equilibrated at open circuit for 6 h before testing.

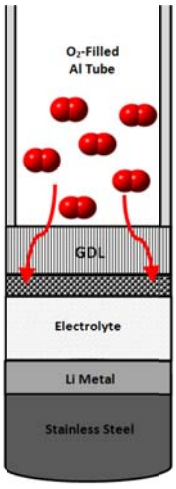

Figure 2.2 The schematic design of the Li-O_2 cells used in this study.

2.3.2 Electrode Fabrication

2.3.2.1 Gas Diffusion Electrodes

Two types of porous electrodes (gas diffusion electrodes, GDEs) were used in this work, depending on the binder utilized. In Chapters 3 and 4, lithiated Nafion® was used as the binder. The Li^+ form of a perfluorosulfonate ionomer (Nafion-Li) was prepared via a solution-based exchange of the protons in Nafion®.[1] A solution of 0.1 M LiOH was

prepared from $LiOH{\cdot}H_2O$ (>98%, Alfa Aesar). The LiOH solution was added over the course of several hours to a magnetically stirred Nafion® perfluorinated resin solution (5 wt. % in mixture of lower aliphatic alcohols and water, Aldrich). The ion-exchange was deemed to be complete once the pH = 8. This solution typically contained 3.24 wt. % Li-Nafion in water and lower aliphatic alcohols. To eliminate the aqueous-based solvent in this binder, the Nafion-Li solution was mixed with *N*-Methyl-2-pyrrolidone (NMP) (≥99.5 %, Aldrich) at heated to 120 °C. At this temperature, the alcohols and water were completely evaporated and exchanged with NMP as the solvent.

Gas diffusion electrodes were prepared by casting an active (carbon black + binder) layer on a gas diffusion layer (GDL). Vulcan XC72 (400 mg), 1 g NMP and 4 g Li-Nafion (10wt%)/NMP were very well mechanically mixed for 10 minutes followed by ultrasonication for 1 hour. Films of this mixture were cast onto Toray carbon paper (TGP-H-030, Fuel Cell Store). After drying at 90 °C for 1 hour, the gas diffusion electrodes were punched from the film (1 cm^2 area) and further dried at 100 °C *in vacuo* for 24 hours. The active layers of these gas diffusion electrodes had an average thickness of 10 μm and masses ranging between 0.5 to 1.5 mg. **Figure 2.3** displays the first discharge curves for a Toray carbon paper GDL and the coated carbon paper GDE. Only the Vulcan XC72 carbon is active for ORR. This is expected to be a result of poor electrolyte wetting of the Toray carbon paper (which is treated with hydrophobic Teflon®).

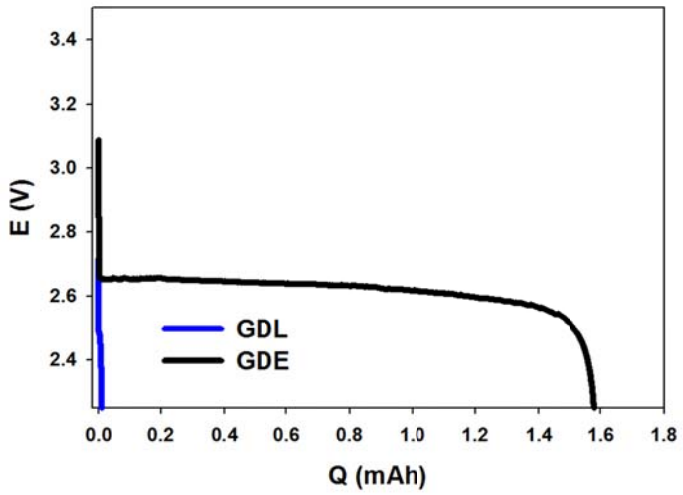

Figure 2.3 Discharge curves with gas diffusion layer (GDL) only and gas diffusion layer with an active coating of Vulcan XC72/Li-Nafion (gas diffusion electrode, GDE). Negligible capacity is observed for the GDL as expected.

In Chapters 5, 6 and 7, polytetrafluoroethylene (PTFE) was used as the binder. Typical gas diffusion electrodes were prepared by casting an active layer on a gas diffusion layer as described in previous publications.[1,2] In Chapter 5, Vulcan XC72 (Cabot Corp.) or titanium nitride nanopowder (<20 nm, >97%, Nanostructured and Amorphous Materials, Inc.) were mixed with PTFE in a ratio of 4:1 and films were cast onto Toray carbon paper (TGP-H-030, Fuel Cell Store). These sheets were first dried at 90°C for 1 hour and then annealed for an additional hour at 300°C under vacuum. After cooling, electrodes were punched (1 cm^2 area).

In Chapter 7, Vulcan XC72 (Cabot Corp.) was dispersed into a solution containing 2-propanol and water (1:2 volume) with 5 wt.% Triton X-100 non-ionic surfactant by ultrasonication. For the OEMS studies, ^{13}C carbon (Aldrich, 99%) was used as the active

carbon in replacement of the Vulcan XC72 which was used for all other studies. Next, PTFE was added (60 wt.% dispersion in H_2O, Sigma-Aldrich) such that the carbon:PTFE mass ratio was 80:20, and mixed well. Films were cast onto Toray carbon paper (TGP-H-030, Fuel Cell Store). These sheets were first dried at 90°C for 1 hour and then sintered for an additional hour at 350°C. After cooling, electrodes were punched (1 cm^2 area) and further dried at 100 °C *in vacuo* for 24 hours. The active layers of these gas diffusion electrodes had an average thickness of 17 μm and masses ranging between 0.5 to 1.5 mg.

Although both types of binders were found to be completely stable to nucleophilic attack in the Li-O_2 battery,[3,4] the switch from Nafion-Li to PTFE binder was made for practical reasons. The fabrication process using PTFE is much less time consuming and PTFE is substantially less expensive than Nafion®.

2.3.2.2 Pre-Filled Electrodes

In Chapter 4, the preloaded Li_2O_2 cathodes were made by combining Vulcan XC72 carbon (Cabot Corp.), Li_2O_2 (Sigma-Aldrich, 90%) and PTFE powder with a weight ratio of 4:1:1 in 2-propanol and casting the mixture on Toray carbon paper (TGP-H-030, Fuel Cell Store). This was carried out in an argon filled glove box (H_2O and O_2 content < 1 ppm). These preloaded Li_2O_2 electrodes were dried under vacuum at room temperature to remove the 2-propanol solvent. An example SEM image of the commercial Li_2O_2 powder and the composite electrode (**Figure 2.4**) reveal that the peroxide crystallite size is approximately 200 – 800 nm.

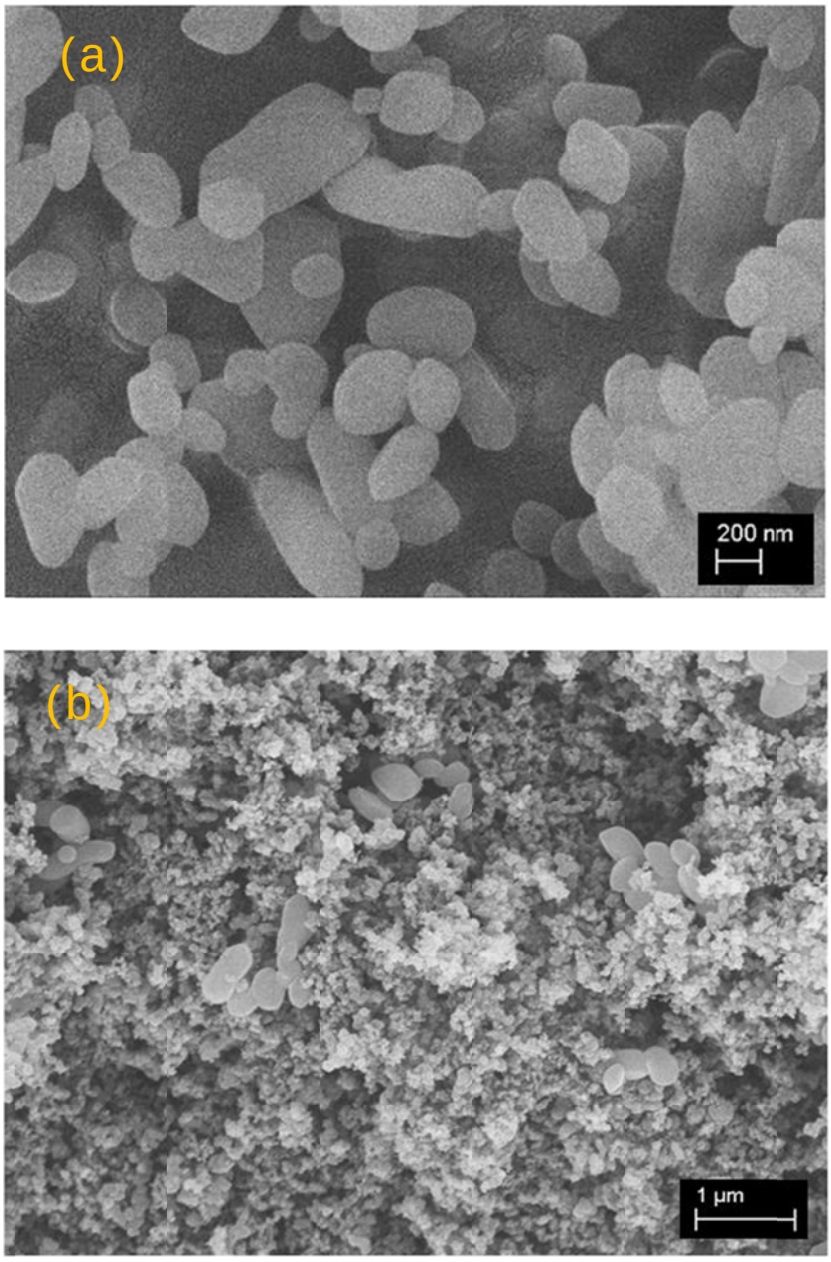

Figure 2.4 SEM images of (a) commercial Li_2O_2 powder, (b) carbon-PTFE-Li_2O_2 composite electrode.

In Chapter 5, a fresh bottle of lithium peroxide (90%, Sigma-Aldrich) was used as received. The actual purity of this powder was determined to be 88% by iodometric titration, using a modified method of what has been previously reported in the literature[5]

(see section 2.5 for details). The e^-/Li_2O_2 ratio, calculated by the electrical charge passed and the mass of Li_2O_2 in the electrode, was adjusted based on this value of purity. In an argon-filled glovebox, the Li_2O_2 powder was hand-mixed with Vulcan XC72 (Cabot Corp.), TiN (titanium nitride nanopowder <20 nm, >97%, Nanostructured and Amorphous Materials), TiO_2 (titanium (IV) oxide, anatase nanopowder, <200nm, 99.7%, Aldrich), TiC-A (titanium (IV) carbide nanopowder, <200 nm, 95%, Aldrich), or TiC-B (titanium carbide nanopowder, <25 nm, 99+%, US Research Nanomaterials) and a PTFE dispersion in 2-propanol. The resulting paste was spread onto Ti mesh (100 mesh, Alfa Aesar) disk substrates (1 cm^2). Stainless steel disks (100 mesh, 316 grade) were used as substrates for the OEMS studies. These formed electrodes were finally dried at room temperature under vacuum. The mass ratios of carbon:Li_2O_2:PTFE and TiX:Li_2O_2:PTFE were 4:1:1 and 4:0.5:1 in all cases.

In Chapter 6, lithium peroxide (90%, Sigma-Aldrich) was used as received. The actual purity of this powder was determined to be 83.4% by iodometric titration.5 The e^-/Li_2O_2 ratio (**Figure 6.4a,b**), calculated by the electrical charge passed and the mass of Li_2O_2 in the electrode, was adjusted based on this value of purity. The other powders used were lithium carbonate (99.997%, Aldrich), lithium hydroxide (anhydrous, 98%, Alfa Aesar), and sodium formate (99.0%, Sigma-Aldrich). These powders were physically mixed with Vulcan XC72 (Cabot Corp.) or lead ruthenium oxide pyrochlore and a PTFE dispersion in 2-propanol. The resulting paste was spread onto Ti mesh (100 mesh, Alfa Aesar) disk substrates (1 cm^2). These formed electrodes were finally dried at room temperature under vacuum. The mass ratios of carbon:active compound:PTFE and pyrochlore:active compound:PTFE were 4:1:1 and 10:1:0.5 in all cases.

2.3.3 Cyclic Voltammetry and Linear Sweep Voltammetry

Linear sweep voltammetry and cyclic voltammetry are potentiodynamic techniques where the potential is swept at a constant scan rate (V/s) (**Figure 2.5a**). A voltammogram is the resultant plot of current versus potential (**Figure 2.5b**). In linear sweep voltammetry, the potential is swept only in one direction, anodically or cathodically, in order to study one reaction. In cyclic voltammetry, the potential is swept in the forward direction, then subsequently, in the reverse direction to study the reversibility of an electrochemical reaction.

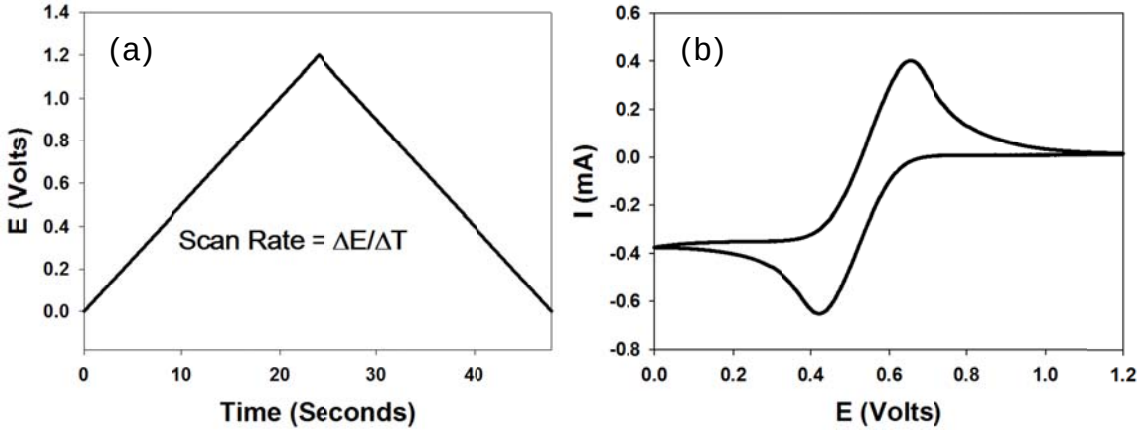

Figure 2.5 (a) Example of the applied signal (voltage/time) for cyclic voltammetry or linear sweep voltammetry and (b) the resultant current-voltage relationship (CV) plot of (a).

The cyclic voltammetric experiments (in Chapters 6 and 7) were performed in an argon-filled glovebox with a three-electrode cell gas-flow enabled setup consisting of a working electrode and Li foil as the counter and reference electrodes. In Chapter 6, the working electrode was a glassy carbon disk (ø=5 mm, Pine Instruments) coated with Vulcan XC72 or lead ruthenium oxide pyrochlore using Li-Nafion as a binder. In Chapter

7, a platinum microelectrode (ø=100 μm, Bio-Logic Science Instruments) or a glassy carbon electrode (ø=1.6 mm, Bio-Logic Science Instruments) were used as the working electrodes. The experiments were controlled with a VMP3 potentiostat and EC-Lab® software (Bio-Logic Science Instruments). The electrolyte used was $[(DMDMB)_2Li]TFSI$ or $[(DME)_2Li]TFSI$ and all experiments were performed at room temperature.

2.3.4 Chronoamperometry

Chronoamperometry is an electrochemical technique in which a potential step is applied and the current response is measured with time. Displayed in **Figure 2.6** is the applied signal (a) and recorded current response (b) for a reduction process. This technique is closely related to chronocoulometry where the coulombs passed can be plotted with respect to time using the same potential step. The charge, Q, can be obtained by integrating the area under the chronoamperometric curve ($Q = \int Idt$).

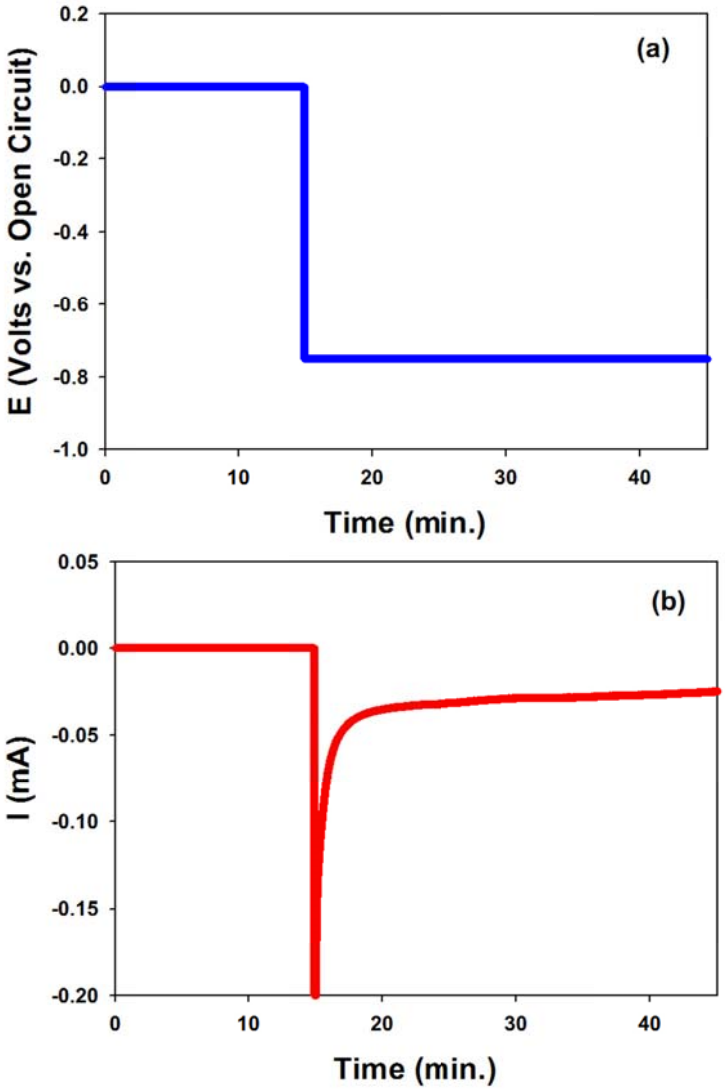

Figure 2.6 (a) Example of the applied signal (voltage) for a chronoamperometric technique and (b) the measured current-time relationship from (a).

This technique was used in chapters 5 and 6 to study the oxygen reduction reaction on TiN, Vulcan XC72, and a lead ruthenium oxide pyrochlore (PRO) by holding the potential at 2.25 V vs. Li/Li^+ in electrolytes saturated in oxygen (or argon as a background measurement).

2.3.5 Chronopotentiometry/Galvanostatic Cycling

Chronopotentiometry is an electrochemical technique where a current is applied and the voltage response is measured. In the field of batteries, this technique is commonly used and referred to as galvanostatic cycling. With this galvanostatic technique, a constant current is applied to the cell until a predetermined cut-off voltage is reached and the current is reversed. When a negative current is applied (drawing current from the cell), the battery is being discharged. When a positive current is applied, charging of the battery occurs. With this technique, single discharge/charge cycles can be analyzed in a plot of cell voltage versus capacity. **Figure 2.7** displays a single discharge-charge cycle, where the applied current displayed is normalized to the mass of the positive electrode. The capacity of the cell can be plotted simply as electrical charge (here $Q = I \cdot t$), or also normalized to the surface area or mass of the electrode. A note on reported capacities and current rates can be found in Appendix A1.

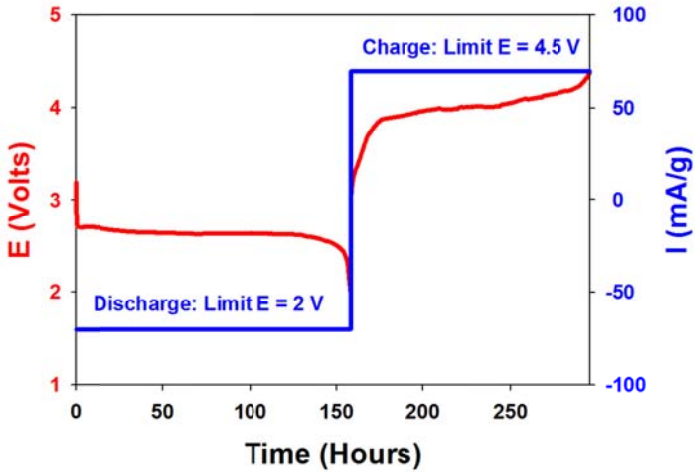

Figure 2.7 Example of typical galvanostatic cycling voltage profile measured (red) and the corresponding applied current (blue).

The $Li–O_2$ cells in this thesis underwent galvanostatic discharge using various current densities to either a lower voltage cutoff or a capacity (mAh) cutoff and charging was cutoff with an upper voltage (reported for each study separately). The cells were equilibrated at open circuit for 6 h before testing and were controlled with a BT2000 battery cycler (Arbin Instruments).

2.3.6 Electrochemical Impedance Spectroscopy

Impedance is a measure of the ability of a circuit to resist the flow of electrical current. In electrochemical impedance spectroscopy (EIS), a small AC potential is applied to an electrochemical cell and the resultant current that is generated in the cell is measured. The AC potential is applied as a sinusoidal excitation within a set frequency range and the resultant AC current signal is analyzed as a sum of sinusoidal functions. The perturbation potential applied to the cell is small so that the cells response is pseudo-linear. In this thesis, impedance data are shown in Nyquist plots (-Z'' vs. Z'), where Z'' represents the imaginary impedance and Z' represents the real impedance. The data in a Nyquist plot can be fitted using an equivalent electrical circuit to separate the impedance components.

Impedance measurements were performed using a VMP3 potentiostat/galvanostat with EIS/Z capabilities and EC-Lab® software (Bio-Logic Science Instruments). The DC voltage was maintained at open-circuit and an AC voltage was applied with an amplitude of 5 mV from 300 kHz to 50 mHz.

2.3.7 Rotating (Ring) Disk Electrode

The rotating disk electrode is a type of hydrodynamic electrode which functions in a regime of forced convection.[6] Under these conditions, the increased transport of electroactive species to the electrode leads to higher currents and greater sensitivity and reproducibility. The Levich equation (2-1) models the diffusion and solution flow conditions at a rotating disk electrode surface.

$$I_L = 0.620nFAD^{2/3}Cv^{-1/6}\omega^{1/2} \quad (2\text{-}1)$$

In this equation, I_L is the diffusion limited current (A), n is the number of electrons transferred, F is the Faraday constant (96,485 C mol^{-1}), D is the diffusion coefficient (cm^2 s^{-1}) , A is the electrode surface area (cm^2), ω represents angular frequency of rotation (rad s^{-1}), ν is the kinematic viscosity of the solution (cm^2 s^{-1}), and C is the concentration of reactant species (mol cm^{-3}). A plot of I_L versus $\omega^{1/2}$ is commonly referred to as a Levich plot. This plot is useful in determining n (if all other parameters are known) or the diffusion coefficient if n is already known.

$$I_L/\omega^{1/2} = \text{slope} = 0.620nFAD^{2/3}\nu^{-1/6}C \quad (2\text{-}2)$$

$$[\text{slope}/(0.620nFA\ \nu^{-1/6}C)]^{3/2} = D \quad (2\text{-}3)$$

$$\text{slope}/(0.62FAD^{2/3}\ \nu^{-1/6}C) = n \quad (2\text{-}4)$$

If a reaction is kinetically limited, at high rotation rates, the current measured is limited by the kinetic properties of a catalyst rather than mass transport. In these cases, the Koutecky-Levich equation (2-5) is applied to separate the kinetic current (I_k) and the diffusion limited current (I_d) from the overall current (I).

$$\frac{1}{I} = \frac{1}{I_k} + \frac{1}{I_d} = \frac{1}{I_k} + \frac{1}{B\omega^{1/2}} \quad (2\text{-}5)$$

$$B = 0.62nFAD^{2/3}\nu^{-1/6}C \quad (2\text{-}6)$$

Alternatively, I, I_k, and I_d can be described as current density (j, j_k, j_d) by removing the electrode surface area from the equation (ie. j=I/A). A plot of j^{-1} versus $\omega^{-1/2}$ is commonly referred to as the Kouteck-Levich plot. From this, the y-intercept yields the kinetic current density (j_k) and the overall number of electrons passed can be extracted from the slope. The experimental details for the aqueous RDE studies in Chapter 6 are described in section 6.2.3.

These fundamental equations could not be applied in the non-aqueous oxygen system with electrolytes containing Li^+ since the products of ORR in these systems were found to adsorb strongly to the disk electrode. No limiting current was observed and the rotation rate had minimal effect on the measured current. For the ORR reaction in non-aqueous solvents, a rotating ring disk electrode was used to determine the solubility of the O_2^- species. In the system displayed below (**Figure 2.8**), mechanical rotation of the RRDE tip (ω = rotational frequency) causes a vortex flow in the bulk electrolyte to bring dissolved oxygen to the center and outward across the disk electrode by convection. The oxygen is reduced at the disk electrode by applying a cathodic potential sweep ($O_2 + e^- \rightarrow O_2^-$). This reduced species is then swept outward to the ring, where it is detected by oxidizing it back to molecular oxygen ($O_2^- \rightarrow O_2 + e^-$) by holding the ring at an anodic potential at which this reaction occurs.

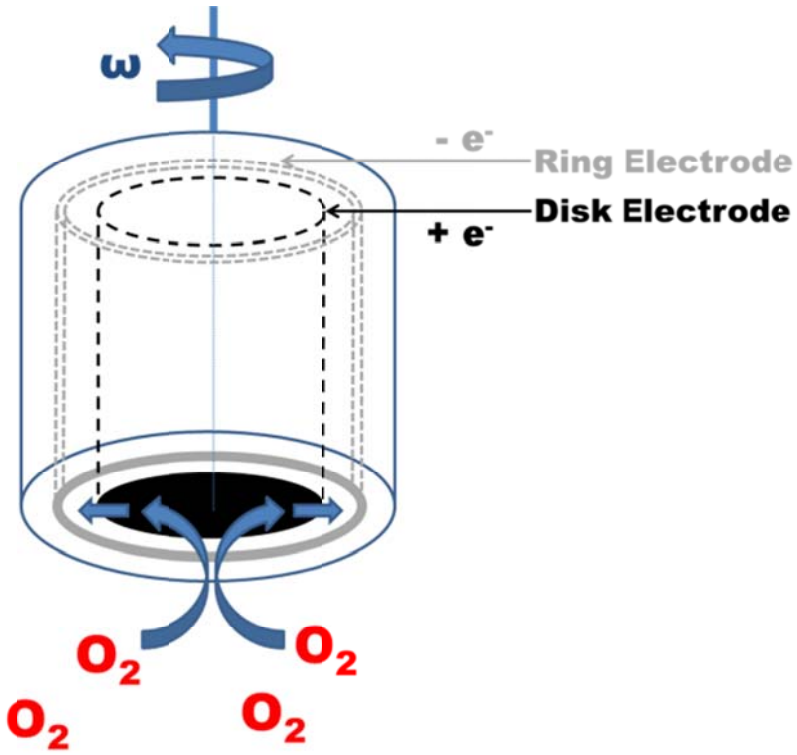

Figure 2.8 A schematic diagram of the RRDE. The RRDE tip used in these study consists of a glassy carbon disk and platinum ring imbedded into a PTFE rod with an insulating gap of PTFE between the two.

A glassy carbon disk and platinum ring RRDE tip was used for the experiments in this thesis (E7R9 RRDE tip, Pine Instruments, Co.). The electrochemical experiments were performed in an argon-filled glovebox with a four-electrode cell gas-flow enabled setup consisting of the RRDE as the two working electrodes. The experiments were controlled on two separate channels with a VMP3 potentiostat and EC-Lab® software (Bio-Logic Science Instruments). The various electrolytes used were argon-purged or saturated with oxygen. For the experiments with acetonitrile electrolytes, the counter electrode was a Pt wire and the reference electrode was a Ag wire immersed in 0.1 M

$TBAPF_6$ + 0.01 M $AgClO_4$ in acetonitrile which was separated from the bulk electrolyte with a porous Vycor™ glass frit. For the experiments with 0.1 M LiTFSI/DME, strips of lithium foil were used for both the counter and reference electrodes. For experiments with 0.1 M TBATFSI/DME, the counter electrode was a Pt wire and the reference electrode was a lithium foil strip immersed in 0.1 M LiTFSI/DME which was separated from the bulk electrolyte with a porous Vycor™ glass frit. The experimental collection efficiency of the RRDE tip was calculated to be 42.4% using the ferrocene/ferrocenium (Fc/Fc^+) redox couple in acetonitrile (3 mM Fc + 0.1 M tetrabutylammoniumhexafluorophosphate). These RRDE studies are presented in the appendices A2 and A3.

2.4 Characterization Techniques

2.4.1 Scanning Electron Microscopy

The scanning electron microscope (SEM) is an imaging tool that provides information about the morphology and topography of a sample at the nanoscale. A SEM targets high energy electrons onto the surface of a sample. Secondary electrons, backscattered electrons and characteristic X-rays are then produced from the sample. In this thesis, the secondary electron detector was used for all images presented.

SEM samples were prepared in an argon-filled glove box, using a stainless steel holder as the substrate and double-sided carbon tape as the contact point between the sample and the holder. Samples were transferred into the SEM (Zeiss Ultra Plus field emission SEM or LEO 1530 field-emission SEM instrument) under anaerobic conditions and images were taken using an accelerating voltage of 5 kV. Electrodes were thoroughly washed with dry THF prior to analysis, and loaded without air exposure.

2.4.2 X-Ray Diffraction

Bragg's Law (equation 2-7) can explain the appearance of a diffraction pattern through interference of X-ray reflections from crystal planes in a sample.

$$n \cdot \lambda = 2 \cdot d \cdot \sin\theta \qquad (2\text{-}7)$$

Bragg's Law is schematically shown in **Figure 2.9** where θ represents the incident angle of the incoming X-ray radiation with respect to the crystallographic planes that are created by the ordering of atoms (represented as blue spheres in **Figure 2.9**) in the sample. Two parallel incident X-rays labeled (A) and (B) are diffracted by the atoms in the sample but X-ray (B) must travel 2·d·sinθ further than X-ray (A) as the distance between lattice planes is defined as d. If the two diffracted X-rays are in phase and a multiple (n) of the X-ray wavelength (λ) then the distance between crystal planes (d) can be obtained by scanning θ.

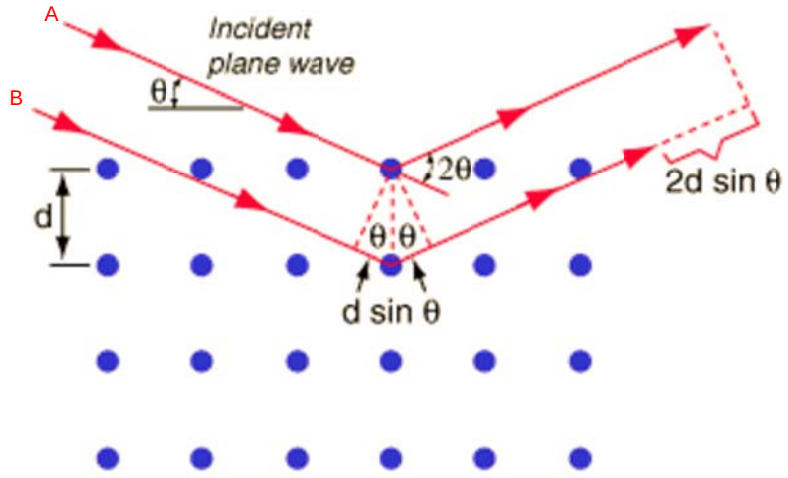

Figure 2.9 Schematic illustration of Bragg's Law.

In powder X-ray diffraction (PXRD), X-rays strikes a powder sample at a certain incident angle and since the powder is comprised of small crystals, a portion of these

crystals will be oriented with their crystallographic planes at the Bragg angle θ. The sample platform is rotated with respect to the incident X-ray radiation and a pattern containing the characteristic diffractions of the sample is obtained. PXRD patterns are unique to crystalline phases and can be used as a fingerprint for phase identification in a sample.

At the nanoscale, peaks in a diffraction pattern will begin to widen as crystallite size diminishes. The Scherrer equation[7] (equation 2-8) relates the broadening of diffraction lines with crystal domain size and can give a good approximation of crystallite size in the sample.

$$L = \alpha \cdot \lambda / (\beta \cdot \cos\theta) \qquad (2\text{-}8)$$

L is the coherence length of the crystal domain and β is the full width in radians at the half maximum intensity (FWHM) measured at angle θ. The wavelength λ is determined by the X-ray source and the constant α (a shape factor) is close to unity.[8] The average coherence length for the Li_2O_2 crystallites in Chapter 3 were calculated by applying this equation to the (101) peaks of the PXRD patterns.

XRD measurements (with the exception of Chapter 4; details provided in section 4.2.3) were carried out using a Bruker D-8 Advance diffractometer employing Cu-Kα radiation (λ = 1.5406 Å) and equipped with a Vantec-1 detector. Discharged or charged electrode samples were mounted on a silicon low-background holder and protected from the atmosphere by coating with paraffin oil. Powder samples which were not air-sensitive were loaded onto plastic holders.

2.4.3 Determination of Surface Area

The nitrogen adsorption isotherms of all solid powder materials used as oxygen electrodes in this thesis were performed on a Quantachrome Autosorb-1 instrument. Nitrogen adsorption isotherms were collected at 77 K. Before analysis, the samples were degassed at 250 °C for a minimum of 3 hours under vacuum. In this type of analysis, the samples are loaded into a quartz tube and evacuated on the instrument. It is immersed in a liquid nitrogen bath at 77 K and, in incremental steps, nitrogen gas is introduced into the sample tube. Nitrogen molecules adsorb on the surface of the sample and the system measures the pressure change in the sample tube compared to a balance tube. A nitrogen adsorption isotherm is a plot of the volume of adsorbed nitrogen vs. relative pressure (P/P_0). The surface area was calculated using the Brunauer-Emmett-Teller (BET) method with five points in the relative pressure range of 0.05-0.3.[9]

2.4.4 Online Electrochemical Mass Spectrometry

Two variations of OEMS was performed. The first set-up, located at the University of Waterloo, ON, was used to obtain the results in Chapters 4 and 5. Here, the residual gas analysis was performed with a modified design based on an OEMS apparatus reported by Tsiouvaras et. al.[10] A commercial electrochemical flow cell (EL-Cell, ECC-DEMS) was attached in-line with a gas flow controller (Bronkhurst, F-200CV) and a quadrupole mass spectrometer (Stanford Research Systems, RGA 200). The cell (and all regular Swagelok™ cells used for galvanostatic (dis)charging) was leak tested under O_2 pressure using a high accuracy pressure transducer to measure any pressure drop (Omega PX409-USBH), and found to be hermetically sealed. During cell operation a controlled flow of Ar

(5.0 Grade) sweeps the evolved gases from the cell to the MS entrance chamber where the gas enters the quadrupole through a fused silica capillary (50 um ID). The pressure inside the MS chamber was 3 x 10^{-6} torr during operation. Prior to measurement, the mass spectrometer was calibrated to establish a relationship between the measured ion current (A) and target gas concentration (ppm). With the use of known gas concentrations (from 2000 ppm O_2/Ar balance and 2000 ppm CO_2/Ar balance mixtures) mixed with different amounts of Ar, a linear relationship between the gas concentration and ion current was established. The quantification was performed with the use of Mathworks Matlab software.

The OEMS results in Chapter 7 were obtained at the Paul Scherrer Institute in Villigen, Switzerland. This OEMS configuration has been described elsewhere.[11] Briefly, the dedicated Li-O_2 cell consists of Ti current collectors, a stainless steel spring for mechanical pressure on the electrodes and rubber O-rings (EPDM) for air-tight sealing; all assembled in a PEEK casing. The OEMS setup operates with a quadrupole mass spectrometer (MS, QMS 200, Pfeiffer Prisma^{TM}, Germany) for partial pressure measurements, a pressure transducer (PS, PAA-33X, Keller Druck AG, Switzerland) for cell pressure and internal volume determination, stainless steel gas pipes and Swagelok fittings (3 mm compression tube fittings, Swagelok, OH, US) to connect the Li-O_2 cell, a set of solenoid valves (2-way magnetic valve, Type 6126, EPDM seal, Christian Bürkert GmbH & Co, Germany) and a membrane pump (Edwards E2M30 oil pump, EDWARDS GmbH, Germany) for efficient cell flushing. Apart from this: Ar (Quality 5.5), O_2 (Quality 5.0) as well as O_2 (1000 ppm O_2 in Ar) and CO_2 (500 ppm CO_2 in Ar) calibration gas

bottles are connected and employed to relate the MS ion-current signal for O_2 (m/z=32) and $^{12}CO_2$ (m/z=44) to the respective gas concentrations before and during a measurement. The magnetic valves were automatically opened/closed during operation with a Solid State Relay Module (NI 9485 Measurement System, National Instruments, TX, US) connected to a computer with a LabView Software (NI Labview 2012, National Instruments, TX, US). Quantification of the amount of O_2 and $^{12}CO_2$ was performed in the same software through a calibration matrix generated by correlating the ion currents generated for known concentrations of O_2 and $^{12}CO_2$ in Ar at specific partial pressures. All cells were discharged to a capacity of 1 mAh under a closed oxygen atmosphere (0.2 bar relative overpressure). The cells were then step-wise flushed (10 min time intervals) with Ar until the amount of oxygen detected in the mass spectrometer approached base-line levels. Charging of the cell was performed at a current of 0.25 mA while the valve between the cell and MS inlet was automatically open (3 s) and closed with 10 min intervals in order to probe the partial pressures of cell atmosphere by the MS. The quadrupole chamber pressure was stably maintained at $7x10^{-6}$ mbar during operation.

2.5 Quantification of Lithium Peroxide

Lithium peroxide reacts with water to form hydrogen peroxide according to the equation below:[12]

$$Li_2O_2 + 2H_2O \rightarrow 2LiOH + H_2O_2 \qquad (2\text{-}9)$$

In a chemical reaction involving H_2O_2 and I^-, the former is reduced to water and the latter is oxidized to iodine, which can then be titrated using standard thiosulfate solution to

quantify the peroxide concentration. The net reaction between peroxide and iodide can be written as follows:

$$H_2O_2 + 3I^- + 2H^+ \leftrightarrow 2H_2O + I_3^- \quad (2\text{-}10)$$

This reaction is slow without a catalyst but can be quite fast in the presence of catalysts such as Mo(VI) and excess I^- that forces the reaction to proceed to the right resulting in the formation of I_3^-. The I_3^- is titrated using thiosulfate based on the following reaction:

$$I_3^- + 2Na_2S_2O_3 \rightarrow Na_2S_4O_6 + 2NaI \quad (2\text{-}11)$$

In a standard iodometric estimation of H_2O_2, one reacts iodide in an acidic media,[5] which is known to catalyze the chemical disproportionation of peroxide to water and oxygen. Furthermore, iodide is prone to oxidation at acidic pH by air exposure. Both these process are likely to introduce significant error in the peroxide quantification. Therefore, in our work, we have adopted a modified iodometric method employing a pH neutral iodide-phosphate buffer reaction media that maintains a steady supply of protons for the peroxide-iodide reaction, while keeping the pH constant. Neutral pH suppresses peroxide disproportionation along with decelerating the areal oxidation of iodide. The inhibition of aerial oxidation of iodide was evident from the unchanged color of the post titration solution (colorless) even hours after the titration. In a standard iodometric procedure, the post titration solution turns blue very quickly from the oxidation of I^- to I_2 that bind to starch to give the blue color.

The buffer-catalyst solution was prepared by dissolving 65 mg of $(NH_4)_6Mo_7O_{24}$ $\bullet 4H_2O$ (ammonium heptamolybdate) along with 0.11 mol of $H_2PO_4^-$ and 0.03 mol of

HPO_4^{2-} in 500 mL of Millipore water. Adding 67 g of KI to this buffer solution and diluting it to 1 L resulted in the reagent buffer solution, which was freshly prepared before use.

For the chemical purity estimation of Li_2O_2, a known mass was dissolved in 500 mL of Milli-Q water (Millipore Corporation, 18.2 MΩ.cm) in a volumetric flask. To a 25 mL aliquot of this solution, 25 mL of water and 50 mL of reagent buffer solution was added. The mixed solution immediately turned yellow indicating the liberation of iodine, which was titrated with standardized thiosulfate solution till a straw yellow color. The titration was continued after adding starch indicator solution with the end point showing a color change from blue-violet to colorless. To determine any decomposition of Li_2O_2 as a result of mixing it with isopropanol during loaded cathode fabrication process, a fixed amount of Li_2O_2 was mixed with isopropanol thoroughly for ~ 10 minutes. The Li_2O_2 was then dried under vacuum to remove the isopropanol before undergoing the above titration protocol.

Typically the aged loaded cathodes (with VC) and the cathodes extracted from a discharged cell were transferred out of a glove-box in a sealed vial. Water (5-10 mL) was added to the vial and the vial content was vigorously shaken before transferring the contents to a beaker containing reagent buffer solution and water. Quantitative titration of the peroxide was performed following the procedure stated above. The effect of cathode support and LiTFSI-TEGDME electrolyte on the titration outcome was neglected.5

Chapter 3

Current Density Dependence on Peroxide Formation and its Effect on Charge

3.1 Introduction

To realize the promise that the Li-O_2 battery might have to offer, a fundamental understanding of the source of the high overpotential on charge and the mechanisms of both oxygen reduction and oxygen evolution reactions (ORR and OER, respectively) in non-aqueous electrolytes are required. The ORR process governs the morphology of the Li_2O_2 and hence its ease of oxidation, which is important because the ability to recharge batteries with good round trip efficiencies is essential for commercial viability.

A toroidal Li_2O_2 morphology was reported by Shao-Horn *et al*., in experiments using carbon nanofiber cathodes,[1] and by our group using carbon membranes where a mechanism was proposed to account for its formation.[2] A similar toroidal morphology has been recently observed using pyrochlore catalyzed systems,[3] and in carbon membranes that employ activated carbon.[4] On the other hand, film formation of Li_2O_2 on low surface area glassy carbon has been suggested by the IBM group.[5] Two mechanisms have also been proposed to account for the 2 e^- reduction of oxygen, both based on an initial 1 e^- reduction to form lithium superoxide, LiO_2: one suggests this is followed by disproportionation to lithium peroxide and oxygen; and the other invokes subsequent electrochemical reduction of the superoxide to peroxide.[6] In addition to these fundamental perplexities, practical concerns will limit commercialization until they can be addressed.

These include the effect of current density on Li-O_2 cell chemistry which has yet to be systematically studied, although it is agreed upon that Li-O_2 cells exhibit poor rate capabilities.

The rate at which current is delivered in the oxygen reduction reaction plays an important role in determining the morphology of the product. Using a combination of electron microscopies and electrochemistry, the role of current density on the ORR steps is reported in this chapter. Identifying the pathways that govern discharge is an important challenge for optimizing charge. It was found that slow current densities strongly favor disproportionation, possibly due to competitive weak binding of the superoxide to the surface. The result is nucleation of large toroidal nanocrystalline peroxide aggregates. In contrast, higher current densities favor film formation and a much less crystalline product that can be oxidized at a lower overpotential. These processes are considered in the context of the thermodynamic principles that underpin the complex chemistry. The electrolyte, 1 M LiTFSI /tetraethylene glycol dimethyl ether (TEGDME), was chosen based on its relative stability to superoxide attack,[2,7] similar to that of dimethoxyethane.[8] The low (albeit not zero) reactivity of TEGDME on reduction is confirmed by our recent time-of-flight secondary ion mass spectrometry (ToFSIMS) studies which demonstrate little carbonate deposition on discharge, although reaction with peroxide and/or its decomposition product occurs to some extent on charge.[9]

Robert Black contributed to the work in this chapter by operating the SEM and obtaining the images in Figures 3.1 and 3.6. Dr. Claudio Radtke assisted with the assembly

of cells and discharging cells displayed in Figure 3.1. Drs. Michel Trudeau and Karim Zaghib obtained the STEM image and EELS mapping shown in Figure 3.4.

3.2 Experimental Details

3.2.1 Post-Discharge Electrode Analysis

After electrochemical studies were completed, the cells were disassembled in an Ar-filled glovebox and the electrodes were recovered. TEM and EELS analysis was performed with a Hitachi HD2700 STEM equipped with spherical aberration correction (CEOS GmbH) and an EELS spectrometer (Enfina; Gatan) at Hydro Quebec. The instrument can provide a resolution of less than 0.10 nm in high-angle annular dark-field mode (HAADF). Films (~ 20 – 40 nm thickness) were prepared from the discharged cathode using focused ion beam (FIB; NB5500) thinning, employing a 40kV Ga ion FIB column providing 3D reconstructions with slicing steps down to 50 nm. The sample was transferred into the TEM chamber without any contact with air.

3.3 Results and discussion

3.3.1 Effect of Discharge Current Density on Li_2O_2 Morphology and Cell Capacity

Results for Li-O_2 cells are shown in **Figure 3.1**, which combines the discharge profile at current densities ranging from 5 – 100 $\mu A/cm^2$ (ie, with respect to the geometric surface area) with field emission scanning electron microscope (FESEM) images of the peroxide product. We note that a majority of the reports to date have used current densities less than or equal to 100 $\mu A/cm^2$ and/or < 200 mA/g_{carbon},[10] although increasing the rate capabilities is a major focus of research.[11] The characteristics of the electrodes are

summarized in **Table 3.1**. The results demonstrate that the current density dramatically affects the morphology of the peroxide in a very systematic way. As expected, the discharge overpotential increases with higher current density, and the overall capacity decreases, with an abrupt change occurring at the transition between 25 and 50 μA/cm^2.

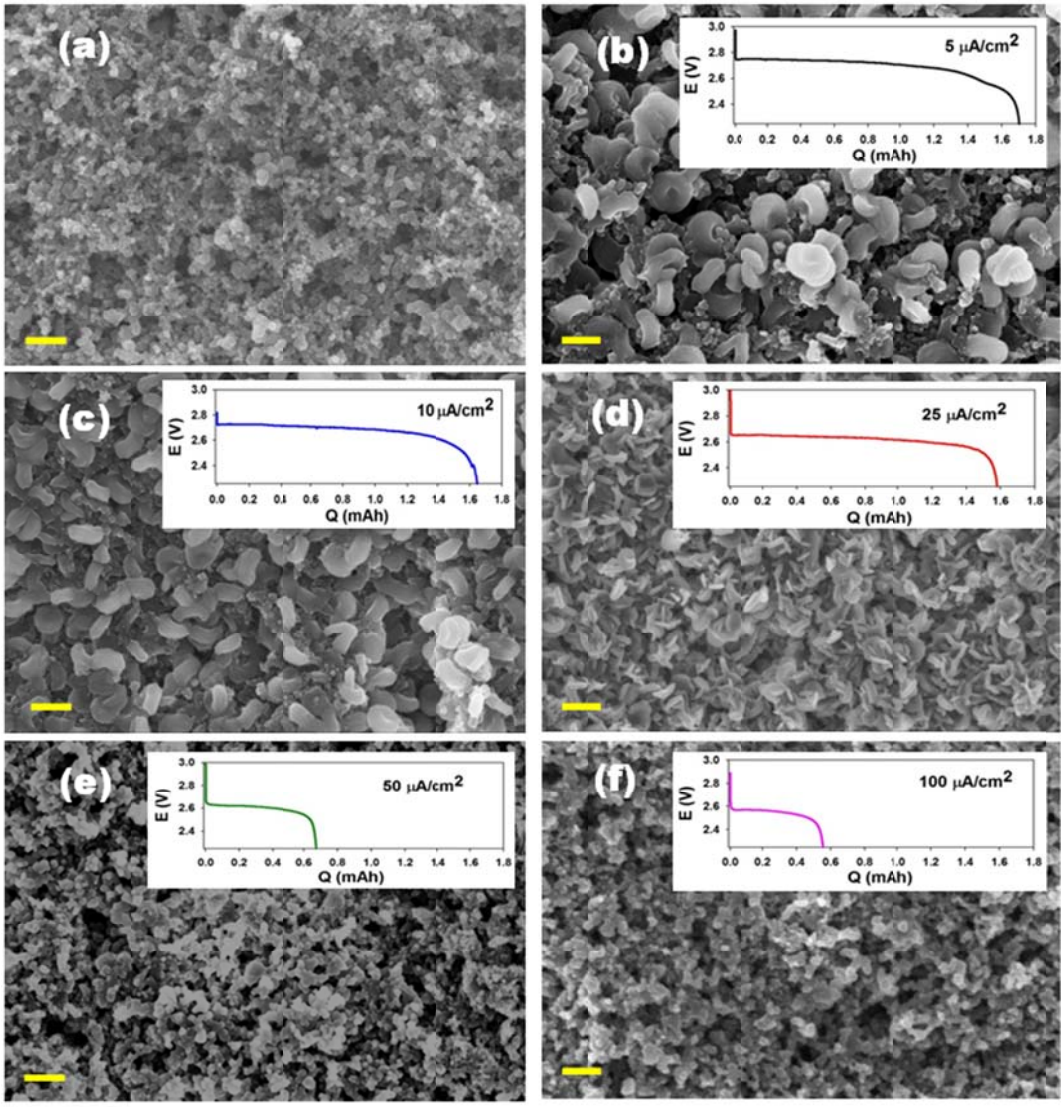

Figure 3.1 FESEM images at a magnification of 20,000x of the pristine cathode (a) and after full discharge at (b) 5 μA/cm^2, (c) 10 μA/cm^2, (d) 25 μA/cm^2, (e) 50 μA/cm^2, and (f) 100 μA/cm^2, with the corresponding discharge curves. Scale bar = 400 nm.

Table 3.1 *Discharge capacities, onset voltages, XRD peak intensities and Scherrer analysis of the cathodes obtained at current densities from 5 – 100 μA/cm^2.*

Current Density (μA/cm^2)	**Discharge Capacity (mAh)**	**Onset ORR Voltage (V)**	**Average Coherence Length along [101] (nm)**
5	1.70	2.75	18 ± 2
10	1.65	2.72	19 ± 2
25	1.58	2.65	18 ± 2
50	0.67	2.63	~15
100	0.55	2.56	-

A plot of the capacity versus current density (**Figure 3.2**) clearly shows the morphological transition regime. For ease of comparison with other studies, this plot displays capacity and current density normalized to both the geometric surface area and the estimated real surface area of the active carbon in the cathodes based on N_2 adsorption experiments (SA_{BET} = 219 m^2/g). The curtailed capacity at fast rates is caused by limited mass transport of Li^+ and/or O_2 to the active surface sites by the build-up of Li_2O_2 product.

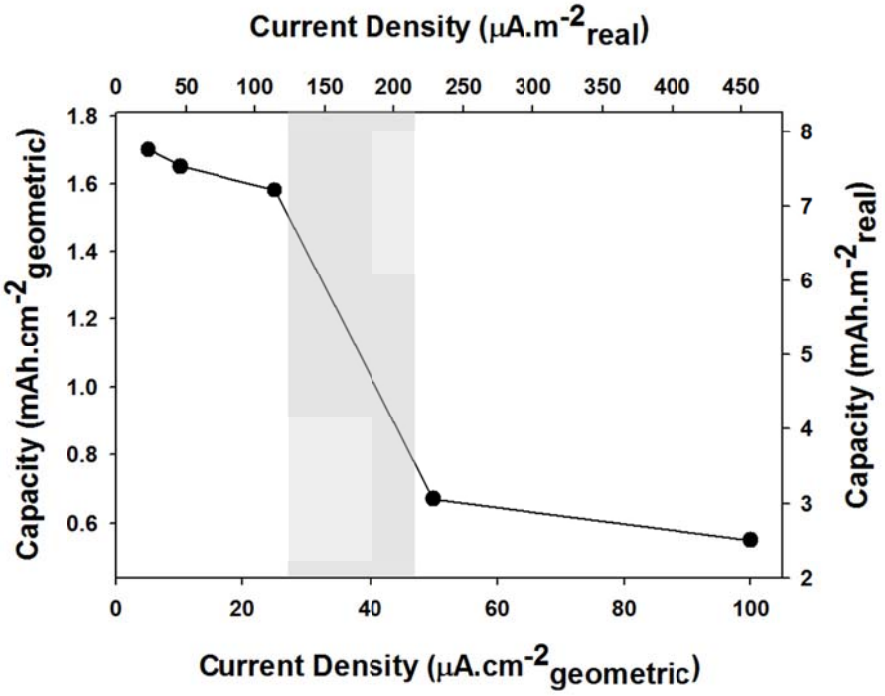

Figure 3.2 Plot of the overall discharge capacity as a function of current density. Units of capacity and current density are normalized to both the geometric surface area of the cathodes (1 cm^2) and the real surface area of active carbon in the cathodes (0.219 m^2). The real surface area of the active carbon was estimated using the BET surface area of Vulcan XC72 carbon black (219 m^2/g) obtained experimentally with N_2 adsorption and the average mass of this carbon in the cathodes (1 mg). The shaded grey box identifies the transitional current density region that prompts the change from toroidal to film Li_2O_2 morphologies.

3.3.2 Characterization of Discharge Products

Although the capacity is limited by the same type of impedance (charge transfer resistance) at all current densities, the significant differences in capacity are correlated to a distinct change in surface structure (**Figure 3.3, Table 3.2**).

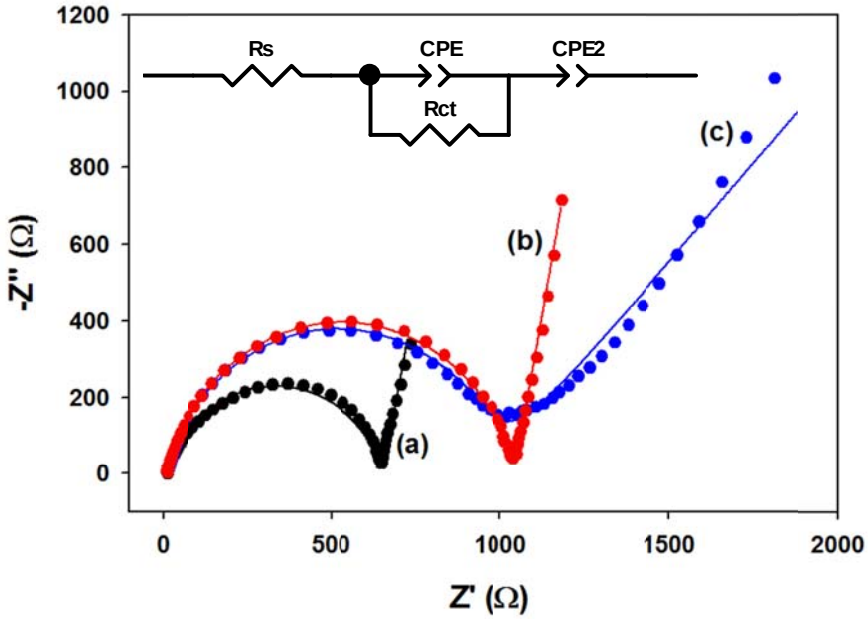

Figure 3.3 Nyquist plots of (a) non-discharged cell, (b) cell discharged at 100 μA/cm^2, and (c) cell discharged at 5 μA/cm^2. The inset shows the equivalent circuit that the data (circles) were fitted with (solid lines).

Table 3.2 *Parameters for Figure 3.3, fitted by the equivalent circuit shown in the inset.*

Element	Non-Discharged (Fig. 3.3a)	Discharged at 100 μA/cm^2 (Fig. 3.3b)	Discharged at 5 μA/cm^2 (Fig. 3.3c)
Rs (Ω)	12.43±1.13%	12.06±0.63%	12.64±0.78%
CPE-T (μF)	6.01±3.53%	2.52±1.70%	3.22±2.46%
CPE-P	0.79±0.46%	0.83±0.21%	0.83±0.34%
Rct (Ω)	643.7±0.68%	1034±0.34%	955±0.80%
CPE2-T (mF)	7.76±4.09%	3.85±1.76%	1.37±1.42%
CPE2-P	0.87±2.95%	0.88±1.26%	0.51±1.69%

Figure 3.3 displays the Nyquist plots of cells discharged at two different current densities along with a non-discharged cell. The equivalent circuit displayed above in **Figure 3.3** consists of an uncompensated ohmic resistance (Rs) in series with a constant phase element (CPE) in parallel with the charge transfer resistance (Rct). These elements cause the depressed semi-circle shape in the Nyquist plots. At the end of the circuit is a second constant phase element (CPE2), that gives rise to the linear tail following the semi-circle at low frequencies. The uncompensated resistance is roughly the same for each cell and is due to the electronic resistances of the electrodes, contacts, and electrolyte resistance. The constant phase elements defined as CPE(2)-T and CPE(2)-P represent the capacitive contributions of the two electrodes, where the value of CPE(2)-P can range between 0 and 1, with 0 being a pure resistor and 1 being a pure capacitor.

The Rct (or polarization resistance) increases after discharge of the cells at both current rates. Increases of 33% and 38% in Rct relative to the non-discharged cell are observed for the cells discharged at 5 $\mu A/cm^2$ (toroid morphology) and 100 $\mu A/cm^2$ (film morphology), respectively. These similar values provide evidence that the sharp increase in polarization at the end of discharge, which limits the capacity, is governed by the same process at all discharge rates. We can conclude that pore-blocking is not the cause of the polarization, since open pores (void space between carbon particles) are evident in both cases in the SEM images. It is more likely that the polarization is caused by limited mass transport of Li^+ and/or O_2 to the active surface sites by the build-up of Li_2O_2 product. The CPE2 is related to diffusion of active species to the surfaces of the electrodes. The morphology of the discharge product is reflected by this element. The degree of

capacitance (CPE2-P) resulting in the linear slope of the Nyquist plot at low frequencies is the same for the cell discharged at high current rate as for the non-discharged cell. This is because the formed Li_2O_2 film of the discharged cell does not significantly change the surface area or morphology of the underlying cathode. However, the CPE2 of the cell discharged at low current rate (Li_2O_2 toroids) has a more resistive character than the others.

Low current densities in the range of 5 – 25 $\mu A/cm^2$ give rise to large toroidal morphologies of Li_2O_2 (**Figure 3.1 b-d**). The lateral dimensions of the toroids progress from about 200 – 500 nm with significant thickness at the slowest rates, to smaller (~ 200 nm) and thinner shapes with an indistinct toroidal morphology when the current density is increased to 25 $\mu A/cm^2$ (**Figure 3.1d**). The highest current densities (50 and 100 $\mu A/cm^2$), conversely, give deposition products on the carbon membrane that are scarcely visible, although detailed examination suggests the existence of very small crystallites. To probe this further, we carried out scanning transmission electron microscopy (STEM) investigations on the cathode obtained at a discharge of 50 $\mu A/cm^2$ using high-angle annular dark field (HAADF) imaging together with electron energy-loss spectroscopy (EELS) mapping. These results indicate that the carbon particles are surrounded by a distinctive Li_2O_x coating, as reflected by the Li and O distribution (**Figure 3.4**). No electron diffraction pattern could be observed, besides the high sensitivity of the coating to the electron beam (similar to crystalline Li_2O_2 under these STEM conditions) prevents a definitive conclusion on its precise nature. We note that numerous recent experimental studies using different techniques show that a lithium superoxide-like species is formed

on/within the peroxide on discharge, which could account for the poor crystallinity of the product.[4,12,13] Computational studies also predict the existence of lithium superoxide-like surface species on the surfaces of stoichiometric Li_2O_2.[14]

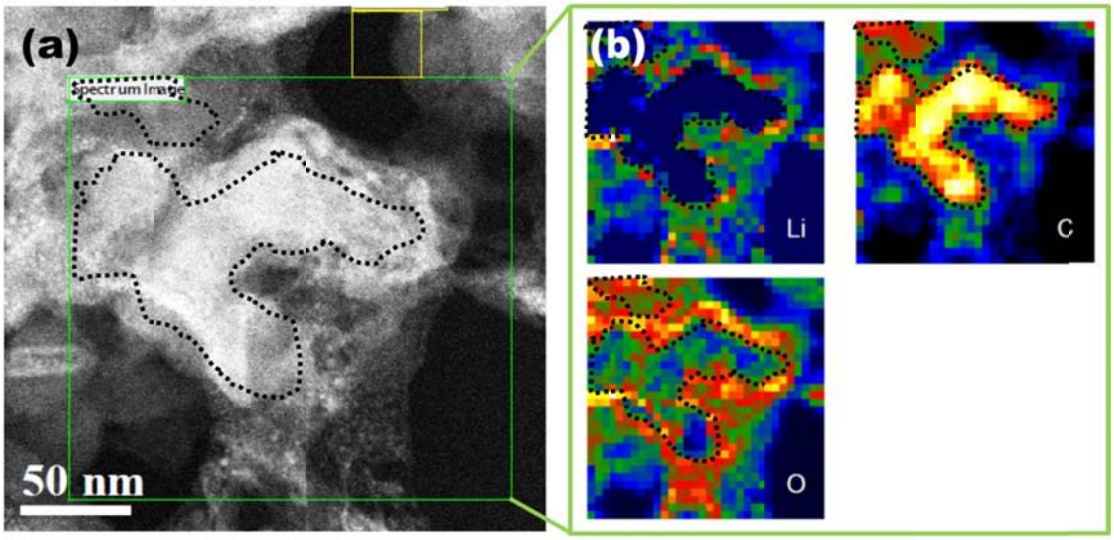

Figure 3.4 a) STEM image in high-angle annular dark field mode (HAADF) of a sample section of the electrode material discharged at 50 μA/cm^2 and prepared by focused ion beam bombardment; b) accompanying Li, C and O compositional maps of the area outlined in green in (a) generated by electron energy-loss spectroscopy in the transmission electron microscope (STEM-EELS); these maps are representative of many observations of the electrode. Acquisition time was < 1sec to prevent beam damage to the sample, leading to poor pixellation quality. The dotted black line in all images is the outline from the carbon map, showing the carbon particle.

The images shown above indicate the presence of a ~ 15 - 20 nm thick lithium oxide film around the surface of the carbon. The lithium oxide was extremely beam sensitive, even more so than a crystalline Li_2O_2 reference material prepared in a similar manner,

which precluded the acquisition of fast Fourier transform (FFT) images in either case.

These data are complemented by the corresponding X-ray diffraction (XRD) patterns (**Figure 3.5)** of the fully discharged cathodes. The patterns were normalized to the intensity of the peak at $2\theta = 54.3°$ arising from the underlying gas diffusion electrode. Crystalline peroxide is detected in all cases, but at the two highest current densities - where no toroidal aggregates are observed with FESEM - the diffraction intensity is greatly reduced. The intensity of the Li_2O_2 reflections is expected to drop with decreased capacity owing to less mass deposited. However, the exception of the strong XRD reflections in the 10 $\mu A/cm^2$ cathode and the significant change in intensity between the 50 and 100 $\mu A/cm^2$ cathodes (despite a very similar capacity) suggests the relationship is more complex. Scherrer broadening of the (101) reflection can be determined with accuracy at the lower current densities and indicates that the average coherence length is approximately the same in this region, ranging between 16 nm to 19 nm (**Table 3.1**). The combination of data strongly point to two peroxide contributions: one which is relatively crystalline that is formed at the limit of solubility *via* nucleation from solution at low current density, and a quasi-amorphous component that increasingly dominates at high current density.

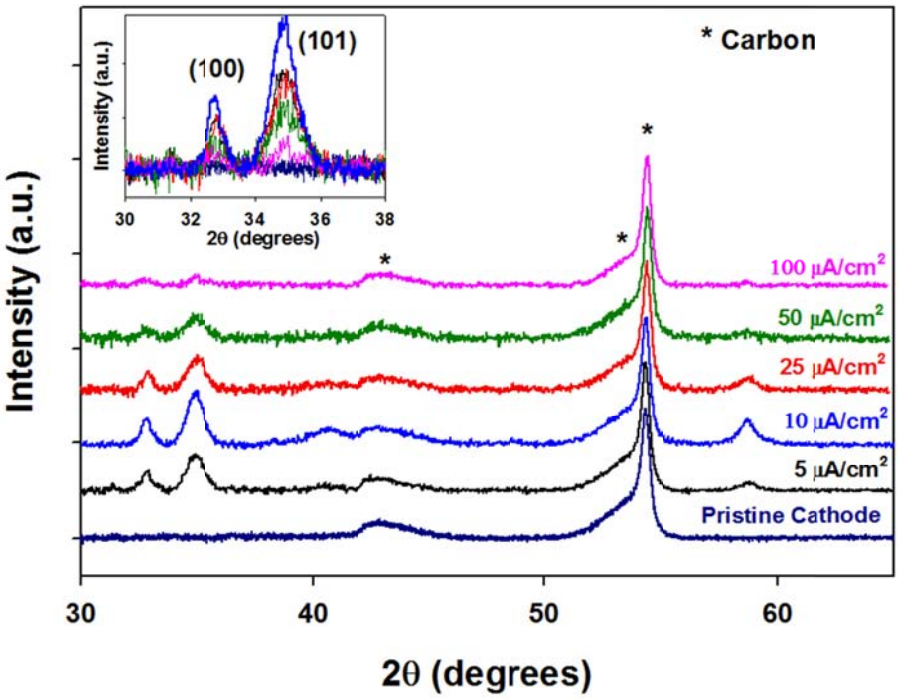

Figure 3.5 XRD patterns after full discharge at the corresponding current rates. All peaks, with the exception of carbon arising from the gas diffusion electrode, can be indexed to Li_2O_2 (PDF # 01-074-0115). The inset displays a close-up of the (100) and (101) reflections.

3.3.3 Proposed Oxygen Reduction Mechanism in Li^+-Containing Aprotic Electrolytes

The question is what governs these different morphologies. There are two possible reaction pathways leading to Li_2O_2, based on the initial formation of superoxide LiO_2 that is widely recognized as the first step in the reduction of oxygen in the presence of Li^+, *vis*: reactions (3-1) or (3-2) below. [4,12]

$$O_2 + e^- \rightarrow O_2^{\cdot -} \textit{ followed by } O_2^{\cdot -} + Li^+ \rightarrow LiO_2 \quad (3\text{-}1)$$

or

$$O_2 + Li^+ + e^- \rightarrow LiO_2 \quad (3\text{-}2)$$

and next

$$2LiO_2 \rightarrow Li_2O_2 + O_2 \quad (3\text{-}3)$$

or

$$LiO_2 + Li^+ + e^- \rightarrow Li_2O_2 \quad (3\text{-}4)$$

In the presence of high [Li^+] concentrations, a cation induced charge transfer reaction (3-2) is thought to be favored over the stepwise (3-1).[5] This also shifts the potential of the reversible O_2/O_2^- couple to higher voltage with respect to bulky cations such as TBA^+ that allow the O_2^- to be stabilized via solvation.[15,16] Regarding (3-3) *vs* (3-4), we consider the thermodynamics of the possible reactions that govern the Li-O_2 cell as summarized in **Table 3.3,** taking ΔG^o_{298} values from literature sources and calculating E^o_{cell} from those values ($\Delta G^o = -nFE^o_{cell}$). The values for Li_2O are excluded because there is little experimental evidence to support its formation on carbon.

Table 3.3 *Thermodynamic values for the possible overall discharge reactions.*

Reaction	ΔG^o_{298} (kcal)	E^o_{cell} (V)	Reference
(A) $Li + O_2 \rightarrow LiO_2$	-70 -52.8	3.0 2.29	6,17,18 [a, d] 21[c]
(B) $2Li + O_2 \rightarrow Li_2O_2$	-145 -136.46 -135	3.1 2.96 2.93	6,17,18 [a] 19[b] 21[c]

[a] Laoire, *et al*.[6,17,18] reported the Gibbs free energy and corresponding E^o_{cell} ($\Delta G^o = -nFE^o_{cell}$) for (A) and (B), respectively as ΔG_1^o = -70 kcal (E^o_{cell} = 3.0 V), ΔG_2^o = -145 kcal (E^o_{cell} = 3.1 V), but no reference were provided for the source of the values.

[b] Shao-Horn et al.[19] corrected the values for (B) using an accurate reference for the thermodynamic properties of Li_2O_2 (ΔG^o = -136.46 kcal and E^o_{cell} = 2.96V).[20]

[c] Although it is particularly difficult to obtain accurate values for (A) owing to the instability of LiO_2, the value of ΔG^o = -52.8 kcal[21] may be considered a reasonable approximation. This provides a potential close to that for $O_2 + e \rightarrow O_2^-$ (2.49V).[22]

[d] A free energy of -70 kcal would predict that disproportionation would be not thermodynamically favored, whereas it is well known to occur.

The free energies of reactions 3-3 and 3-4 can be estimated as follows:

(3-3) $2LiO_2 \rightarrow Li_2O_2 + O_2; \Delta G_c = \Delta G_B - 2\Delta G_A$ = *-136.46 kcal – 2(-52.8 kcal) = -30.86 kcal*

(3-4) $LiO_2 + Li \rightarrow Li_2O_2; \Delta G_{ec} = \Delta G_B - \Delta G_A$ = *-136.46 kcal – (-52.8 kcal) = -83.66 kcal*

Although both reactions have a negative free energy, (3-4) is thermodynamically favored over chemical disproportionation (3-3). Reduction of LiO_2 would also necessarily dominate if it has zero solubility, and/or if it were strongly bound to the surface. However, although the insolubility of LiO_2 in ether solvents has been previously suggested,[23] it *must* dissolve to some limited extent. This is clearly demonstrated by the nanocrystalline aggregate structure of the toroids, which precludes a simple single-crystal growth mechanism from the surface of the carbon.

Proof of LiO_2 solubility is also demonstrated by the chemical disproportionation that occurs on reaction of KO_2 with Li^+, where sequestration of the K^+ by crown ether leads to nucleation of crystalline Li_2O_2 from solution via (3-3).[2] Further proof of a solution phase

O_2^- is provided in the appendix A3 using a rotating ring disk electrode to detect the fraction of soluble reduced oxygen species in a LiTFSI/DME electrolyte. In other words, although the thermodynamics show that (3-4) is favored over (3-3), other factors such as kinetics, electrolyte and surface interactions contribute. These include desorption of the LiO_2 via solvation, which can compete with reaction (3-4). The relative binding strength of O_2 (and LiO_2) to the surface *vs* the solubility of the LiO_2 product has major implications for ORR. In the case of carbon for example, recent studies have shown an oxygen adsorption step precedes the first charge transfer step: the surface edge structure on the carbon comprised of defects activates the Li^+-ORR process, resulting in an increase in the discharge voltage.[24] This can account for the variable ORR activity between different carbonaceous materials and their resulting "catalytic" behavior. Shao-Horn et al,[25] have proposed that on surfaces with weak O_2 adsoption strength, such as carbon, the discharge product is Li_2O_2, whereas, on surfaces with a greater O_2 adsorption strength, even Li_2O can be generated via cleavage of the O-O bond. The universal growth of toroids on a variety of different substrates,[9,26] and even different non-conducting components of the cell (See **Figure 3.6**), also indicates that they form by nucleation of crystallites formed in solution rather than from surface diffusion and aggregation.

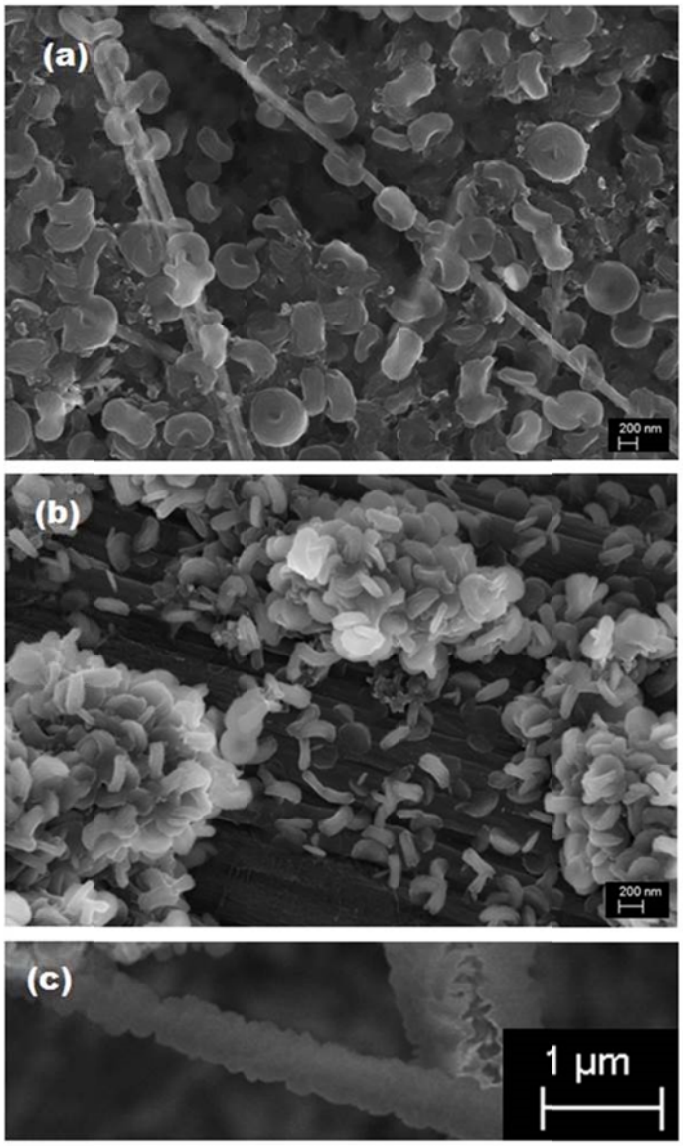

Figure 3.6 FESEM images of Li_2O_2 on (a) $Na_{0.44}MnO_2$ nanowires, (b) the Toray carbon paper GDL at a crack in the active carbon coating and (c) a glass fiber from the separator. We note that the bare GDL has negligible capacity (Figure 2.1). Thus, the Li_2O_2 toroids in (b) *must* have been produced and deposited from the active carbon coating and solution. The glass fiber coated with Li_2O_2 in (c) is from the separator in the cell which has no electrical conductivity.

Our proposed mechanism to account for the differences in peroxide morphology is shown in **Figure 3.7**. At very low current rates, where the electron transfer rate from the surface is slow, the observed toroid production implies that solvation of the LiO_2 molecules occurs at a faster rate than step (4), leading to chemical disproportion to the peroxide. When the concentration of Li_2O_2 exceeds the solubility limit, crystallites precipitate on the surface of the electrode at nucleation sites. Because the generation of LiO_2 (solvated) is controlled by the current rate, as the current is increased from 5 $\mu A/cm^2$ to 25 $\mu A/cm^2$, the number of toroids increases and their relative size decreases. At higher current density (greater than 25 $\mu A/cm^2$ in this study) no toroids are observed: only quasi-amorphous Li_2O_2 is formed with film morphology (see above). The lithium superoxide generated under these conditions in higher concentrations on the surface may undergo disproportionation via surface migration, thus accounting for the poorly crystalline small particles. Even as likely, direct electron transfer at high current densities (ie, reaction 3-4) which necessarily incurs a significant overpotential, could also govern the pathway and give rise to the same result. In this region, the thickness and conductivity of the Li_2O_2 film become important. The electrical conductivity of Li_2O_2 films has been estimated to be in the range of 10^{-12} to 10^{-13} S/cm,[27,28] which is quite low, and on smooth glassy carbon surfaces, a film of 5-10 nm is sufficient to completely curtail discharge.[27] In the film morphology region, the LiO_2 undoubtedly has a stronger adsorption to the Li_2O_2 substrate than carbon, which would favor the kinetics *vs*. the de-adsorption/solvation of LiO_2. In the transitional current density region (**Figure 3.2**), it is likely that there is competition between these factors. We note that recent studies using an electrochemical quartz microbalance to probe cathode deposition processes,[29] suggest that the direct second

electron reduction pathway is favoured. Caution is needed though, since this could also be in part due to the use of Pt as the working electrode, which has a stronger O_2 binding strength than carbon, [30] and/or because the experiments were performed under potentiodynamic control rather than galvanostatic control as used in this study. Another factor in the relationship between current density and growth mechanism of Li_2O_2 observed in this study is the solvent properties. The solubility and diffusion of oxygen and the solvation of LiO_2 will have a major influence on the different morphologies of peroxide and the actual current density at which they are formed at. Therefore, this study is solvent specific (TEGDME) but the findings have major implications that can carry over to new electrolyte/solvent systems. For example, ionic liquids would probably not give rise to toroidal morphology even at very low current densities, since their properties with respect to all of the above are quite different than TEGDME.

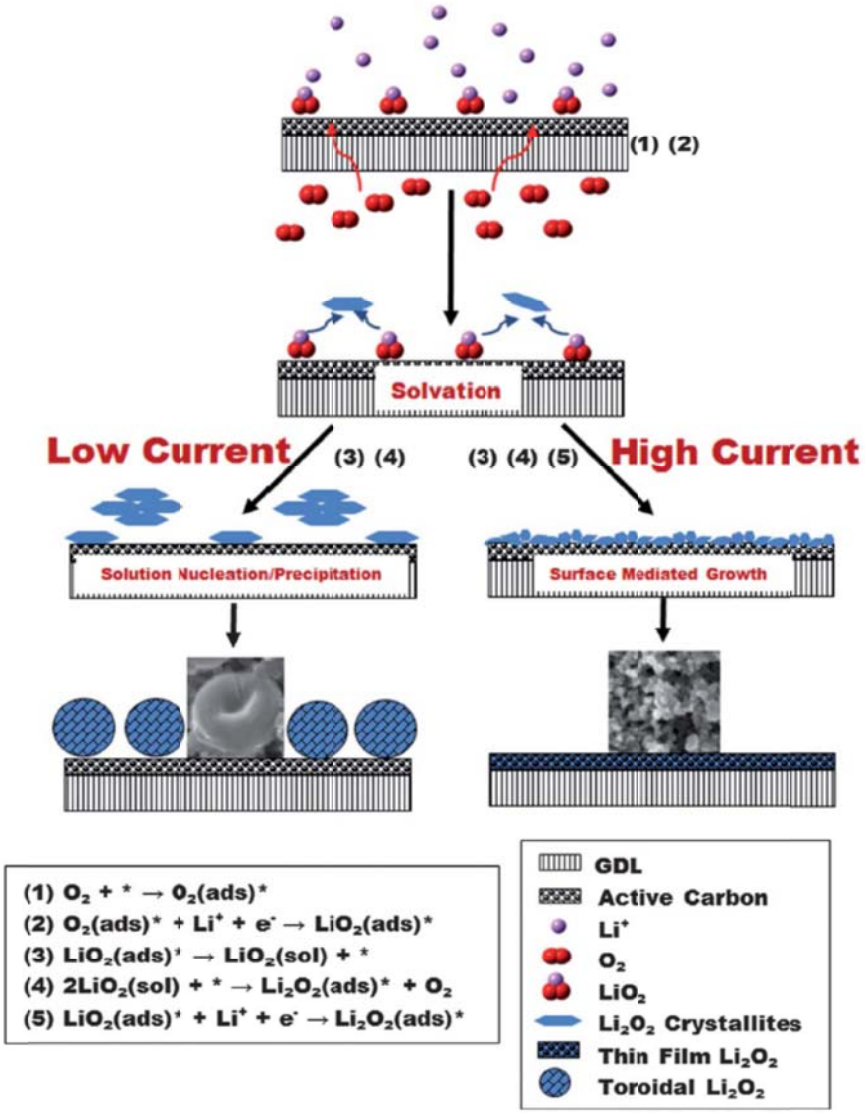

Figure 3.7 Proposed ORR mechanisms as a function of current density.

3.3.4 The Nature of Li_2O_2 and its Role in Charging Performance

Figure 3.8 shows how OER – which is expected to be governed by much slower kinetics than discharge[28] – is affected by the current density and the morphology of the discharge products. The charging profiles are all similar, and exhibit four regions

characterized by distinct differences in slope displayed in **Figure 3.8a**: The first region I at low voltage (*ca.* 3.3V) is followed by an increase in slope in region II, followed by a nearly flat plateau (III) which rises gently at the end of charge (IV). The voltage cutoff used in these studies was 4.7 V because this is the approximate anodic electrolyte decomposition limit (**Figure 3.9**); however, this value was obtained in the absence of Li_2O_2 and was also found to be dependent on current density. In **Figure 3.8b**, the Li-O_2 cells were discharged at the same intermediate rate (25 μA/cm^2) and then charged at different rates. The overall voltage is lowered with decreasing charge density, as expected from polarization effects. The initial stage of peroxide oxidation at the end of region I is associated with the onset of carbonate deposition, which continues to progress through region II. We believe that the upper voltage plateau (III) reflects the oxidation of accumulated inorganic and organic carbonates at the carbon surface in the presence of lithium peroxide. This is supported by our recent ToFSIMS studies which clearly delineate the carbonate fragment contribution in these regions,[9] and by other reports on carbonate formation based on OEMS studies.[31] The role of the nature and morphology of the Li_2O_2 in determining the charge characteristics was isolated by discharging cells at different current density and then charging them at the same current rate. As shown in **Figure 3.8c**, an increase in the *discharge* current leads to a more defined lower potential region I on charge which is particularly evident at the high discharge rate of 50 μA/cm^2 (green curve). In **Figure 3.8d**, we compare a cell fully discharged at 100 μA/cm^2 (pink curve) and charged at 10 μA/cm^2 - with a cell discharged at 25 μA/cm^2 to a similar capacity (red dotted curve) and charged at the same density of 10 μA/cm^2. The faster discharge yields a charge profile with an extended region I at low potential compared to

the slower discharge. This could be the consequence of the quasi-amorphous peroxide formed at fast discharge rates, which may have a substantial superoxide component as discussed above. A theoretical study by Mo *et al.* [32] found that lithium deficient Li_2O_2 surfaces have a low charge overpotential, and Yang *et al.* [4] have observed a lowered charge region where superoxide-species are detected by magnetic measurements. Furthermore, contact of the lithium peroxide film with the carbon surface undoubtedly also lowers the overpotential compared to the toroids.

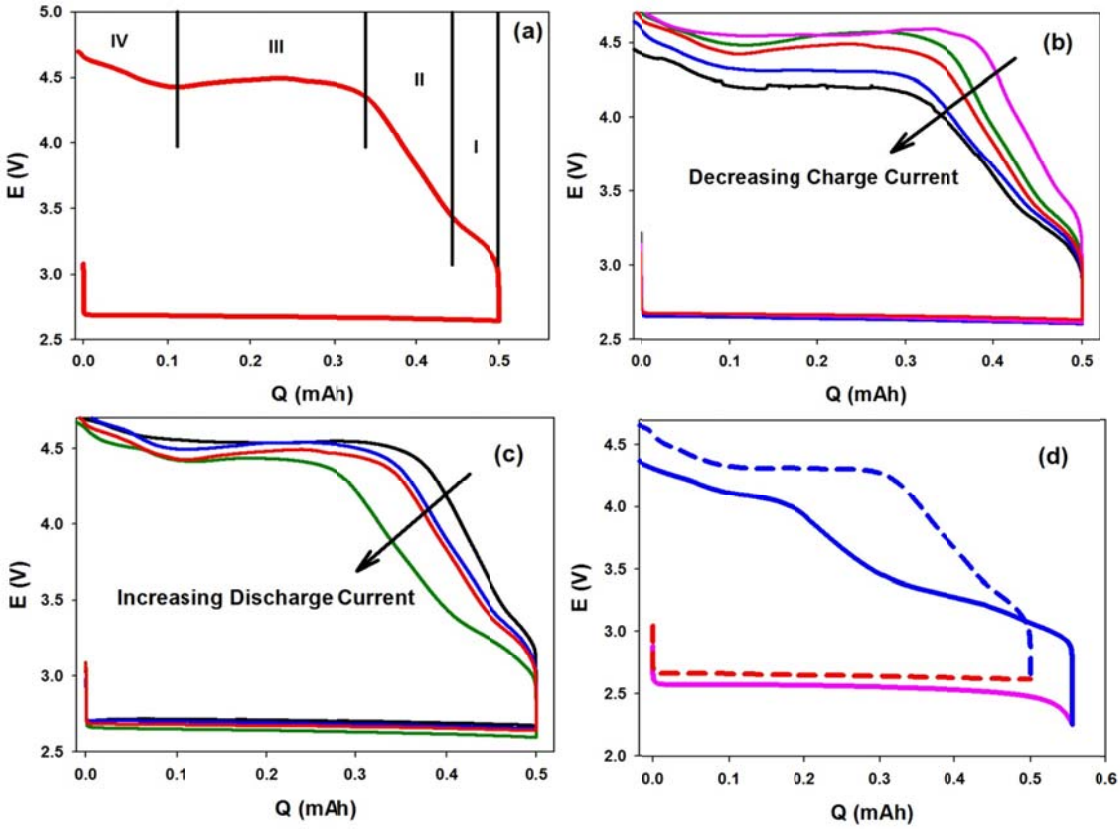

Figure 3.8 (a) A discharge/charge curve showing the regions of the charge portion; (b) cells discharged at 25 μA/cm^2 then charged at different rates from 5 – 100 μA/cm^2 (colors of curves listed below) ; (c) cells discharged at different rates from 5 – 50 μA/cm^2 (colors of curves listed below) then charged at 25 μA/cm^2; and (d) comparison of a cell fully discharged at 100 μA/cm^2 (pink curve) then charged at 10 μA/cm^2 with a cell discharged at 25 μA/cm^2 to a similar capacity (red dotted curve) and charged at 10 μA/cm^2. The colours in (b) and (c) on charge and discharge, respectively, are black = 5 μA/cm^2, blue = 10 μA/cm^2, red = 25 μA/cm^2, green = 50 μA/cm^2, and pink = 100 μA/cm^2.

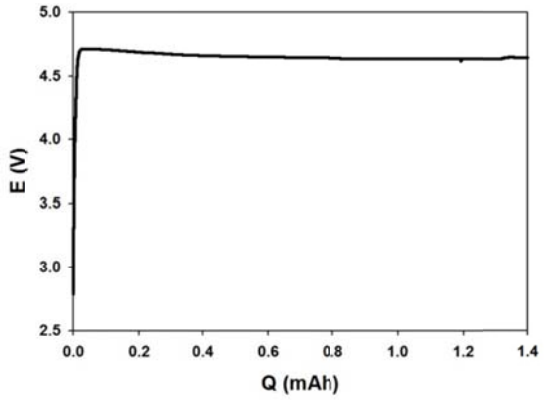

Figure 3.9 Charge curve of a pure GDE at 25 μA/cm^2 under O_2 in the absence of peroxide showing that the inherent electrolyte anodic stability limit is at approximately 4.7V.

3.4 Conclusions

The results unequivocally demonstrate that the current density on discharge indirectly affects the charge overpotential by determining the nature and morphology of the discharge product. The proof of a quasi-amorphous peroxide film formation at fast current rates and crystalline toroid morphologies at slower rates is significant with respect to the mechanistic understanding of ORR. The discharge pathway, in turn, determines the OER characteristics. A more ″defective″ peroxide leads to lowered charge overpotential with improved round trip efficiency but reduced capacity. The results also point the way for possible improvements in cell design that are the subject of our future studies. Higher active surface area (of non-carbonaceous materials)[31] and improved electronic conductivity of the oxygen electrode will enable better rate capabilities and support peroxide film formation. Alternatively, increasing the solubility of Li_2O_2 by electrolyte additives or surface modification of the carbon,[33,34,35] to inhibit passivation of the cathode surface are other valuable directions. The results of this chapter have since been used by

our group in a kinetic model.[36] In this study we show that the mysterious curvature in Tafel plots for Li-O_2 batteries is in fact due to the competitive uptake of LiO_2 by the surface *and* solution.

Chapter 4

The Nature of Lithium Peroxide Oxidation Revealed by *Operando* X-Ray Diffraction

4.1 Introduction

Several bottlenecks that impede the functioning of the Li-O_2 battery system need to be addressed before it can become viable. These include the high (dis)charge overpotential resulting in a lower round trip efficiency,[1,2] slow kinetics, electrolyte instability (side product formation)[3,4,5,6] leading to poor cyclability, and the requirement of high purity O_2. Of fundamental importance is the understanding of the mechanism of lithium peroxide formation and oxidation and the governing factors. Over the past years there has been significant progress in the understanding of the Li_2O_2 formation process during discharge. Clear correlations have been established between the solvent donor number,[7] discharge voltage, current density[8,9] and composition of the gas diffusion electrode on the morphology of Li_2O_2 formed and the mechanism of their formation, be it via solution[8] or on the electrode surface (as discussed in the previous chapter).[4] But one of the many challenges of the Li-O_2 system includes the mechanism of Li_2O_2 oxidation which remains less well understood, with the elusive LiO_2 superoxide intermediate remaining experimentally very difficult to observe. There are only a few inconclusive reports of superoxide observation both *in-* and *ex-situ*.[9,10,11] Modeling approaches suggest a Li deficiency driven solid solution reaction resulting in the formation of $Li_{2-x}O_2$ [12] or that smaller crystallites would decompose first at lower potential.[13] Experimentally, it has been

suggested that amorphous Li_2O_2 decomposes first at lower potentials[14] whereas a solid solution reaction has not been observed.

In this chapter, *operando* X-ray diffraction (XRD), Rietveld refinement, calculations, and on-line electrochemical mass spectrometry (OEMS) are combined to elucidate the mechanism of the oxidation evolution reaction, comparing electrochemically generated Li_2O_2 (E-Li_2O_2) and bulk crystalline (commercial) Li_2O_2 (C-Li_2O_2) during the charge reaction in a Li-O_2 cell. A clear difference is observed between the oxidation of E-Li_2O_2 and C-Li_2O_2 which can be explained by the difference in the nature of the particles and crystallites. The OER mechanism, however, appears similar for both E-Li_2O_2 and C-Li_2O_2 as Rietveld refinement of the *operando* data reveals Li deficiency in both cases indicating that the OER takes place via a solid solution reaction.

Drs. Swapna Ganapathy and Marnix Wagemaker conducted all *operando* XRD experiments, Rietveld refinements, and theoretical calculations in this chapter. Robert Black conducted the OEMS measurements and acquired the SEM images. I designed all experiments, prepared all electrodes and electrolytes, and assisted in the design of the operando XRD cell.

4.2 Experimental Details

4.2.1 *Operando* XRD Cell

A Li-O_2 cell that allows X-ray diffraction measurements to be conducted in reflection mode during battery cycling was designed and custom built. The top half of the cell is comprised of a Kapton® window with a diameter of 20 mm enclosed in a stainless steel casing with a small inlet to allow the intake of O_2 gas. An Al mesh current collector was

integrated into this top half. The bottom half consisted of a stainless steel coin attached to a spring, also enclosed in stainless steel, akin to that of a typical Swagelok® cell design. This formed the current collector on the anode side. The top and bottom halves of the cell were separated with a Teflon® spacer to prevent a short circuit, after which they were clamped together from the outside with a non-conductive clamp. The battery stack was assembled within, with the cathode on the side of the Kapton® window. The schematic is shown below in **Figure 4.1**.

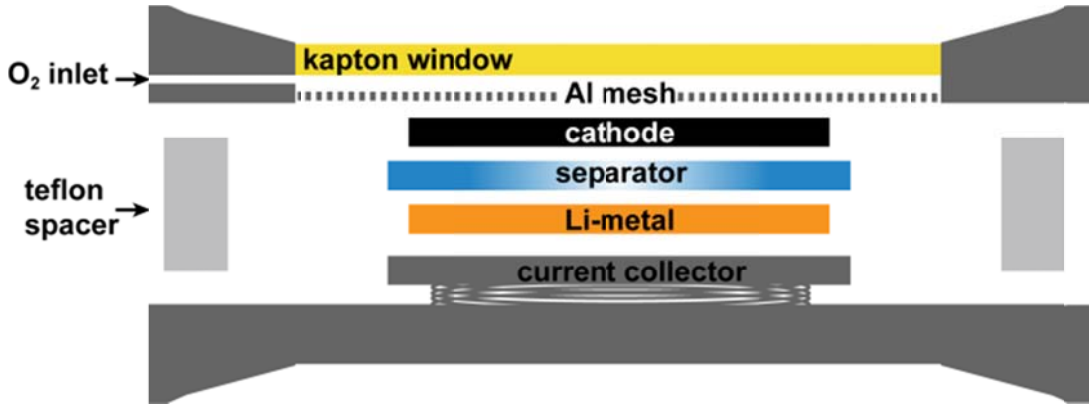

Figure 4.1 Schematic of the Li-O_2 cell used for in-situ XRD measurements.

4.2.2 Electrochemistry

Gas diffusion electrodes (cathodes) were fabricated by casting a mixture of activated carbon (Kuraray Chemical) and a lithiated Nafion® binder[8, 15] on carbon paper (Spectracarb). The cathodes were dried at 100°C for 24 hours to remove all surface adsorbed water, after which discs of 16 mm were punched from the sheets. The electrolyte consisted of a solution of 1 M lithium bis(trifluoromethanesulfonyl)imide (LiTFSI, Aldrich) dissolved in dried and distilled tetraethylene glycol dimethyl ether (TEGDME, <1

ppm H_2O). The battery, comprised of the cathode, a glass microfiber separator (Whatman) soaked with the electrolyte and a Li-metal anode, were assembled in the previously described *operando* XRD cell in the glove box. The cell was subsequently connected to O_2 (Linde, 99.995%) under a pressure of 1.5 bar where it was allowed to equilibrate for between 2 and 6 hours before it was tested. Electrochemical (dis)charge tests were performed with a MACCOR 5300 battery cycler.

4.2.3 XRD Measurements

X-ray diffraction measurements were performed on a PANalytical X'Pert Pro PW3040/60 diffractometer with Cu Kα radiation operating at 45 kV and 40 mA in an angular 2θ range of 31 – 66/71°. Scans of 1 hour and 7 minutes each were recorded for the batteries that underwent a complete (dis)charge cycle and of 30 minutes each for batteries that contained the pre-Li_2O_2 loaded cathodes that underwent charge only. Refinement of the diffraction data was carried out using the Rietveld method as implemented in the General Structure Analysis System (GSAS) program.[16] The lattice parameters, lithium occupancy, peak broadening and corresponding anisotropy (where present) were fit assuming that the thermal parameters remained constant. To more accurately fit the zero-position of the Li_2O_2 diffraction pattern, peaks arising from aluminum mesh as well as carbon (carbon paper) were excluded from the fits.

There has been much controversy on the precise crystal structure of lithium peroxide. In 1953, Fehér *et al.* first placed Li_2O_2 into the *P*-6 space group.[17] A few years later, in 1957, Föppl re-characterized the structure and modified the O – O distance from 1.28 Å to 1.55 Å.[18] Very recently, Föppl's structure was confirmed to be more accurate with the aid

of DFT calculations and the authors were able to place this structure into the $P6_3/mmc$ space group by slightly modifying the atomic positions.[19,20] Our experimental results match closest with Föppl's structure in the $P6_3/mmc$ space group (PDF # 01-074-0115). This model was used as a basis for the refinements and calculations throughout this chapter.

4.2.4 Theoretical Calculations

First-principle calculations were performed using the Heyd-Scuseria-Ernzerhof (HSE) hybrid functional[21,22] as implemented in the Vienna Ab-initio Simulation Package[23] (VASP) with the projector augmented wave (PAW) method,[24] due to its demonstrated ability to accurately describe the electronic properties of the Li_2O_2 system.[25] An energy cutoff of 800 eV was employed and ionic relaxation was performed until a 10^{-4} eV per formula unit difference in energy was obtained.

4.3 Results and Discussion

4.3.1 Dis(charging) of E-Li_2O_2

Operando X-ray diffraction patterns were collected on Li-O_2 cells run for a complete (dis)charge cycle at low and intermediate current densities of 25 $\mu A/cm^2$ and 50 $\mu A/cm^2$. The appearance and disappearance of the reflections in **Figure 4.2(a) and (b)** belonging to Li_2O_2 (hereafter called E-Li_2O_2) prove its electrochemical formation and removal upon discharge and charge, respectively. **Figure 4.2(c)** shows a section of the diffraction patterns at the end of discharge for both current densities along with their Rietveld refinement. Using the Scherrer formula, we determined that smaller average crystallite

sizes for E-Li_2O_2 are generated at a current density of 50 μA/cm^2 and larger crystallite sizes are formed at 25 μA/cm^2 (see **Table 4.1**) at the end of discharge. This is in agreement with the results presented in Chapter 3. Comparing 25 μA/cm^2 (**Figure 4.2(c)**, upper panel) and 50 μA/cm^2 (**Figure 4.2(c)**, lower panel), the peaks corresponding to the (1 0 0) reflection are at the same angle in 2θ, whereas those corresponding to the (1 0 1) and (1 0 4) reflections are not. This is due to different *c*-lattice parameters for Li_2O_2 formed at the lower and higher current rates, of 7.696 Å and 7.781 Å respectively (see **Table 4.1**). The value for the *a*-lattice parameter remained constant at ~3.141 ± 0.002 Å. As discussed previously in Chapter 3, the current density has a strong impact on the nature and morphology of the Li_2O_2 crystallites that are formed. The current density dependent mismatch in peak positions shown here has not been reported for *ex-situ* measurements, possibly due to relaxation effects that occur during the time between discharge and the actual XRD measurement of the cathode. During this time, the *c*-lattice parameter can readily relax to values that are closer to the equilibrium value of bulk Li_2O_2 (7.64 Å). There was no significant variation or trend observed in the evolution of the lattice parameters as a function of discharge time. On the other hand, during charge there were subtle changes in the *c*-lattice parameter, especially visible for the battery run at a low current density (**Figure 4.3(a)**). It remained constant for the first part of charge and showed a gradual increase in value towards the latter part of charge. These changes will be discussed below in correlation with the nature of the crystallites and the Li composition.

Table 4.1 *Lattice parameters and domain sizes obtained via Rietveld refinement of both electrochemically produced E-Li_2O_2 (end of discharge) and bulk crystalline C-Li_2O_2.*

Type of Li_2O_2	Lattice parameters		Average Domain Size (nm)
	a **= *b*** **(Å)**	***c*** **(Å)**	
E-Li_2O_2 (25 μA/cm^2)	3.140	7.696	45.3 ± 0.9
E-Li_2O_2 (50 μA/cm^2)	3.143	7.781	26.3 ± 1.0
C-Li_2O_2	3.141	7.646	87.3 ± 1.4

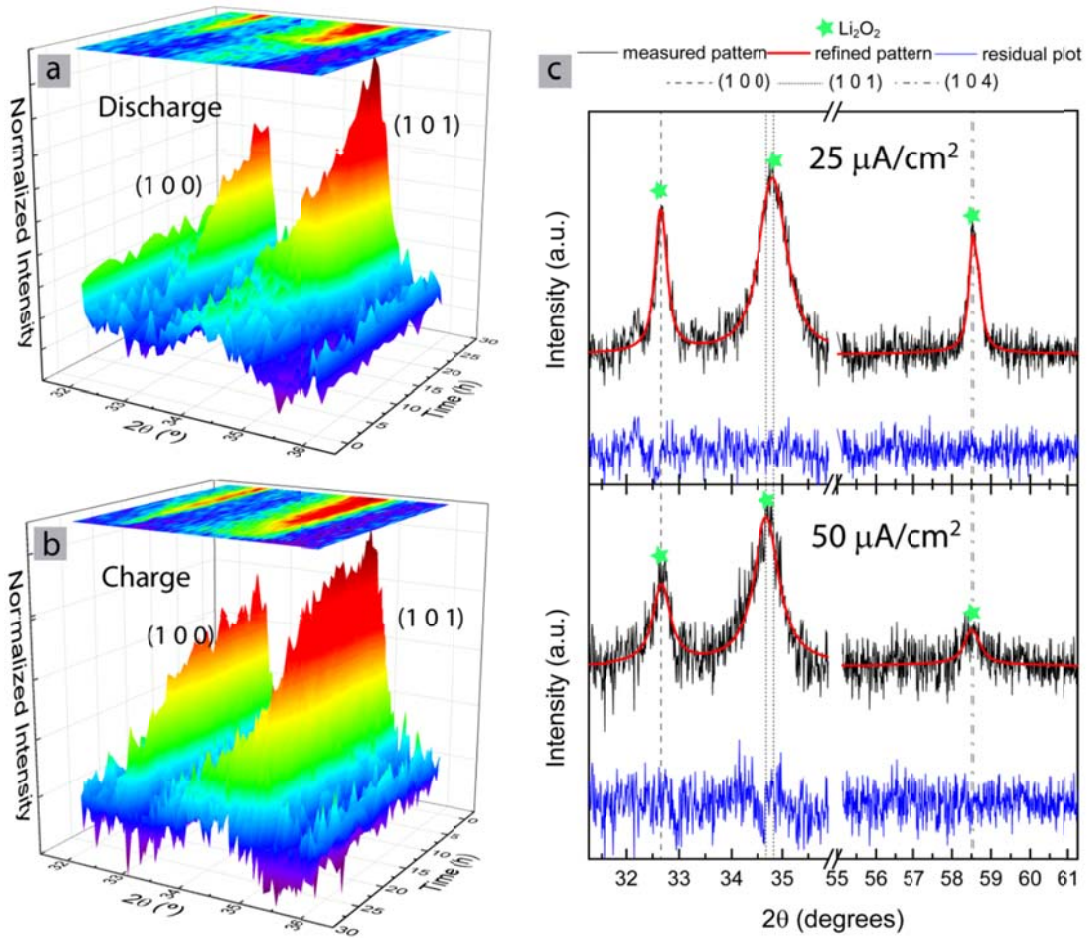

Figure 4.2 (a) /(b) Three dimensional discharge and charge plots of the XRD patterns in the 2θ region of 32 – 36°, recorded *operando* as a function of time during of E-Li_2O_2 with a constant current of 50 μA/cm^2. (c) Background subtracted diffraction patterns recorded *operando* after full discharge of the Li-O_2 cell, and their Rietveld refinement with an R_{wp} of less than 2%. Differences in peak positions corresponding to the (1 0 1) and (1 0 4) reflections for the E-Li_2O_2 produced at current densities of 25 μA/cm^2 and 50 μA/cm^2 respectively are indicated.

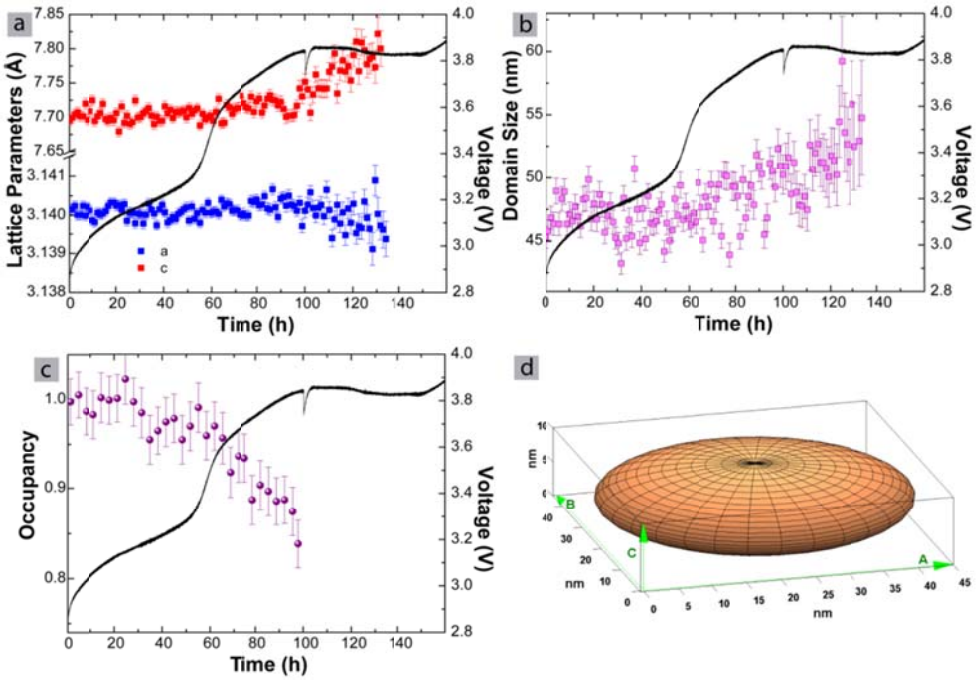

Figure 4.3 Galvanostatic charging of electrochemically formed Li_2O_2 (E-Li_2O_2) showing the evolution of the lattice parameters (a), average domain size (b) and average lithium occupancy (c) as a function of charge time. The corresponding voltage profiles as measured during charge have been illustrated in each graph. (d) Crystallite shape derived from the apparent coherence lengths obtained for the (1 0 0) and (1 0 1) reflections using FULLPROF.[26,27]

In order to fit the peak broadening, a variation on the pseudo-Voigt function with reflection asymmetry was implemented in GSAS.[16] Reflections appeared anisotropically broadened in the *c*-direction, with the magnitude being larger at lower current density. In GSAS, this was fitted by the micro-strain broadening description given by Stephens,[28] resulting in non-zero values for coefficients corresponding to the anisotropic parameter in the *c*-direction (S_{004}). We cannot unequivocally distinguish between size and strain

broadening given the limited 2θ data range. However, at lower discharge current densities, E-Li_2O_2 is known to form toroidal[29,30] aggregates, which consist of stacked Li_2O_2 crystalline platelets.[31] Published transmission electron micrographs of the Li_2O_2 toroids,[31] albeit those grown at a lower current density, show that the stacked plate-like crystallites have large (0 0 0 1) crystal facets that grow plate by plate along the [0 0 1] direction. This results in anisotropic crystalline Li_2O_2 platelets that are approximately 10 nm in the *c*-direction and 400-600 nm in the *ab*-plane.[31] Assuming the our observed anisotropic broadening is solely due to size broadening, the X-ray diffraction pattern was further analyzed using the FULLPROF program[26,27] for which the Rietveld refinement includes an anisotropic size-broadening model based on spherical harmonics.[32] From this refinement we obtained apparent dimensions of 45.4 nm and 14.4 nm for the (1 0 0) and the (1 0 1) reflections, respectively. Note that diffraction is sensitive to the coherence length of the crystalline planes, which is in this case determined by the platelets and not the toroid shape. This translates into a disc-like crystallite plate shown in **Figure 4.3(d)** which is in agreement with that reported in literature.[31] The peak broadening as well as the anisotropic broadening as a function of charge time (**Figure 4.4**), both showed a small decrease towards the end of charge, suggesting an *increase* in average crystallite size, **Figure 4.3(b)**, as well a slightly more isotropic crystalline platelet shape towards the end of charge. The average increase in domain size shown in **Figure 4.3(b)** supports the model put forth by Radin and co-workers[13] proposing the initial decomposition of the smallest crystals, which should lead to an average narrowing of the reflections and therefore an increased average domain size. The limited decrease of the anisotropic broadening at the end of charge (**Figure 4.4**) indicates a small change in average particle shape, with the

particles becoming more isotropic. In combination with the increase in isotropic domain size, this may indicate that thinner/flatter platelet crystallites are oxidized first. The limited change in average platelet dimensions, even at 80% state of charge, points towards a small active fraction of Li_2O_2 particles, and hence, a plate-by-plate like oxidation. This as opposed to a larger active fraction, where an average decrease in crystallite size upon charge should lead to increased domain size broadening which is not observed here. It should be noted that diffraction is unable to probe the last stages of charge (corresponding to higher voltages) because of the low intensity of the reflections.

By following the evolution of peak intensity as a function of charge time for the (1 0 0) and (1 0 1) peaks of E-Li_2O_2 (**Figure 4.2**), we note that the growth of the peaks during the discharge is linear (**Figure 4.2(a)**), but a nonlinear decrease in peak intensity was observed during charge (**Figure 4.2(b)**). The non-linearity in the decay processes, as first reported by Lim and co-workers,[33] is observed irrespective of the current density used. From the integrated and normalized area under the (1 0 0) and (1 0 1) reflections as shown in **Figure 4.5**, we see that the decay takes place in two-stages during charge, first slowly (static for a current density of 25 $\mu A/cm^2$) then faster (linear). The decay in peak intensity (**Figure 4.5(a)**) coincides with an increase in voltage starting at 3.4 V and declines linearly over the second plateau up to a voltage of ~ 3.9 V. This is less obvious at the higher current densities (**Figure 4.5(b)**) due to the limited number of data points recorded. What is clear from both datasets, however, is that the decay of peak intensity begins only *after* the first voltage plateau. The total lifetime of the peak intensity as seen through diffraction is also longer for discharge (**Figure 4.2 (a)/(b)**). The linear growth in peak intensity

indicates a continuous uptake of O_2 to form E-Li_2O_2. This could occur either 1) *via* a two-electron process ($2Li^+ + O_2 + 2e^- \rightarrow Li_2O_2$); or 2) *via* sequential one-electron processes[4,34] ($Li^+ + O_2 + e^- \rightarrow LiO_2$; $LiO_2 + Li^+ + e^- \rightarrow Li_2O_2$); or 3) *via* a one-electron process to form LiO_2 followed by its disproportionation to form Li_2O_2[7,35] ($Li^+ + O_2 + e^- \rightarrow LiO_2$; $2LiO_2 \rightarrow Li_2O_2 + O_2$). At a constant reaction rate, the processes in mechanisms 2) and 3) must be rapid. During the first stage of charge the integrated area under the reflections is practically constant, indicating preferential decomposition of surface LiO_2 species and/or of any *amorphous* Li_2O_2 component that may be present in the lower voltage regime (2.8 – 3.4V).[3,9,10,11,36] The second stage is characterized by a linear decrease in integrated area under the reflections indicating the complete oxidation of E-Li_2O_2 grains and evolution of O_2. Despite the relative stability of TEGDME towards peroxide, it has already been reported by some authors[35] that small amounts of Li_2CO_3 are formed in the initial part of the charge process, which has been attributed to the possible reaction of highly active nascent O_2^* that is released, or due to the reactivity of the sub-stoichiometric $Li_{2-x}O_2$ intermediates. These reactions could be responsible for the disparity in peak decay rates observed for charge *vis-à-vis* discharge (**Figure 4.2(a)/(b)**).

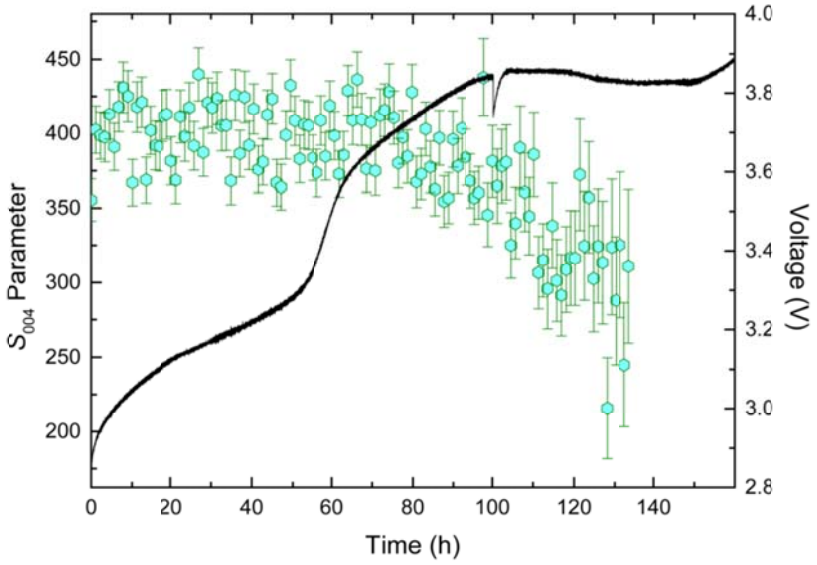

Figure 4.4 Refined values of the S_{004} anisotropic parameter as a function of charge time for E-Li_2O_2.

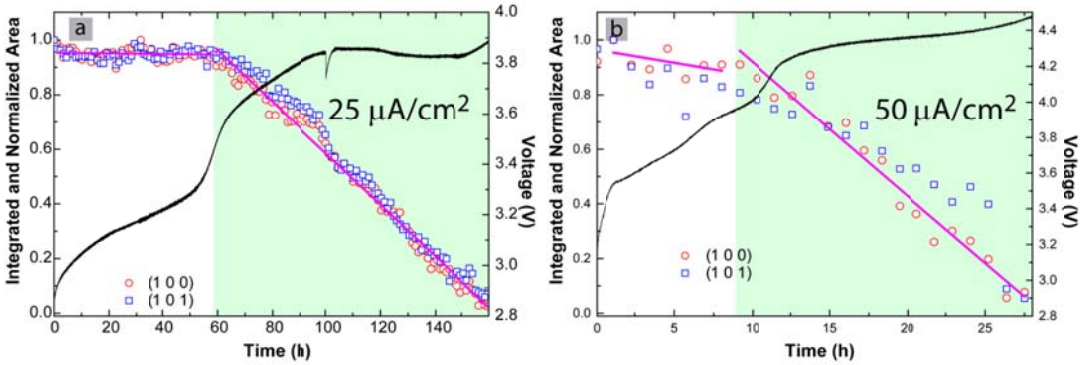

Figure 4.5 Galvanostatic charging of electrochemically formed Li_2O_2 (E-Li_2O_2). Integrated and normalized area under the (1 0 0) and (1 0 1) peaks as a function of charge time have been plotted for current densities of (a) 25 and (b) 50 μA/cm^2 respectively. The pink lines indicate the linear fit of the points within the shaded or unshaded areas. The corresponding voltage profiles as measured have also been illustrated in each graph.

From the Rietveld refinement of the diffraction data during charge, a clear evolution of the Li-occupancy was observed as a function of charge duration (**Figure 4.3(c)**). Obtaining Li-occupancies from X-ray diffraction is usually quite difficult due to the low atomic number of Li compared to the other typically heavier elements present. However, in Li_2O_2, the reflections are very sensitive to both oxygen and lithium occupancies, and thus they can be easily determined. The results show there is a gradual decrease in the lithium occupancy from ~ 3.2 V that begins slightly before the decline in the diffraction peak intensity (**Figure 4.5(a)**). This indicates that the decomposition of E-Li_2O_2 must take place via sub-stoichiometric E-$Li_{2-x}O_2$ intermediates, and that during charge, the system becomes on average, increasingly lithium deficient. Given the predicted decrease in the *c*-lattice parameter for Li sub-stoichiometric $Li_{2-x}O_2$ by DFT calculations,[37] this poses a contradiction to the almost constant *c*-lattice parameter on charge in **Figure 4.3(c)**. To investigate the dependence of the lattice parameters change on lithium vacancies in more detail, two similar DFT calculations were performed on a 2×2×1 super cell of Li_2O_2 by removing one lithium from either of the two crystallographically distinct lithium sites in the structure (Li1 and Li2): both resulting in a 0.93 occupancy. On relaxation, both structures showed virtually no decrease in the *a*-lattice parameter upon lithium removal (*i.e.*, <1%). For removal of the lithium atom between the O – O position (Li2, **Figure 4.6**), a noticeable decrease (1.6%) in the *c*-lattice parameter was observed, compared to the removal of the interlayer lithium atom (Li1), which shows virtually no change in the *c*-lattice parameter (<0.15%; **Table 4.2**). Hence, the creation of lithium vacancies observed in **Figure 4.3(c)** is most likely due to vacancies on the Li1 site consistent with the absence of a significant change in lattice parameters, at least for dilute vacancy concentrations.

This is reasonable because the energy required to create a lithium vacancy at the Li2 position is higher than at Li1.[38] This energy is a result of the greater bond strength of Li2 – O than Li1 – O which is reflected in the bond lengths (Li2 – O = 1.966 Å and Li1 – O = 2.151 Å). In addition, the small increase observed in the *c*-lattice parameter as a function of charge time may be correlated to the disintegration of the toroid shaped secondary particles. By stripping primary platelet crystallites from the toroids, additional low energy (0 0 0 1) surfaces of the platelets would be exposed. For nano-structured metal oxides, this typically leads to an expansion of lattice parameters[39] attributed to an increase in the surface energy due to larger exposed surfaces that is manifested at smaller crystallite sizes. A widely studied example of this phenomenon is CeO_2, which exhibits an increase in the fraction of surface oxygen in the form of superoxide at nano-crystallite dimensions.[40] Therefore, this increase in the *c*-lattice parameter could be indicative of more exposed surfaces in E-Li_2O_2 as the state-of-charge progresses.

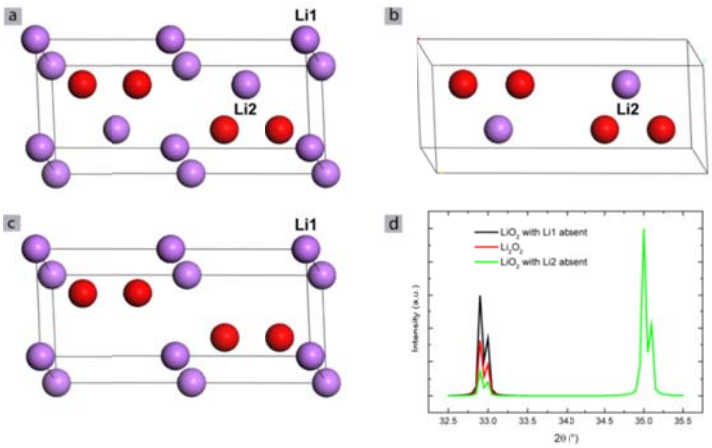

Figure 4.6 Models of unit cells of Li_2O_2 with (a) both lithium sites Li1 and Li2 occupied (b) only Li2 occupied and (c) only Li1 occupied. (d) Simulated diffraction patterns in the 2θ range of 32.5 – 35.5° of (a) – (c).

Table 4.2 *Lattice parameters obtained from first-principle structural relaxations of a 2x2x1 supercell of stoichiometric Li_2O_2 and with vacancies at the Li1, Li2 and O sites respectively.*

Type of Li_2O_2	Lattice parameters	
	a = b (Å)	c (Å)
Li_2O_2	3.160	7.692
$Li_{1.875}O_2$ (Li1 vacancy)	3.129	7.681
$Li_{1.875}O_2$ (Li2 vacancy)	3.123	7.568
$Li_2O_{1.875}$ (O vacancy)	3.155	7.669

4.3.2 Charging of C-Li_2O_2

To probe the oxygen evolution mechanism, charge-only *operando* XRD experiments were performed using electrodes pre-loaded with bulk, crystalline commercial Li_2O_2 (hereafter called C-Li_2O_2). As this material has a higher degree of crystallinity than that formed upon electrochemical reduction, higher X-ray diffraction peak intensities result. This allows for better statistics and/or time resolution of the measurement during charge. In addition, the different nature of these particles may provide insight in the charge mechanism. Experiments were performed using current densities of 25 and 50 $\mu A/cm^2$, comparable to the E-Li_2O_2 experiments. The sharp voltage rise and drop at the beginning of the voltage profiles (see **Figure 4.9**) is due to a reaction between carbon and Li_2O_2 at their interface and is referred to as the "activation process".[41] The pristine cathode diffraction pattern, measured before charging, along with its Rietveld refinement is given

in the supporting information (**Figure 4.7**). Only peaks from Li_2O_2 are visible indicating that any LiOH impurities[42] present are obviously amorphous and should not influence the monitoring of crystalline Li_2O_2 oxidation. From this, the initial lattice parameters of Li_2O_2 were obtained; a = 3.141 Å and c = 7.646 Å (**Table 4.1**). At 50 μA/cm^2, the *a*- and *c*-lattice parameters remained relatively constant until higher charge overpotentials were reached ((after the plateau at ~3.7 V; **Figure 4.8**) at which point the *a*- parameter increased. The opposite trend was observed for the *c*- parameter. At a lower current density (25 μA/cm^2; **Figure 4.9(a)**), more complex behavior was observed. Initially, both the *a* and *c*- parameters remained constant, followed by a gradual decrease in *a.* A small shift in the discharge profile to higher voltage is accompanied by the sharp onset of an increase in the *a*- parameter accompanied by the opposite in *c*. No anisotropic broadening was observed, indicating an isotropic crystallite shape (refer to Chapter 2, equation 2-8), in contrast to the plate-like Li_2O_2 crystallites formed electrochemically. The evolution of domain sizes (**Figure 4.9(b)**) obtained from the peak widths remained relatively constant up to about the 50 hour point, after which the average domain size continuously decreased. Values for the lattice parameters and domain sizes beyond 70 hours of charge are unreliable due to very low peak intensities.

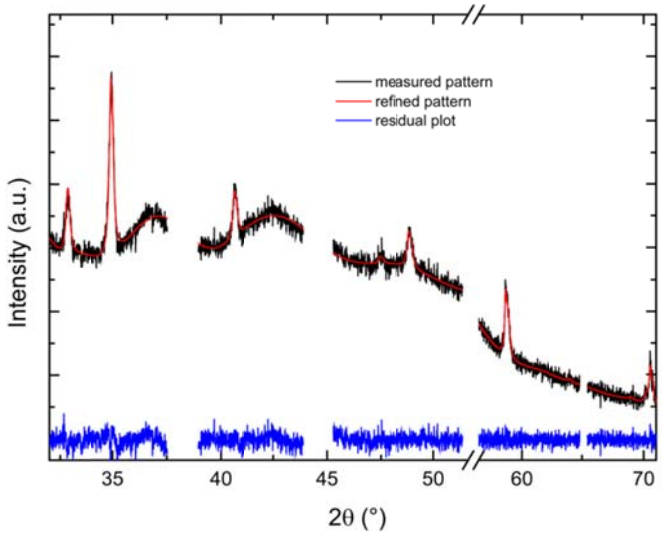

Figure 4.7 The first diffraction pattern recorded of the pre-loaded C-Li_2O_2 battery along with its Rietveld refinement. Regions with peaks corresponding to the Aluminium mesh and carbon/carbon paper were excluded from the fit.

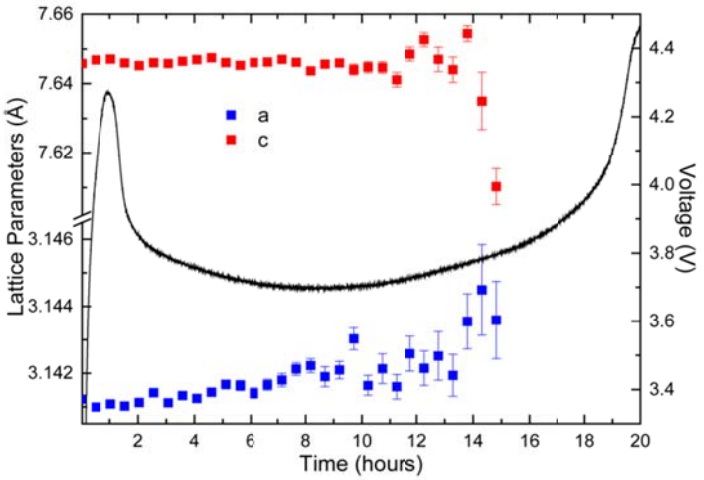

Figure 4.8 Evolution of lattice parameters as a function of charge time obtained from Rietveld refined XRD patterns recorded in-situ at a current density of 50 μA/cm^2. The corresponding voltage profile as measured has also been illustrated.

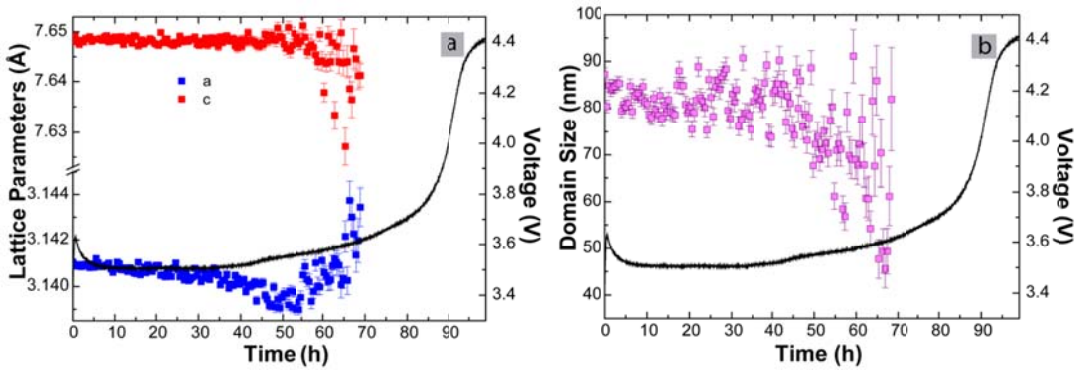

Figure 4.9 Evolution of (a) lattice parameters and (b) domain sizes as a function of charge time for C-Li_2O_2 electrodes obtained from Rietveld refined XRD patterns recorded operando at a current density of 25 μA/cm^2. The corresponding voltage profiles as measured have also been illustrated in each graph.

For the charge at 25 μA/cm^2, the increase in the charge overpotential and *a*-parameter along with the decrease in the *c*- parameter at the 50-hour mark of charge suggests the emergence of a dominant lithium sub-stoichiometric $Li_{2-x}O_2$ phase (**Figure 4.9(a)**). Theoretical calculations[12] have shown that bulk species (tending towards LiO_2) would have an increasingly smaller *c*- parameter. Most likely, the lower surface to bulk ratio of the larger isotropic C-Li_2O_2 crystallites does not introduce the competing increase in *c* observed for the oxidation of E-Li_2O_2. Hence, the decrease in the *c*-parameter appears to be directly related to lithium sub-stoichiometry. The evolution of domain sizes for C-Li_2O_2 determined from the isotropic broadening over charge as shown in **Figure 4.9(b)**, assuming the absence of strain, remains practically constant in the plateau (up to 50 hours

of charge) after which there is a continuous decrease with higher voltage. Although this could indicate a two-stage transformation mechanism, this appears unlikely given the linear decrease in X-ray reflections shown in **Figure 4.10(a)**. In this context, the evolution of the average domain size in **Figure 4.9(b)** most likely indicates a small oxidizing fraction of Li_2O_2 for which the domain size reduces due to disintegration. Such a small actively transforming fraction will have negligible impact on the average domain size at the early stage of charge. At the end of charge the same amount of actively transforming material will constitute a relatively larger fraction of the remaining Li_2O_2, resulting in an average decrease in domain size at the end of charge.

Online electrochemical mass spectrometry (OEMS) was performed on the C-Li_2O_2 material. This is a widely used tool for studying the stability of Li-O_2 cell electrolytes,[3,4,5,41,42,43,45] and quantification of the gases evolved can reveal a great deal of information about the behavior during different stages of charge. Ideally, only oxygen should be evolved with a ratio of 2 e^-/O_2. Practically, the detection of CO_2 is common as a result of the oxidation of Li_2CO_3 or other side-products formed in the cell.[45] In **Figure 4.11**, the constant oxygen evolution rate measured (after an initial overpotential, see discussion below) supports a single stage oxidation process for C-Li_2O_2.

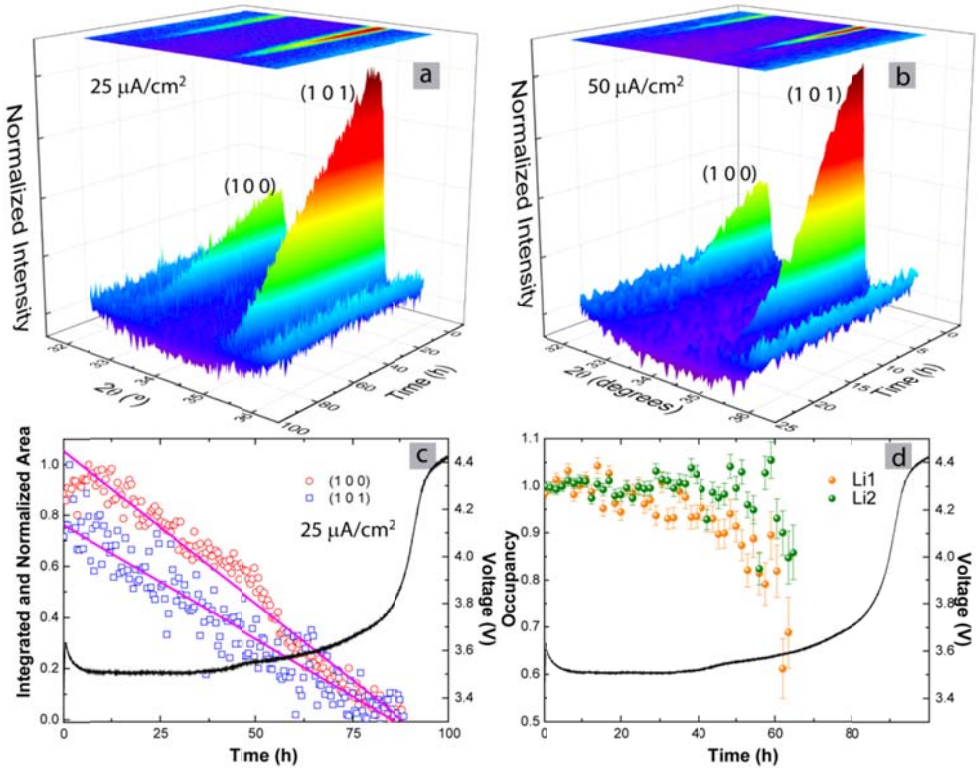

Figure 4.10. Galvanostatic charging of commercial Li_2O_2 (C-Li_2O_2). (a)/(b) Three dimensional plots of the XRD patterns in the 2θ region of 32 – 36°, recorded in-situ as a function of time during charge with constant currents of 25 μA/cm^2 and 50 μA/cm^2, respectively. Peaks corresponding to the (1 0 0) and (1 0 1) reflections of C-Li_2O_2 are visible. (c) Integrated and normalized area under the (1 0 0) and (1 0 1) peaks as a function of charge time recorded with a current density of 25 μA/cm^2. The pink lines represent a linear fit of the intensities of the (1 0 0) and (1 0 1) reflections. (d) The evolution of the lithium occupancy for the Li1 and Li2 sites obtained via Rietveld refinement of the diffraction patterns as a function of charge time recorded with a current density of 25 μA/cm^2. Charge voltage profiles for both are shown.

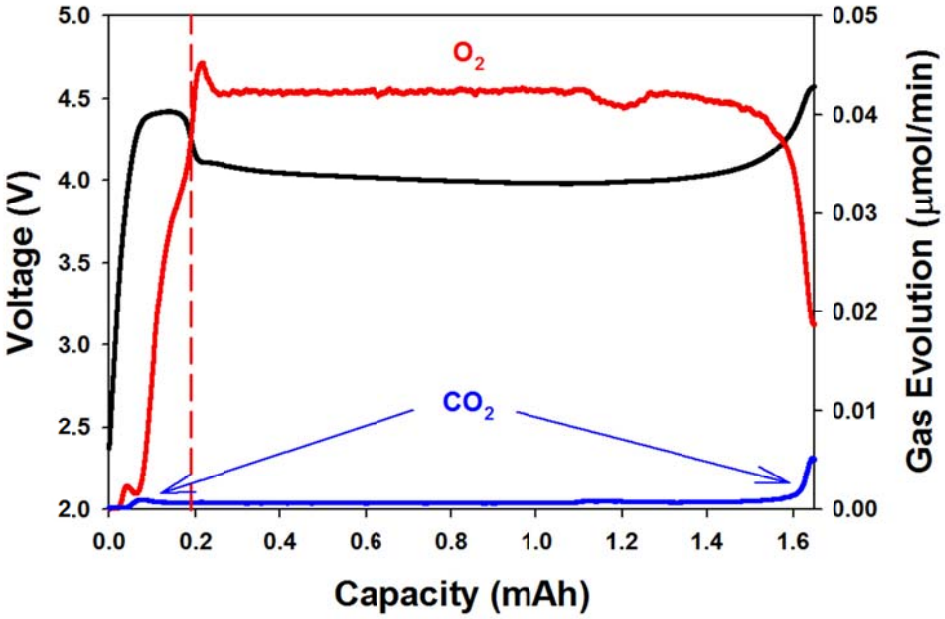

Figure 4.11 The voltage profile for the charge reaction of a Li_2O_2-loaded Vulcan XC72 electrode at 75 μA/cm^2 in 1 M LiTFSI/TEGDME, along with the gas evolution monitored by online electrochemical mass spectrometry (OEMS).

Comparing the voltage profiles for the galvanostatic charging of electrodes pre-loaded with Li_2O_2 (**Figure 4.10c, 4.11, and 4.12**) at different current densities (25, 50, and 75 μA/cm^2, respectively), distinct differences can be observed. First, the main voltage plateau is very sensitive to the current density, which increases from approximately 3.6 V at 25 μA/cm^2 to approximately 4.0 V at 75 μA/cm^2. The duration of the initial overpotential is also extended, and is most apparent in the OEMS experiment above (**Figure 4.11**) at the highest current density examined. This overpotential is attributed to the interfacial contact resistance between the Li_2O_2 particles and the carbon particles in the composite electrodes.

Although the decline in diffracted intensity during charge of the C-Li_2O_2 cathodes is on average linear, as is evident from **Figure 4.10(a)**, the individual decline of the (1 0 0) and (1 0 1) reflections show a marked difference as observed from the integrated area under the (1 0 0) and (1 0 1) peaks as a function of charge duration shown in **Figure 4.10(c).** Factors that commonly affect the relative intensities between reflections include changes in atomic positions as well as in their occupancies. Lithium occupies two distinct crystallographic sites in Li_2O_2; the interlayer Li1 position and the Li2 position next to the oxygen dumbbell, as shown in **Figure 4.6**. If both sites are occupied, the ratio of the normalized and integrated intensity under the (1 0 0) and (1 0 1) peaks should be 1 *i.e.* (1 0 0):(1 0 1) = 1. On the other hand, an isostructural LiO_2 system constructed with only Li1 missing gives rise to diffraction patterns with (1 0 0):(1 0 1) > 1 and a system with Li2 absent gives rise to diffraction patterns with (1 0 0):(1 0 1) < 1 (simulated diffraction patterns are given in **Figure 4.6**). Therefore, **Figure 4.10(c)** indicates preferential Li1 vacancies occurring upon charge. This was quantified by Rietveld refinement of both Li1 and Li2 occupancies of the C-Li_2O_2 diffraction data as a function of charge time (**Figure 4.10(d)**). The Li occupancy of the Li2 site remains constant (close to 1) until the 50 hour mark of charge, whereas the occupancy at the Li1 site shows a gradual decrease, creating Li1 vacancies, from the onset of charge. After 50-hours of charge Li2 vacancies also appear to be created, consistent with evolution of the integrated intensity of the (1 0 0) reflection in **Figure 4.10(c)**. Consistent with the DFT calculations discussed above, and the reported lower energy of Li1 vacancy formation, the *operando* diffraction of C-Li_2O_2 indicates preferential formation of Li1 vacancies at the onset of charge. This again points towards oxidation through a Li-deficient solid solution reaction. The increase in average

vacancy concentration observed at the end of charge in **Figure 4.10(d)** is most likely the consequence of the small actively oxidizing $Li_{2-x}O_2$ fraction, the properties of which become more apparent at the end of charge when almost no passive Li_2O_2 is present.

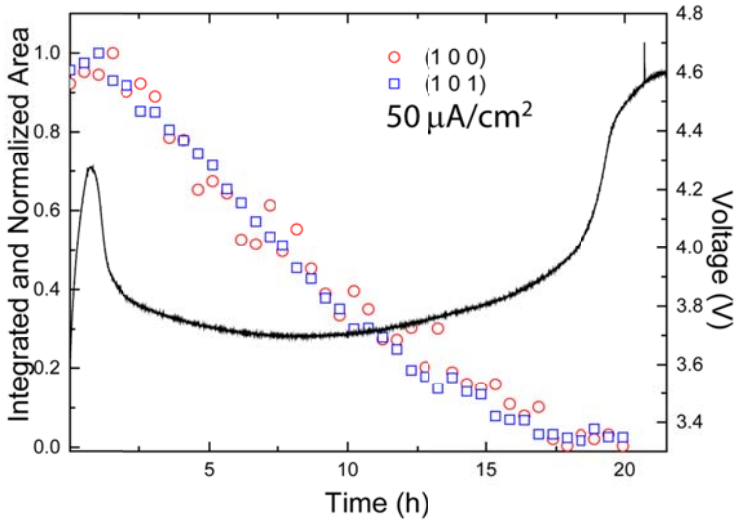

Figure 4.12 Integrated and normalized area under the (1 0 0) and (1 0 1) peaks as a function of charge time recorded with a current density of 50 μA/cm^2.

4.3.3 Charge Mechanism

From the data extracted from the *operando* diffraction patterns measured during the charge of E-Li_2O_2, two oxidation stages can be distinguished (**Figure 4.13(a)**). During the first stage, amorphous Li_2O_2 and the smallest crystallites oxidize at the low voltage plateau between 2.8 – 3.4 V. This is supported by the absence of change in diffracted intensity and absence of any evolution in the parameters obtained from Rietveld refinement, with the exception of the Li-occupancy. This indicates that some Li vacancies are created, resulting in a small fraction of sub-stoichiometric $Li_{2-x}O_2$. During the second stage, in the

voltage range 3.4 – 3.9 V, a continuous drop in the XRD peak intensity is observed, accompanied by a continuing decrease in the Li-occupancy. This indicates that the oxidation is solid solution driven, proceeding in two steps *i.e.* (1) $Li_2O_2 \rightarrow Li_{2-x}O_2 + xLi^+ + xe^-$ and (2) $Li_{2-x}O_2 \rightarrow (2\text{-}x)Li^+ + (2\text{-}x)e^- + O_2$. In addition, the decrease in both isotropic and anisotropic peak broadening indicates that the smallest and thinnest platelet crystallites are oxidized preferentially, leaving the largest platelets at the end of charge. This model is further validated by scanning electron microscopy (SEM) images recorded at different states of charge of E-Li_2O_2 (dis)charged at a current density of 25 $\mu A/cm^2$ as shown in **Figure 4.13(b)**. In image A, which represents the state of the cathode at the end of discharge, toroids of Li_2O_2 are covered by an amorphous lithium sub-oxide blanket.[10] At ~25% of charge (image B) more toroids become visible, indicating that the lithium sub-oxide blanket is oxidized first. By ~50% of charge (image C) the amorphous blanket has completely disappeared and the toroids are noticeably thinner. Image C, measured at the end of charge shows no Li_2O_2 remains either amorphous or toroidal. Thereby, the *operando* diffraction study supports both the charge model *via* solid-solution compositions brought forward by Kang *et al.*[12] and the preferable decomposition of the smallest crystallites brought forward by Radin *et al*.[13,14,36] In addition, the limited change in average crystallite dimensions at the end of charge indicates that a plate-by-plate-like oxidation process occurs. This "two-stage" oxidation mechanism for E-Li_2O_2 is slightly complicated by electrochemical decomposition which occurs during discharge and the subsequent oxidation of these side-products during charge.[43,44] We note that the rise in voltage from the amorphous region (2.8 V – 3.4 V) to the second plateau can be influenced

by these side-products, yet the observed diffraction data for Li_2O_2 should not be affected. Although lithium carbonate is not oxidized below 4 V, lithium formate can be oxidized around 3.8 V,[45] which most likely impacts the upper voltage plateau.

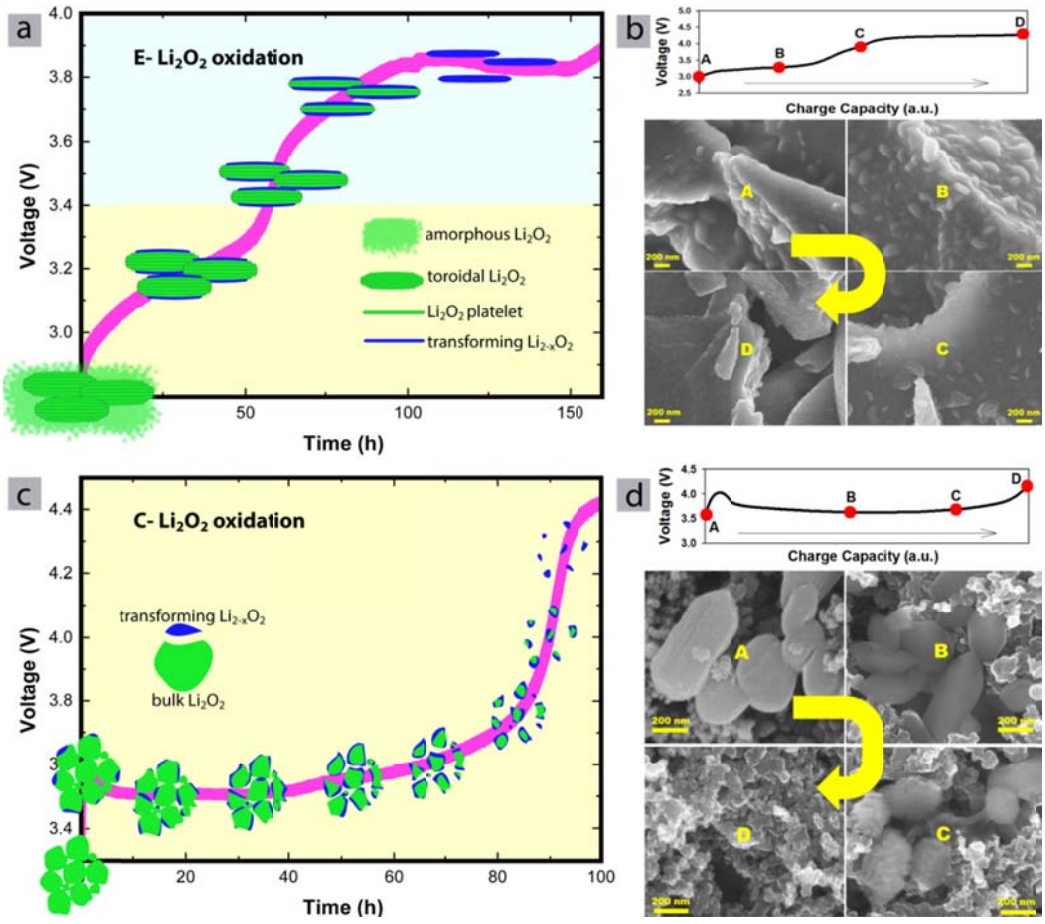

Figure 4.13 Cartoon showing the mechanism of (a) E-Li_2O_2 and (c) C-Li_2O_2 oxidation during the charge process as determined from X-ray diffraction. Scanning electron microscopy images (SEM) recorded at different stages of oxidation of E-Li_2O_2 and C-Li_2O_2 are depicted in panels (b) and (d) respectively.

The *operando* X-ray diffraction data for charging of C-Li_2O_2 supports a single oxidation stage via a small actively transforming fraction (**Figure 4.13(b)**). The continuous decrease in peak intensity of the (1 0 0) and the (1 0 1) reflections indicates the continuous decomposition of C-Li_2O_2 throughout the charge process (**Figure 4.10(a)**). This is consistent with *operando* mass spectrometry measurements[41,42,46,47] that have been performed during charge with preloaded cathodes, which report a continuous evolution of O_2 also during the initial part of charge. Noteworthy is the delay in oxygen evolution observed here (**Figure 4.11**, red dashed line) until this overpotential is overcome. This, along with the small amount of CO_2 evolved during this initial stage of charge in the pre-loaded (C-Li_2O_2) electrodes indicates a chemical reaction between the Li_2O_2 and carbon to form an oxidized carbon interface. After the overpotential is surmounted, a single-stage oxidation process dictates a constant O_2 evolution rate until the end of charge. The small amount of CO_2 which is produced at the end of charge is presumed to be due to the oxidation of electrolyte decomposition products (lithium formate, carbonate, etc.) as the voltage increases. These are formed at the reactive $Li_{2-x}O_2$ surface throughout the charge process.

The evolution of the Li1 occupancy (**Figure 4.10(d)**, reflecting the Li deficiency), and the isotropic broadening of the reflections (indicating a decrease in average crystallite size, **Figure 4.9(b)**), both show a change that increases with the state of charge. This can be explained by a small actively oxidizing C-Li_2O_2 fraction. This fraction is most likely limited to the surface regions of the larger peroxide crystallites at the onset of charge, resulting in no discernible changes in broadening of the diffraction peaks. This is

confirmed by additional SEM images (**Figure 4.13(d))** measured on C-Li_2O_2 oxidized to different states of charge. In image C at ~75% charge, there is clear evidence of a decrease in particle size as well as surface oxidation. As the state-of charge progresses, the actively transforming C-$Li_{2-x}O_2$ fraction increases relative to the untransformed C-Li_2O_2 that remains and the Li1 vacancies become apparent in the average Li occupancies. In this case, the decrease in *c*-lattice parameter indicates that the C-Li_2O_2 crystallites are much less exposed compared to E-Li_2O_2. The strong current rate dependence for the charge process supports the oxidation occurring preferentially at the outer surface of the crystallites for both C-Li_2O_2 and E-Li_2O_2 (as depicted in **Figure 4.13**). In Chapter 3, **Figure 3.8**, the overall charge profiles were lowered in voltage with decreasing charge current density when electrodes were discharged at the same current density (E-Li_2O_2). The same effect is seen here for C-Li_2O_2, when examining the voltage plateaus at different current densities. In **Figures 4.9/4.10**, **4.8/4.12**, and **4.11**, the main voltage plateaus occur at approximately 3.6, 3.8, and 4.0 V, when current densities of 25, 50, and 75 $\mu A/cm^2$ are used, respectively. This current/voltage relation can be explained by the necessity of electron transport from the carbon support, through the insulating Li_2O_2, to the active oxidizing surface fraction ($Li_{2-x}O_2$).

4.4 Conclusions

In conclusion, *operando* X-ray diffraction, Rietveld refinement, OEMS and theoretical calculations were used to characterize the different stages of Li_2O_2 oxidation during the charge reaction in a Li-O_2 cell for both electrochemically and bulk crystalline Li_2O_2 (E-Li_2O_2 and C-Li_2O_2, respectively). Different oxidation processes were observed

for E-Li_2O_2 and C-Li_2O_2 associated with the differences in their nature. For electrochemically formed Li_2O_2 we propose a two-stage oxidation. At low potentials this involves the decay of amorphous Li_2O_2, whereas at higher potentials, crystalline Li_2O_2 is decomposed via a small actively transforming fraction that evolves oxygen via a Li deficient solid-solution reaction. This preferentially starts with the smallest crystallites. Rietveld refinement of the diffraction data measured during charge additionally reveals a very small increase in the *c*-lattice parameter as a function of charge duration, which can be correlated to an increase in surface energy due to more exposed E-Li_2O_2 surfaces: the consequence of removing the crystallite platelets that build up the toroidal aggregates. DFT calculations indicate that dilute Li deficiencies do not significantly affect the lattice parameters when they occur on the energetically preferred interlayer Li position. This allows for a small increase in the *c*-lattice parameter concomitant with a decrease in lithium occupancy *i.e.* more exposed surfaces having higher surface energies (hence leading to slightly larger lattice parameters). For bulk crystalline Li_2O_2 with an isotropic crystallite shape and larger crystallite dimensions, we propose a single stage oxidation on the basis of the XRD data. The observation of sub-stoichiometric $Li_{2-x}O_2$ at the early stage of oxidation and the gradual decreasing average crystallite size suggests a small active fraction that is also evolves oxygen via a Li deficient solid solution reaction at the surface of the particles. However, in this case the oxidation process gradually consumes the larger C-Li_2O_2 crystallites. Detailed refinement of the C-Li_2O_2 patterns indicates that sub-stoichiometric $Li_{2-x}O_2$ is created by the formation of vacancies on the interlayer Li1 position - and in particular - at the early stages of oxidation. These findings not only reveal the fundamental nature of the charge reaction in Li-air batteries, but also show the impact

that the nature of the lithium peroxide (size, shape and crystallinity) has on the oxidation mechanism. Controlling this process may be the key to high performance Li-air batteries. Correlation of the observed overpotential during charge and the applied current density suggest that conductivity of the Li_2O_2 particles is the limiting factor in this process. Enhancing the conductivity of the formed Li_2O_2 crystallites (or the formation of exclusively defective, amorphous product) could be a new avenue of exploration in this field.

Chapter 5

The Importance of Nanometric Passivating Films on Cathodes

5.1 Introduction

Much fundamental work has been carried out to identify the reaction pathways of both discharge (chapter 3) and charge (chapter 4) of the Li-O_2 cell.[1,2,3] However, complications arise in most studies due to the detrimental reactivity of most common electrolytes during discharge[4,5,6,7,8] and the known reactivity of carbonaceous positive electrode (cathode) materials on both discharge and charge.[9,10,11] Such studies and others have recently led to the introduction of non-carbonaceous electrode support materials such as Au,[12,13] TiC,[14] TiO_2,[15] and Al_2O_3-coated carbon fibers[11] in order to overcome the impedance owing to the formation of interfacial Li_2CO_3 via reaction of lithium peroxide with carbon.

Amongst the above, conductive titanium-based materials (i.e, TiN, TiC) are particularly attractive candidates for aprotic Li-O_2 cathodes. They have been utilized as alternative light-weight supports to carbon in electrodes for aqueous fuel cells and metal-air batteries due to their excellent oxidative stability.[16,17] Titanium nitride has been used in an acidic aqueous Li-air fuel cell and was found to have enhanced electrocatalytic activity for aqueous oxygen reduction relative to carbon.[18] Titanium nitride has also been used in the non-aqueous Li-O_2 battery,[19,20] but contrary to the study on TiC,[14] it has been used in combination with carbon, thus providing limited insight to its stability as a carbon replacement support material.

Surprisingly, little is understood regarding how the surface properties of these materials correlate to their performance, especially since the detrimental oxidation of carbon in the presence of super-/per-oxide is known to be surface specific.[9,10] A related, and very interesting recent discovery has shown that ultrathin (< 2nm) Ni/NiO_x films on silicon photoanodes act to passivate the silicon in alkaline solution with no detrimental effect on the water splitting performance.[21] Only slightly thicker (>5 nm) Ni/NiO_x films, result in higher onset potentials, attributed to reduced light transmittance through the Ni film. Although the oxygen evolution reaction (OER) is clearly different in aqueous *vs*. aprotic media, the work of Kenney *et al.*[21] highlights the critical role (and thicknesses) of passive surface films on oxygen evolving materials.

The above mentioned reports have prompted us to examine how the cathode surface determines OER properties, by using a combination of transmission electron microscopy (TEM), X-ray photoelectron spectroscopy (XPS) and on-line electrochemical mass spectrometry (OEMS) in conjunction with electrochemical studies. Here, we report the results obtained on charging TiN and TiC electrodes prefilled with commercial Li_2O_2, and compare those to carbon, and also to cathodes that were electrochemically discharged. This has also allowed us to investigate how ORR side-reactions with the surface and electrolyte on discharge affect subsequent OER. We show that the precise surface nature of TiC plays a critical role in OER by either promoting or limiting charge transport, and that the inability to charge TiN electrodes relates solely to their extensive interfacial surface passivation by TiO_2. The extent of oxidation for carbon, TiC, and TiN is discussed in terms of thermodynamics and the outcome of this oxidation is the observed overpotential during charge. Facile electron transfer from the solid Li_2O_2, through a

nanometric surface layer, and into the bulk of a conductive component in a Li-air cathode is the key to efficiency in this system.

Titanium carbide (TiC) has been shown to be a highly promising electrode when coupled with a DMSO electrolyte, exhibiting enhanced stability and long-term cycling behavior that was ascribed to the formation of a passivating layer of TiO_2 on the surface.[14] In contrast, the only study of TiN as a single support material has demonstrated that it is effective for ORR, but it does not promote OER: this was suggested to be the result of poor electronic conductivity.[14] Although the study by Thiotyl *et al.* clearly proved that TiC is a promising cathode material, no comparisons were made to the carbon "standard" cathode in aprotic systems. In our work, we shed light on the underlying factors which enable the long-term cycling with TiC (and not TiN) and compare the OER performance to that of carbon.

In this chapter, Dr. Claudio Radtke assisted with the electrochemical experiments relating to TiN (Figures 5.4 and 5.5). Zack Williams fabricated all "pre-filled" electrodes. Robert Black conducted all OEMS experiments. Drs. Layla Mehdi and Nigel Browning acquired the STEM images and SAED patterns in Figure 5.13.

5.2 Experimental Details

5.2.1 Characterization

Nitrogen adsorption was measured using a Quantachrome AUTOSORB-1 system and the Brunauer-Emmett-Teller (BET) method was utilized to calculate the surface area. The TiC-A (titanium (IV) carbide nanopowder, <200 nm, 95%, Aldrich) and TiC-B (titanium carbide nanopowder, <25 nm, 99+%, US Research Nanomaterials) samples were pressed

into 13 mm diameter pellets of approximately 0.5-1 mm thick. A Jandel multi height four-point probe combined with a RM300 test unit was used to measure the resistivity which was subsequently converted to values of bulk conductivity. XPS analysis was performed on a Thermo ESCALAB 250 instrument configured with a monochromatic Al Kα (1486.6 eV) source. All spectra were fitted with Gaussian-Lorentzian functions and a Shirley-type background using XPSPEAK software. The binding energy values were calibrated using the C *1s* peak at 285.0 eV. The STEM images TiC-A and TiC-B used in this study were acquired with a FEI Titan aberration-corrected scanning transmission electron microscope (STEM) operated at 300 kV and equipped with CEOS GmbH double-hexapole aberration corrector for the probe-forming lens, which allows imaging with ~0.1 nm resolution STEM mode. The STEM imaging and electron diffraction was performed at the Pacific Northwest National Laboratory by B. Layla Medhi and Nigel D. Browning.

5.2.2 Three-Electrode Studies of TiN

Catalyst inks were prepared by homogeneously dispersing TiN nanopowder in 1 mL of NMP solution containing Li^+-ion exchanged Nafion (Nafion-Li).[1,22] Dispersions were prepared with a Nafion-Li:TiN mass ratio of 1:2. A glassy carbon electrode (Pine Instruments, Co., 0.196 cm^2) was coated with the ink and dried at 100 °C for 24 hours to obtain coating loads of 250 μg TiN/cm^2. The electrochemical experiments were performed in an Argon-filled glovebox, with a three-electrode cell gas-flow enabled setup consisting of the coated glassy carbon electrode as the working electrode and Li foil as both the counter and reference electrodes. Cyclic voltammetry, chronoamperometry, and linear sweep voltammetry experiments were controlled with a VMP3 potentiostat and EC-Lab®

software (Bio-Logic Science Instruments). The electrolyte used was 0.1 M lithium hexafluorophosphate ($LiPF_6$, Novolyte) in TEGDME, and all experiments were performed at room temperature.

5.2.3 Ferrocene Experiments

Cyclic voltammetry was performed with a three-electrode cell gas-flow enabled setup. The working electrodes were prepared by painting mixtures of TiC-A or TiC-B and PTFE dispersions in 2-propanol onto stainless steel mesh disks (316 Grade, 1 cm^2) with Ti wire leads such that the mass ratio of TiC:PTFE was 4:1. The counter electrode was Pt gauze (3 cm^2) and a Ag/Ag^+ (0.01 M $AgNO_3$ + 0.1 M TBAP in MeCN) reference electrode was used. A solution of 0.1 M tetrabutylammonium perchlorate (TBAP, ≥ 99.0%, Fluka) in acetonitrile (MeCN, anhydrous HPLC Grade, 99.8%, Caledon) with 3 mM ferrocene constituted the electrolyte. The ferrocene (98%, Aldrich) was purified by sublimation at 110 °C prior to use. Argon was bubbled through the electrolyte solution before and over the solution during the experiments. The experiments were controlled with a VMP3 potentiostat and EC-Lab® software (Bio-Logic Science Instruments).

5.2.4 Quantification of Li_2O_2

To determine any decomposition of Li_2O_2 as a result of mixing it with isopropanol during loaded cathode fabrication process, a fixed amount of Li_2O_2 was mixed with isopropanol thoroughly for ~ 10 minutes. The Li_2O_2 was then dried under vacuum to remove the isopropanol before undergoing the above titration protocol.

Typically the aged loaded cathodes (with VC) and the cathodes extracted from a discharged cell were transferred out of a glove-box in a sealed vial. Water (5-10 mL) was

added to the vial and the vial content was vigorously shaken before transferring the contents to a beaker containing reagent buffer solution and water. Quantitative titration of the peroxide was performed following the procedure outlined in section 2.5.

5.3 Results and Discussion

5.3.1 Differences Between Electrochemically Generated Lithium Peroxide and Commercial Li_2O_2 Powder

The typical discharge-charge voltage profile for the first cycle of a Li-O_2 battery in LiTFSI/TEGDME with a carbon electrode is displayed in **Figure 5.1a**, to serve as comparison for the studies on the TiN and TiC electrodes. Powder X-ray diffraction of the electrode after discharge shows that Li_2O_2 is the sole crystalline product, and this is completely oxidized after charge (**Figure 5.1b**). Online electrochemical mass spectrometry (OEMS) was carried out to analyze the gases produced during the charge reaction after discharging in oxygen to 1 mAh (**Figure 5.1c**). The oxygen evolution profile occurs in two steps and a relatively large amount of CO_2 is evolved near the end of charge. The e^-/O_2 ratio is well above the expected value of 2 ($Li_2O_2 \rightarrow 2Li^+ + 2e^- + O_2$) throughout the charge process (**Figure 5.1d**). Quantification of the total amount of O_2 evolved after full charge to 1 mAh yields a value of 3.58 e^-/O_2. The CO_2 evolution indicates the oxidation of other compounds, including lithium carbonate, formate, and acetate, which are known to be the result of electrolyte decomposition during discharge.[2,4] Reactivity between the discharge intermediate LiO_2/O_2^- and the electrolyte salt[5,23] can also consume O_2 from the desired discharge product, contributing to the much less than theoretically presumed O_2 evolved on charge.

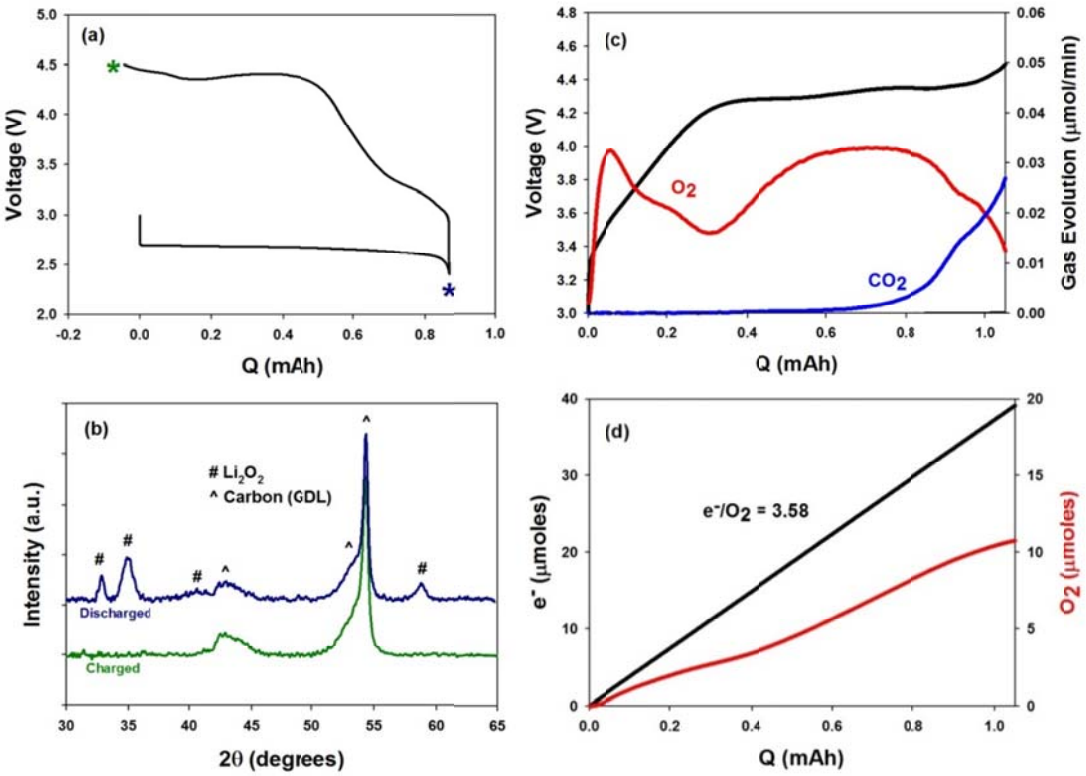

Figure 5.1 (a) Voltage profile of discharge/charge cycle with a Vulcan XC72 electrode at a current density of 25 µA/cm^2 in 1 M LiTFSI/TEGDME. (b) XRD patterns after discharge (Li_2O_2) and after charge (no Li_2O_2). (c) Gas evolution analysis with OEMS during the charge reaction (75 µA/cm^2) after discharging first to 1 mAh in O_2 (25 µA/cm^2). (d) The total integrated O_2 signal (m/z=32) evolved from the cell in (c) along with the electrons passed. The overall e^-/O_2 ratio after full charge was 3.58.

As an extension to the work in Chapter 4, to disentangle the oxygen reduction (ORR) and evolution reactions (OER), and to examine the oxidation reaction in isolation on charge, studies were carried out by charging cathodes that were prefilled with commercial Li_2O_2. This approach has been used by Shao-Horn *et al.*[24,25] to study the catalytic effect of adding various noble metals to carbon. Meini *et al.*[26] evaluated the charging characteristics

of lithium peroxide and the possible discharge products (LiOH, Li_2CO_3, and Li_2O) on carbon. They found that Li_2O_2 is the only product that can be oxidized, and that it enhances oxidation of the electrolyte and the carbon support during charge.[27] The Li_2O_2 oxidation mechanism was previously studied in Chapter 4 with *operando* X-ray diffraction, using both commercial peroxide powder and electrochemically deposited Li_2O_2.[28] Here, we compare the XRD and OEMS results of electrochemically-formed Li_2O_2 (discharged, **Figure 5.1**) to a Li-O_2 battery charge reaction which is isolated and independent from discharge by mixing commercial Li_2O_2 powder with the carbon support and then charging the electrodes. This eliminates any possibility of electrolyte decomposition on discharge. **Figure 5.2a** shows the charging voltage profile for an electrode which was prefilled with Li_2O_2. The charge capacity was adjusted to an e^-/Li_2O_2 scale based on the mass of Li_2O_2 contained in the electrode. The profile is defined by a high initial overpotential, followed by a plateau at approximately 3.7 V, and an eventual rise to 4.6 V (electrolyte oxidation voltage) after 2 e^-/Li_2O_2 is reached. The X-ray diffraction patterns of the initial electrode composite (carbon + Li_2O_2 + PTFE binder) show the characteristic peaks of the crystalline Li_2O_2 which completely disappear after charge (**Figure 5.2b**), as discussed previously in Chapter 4. OEMS analysis (**Figure 5.2c,d**) shows that oxygen starts to evolve mainly after the initial overpotential is surpassed. The total e^-/O_2 is 2.43 after full charge, not the theoretically expected 2.0.

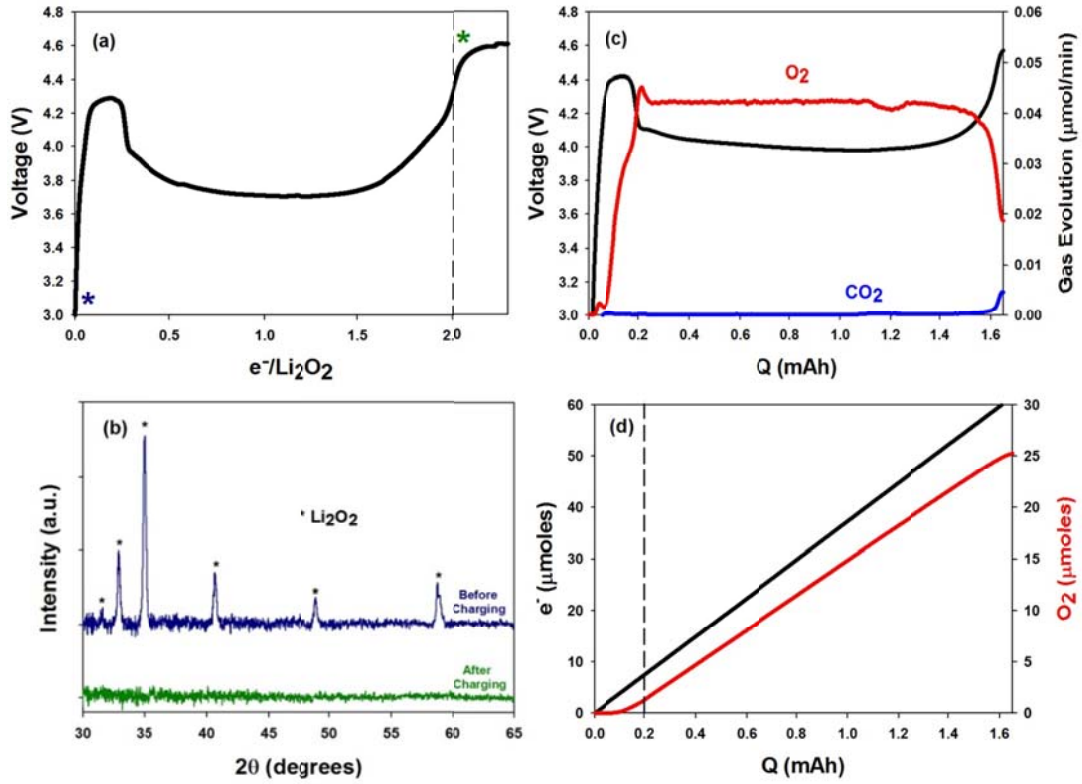

Figure 5.2 (a) The voltage profile for the charge reaction of a Li_2O_2-loaded Vulcan XC72 electrode at 50 μA/cm^2 in 1 M LiTFSI/TEGDME. (b) The XRD patterns of the composite electrode (Vulcan XC72 + Li_2O_2 + PTFE) before and after charging. (c) The gas evolution monitored by OEMS of a Li_2O_2-loaded Vulcan XC72 electrode charged at a current of 75 μA/cm^2. (d) The total integrated O_2 signal (m/z=32) evolved from the cell in (c) along with the electrons passed. The overall e^-/O_2 ratio after full charge was 2.43.

The purity of the commercial Li_2O_2 powder was determined to be 88 % by iodometric titrations. After exposure to 2-propanol followed by vacuum drying at room temperature - under the same conditions and timescale as preparing the prefilled electrodes - the purity of Li_2O_2 remains at 88 %. This indicates that Li_2O_2 does not react with dry 2-propanol to a measurable degree. After the prefilled electrodes are prepared, however, the purity

decreases by 3 % (to 85%), which can be attributed to the reaction between Li_2O_2 and carbon. After fully discharging carbon electrodes in 1 M LiTFSI/TEGDME electrolyte, the fraction of Li_2O_2 formed is 82 % (determined by an average of several different electrodes) based on the total electrical charge passed during the galvanostatic discharge.

Both the voltage profile and gas evolution are similar to what has been observed previously.[27,29] The chemical reactivity of Li_2O_2 and carbon is well known, and forms carbonates and epoxy groups.[9,10,30] This reaction at the Li_2O_2/carbon interface also causes interfacial resistance[30] and is responsible for the observed overpotential. Meini *et al*. carefully studied this "electrode activation" process with prefilled carbon electrodes and conclude that the cause of this initial overpotential is indeed the result of carbon/Li_2O_2 interfacial resistance rather than LiOH or Li_2CO_3 surface layers on the Li_2O_2 particles.[29] A ^{13}C electrode was used in our studies to distinguish between carbon electrode oxidation ($^{13}CO_2$) and electrolyte decomposition ($^{12}CO_2$). CO_2 from both sources is evolved near the end of charge (**Figure 5.3**), but its evolution from the carbon electrode dominates at the higher potentials owing to carbon corrosion. Obviously, there is a miniscule amount of $^{12}CO_2$ evolved at the beginning stage of charge and more at the end as the voltage increases. This is attributed to a superoxide-rich surface of the Li_2O_2 during charge reacting with the electrolyte.[31] The decomposition products are oxidized to CO_2 as the voltage increases at the end of the charge process. The relatively flat voltage profile on charging carbon electrodes prefilled with peroxide with an e^-/O_2 ratio of 2.43, compared to the sloping charge profile of electrodes that have undergone electrochemical discharge ($e^-/O_2 = 3.58$) furthermore suggests that side-reactions on discharge are more important than

previously thought. The relative amounts of Li_2O_2 in the electrodes after discharging (**Figure 5.1**) and those pre-filled with Li_2O_2 (**Figure 5.2**) prior to charging are quite close. The electrochemical discharge product contains ~82 % Li_2O_2 (titrated Li_2O_2/discharge capacity), which is similar to that of the electrodes pre-filled with commercial Li_2O_2 (~85 %, titrated Li_2O_2/mass). However, the difference in evolved gases (CO_2 and O_2) during charge indicates that the impurities in the commercial powder are much different than what is formed via electrolyte decomposition during electrochemical discharge. Specifically, the nature of these side-products is confirmed to be mainly LiOH (where no CO_2 evolution is observed) for the commercial Li_2O_2 as previously reported[25] and formate, acetate, and carbonates in the electrochemically discharged electrodes (where CO_2 is evolved).[4] The fact that < 100% of the theoretical amount of O_2 is evolved (82 %) for prefilled electrodes, however, indicates that the electrolyte/electrode surface is reacting with Li_2O_2 during its oxidation. The current density on charge also strongly affects the potential for Li_2O_2 oxidation, as expected. The voltage plateau is at 3.7 V (**Figure 5.2a**) compared to 4.0 V (**Figure 5.2c**) for applied current densities of 50 $\mu A/cm^2$ and 75 $\mu A/cm^2$, respectively. The poor contact of the Li_2O_2 crystallites with the support as well as their larger particle size[26] also undoubtedly contributes to the initial high charging potentials compared to the "electrochemically loaded" electrode.

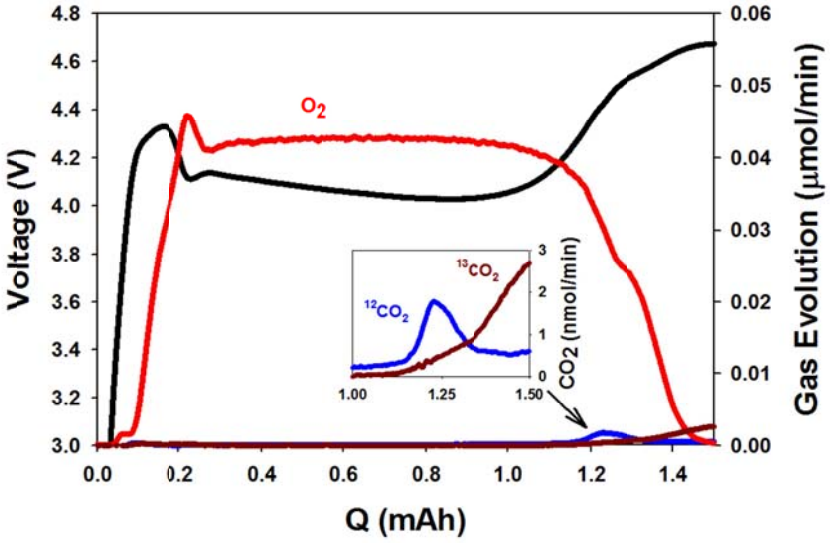

Figure 5.3 The gas evolution monitored by OEMS of a Li_2O_2-loaded ^{13}C electrode charged at a current of 75 µA/cm^2. The voltage profile is similar to the Vulcan XC72 electrodes shown in Figure 5.2. Both $^{12}CO_2$ (from electrolyte decomposition) and $^{13}CO_2$ (from carbon oxidation) evolution are observed at the end of charge.

5.3.2 Oxygen Reduction and Evolution Performance of Titanium Nitride

Turning to the non-carbonaceous electrodes, the activity of TiN for ORR/OER was probed using both half-cell (three electrode) studies and full cells (two electrodes). The results of the half-cell study employing chronoamperometry for ORR and linear sweep voltammetry for OER on a TiN film are shown in **Figure 5.4**. They suggest that although oxygen reduction readily occurs, oxygen evolution does not. This was confirmed by full cell studies shown in **Figure 5.5a** which demonstrate a voltage profile similar to that presented by Thotiyl *et al.* for a TiN electrode.[14] Li_2O_2 is formed on discharge, but it remains in the positive electrode even after charging to 4.8 V (**Figure 5.5b**) as shown by

XRD. A Li_2O_2-loaded TiN electrode gives the same result as the cell examined on discharge and charge (**Figure 5.5c,d**), suggesting a path towards a simplified screening process of support materials suitable for OER in the Li-O_2 battery using these prefilled electrodes. The underlying cause of this lack of OER capability was examined by comparison of TiN with Vulcan™ carbon using electrochemical impedance spectroscopy (**Figure 5.6**). The charge transfer resistance increases for both electrodes during the course of discharge owing to the accumulation of insulating Li_2O_2.[1] On switching to an anodic polarization of the electrode, a drastic increase in the charge transfer resistance is observed for TiN, indicating substantial oxidation of the nitride surface in the presence of Li_2O_2. This causes the voltage to rise to 4.7 V, with this upper limit thus ending charge. This is analogous behavior to that observed in aqueous media. Avasarala and Haldar report that the nitride surface becomes passivated by hydroxide groups at elevated temperature which reduces its electrical conductivity, thereby inhibiting its electron transportation properties.[32] In contrast, the impedance for the carbon electrode remains the same on anodic polarization, in accord with the fact that carbon is capable of fully charging below 4.7 V.

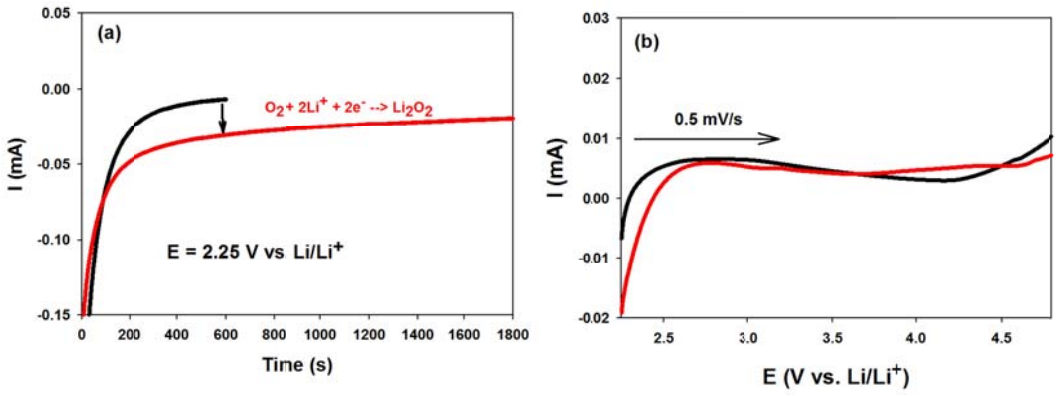

Figure 5.4. The catalytic activity of TiN for the oxygen reduction (a) and evolution (b) reactions in non-aqueous O_2-saturated 0.1 M $LiPF_6$/TEGDME electrolyte. The oxygen reduction activity in (a) was probed using chronoamperometry with an applied voltage of 2.25 V vs. Li/Li^+. The oxygen evolution activity in (b) was determined with linear sweep voltammetry at a scan rate of 0.5 mV/s to 4.75 V vs. Li/Li^+ after a layer of Li_2O_2 was formed in (a). The background curves performed under argon are displayed with black lines and the experiments performed under O_2 flow with red lines. Due to the increased reduction current in (a) under O_2 relative to Ar, oxygen reduction occurs, however, in (b) no oxidation peaks are visible, indicating the reverse reaction (ie. oxygen evolution) does not occur.

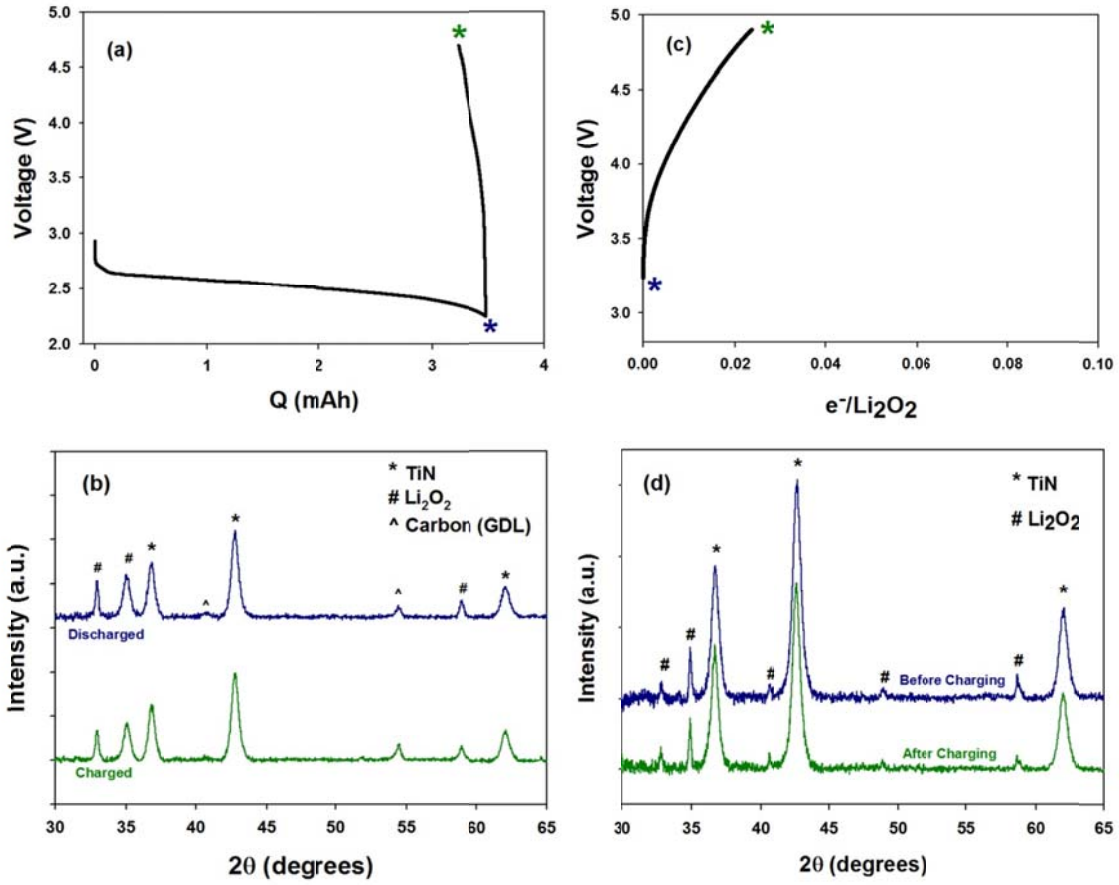

Figure 5.5 (a) The voltage profile of a TiN electrode discharge and charged at a current density of 25 μA/cm^2 in 1 M LiTFSI/TEGDME. (b) The XRD patterns of the electrode after discharge and charge. Li_2O_2 is present after discharge and remains after charge. (c) The voltage profile for the charge reaction of a Li_2O_2-loaded TiN electrode at 50 μA/cm^2 in 1 M LiTFSI/TEGDME. (d) The XRD patterns of the composite electrode (TiN + Li_2O_2 + PTFE) before and after charging.

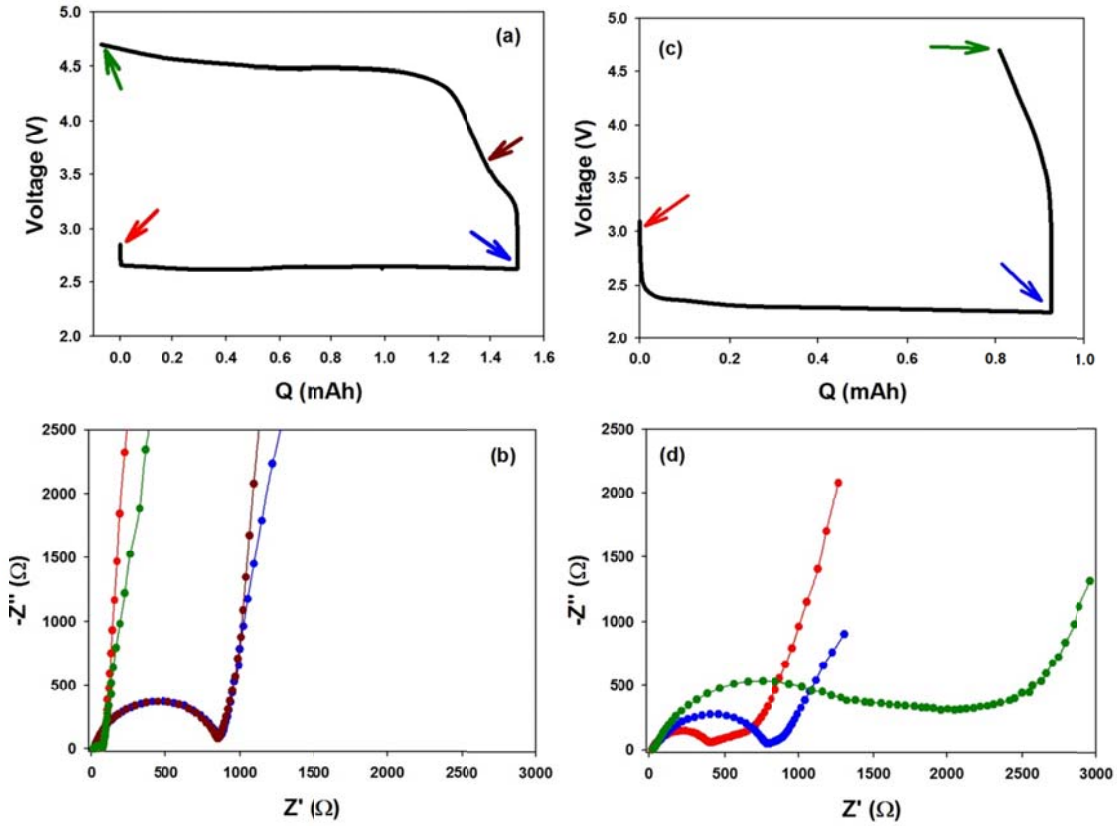

Figure 5.6 The voltage profiles of the 1st discharge/charge cycle and corresponding Nyquist plots from electrochemical impedance spectroscopy taken at various points indicated for Vulcan XC72 (a,b) and TiN (c,d). Both cells were cycled in 1 M LiTFSI/TEGDME. The Vulcan XC72 was cycled at 50 μA/cm^2 and the TiN was cycled at 200 μA/cm^2. These current densities were chosen such that the Li_2O_2 formed during discharge had film morphology in both cases as monitored by SEM (not shown).

The discharge plateau is at a lower voltage for TiN than carbon. Although the discharge reaction seems to be less sensitive to the surface chemistry of the electrode material than the charge reaction (solution based reactants vs. solid reactants), this voltage is attributed to differences in the charge transfer resistance. Before discharge (red curve),

the Vulcan XC72 electrode exhibits a lower impedance than the TiN electrode due to the oxidized surface of the TiN nanoparticles (see **Figure 5.10**). After discharge, the Li_2O_2 film causes an increase in the charge transfer resistance to ~800 Ω for both electrodes (blue curve). Upon initial change in polarization to anodic current, the impedance for the carbon remains the same, whereas that of the TiN electrode increases dramatically (brown curve). This causes the voltage to reach the upper limit of 4.7 V, thus ending charge. The carbon is capable of fully charging below 4.7 V and the Zyquist curve (green curve) overlays with the original, demonstrating the complete removal of the Li_2O_2 film.

5.3.3 Charging Li_2O_2-Loaded Titanium-Based Electrodes

With the idea that surface oxidation of Ti-based materials is the factor that determines the ease of electron transfer between Li_2O_2 and the support on charge, we examined other commercial Ti-based oxide and carbide support materials. **Figure 5.7** shows the charge curves for anatase TiO_2, and two different TiC nanopowders (TiC-A and TiC-B, obtained from two different suppliers), compared to TiN. As expected, the (poor) semi-conducting TiO_2 electrode (fully oxidized) did not support OER, similar to TiN discussed above, as a result of its completely "insulating" bulk and surface. Surprisingly, however, one TiC material promoted OER whereas the other did not. TiC-A was inactive for OER, but the voltage profile of TiC-B exhibits a very flat plateau at 3.6 V corresponding to the oxidation of Li_2O_2. This appears complete at the expected ratio of 2 e^-/Li_2O_2, and beyond this point, the upturn in voltage suggests that other oxidation processes (ie, electrolyte side-reactions) occur. It is interesting to note that the profile is very different compared to that reported for the full cycling of TiC in DMSO as reported by Thiotyl *et al.*, namely a

charge curve that exhibits a very pronounced slope from 3.0 to 4.0 V.[14] The higher initial oxidation voltage in the prefilled cathode studied here is partly a consequence of the electrode-Li_2O_2 contact as explained above; the flat charging voltage observed here indicates that oxidation of electrochemically peroxide-loaded TiC (*i.e*, from discharged cells as reported elsewhere)[14] involves additional processes than those involving Li_2O_2 alone. These could be derived from oxidation of $Li_{2-x}O_2$ that would occur at a lower potential, and/or electrolyte reactivity.

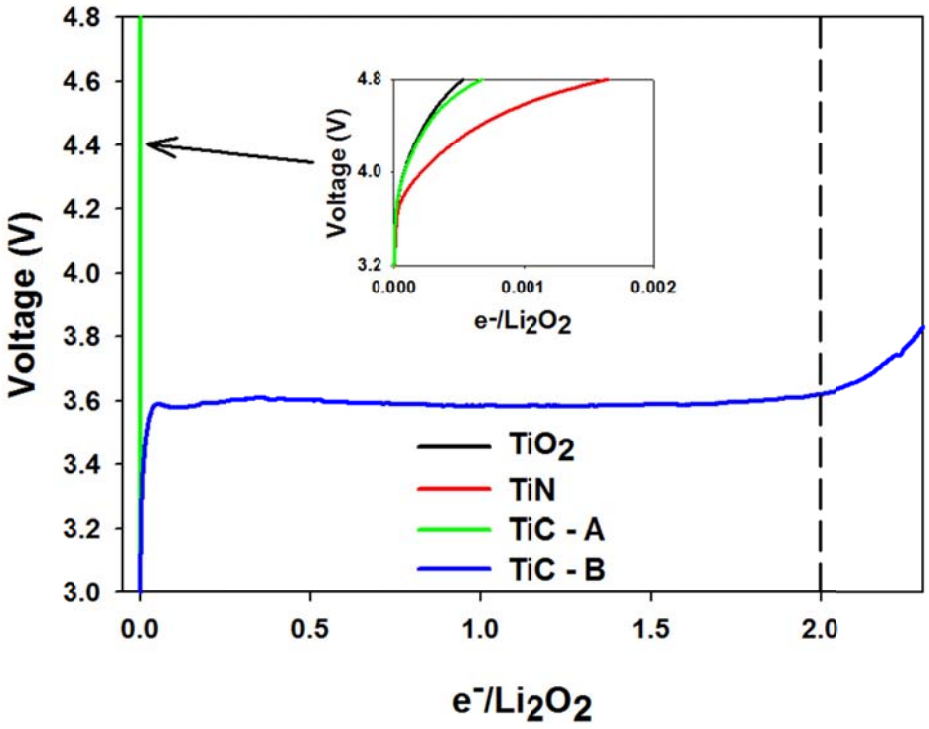

Figure 5.7 The voltage profiles of Li_2O_2-loaded TiC-A, TiC-B, TiN, and TiO_2 electrodes which were charged in 1 M LiTFSI/TEGDME at current densities of 50 μA/cm^2. Of these electrodes, only TiC-B was capable of oxidizing Li_2O_2.

5.3.4 Performance of Li_2O_2 Oxidation at Titanium Carbide Nanopowders

OEMS analysis of a Li_2O_2-loaded TiC-B electrode resulted in a similar gas evolution profile compared to the carbon-based electrodes, but with no initial lag in O_2 evolution or overpotential (**Figure 5.8**). The overall e^-/O_2 ratio after full charge was 2.45. The reaction between Li_2O_2 and the electrolyte on charge in the case of TiC is identical to that on carbon (accounting for an e^-/O_2 of 2.43 *vs*. 2.45 for carbon and TiC, respectively), but again, is clearly not as significant as the reactivity which occurs on discharge in the case of carbon electrodes as shown in **Figure 5.1c,d.** Based on this, as well as the minor CO_2 evolution at the end of charge, we conclude that electrolyte decomposition is a factor on both discharge and charge but the support material has little effect, indicating a solution-phase reaction rather than electrode surface reactivity. In attempt to shed light on the outstanding cycling behavior of the TiC/DMSO system studied by Thiotyl *et al.,*[14] we compared the OEMS analysis for Li_2O_2-loaded TiC-B electrodes in TEGDME and DMSO electrolytes (**Figure 5.9**). Unfortunately, the voltage for Li_2O_2 oxidation was higher in DMSO than in TEGDME and was accompanied by less O_2 evolution and more CO_2 evolution. We were not able to authenticate the claims of enhanced stability of the DMSO electrolyte by Thiotyl *et al.*[14] Failed attempts to replicate the results of the Bruce group for the Au/DMSO[12,13] and TiC/DMSO[14] systems have also been published by the IBM research group.[33,34] Detailed reports of experimental conditions are clearly necessary for universal progress on this battery system, since miniscule differences in material properties have a drastic effect on performance (eg. TiC-A vs. TiC-B shown here in **Figure 5.7**).

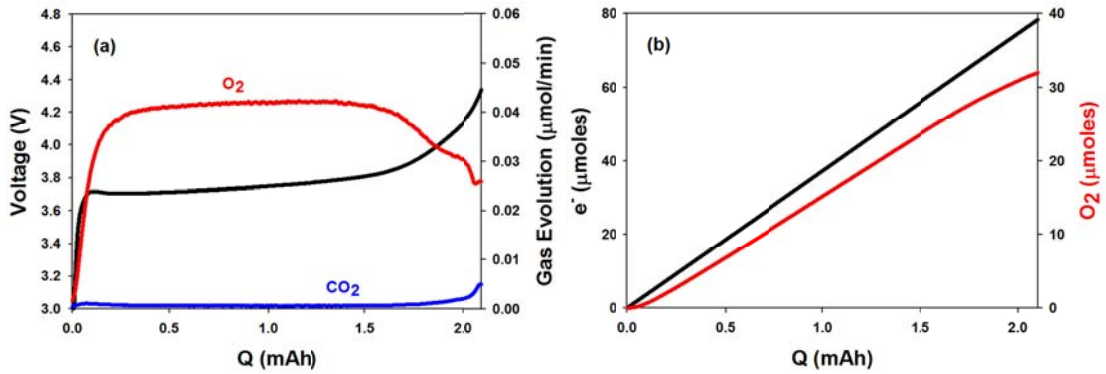

Figure 5.8 (a) The gas evolution monitored by OEMS of a Li_2O_2-loaded TiC-B electrode charged at a current density of 75 μA/cm^2 in 1 M LiTFSI/TEGDME. (b) The total integrated O_2 signal (m/z=32) evolved from the cell in (a) along with the electrons passed. The overall e^-/O_2 ratio after full charge was 2.45.

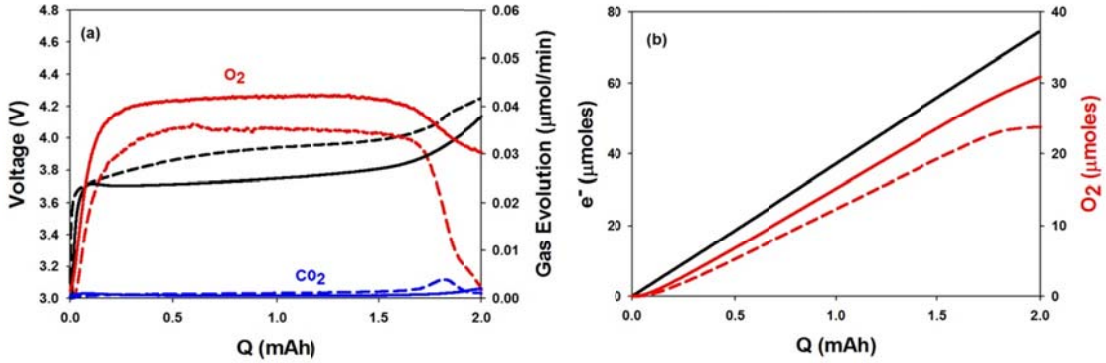

Figure 5.9 (a) The gas evolution monitored by OEMS of Li_2O_2-loaded TiC-B electrodes charged at a current density of 75 μA/cm^2 in 1 M LiTFSI/TEGDME (solid lines) and 0.5 M $LiClO_4$/DMSO (dashed lines). (b) The total integrated O_2 signal (m/z=32) evolved from the cells in (a) along with the electrons passed.

5.3.5 Surface Characterization of Titanium Carbide Nanopowders

Our studies of the surface *vs* the bulk properties of the two TiC nanocrystalline materials indicate that the bulk properties are identical, but the nature of the surface is quite different. The XRD patterns for TiC-A and TiC-B show that they both have similar crystallinity and the SEM images show that the morphology and particle size distribution are identical (**Figure 5.10**). The BET surface area of these two materials as determined by N_2 adsorption experiments was the same (24 m^2/g and 26 m^2/g for TiC-A and TiC-B, respectively), as were the bulk conductivities determined by the four-point probe technique (73 S/cm and 75 S/cm for TiC-A and TiC-B, respectively). However, the surface of the materials - examined by X-ray photoelectron spectroscopy (XPS) - reveals distinct differences. The XPS data displayed in **Figure 5.11** clearly shows that the TiC-A surface is TiO_2-rich, whereas the TiC-B is TiC-rich. The surface ratios of TiC:TiOC:TiO_2 are 0.22:0.23:0.55 and 0.45:0.21:0.34 for the TiC-A and TiC-B, respectively, determined by the areas under the fitted Ti 2p peaks in the XPS spectra. We conclude that, as in the case of TiN (**Figure 5.12**), the dominance of insulating TiO_2 on the surface of TiC-A inhibits electron transfer from Li_2O_2 during charge. Noteworthy is the fact that the XPS spectrum of "inactive" TiC-A is virtually identical to that reported for "active" but passivated TiC formed on cycling,[14] suggesting that the nature of the interfacial contact is more complex than revealed by XPS spectra alone. Furthermore, although the surface of TiC-B consists predominantly of TiC (45%), there are still contributions of TiO_2 (34%) and TiOC (21%). This means that the surface layer (TiO_2/TiOC) is either extremely thin or non-homogenous. This surface layer was further examined by scanning transmission electron microscopy, STEM, as shown in **Figure 5.13**. The TiC-A crystallites are

characterized by an amorphous layer which completely surrounds the particles and is approximately 2-3 nm thick (**Figure 5.13b,c,d**). However, no surface layer can be observed on the TiC-B particles (**Figure 5.13e-h**). Lattice fringes extend to the outer edge of the particle even at the highest magnification (**Figure 5.13h**).

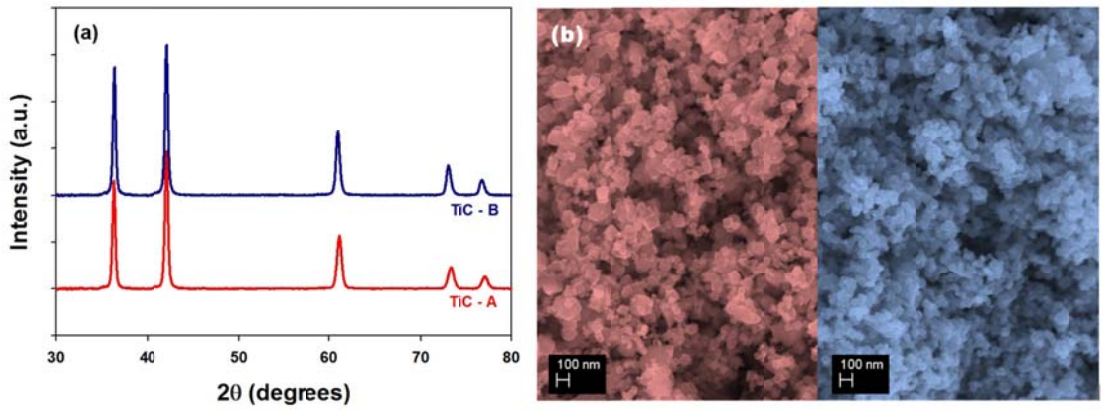

Figure 5.10 The powder XRD patterns (a) and SEM images (b) of the two commercial TiC-A and TiC-B nanopowders. The red SEM image corresponds to TiC-A and the blue to TiC-B.

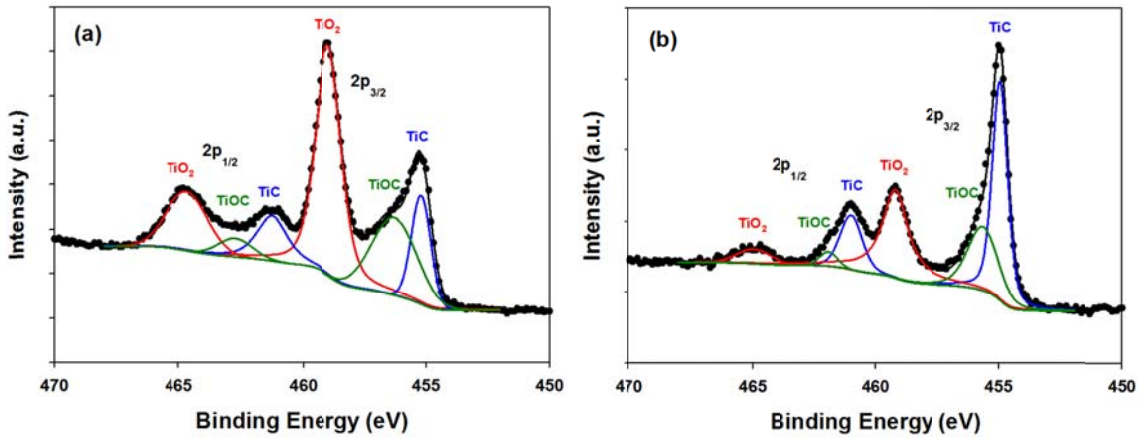

Figure 5.11 The Ti 2p XPS spectra for (a) TiC-A nanopowder and (b) TiC-B nanopowder.

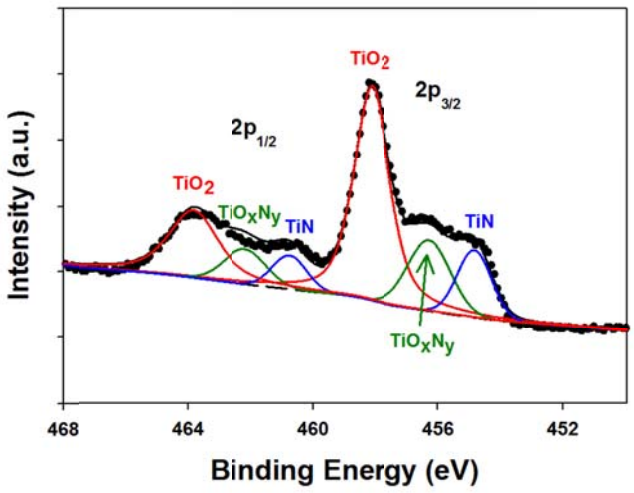

Figure 5.12 The Ti 2p XPS spectra for TiN nanopowder.

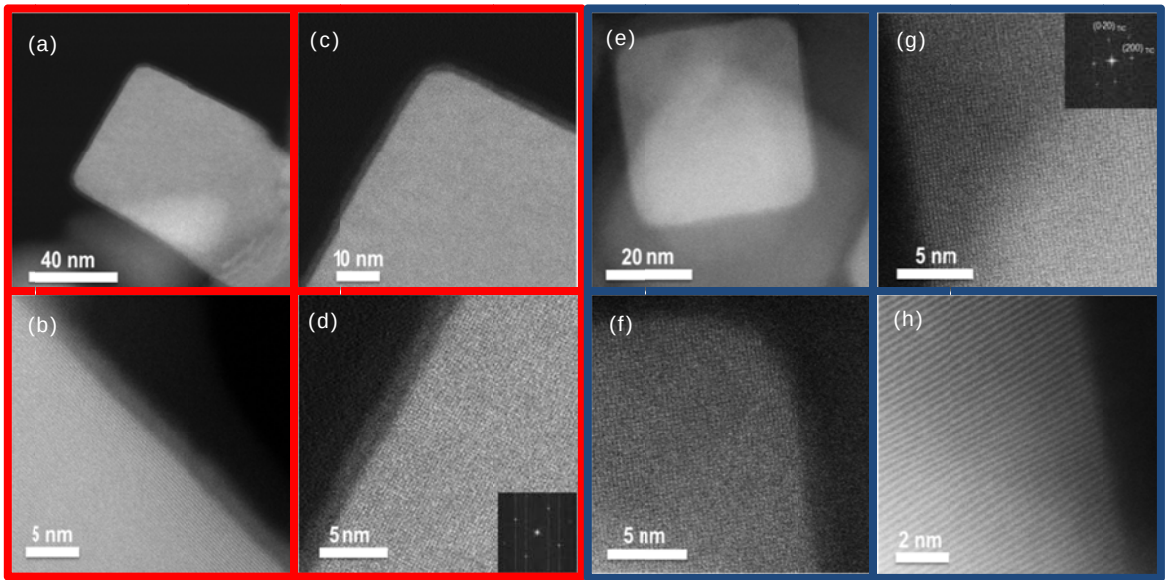

Figure 5.13 STEM images of individual nanocrystallites of TiC-A (a-d) and TiC-B (e-h). The insets in (d) and (g) show the corresponding SAED patterns of TiC-A and TiC-B, respectively.

5.3.6 Probing Electron Transfer of Composite Electrodes

Electron transfer on these two TiC nanocrystallite materials was probed with the ferrocene (Fc) solution-based redox couple (**Figure 5.14**). TiC-B presented a reversible Fc/Fc^+ couple, whereas the TiC-A exhibited an ill-defined oxidation peak with reduction far from its kinetically reversible position. We have found this behavior for a variety of insulating electrode materials where the oxidation of ferrocene is slow and not kinetically reversible due to poor electron transfer rates. Electron transfer with the TiC-A is inhibited by its insulating surface layer and TiC-B (that lacks an impeding surface layer) displays fast electron transfer kinetics.

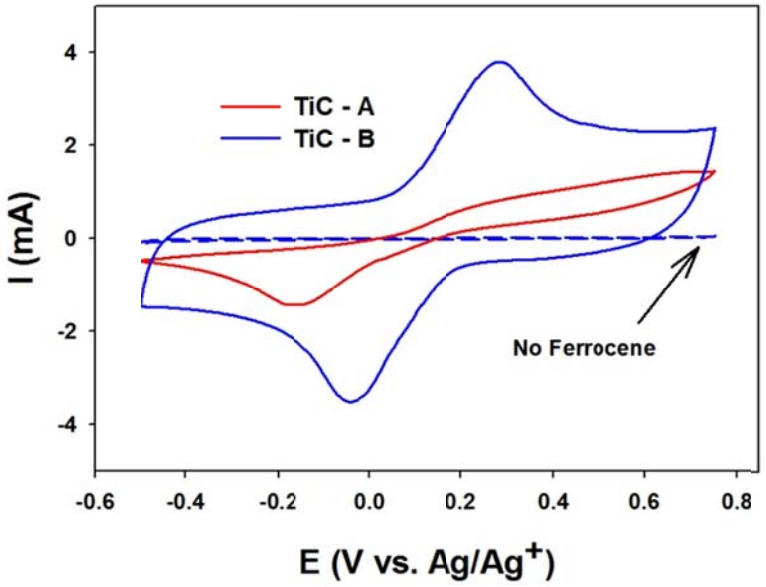

Figure 5.14 Cyclic voltammograms at a scan rate of 100 mV/s in 0.1 M TBAP/MeCN + 3 mM ferrocene on electrodes made from TiC-A (red) and TiC-B (blue). The dashed line is a voltammogram in the supporting electrolyte only on TiC-B (ie. 0.1 M TBAP/MeCN) to show that the activity is entirely due to the Fc/Fc^+ redox couple.

It was found that the $TiOC/TiO_2$ surface coating on the TiC-A particles could be removed by vacuum annealing at 300 °C in order to provide sufficient electron transfer, as probed by the ferrocene/ferrocenium redox couple shown in **Figure 5.15** (dashed red voltammogram). Vacuum annealing of the TiC-B, which already lacks the impeding oxide layer, had an identical CV to that shown in blue.

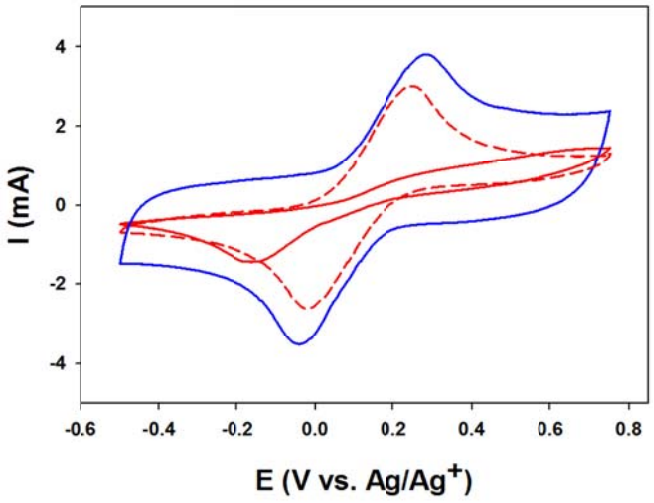

Figure 5.15 Cyclic voltammograms at a scan rate of 100 mV/s in 0.1 M TBAP/MeCN + 3 mM ferrocene on electrodes made from TiC-A (red) and TiC-B (blue). The solid curves are electrodes fabricated with TiC-A (or TiC-B) and PTFE binder (4:1) on a SS mesh disk which were dried at room temperature under vacuum. The dashed red voltammogram is for a TiC-A electrode which was vacuum annealed at 300 °C.

By charging Li_2O_2-filled electrodes of TiC-B under both argon and oxygen environments yielded identical voltage profiles to that of **Figure 5.7**. The attempt to oxidize the TiC-B under a pure oxygen environment was unsuccessful. These results

indicate that it is difficult to oxidize the TiC-B material at ambient temperature, indicating that the surface oxide layer on TiC-A must be a result of the conditions used for its commercial production.

5.3.7 Correlation of Surface Films on Electrode Materials to Li_2O_2 Oxidation Performance

Although both TiN and TiC are used in practical applications due to their oxidation resistance,[17] there has been much work on comparing the oxidation resistance between these two materials.[35,37] The oxidation reactions of these materials with oxygen are displayed in equations 6-1 and 6-2.

$$2TiN + 2O_2 \rightarrow 2TiO_2 + N_2 \qquad \Delta G^\circ = -611.8 \text{ kJ mol}^{-1} \text{ (298 K)}^{16} \qquad (6\text{-}1)$$

$$TiC + 2O_2 \rightarrow TiO_2 + CO_2 \qquad \Delta G^\circ = -551 \text{ kJ mol}^{-1} \text{ (298 K)}^{36} \qquad (6\text{-}2)$$

In the work of Komratov,[37] it was shown that TiC oxidizes more slowly than TiN in air, and this was attributed to the formation of a protective oxide film on TiC which inhibits further oxidation. This is in complete accord with the Gibbs free energies for these reactions (ie. the oxidation of TiN is more favorable than TiC). The Gibbs free energy for the oxidation of carbon (graphite) by molecular oxygen is only -394.4 kJ mol^{-1} at 298 K ($C + O_2 \rightarrow CO_2$). This is unlikely to occur under the conditions of the Li-O_2 battery, and as such it has been shown that other products are indeed formed, including Li_2CO_3, from direct reaction between carbon and Li_2O_2 (equations 6-3,6-4).

$$C + Li_2O_2 + 1/2O_2 \rightarrow Li_2CO_3 \qquad \Delta G^\circ = -542.4 \text{ kJ mol}^{-1} \text{ (300 K)}^{30} \qquad (6\text{-}3)$$

$$C + Li_2O_2 \rightarrow Li_2O + Li_2CO_3 \qquad \Delta G^\circ = -533.6 \text{ kJ mol}^{-1} \text{ (300 K)}^{30} \qquad (6\text{-}4)$$

Determining the oxidation resistance of a material is obviously more complex than the simple thermodynamics, although this can act as a preliminary guideline. Based on our results, the excessive oxidation of TiN occurs with ease. The thermodynamics tell us that this is reasonable, given the low free energy for this reaction (-611.8 kJ mol^{-1}). The Gibbs free energies for the oxidation of TiC vs. carbon are close (-551 kJ mol^{-1} vs. -542.4 kJ mol^{-1}). In agreement with Komratov,[37] when the starting TiC material lacks an oxide layer (TiC-B), any surface film that forms during the charge process is thin enough to inhibit further oxidation and still allows for facile electron transfer. The observed voltage for OER from Li_2O_2 for carbon electrodes is slightly higher than that of TiC-B. This is likely due to the defective nature of carbon and surface functional groups, which leads to oxidation products such as epoxy groups and carbonates.[10]

The results above are summarized in **Figure 5.16**. Electron transfer from Li_2O_2 through insulating surface layers on conductive materials plays the most critical role in the charge reaction of the non-aqueous Li-O_2 battery. If the passive surface layer is thin enough (TiC-B), Li_2O_2 can be charged at a constant voltage. In fact, such an ultra-thin passivating layer undoubtedly stabilizes the material on cycling, as previously proposed.[14] In the case of slightly thicker or more insulating surfaces (i.e., oxidized carbon), charging still occurs, but an overpotential needs to be overcome. If the surface layer is too thick (TiN and TiC-A), electron transfer that is critical to the charging process is inhibited. In the case of TiC, an oxide layer of even 2-3 nm (**Figure 5.13**) is enough to terminate electron transfer. This critical thickness is meaningful in the consideration of oxidation resistant materials for cathodes for the Li-O_2 battery.

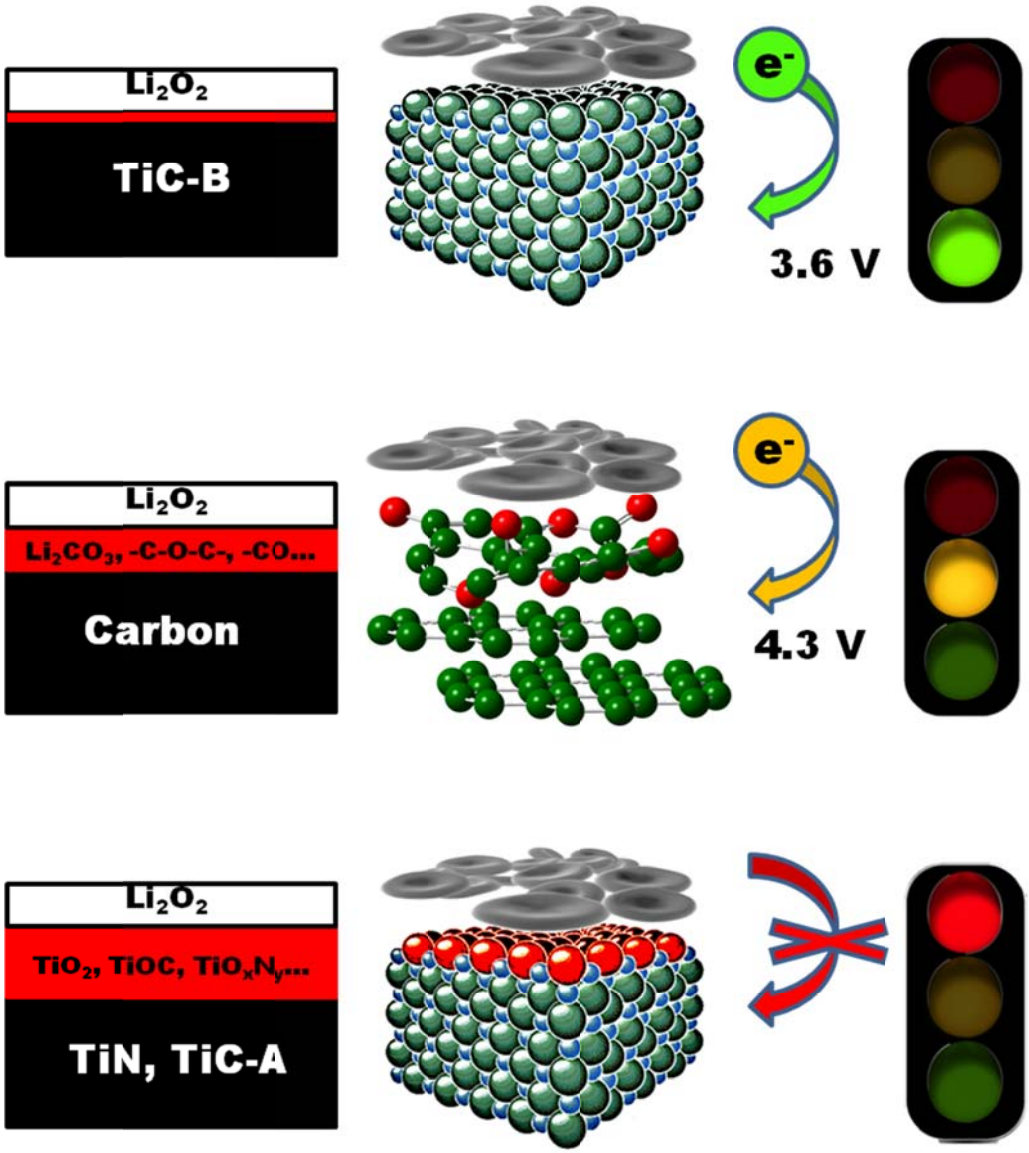

Figure 5.16 The concept of Li_2O_2 oxidation on the various materials examined in this study. Electron transfer from Li_2O_2 to the bulk TiC-B occurs readily with a very thin passivating TiO_2/TiOC surface as evidenced by XPS and (S)TEM. The surface of carbon is oxidized to form carbonates, epoxides, and carbonyl groups which still allows for electron transfer, but with a substantial charging overpotential. On the TiN and TiC-A, the thick insulating TiO_2/TiOC/TiO_xN_y surfaces completely inhibit electron transfer.

5.4 Conclusions

Although bulk conductivity is required for electron transfer to promote oxidation of lithium peroxide on cathode supports for the Li-O_2 battery, the surface chemistry of the support is most critical in determining the efficiency of electron transfer to the insulating Li_2O_2 during the charge reaction. In this study, we have confirmed that carbon electrodes react directly with Li_2O_2, causing an overpotential on charge due to an oxidized, high impedance surface. The surface of TiN is fully oxidized by Li_2O_2 when an anodic current is applied, to the extent where electron transfer is inhibited and the charge reaction is halted. Obviously, TiN is not as oxidatively stable as TiC. Thin surface layers of insulating TiO_2 on TiC (ie. TiC-A) also inhibit the charge reaction, but TiC which lacks this surface layer or where the layer is thinner than the critical value of 2 nm (ie. TiC-B) facilitates Li_2O_2 oxidation with a greatly decreased overpotential. Oxidation of the solid and insulating Li_2O_2 product in the non-aqueous Li-O_2 battery is a very sluggish reaction and sensitive to the applied current rates. Precise control of passivating surface layers will be a significant breakthough in research on the aprotic Li-O_2 battery system.

This chapter also shows that the main effect of material variation in cathodes for the Li-O_2 battery is the voltage at which Li_2O_2 is oxidized, rather than changes in O_2/CO_2 evolution. This indicates that electrolyte decomposition is a solution-based process (or surface of Li_2O_2) which is unaffected by cathode interactions. Bulk conductivity is required, yet surface conductivity is of equal importance and the Li_2O_2 charging voltage is directly related to the nature of surface layers (thickness and conductivity). Under the harsh conditions of the cell, it is expected that surface oxidation will always occur. However, new cathode materials can now be designed such that their surfaces inhibit

excessive oxidation (leading to an insulating oxide) and/or are concealed by conductive oxide layers.

Chapter 6

Investigation of the Electrochemical Properties of a Metallic Lead Ruthenium Oxide Pyrochlore

6.1 Introduction

Metallic mesoporous oxide frameworks are amongst the most fascinating emerging materials in solid-state chemistry because their nano-scaled wall structure and high surface area - together with a high electronic conductivity - enable various potentially revolutionary applications in electronic circuits, sensors, energy conversion and storage devices.[1,2,3,4,5,6] However, only a handful have been reported to date. These include rutile-type MoO_2, prepared via a replica synthesis from a hard silica template;[5] a Magnéli phase Ti_4O_7, prepared via carbothermal polymer-mediated reduction (which is strictly speaking, nanostructured);[7] and the pyrochlore $Pb_2Ru_2O_{6.5,}$ first reported two years ago.[8] It is of interest to understand this family better in order to explore the effect of confined electron transport that could lead to many other novel properties.

Pyrochlores represent a particularly interesting class of oxides, where the compositions $A_2B_2O_{7-\delta}$ (A = Pb or Bi, B = Ru or Ir) exhibit metallic conductivity,[9,10,11,12,13,14] that ranges up to 4.3×10^3 S/cm at 300 K for single crystals of $Pb_2Ru_2O_{6.5}$.[9] The structure of these pyrochlores is typically viewed as two interwoven metal oxide substructures with an overall composition of $A_2B_2O_6O'_{1-\delta}$. Corner-shared noble metal-oxygen octahedra (BO_6) generate a cage-like structure, which provides a continuous conduction path for the electrons, while the A element is linearly connected in

the structure with special oxygen (O') atoms to form O'-A-O' linkages.[10] These special oxygen sites can be partially or completely absent, which gives rise to oxygen non-stoichiometry within the structure. Although these pyrochlore structures generally belong to the cubic space group *Fd*-3*m*, in case of $Pb_2Ru_2O_{6.5}$ where half of the special oxygen is systematically absent, the ordered vacancy structure results in additional symmetry and a space group assigned to *P*-43*m*.[11] The bulk oxides were shown to have very good bifunctional properties for oxygen electrocatalysis, reducing activation energies for both oxygen reduction and evolution reactions (ORR and OER, respectively) in rotating ring disk-electrode studies using KOH as an electrolyte.[13,15,16,17,18] The fundamental properties of the Pb congener have been explored in both acidic and basic aqueous media[19] and they have been used practically as catalysts in aqueous based metal-air batteries, fuel cells, and electrolysers.[13,14,20,21,22] The electrocatalytic oxygen capability is believed to originate from the multi-valent characteristics of the redox-active metals, and the compensating effect of the oxygen vacancies which lead to variable stoichiometry.[13,19] In this chapter, the electrochemical properties for oxygen reduction and evolution of the electronically-conducting mesoporous mixed metal oxide based on the pyrochlore structure ($Pb_2Ru_2O_{6.5}$) are presented. Here, we expand on our preliminary report that first demonstrated the excellent properties of mesoporous $A_2Ru_2O_{6.5}$ oxides (A= Pb, Bi) as catalysts (or "promoters") for aprotic Li-air batteries.8 A deeper understanding of the origin of the observed electrocatalysis in Li^+-containing non-aqueous electrolytes on this same "model catalyst" material (lead ruthenium oxide, PRO) is presented.

The electrocatalytic properties of this material for oxygen reduction and evolution in aqueous and non-aqueous media were evaluated by cyclic voltammetry, chronoamperometry, and linear sweep voltammetry. These techniques show that the synthesized pyrochlore lowers the overall oxidation voltage by 0.7 V relative to carbon in non-aqueous, Li^+-containing electrolyte. This observed effect is the result of its ability to both completely oxidize Li_2O_2 (at a relatively low potential) *and* electrocatalytically oxidize all known side-products formed from electrolyte decomposition in the Li-O_2 battery. This further helps to explain the nature of "electrocatalysis" in the Li-O_2 battery.

Dr. Sihyoung Oh synthesized the pyrochlore catalyst used in this chapter with the assistance of Boeun Lee.

6.2 Experimental Details

6.2.1 Materials Synthesis

To prepare the templated, mesostructured crystalline lead ruthenate (PRO), 0.900 g of 25 % (w/w) aqueous hexadecyl-trimethylammonium chloride (Fluka, $C_{16}TMA^+Cl^-$) solution, 3.303 g of ruthenium(III) nitrosyl nitrate solution (1.53 wt. % Ru, Sigma-Aldrich), 0.134 g of lead sub-acetate ($Pb(OAc)_2 \cdot 2Pb[OH]_2$) and 5.0 g of deionized water were mixed in a 20 mL PTFE container and stirred for 1 h at room temperature. The solution was transferred to a 100 ^oC oven and stored for 3 h in a sealed flask. In a separate beaker, 3.3 g of 2 M aqueous NaOH solution was prepared and added dropwise into the stirred lead ruthenate solution immediately after it was taken out from the oven. The mixture was stirred for 3 h at room temperature and then 0.57 mL of sodium hypochlorite solution (11.9 % active Cl, Sigma-Aldrich) was added dropwise into the reaction flask.

The reaction was stirred for an additional 12 h with the flask tightly sealed. The solid was then filtered, washed with copious amounts of deionized water and dried in a vacuum oven at room temperature. To extract surfactant from the mesopores, the powder was dispersed in 5 mL of water, and stirred while 7 mL of ethanol was slowly added over the period of 3 h. The resulting power was filtered and dried on a vacuum line at room temperature. More details of the synthetic procedure and characterization of this material are reported elsewhere.[23]

The $NiCo_2O_4$ inverse spinel was synthesized by a combustion method utilizing glycine as the fuel and nitrate as the oxidizer.[24] The metal nitrate precursors, $Co(NO_3)_2.6H_2O$ (6 mmol) (98%, Sigma-Aldrich) and $Ni(NO_3)_2.6H_2O$ (3 mmol) (≥97%, Sigma-Aldrich), and glycine (4.5 mmol) (≥98.5%, Alfa Aesar) were dissolved in deionized water (50 mL) in an alumina beaker. The water was slowly evaporated on a hotplate to form a viscous gel. The gel was allowed to undergo rapid combustion by adding the beaker to a preheated oven at 300 °C and annealed at the same temperature for 4 hours.

Vulcan XC72 carbon black (Cabot Corp.) was used as the support material for the Pt/C catalyst in this study. To improve its hydrophillicity, the carbon black was treated with ozone for 1 h by bubbling ozone into a water/carbon mixture. The Pt catalysts were prepared using a room temperature impregnation method. The metal precursor used was $H_2PtCl_6.6H_2O$ (99.9, Alfa Aesar). A 0.025 M solution of this salt was prepared in deionized water. The metal precursor solution, water (50 mL), and carbon (0.5 g) were mixed such that the coating load was 20 wt % metal. This mixture was sonicated for 30 min. Using 1 M NaOH, the pH was adjusted to between 9.5 and 10, and the mixture was

stirred for 5 minutes. The reducing agent (5x excess of 0.05 M $NaBH_4$) was added dropwise while continuously stirring. The mixture was allowed to react for 1 h then neutralized with 3 M HCl before the catalysts were filtered with 0.2µm nylon membrane and washed with pure water. The catalyst was finally dried in a drying oven at 100°C for 12 h.

6.2.2 Aqueous Rotating Disk Electrode Studies

Catalyst inks were prepared by homogeneously dispersing the prepared catalyst and/or Vulcan XC72 carbon black (Cabot Corp.) in 1 mL of NMP solution containing K^+-ion exchanged Nafion (Nafion-K). The Nafion-K was prepared in house according to the procedure outlined in section 2.3.2.1 using KOH in replacement for LiOH. Vulcan XC72 was mixed with each catalyst in the same ratio (80:20 carbon:catalyst) to avoid issues of conductivity. Dispersions were prepared with Nafion-K:Carbon mass ratio of 1:2. A glassy carbon electrode (Pine Instruments, Co., 0.196 cm^2) was coated with the ink and dried at 100 °C for 24 hours to obtain coating loads of 250 µg/cm^2. The electrochemical experiments were performed with a three-electrode cell gas-flow enabled setup consisting of the coated glassy carbon electrode as the working electrode, a Pt wire counter electrode, and a double junction Ag/AgCl (3 M KCl) reference electrode. The experiments were controlled with a VMP3 potentiostat and EC-Lab® software (Bio-Logic Science Instruments) and the rotation rate of the working electrode was controlled with a modulated speed rotator (Pine Instruments Co.). The electrolyte used was oxygen-saturated 0.1 M KOH and all experiments were performed at room temperature. Prior to analysis of the catalysts, under argon atmosphere, cyclic voltammetry was used to clean

the electrode surface by cycling in the range of -0.8 V to 0.2 V vs. Ag/AgCl at 100 mV/s until a steady-state voltammogram was obtained. The rotating disk electrode linear sweep voltammograms were corrected for capacitance by subtracting the background current acquired under argon atmosphere.

6.2.4 Non-Aqueous Electrocatalytic Studies

Catalyst inks were prepared by homogeneously dispersing the prepared lead ruthenium oxide (PRO) catalyst and/or Vulcan XC72 (Cabot Corp.) carbon black in 1 mL of NMP solution containing Li^+-ion exchanged Nafion (Nafion-Li) (refer to section 2.3.2.1). Dispersions were prepared with Nafion-Li:Carbon and Nafion-Li:PRO mass ratios of 1:2 and 1:8, respectively. A glassy carbon electrode (Pine Instruments, Co., 0.196 cm^2) was coated with the ink and dried at 100 °C for 24 hours to obtain coating loads of 250 μg carbon/cm^2 and 1 mg PRO/cm^2. The electrochemical experiments were performed in an Argon-filled glovebox, with a three-electrode cell gas-flow enabled setup consisting of the coated glassy carbon electrode as the working electrode and Li foil as both the counter and reference electrodes. Cyclic voltammetry, chronoamperometry, and linear sweep voltammetry experiments were controlled with a VMP3 potentiostat and EC-Lab® software (Bio-Logic Science Instruments). The electrolyte used was 0.1 M lithium hexafluorophosphate ($LiPF_6$, Novolyte) in tetraethylene glycol dimethyl ether (TEGDME, 99%, Sigma-Aldrich, distilled) in all cases, and all experiments were performed at room temperature.

6.2.5 Preparation and Galvanostatic Charging of Pre-Loaded Electrodes

Galvanostatic charging of the electrodes pre-filled with Li_2O_2 or the various known discharge side-products was carried out using a modified Swagelok™ design with 1 M lithium bis(trifluoromethanesulfonyl) imide (LiTFSI, Novolyte) in tetraethylene glycol dimethyl ether (TEGDME, 99%, Sigma-Aldrich, distilled) as the electrolyte. Cells were assembled in an argon filled glovebox with a lithium metal counter electrode, three porous separators (Millipore glass fiber), and the as-prepared pre-filled electrodes as the working electrodes. The electrolyte (200 μL) was added to the separators during cell assembly. All cells were charged at room temperature (25±2°C) at a current density of 50 $\mu A/cm^2$.

6.2.6 Preparation and Galvanostatic Cycling of Gas Diffusion Electrodes

The Vulcan XC72, TiC, and TiC+PRO electrodes were prepared by mixing the powders with PTFE powder (in a 2-propanol dispersion) in a mass ratio of 4:1. For the TiC+PRO electrode, the PRO was present in a 4:1 ratio of TiC:PRO. These mixtures, in 2-propanol, were painted onto stainless steel mesh substrates (1 cm^2) and vacuum annealed at 300 °C. The cells were prepared with 1 M LiTFSI/TEGDME as the electrolyte and lithium foil negative electrodes in the two-electrode configuration described in section 2.3.1.2.

6.3 Results and discussion

6.3.1 Aqueous Oxygen Reduction and Evolution Reactions

The ORR and OER catalytic activities probed in alkaline medium (0.1 M KOH) using rotating disk electrodes are displayed in **Figures 6.1 and 6.2**. For comparison, other model catalysts were used. Pt/C was included as a reference for ORR activity and $NiCo_2O_4$[25,26]

was used because it is known to be amongst the best bifunctional ORR/OER candidates. **Figure 6.1** shows the linear sweep voltammograms for oxygen reduction and the corresponding Koutecky-Levich plots for each catalyst. The onset potential was taken at a current density of -0.2 mA/cm^2. For the Koutecky-Levich analysis, the diffusion coefficient for O_2 is 1.9×10^{-5} cm^2.s^{-1}, the kinematic viscosity of the electrolyte is 0.010 cm^2.s^{-1}, and the solubility of oxygen is 1.14×10^{-6} mol.cm^{-3} in 0.1 M KOH at 25°C under 1 atm O_2.[27, 28]

The ORR activity (as determined by the kinetic current density and onset potentials) of the lead ruthenium oxide (PRO) surpasses that of $NiCo_2O_4$, and approaches the Pt/C reference. Namely, the onset potential for ORR is at -0.11 V vs. Ag/AgCl for the PRO catalyst which is slightly lower than that of Pt/C (-0.04 V vs. Ag/AgCl) but higher than the $NiCo_2O_4$ (-0.19 V vs. Ag/AgCl). The Vulcan XC72 used as a support for the Pt/C catalyst (and as a conductive additive with PRO and $NiCo_2O_4$) has very poor activity, and through Kouteky-Levich analysis (**Figure 6.1b,d,f,h**), ORR was found to primarily proceed through the 2 e$^-$ pathway on the carbon. On the other hand, the 4 e$^-$ pathway was observed for Pt/C and the oxides. These values are summarized in **Table 6.1**.

Table 6.1 *Oxygen reduction parameters for Vulcan XC72, Pt/C, $NiCo_2O_4$, and PRO catalysts in 0.1 M KOH electrolyte.*

Catalyst	n	j_k (mA cm^{-2})	Onset Potential (mV vs. Ag/AgCl)
Vulcan XC72 carbon	2.3	12	-0.28
Pt/C	4.0	∞	-0.04
$NiCo_2O_4$	4.1	21	-0.19
PRO	4.0	53	-0.11

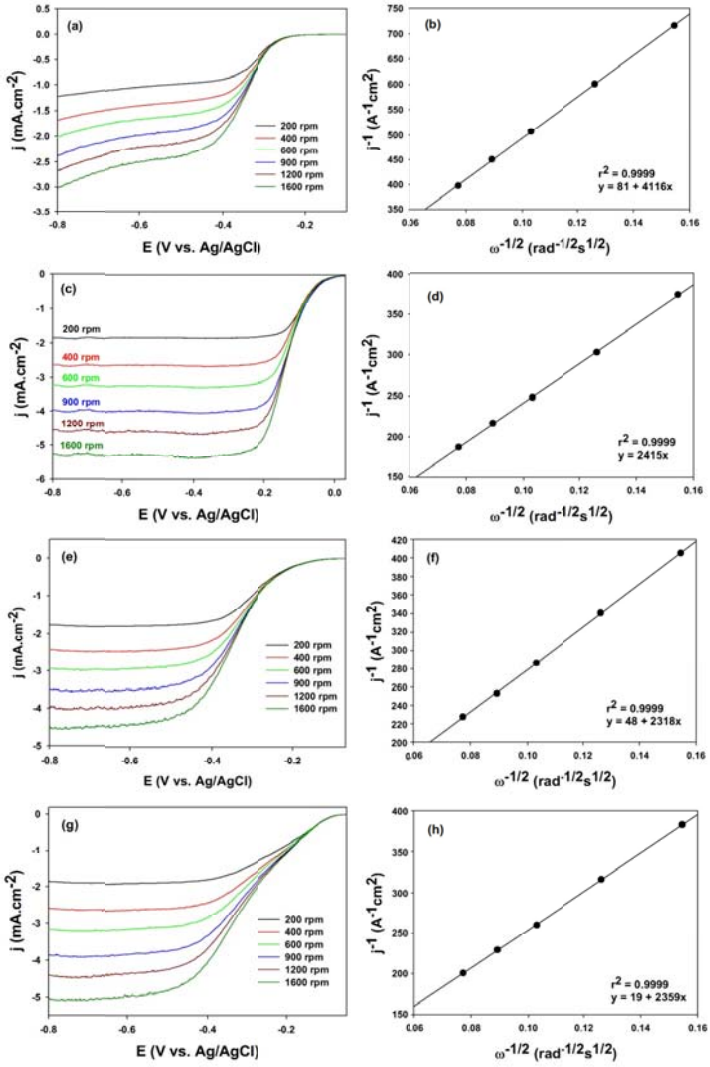

Figure 6.1 The linear sweep voltammograms and corresponding Koutecky-Levich plots of Vulcan XC72 (a,b) Pt/C (c,d), $NiCo_2O_4$ (e,f), and PRO (g,h) in O_2-saturated 0.1 M KOH at a scan rate of 5 mV/s.

The linear sweep voltammograms for oxygen reduction at 1600 rpm are displayed in **Figure 6.2a**. **Figure 6.2b** shows the oxidative linear sweep voltammograms, where the onset of oxygen evolution occurs at 0.47 V vs. Ag/AgCl for PRO, 0.61 V vs. Ag/AgCl for

$NiCo_2O_4$, and 0.66 V vs. Ag/AgCl for Pt/C. The far superior OER activity of the PRO owes to its high conductivity, high surface area, and the existence of higher and lower valent oxides (Pb_2 $[Ru_{2-x}Pb_x]O_{6.5}$) in the potential region of oxygen evolution.[13] These attributes of the pyrochlore can extend its electrocatalytic performance to a plethora of oxidation reactions, and also provide a practical alternative to Pt/C in aqueous media for ORR. It also shows the promise of the material as a catalyst for aqueous Li-O_2 batteries.

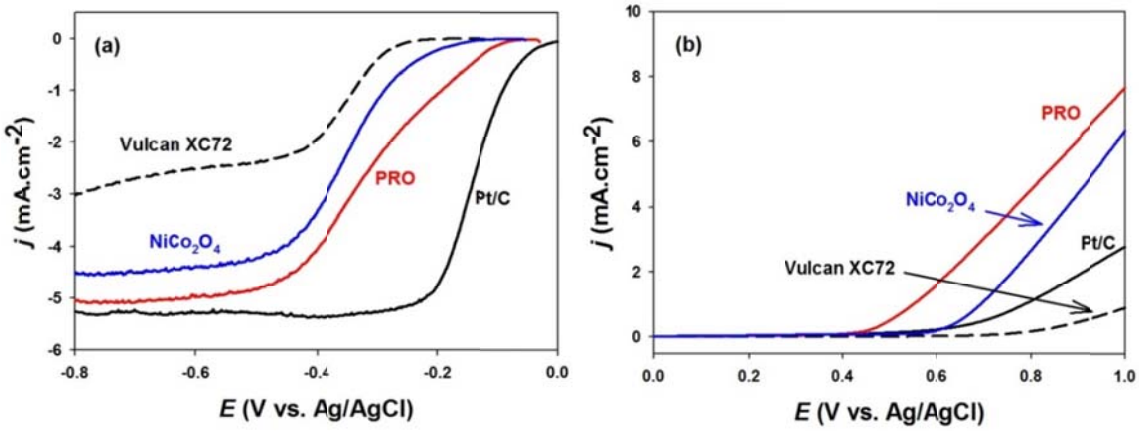

Figure 6.2 The linear sweep voltammograms of the lead ruthenate oxide (PRO) catalyst compared to Pt/C, $NiCo_2O_4$, and Vulcan XC72 in O_2-saturated 0.1 M KOH at a scan rate of 5 mV/s and a rotation rate of 1600 rpm. The curves in (a) and (b) show the oxygen reduction and evolution reactions, respectively.

6.3.2 Non-Aqueous Oxygen Reduction and Evolution Reactions

Our group has utilized this material as a cathode catalyst in the non-aqueous lithium oxygen battery, where it exhibits enhanced cycle life and a drastic lowering of the charge potential.[8,29] **Figure 6.3** shows the cyclic voltammograms of carbon (**Figure 6.3a**) and the pure mesoporous pyrochlore (**Figure 6.3b**) in 0.1 M $LiPF_6$/TEGDME electrolyte. On carbon black, a clear distinction between ORR/OER and the argon background (dashed curve) is observed. The pyrochlore, on the other hand, shows minimal differences under these non-steady-state conditions. This is attributed to the surface metal oxide redox couples giving rise to large pseudo-capacitance behavior (which occurs under argon as well), due to the high surface area of this pyrochlore oxide (155 m^2/g).

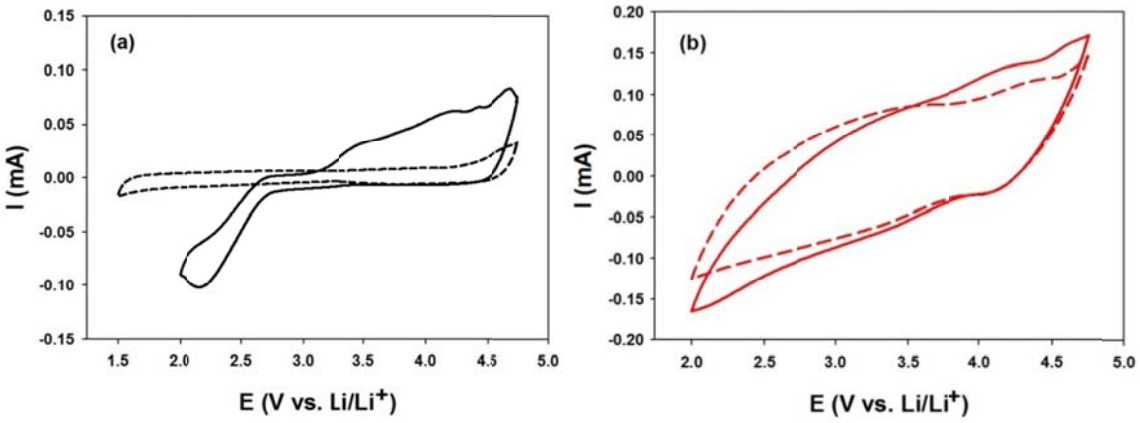

Figure 6.3 Cyclic voltammetry on Vulcan XC72 (a) and lead ruthenium oxide pyrochlore (b) in non-aqueous O_2-saturated 0.1 M $LiPF_6$/TEGDME electrolyte at a scan rate of 5 mV/s. The dashed lines are the experimental background CVs performed under Argon flow.

To further probe the ORR/OER performance in non-aqueous media, a combination of chronoamperometry (**Figure 6.4a**, ORR) and linear sweep voltammetry (**Figure 6.4b**, OER) were applied.[30] Lithium peroxide was deposited onto thin films of the Vulcan XC72 and pyrochlore (on glassy carbon substrates) by applying a reduction potential of 2.25 V vs. Li/Li^+ for 30 minutes. After the oxygen reduction step, the system was allowed to rest for 1 hour to ensure that any LiO_2 remaining in solution or on the surface had fully converted to Li_2O_2 via the disproportionation reaction ($2LiO_2 \rightarrow Li_2O_2 + O_2$).[31] The capacitance contribution mentioned above can be observed more clearly by the dashed i-t curves (2.25 V vs. Li/Li^+ under argon flow) in **Figure 6.4a.** The Vulcan XC72 quickly reaches 0 mA but the pyrochlore takes the full 30 minutes to approach zero current. Under an O_2 flow, anodic linear sweep voltammommetry at 0.5 mV/s was used to oxidize the formed Li_2O_2 (**Figure 6.4b**). For the carbon black, at least three peaks are clearly visible, suggesting that more than Li_2O_2 is being oxidized (as fully explained below). On the pyrochlore only two peaks are observed; one just above 3 V and a second peak at 4 V. The shift in the main oxidation peak centered at 4.7 V for Vulcan XC72 to 4.0 V for the lead ruthenate oxide indicates a substantial electrocatalytic effect. It should be noted that the overall electrical charge by integration of the peak area is greater for the Vulcan XC72 because of the higher relative amount of Li_2O_2 formed by ORR at 2.25 V.

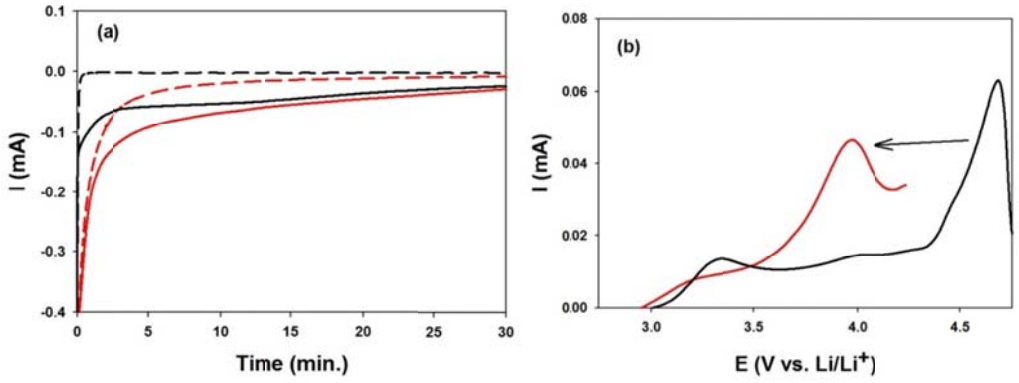

Figure 6.4 Comparison of the catalytic activity of Vulcan XC72 (black) and lead ruthenium oxide pyrochlore (red) for the oxygen reduction (a) and evolution (b) reactions in non-aqueous O_2-saturated 0.1 M $LiPF_6$/TEGDME electrolyte. The oxygen reduction activity in (a) was probed using chronoamperometry with an applied voltage of 2.25 V vs. Li/Li^+. The background i-t curves are displayed with dashed lines and the experiments performed under O_2 flow with solid lines. The oxygen evolution activity in (b) was determined with linear sweep voltammetry at a scan rate of 0.5 mV/s to 4.25 V vs. Li/Li^+ (pyrochlore) and 4.75 V vs. Li/Li^+ (Vulcan XC72) after a layer of Li_2O_2 (and potential side-products) was formed in (a).

6.3.3 Charging of Pre-Loaded Electrodes

To understand the electrocatalytic effect of the OER, electrodes utilizing the Vulcan XC72 and pyrochlore as support materials were combined with commercial powders of Li_2O_2 and the known side-products of ORR from electrolyte decomposition (lithium hydroxide, carbonate, and formate). Charging of these electrodes under galvanostatic conditions are shown in **Figure 6.5**. Sodium formate was used to replace lithium formate since it can be obtained in the pure anhydrous state. Charging of Li_2O_2 on carbon proceeds

with a high initial overpotential followed by a flat plateau at 3.7 V and a rise to 4.6 V (electrolyte oxidation voltage) after $2e^-/Li_2O_2$ is achieved. The overpotential is thought to be due to the direct chemical oxidation of the carbon surface at the Li_2O_2/carbon interface to form an insulating layer of lithium carbonate.[32,33] The only other compound which could be oxidized on carbon below the voltage of electrolyte decomposition was formate. This compound exhibited a plateau of 3.8V and proceeded via a 1 e^- process (actual 0.9 e^-), which has been observed previously.[34] In contrast, the pyrochlore electrode was capable of oxidizing *all* of these compounds below the onset of electrolyte oxidization (**Figure 6.5b**). However, compared to carbon, the pyrochlore also oxidizes the electrolyte at a lower voltage (by about 0.5V). The Li_2O_2 was oxidized with virtually no overpotential at 3.3 V, indicating a lack of interfacial resistance. The hydroxide and formate compounds were oxidized via 1 e^- processes with a slight excess of charge being necessary. The X-ray diffraction patterns of the electrodes before and after charging the peroxide show that the Li_2O_2 was completely oxidized by both electrode materials (**Figure 6.5c,d**). These results indicate that the dominant oxidation peaks observed in **Figure 6.4b** following discharge are a result of the oxidation of not only Li_2O_2, but a combination of side-products which form via electrolyte decomposition by O_2^-/LiO_2. Electrochemical oxidation of the electrolyte occurs only after these compounds are completely oxidized (ie. >4.7 V for Vulcan XC72 and >4.2 V for the pyrochlore).

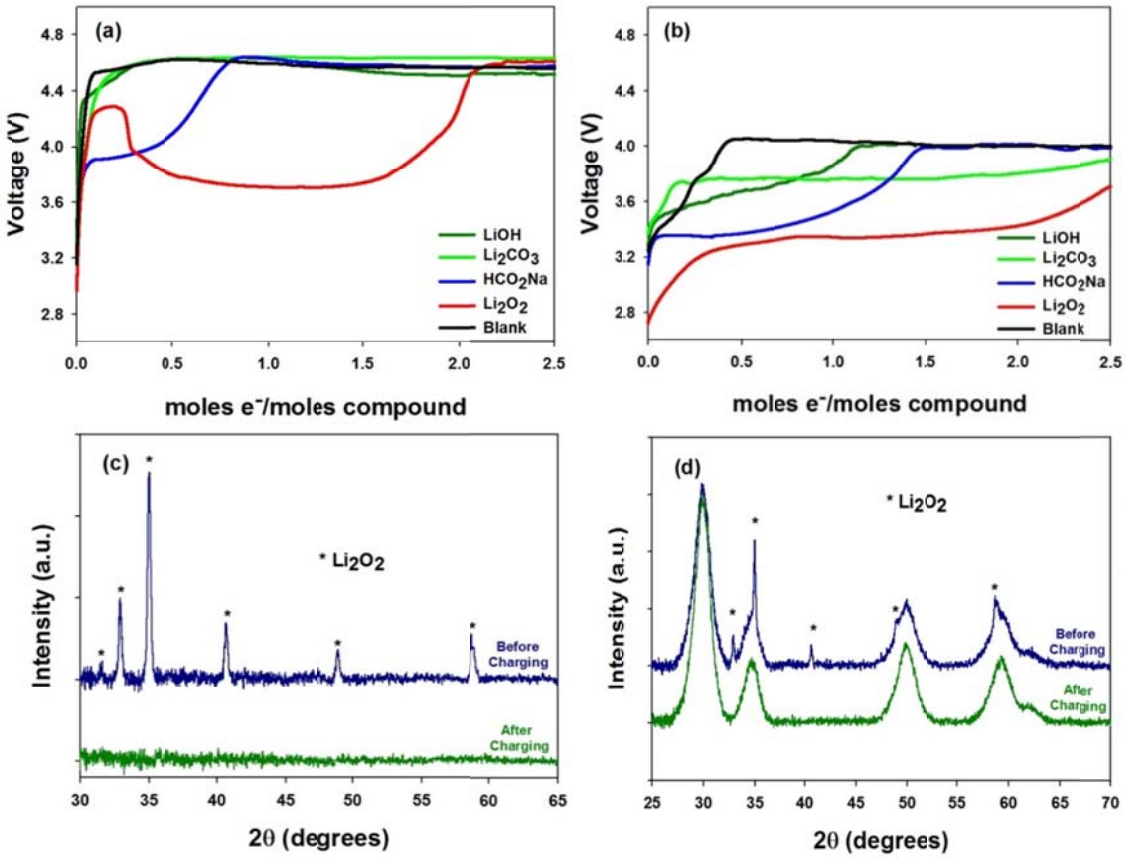

Figure 6.5 Charging of pre-filled electrodes in 1 M LiTFSI/TEGDME at 50 μA/cm^2. The electrodes were filled with lithium hydroxide, lithium carbonate, sodium formate, and lithium peroxide using Vulcan XC72 carbon black (a) and the PRO catalyst (b) as the support materials. The powder XRD patterns of the Li_2O_2/Vulcan XC72 (c) and Li_2O_2/PRO (d) composites before and after charging show that the commercial Li_2O_2 is completely oxidized on both materials. The unlabeled broad peaks in (d) are attributed to the pyrochlore structure.

To study the catalytic effect on the cycling performance of Li-O_2 batteries, full cells were assembled with lithium negative electrodes, 1 M LiTFSI/TEGDME electrolytes, and Vulcan XC72, TiC, or TiC+PRO positive electrodes. Vulcan XC72 itself has been shown

to readily oxidize in the presence of Li_2O_2 (Chapter 5) and cannot remove discharge side-products or its surface Li_2CO_3 layer (**Figure 6.5**). TiC (TiC-B from Chapter 5), on the other hand, was used as a more stable, conductive support for PRO here. PRO was mixed with TiC in a mass ratio of 1:4.

Figure 6.6 displays the cycling behaviour of Vulcan XC72. It can be seen that the capacity decays rapidly to nearly zero after 10 cycles. The cell had died after approximately 100 hours (**Figure 6.6a**).

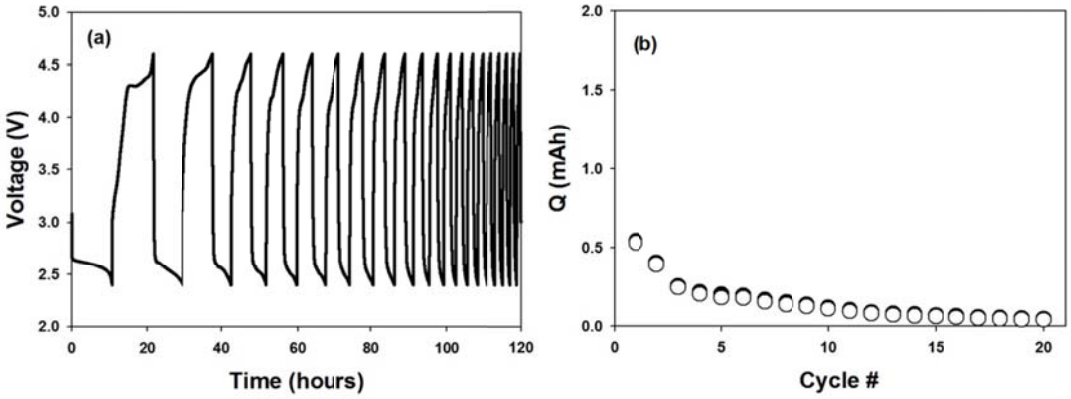

Figure 6.6 (a) Galvanostatic cycling of a Vulcan XC72 electrode in 1 M LiTFSI/TEGDME at 50 μA/cm^2. (b) The corresponding capacity vs. cycling number. The open circles represent the discharge capacity and the filled circles represent the charge capacity.

When TiC was used as the positive electrode, the cell lasted for approximately 200 hours, twice as long as the Vulcan XC72 (**Figure 6.7a**). The capacity actually increased during the second cycle (**Figure 6.7b**), which is attributed to activation of the electrode during the first cycle.[35] After the second cycle, continuous fading was observed. Again, the cell had died after 10 cycles.

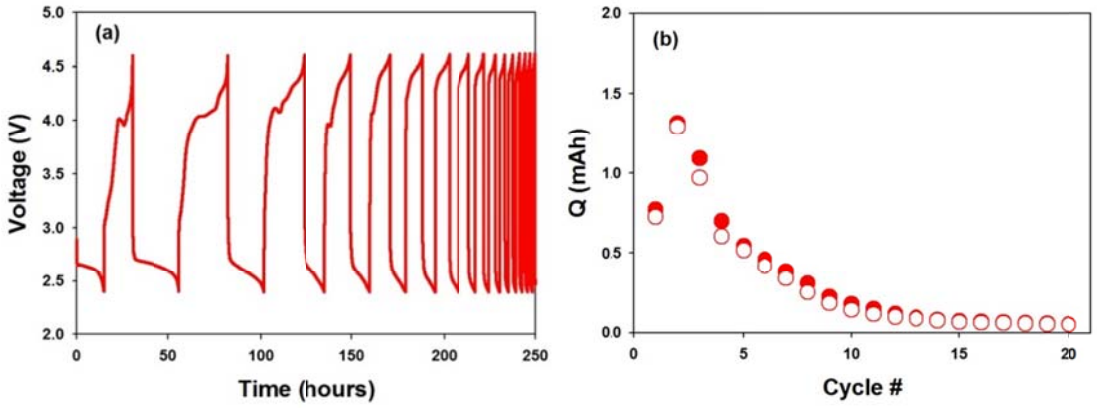

Figure 6.7 (a) Galvanostatic cycling of a TiC electrode in 1 M LiTFSI/TEGDME at 50 $\mu A/cm^2$. (b) The corresponding capacity vs. cycling number. The open circles represent the discharge capacity and the filled circles represent the charge capacity.

The PRO catalyst was added to TiC to observe the cycling behavior when the passivating discharge side-products are removed during each charge. In this case, the cell lasted for about 380 hours (**Figure 6.8a**). The same activation phenomenon was observed for the first two cycles. Notable to this cell was the higher charge capacity (than discharge) for the first eight cycles, before the capacity started to fade. An excess of charge is required to completely oxidize Li_2O_2 plus the side-products. Similar to the other electrode materials, the cell died after 10 cycles (**Figure 6.8b**). This suggests that 10 cycles to maximum discharge capacity is the maximum achievable when TEGDME is used as the electrolyte (and at this current density = 50 $\mu A/cm^2$). Obviously, as the electrolyte is progressively attacked by superoxide/peroxide, the ionic conductivity, voltage window, and other physical properties of the electrolyte are altered.

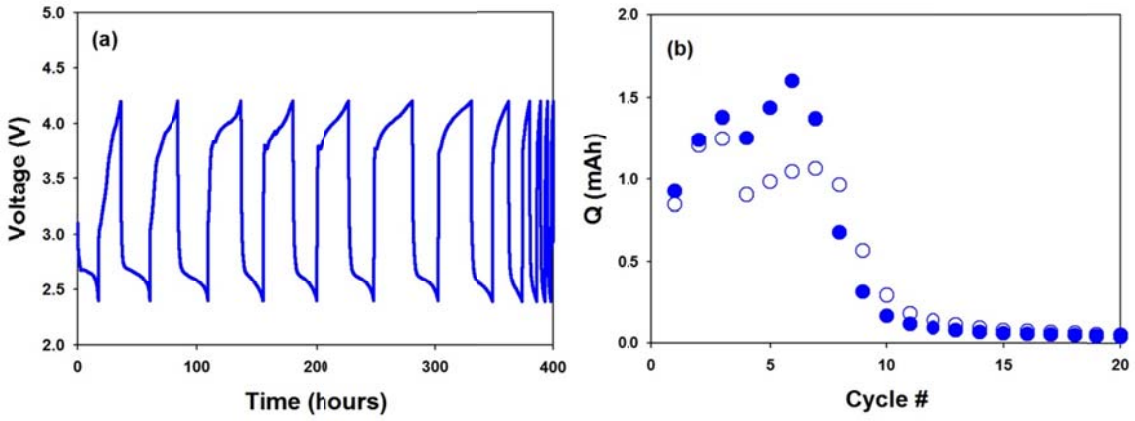

Figure 6.8 (a) Galvanostatic cycling of a TiC+PRO electrode in 1 M LiTFSI/TEGDME at 50 μA/cm^2. (b) The corresponding capacity vs. cycling number. The open circles represent the discharge capacity and the filled circles represent the charge capacity.

A summary of the cycling performance with the above three electrode materials is presented in **Figure 6.9**. On the first cycle (**Figure 6.9a**), the capacities increase and the overpotentials for both discharge and charge decrease in the order: Vulcan XC72 < TiC < TiC+PRO. On the third cycle (Figure 6.9b), the cells with TiC and TiC+PRO had similar capacities (~1.0 and 1.2 mAh, respectively) whereas the Vulcan XC72 had a much lower capacity of only ~0.2 mAh. By the fifth cycle (**Figure 6.9c**), the TiC had also began to decrease in capacity. By the 10th cycle (**Figure 6.9d**), all cells had essentially died. The inset to **Figure 6.9d** displays the discharge capacity with respect to cycle number. This shows how the TiC allows for slightly extended cycling versus carbon due to the lack of interfacial resistance caused by reactivity of Li_2O_2 and the electrode surface. The additional advantage of PRO in prolonging the cycle life is attributed to its lack of interfacial resistance and its ability to catalytically oxidize electrolyte decomposition products.

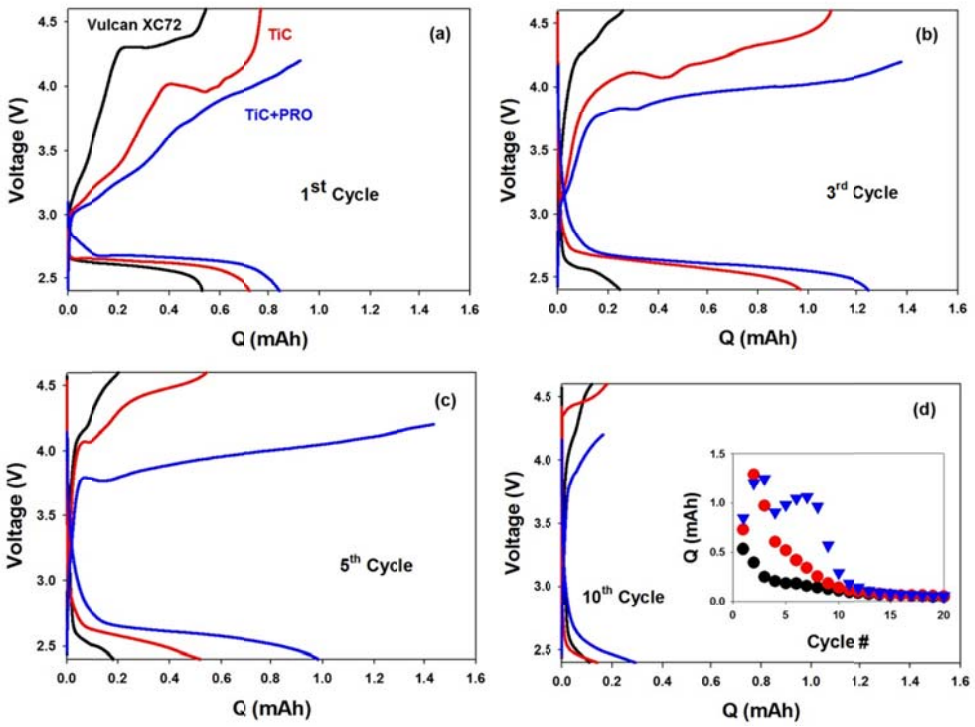

Figure 6.9 Voltage profiles for Vulcan XC72 (black), TiC (red), and TiC+PRO (blue) electrodes cycled in 1 M LiTFSI/TEGDME at 50 μA/cm^2 for the first cycle (a), the third cycle (b), the fifth cycle (c), and the tenth cycle (d). The inset to (d) displays the discharge capacity versus cycle number for the three types of electrodes.

6.4 Conclusions

The lead ruthenium oxide pyrochlore material was examined for the electrocatalytic oxygen reduction and evolution reactions in aqueous and aprotic media with application for the lithium oxygen battery. In the non-aqueous electrolyte, it was found that the lead ruthenium oxide pyrochlore lowers the overall charging oxidation voltage by 0.7 V relative to carbon, primarily because of its ability to both completely oxidize Li_2O_2 (at a relatively low potential) *and* electrocatalytically oxidize all known side-products formed

from electrolyte decomposition in the Li-O_2 battery. This further helps to explain the nature of electrocatalysis in the Li-O_2 battery, and shows that while high surface area, oxidatively stable metallic oxides are desired as cathode supports in the cell, their role can be beneficially two-fold. As an extension to Chapter 5, the better cycling stability of TiC relative to Vulcan XC72 was confirmed. This is a result of the enhanced oxidative stability of TiC in the presence of Li_2O_2. Additionally, when PRO is added to TiC, the buildup of insulating side-products formed during discharge, can be catalytically cleaned from the electrode surface to further prolong the lifetime of the cell. In all cases, the limited cycling performance of the Li-O_2 cells is attributed to the decomposition of the TEGDME electrolyte.

Chapter 7

Synthesis and Study of a Novel Electrolyte System

7.1 Introduction

The most prominent of challenge to be overcome in the creation of an improved lithium-oxygen battery is creating an electrolyte for the non-aqueous cell which is inert to nucleophilic attack on discharge and charge of the battery, is stable to metallic lithium and solvates Li salts. Although the search for more stable systems has resulted in many investigations of different solvent/salt combinations, it is generally agreed that there is presently *no* electrolyte that fits these requirements. Dimethylacetamide (DMA)[1] and dimethylformamide (DMF)[2] have recently been shown to be quasi-stable in combination with the LiTFSI salt. Nonetheless, both solvents react to form Li-X salts on cycling (X = formate, acetate and carbonate).[3] These decomposition products, particularly Li_2CO_3, precipitate on the cathode where they increase impedance and create high cell polarization on charge owing to their high oxidation potentials.[4,5,6] Similar problems are created by the carbon support typically used for the gas diffusion membrane cathode which has been shown in the previous two chapters to react with the peroxide discharge product and produce Li_2CO_3 interfacial impedance layers.[3] Two promising solutions to this dilemma have been presented by Peng *et al.*,[7] who employed dimethyl sulfoxide (DMSO) as a solvent in combination with a nanoporous gold foil as a gas diffusion membrane, or Thotiyl *et al.*,[8] utilizing TiC as a stable cathode material. Decomposition of DMSO leads to soluble products such as dimethyl sulfone and lithium sulfate,[9,10,11] which do not

passivate the cathode surface to the same extent as do the carbonates. The high reactivity of DMSO with the lithium metal anode, and the eventual precipitation of the decomposition products renders this a first-step solution. TiC exhibits limited cycling behavior even with TEGDME (Chapter 6, **Figures 6.7** and **6.9**). TEGDME was used in all previous chapters since it was the most suitable option to date. This ether, and the monoglyme (1,2-dimethoxyethane, DME), have been used extensively as electrolytes for Li-O_2 cells owing to their good stability with respect to the Li anode, and their good electrochemical potential window. [12] Nonetheless, it has been shown that DME and other glymes undergo attack by the superoxide radical in the presence of oxygen.[5, 13-20] It is widely accepted that carbonates are progressively formed with all glymes in increasing quantities on cycling, owing to a combination of reactivity on discharge (accentuated by carbon supports), and to oxygen-driven reactivity on charge (in the presence of lithium peroxide). Theoretical calculations suggest this may be governed by interactions of lithium-rich peroxide/superoxide-like surfaces with the solvent.[21]

One very important question concerns what chemistry is responsible for carbonate formation. A possible reaction mechanism for the degradation of glymes by the superoxide radical is provided by Freunberger *et al*.,[17] who propose the reaction begins with hydrogen abstraction from the β–methylene carbon (**Figure 7.1a**), and subsequent reactions lead to lithium- and alkyl carbonates. Numerous other studies have suggested that the β–carbon would be the site of attack by superoxide, or other strong bases such as $Li_{2-x}O_2$.[22,23] Proton or hydrogen abstraction from the terminal α–methyl carbon[21,23] was investigated by Zhang *et al*.,[24] who synthesized a trimethylsilyl protected glyme, dubbed "1NM3". Only one of

the glycol termini was protected, giving inconclusive results. The 1NM3 compound was also shown by Ryan *et al.* to decompose via a different mechanism.18

In this chapter, it is reported that substitution of the backbone protons on DME with methyl (-CH_3) groups eliminates the possibility of methylene hydrogen abstraction. The resulting compound, 2,3-dimethoxy-2,3-dimethylbutane (DMDMB), possesses a hydrophobic backbone and Lewis basic ethereal oxygens, and affords a stable [$(DMDMB)_2Li$]TFSI salt complex with LiTFSI. This electrolyte suppresses formation of lithium formate, dimethyl oxalate, and lithium carbonate via hydrogen abstraction from the solvent on discharge. On charge, online electrochemical mass spectrometry shows that no CO_2 is evolved. This demonstrates that much less decomposition product is deposited on the surface compared to DME, as their oxidation releases CO_2 as previously shown.[3] In combination with a non-carbonaceous cathode such as TiC, this results in significantly improved cycling stability.

Many different people contributed to the work in this chapter. Dr. Graham Murphy provided insightful advice on the topic of organic chemistry and assisted with the synthesis of DMDMB. Discussions with Dr. Murphy lead to the proposed mechanism (Figure 7.14) for the decomposition of DME. Robert Black obtained the Raman spectrum for DMDMB in Figure 7.4. Dr. Marine Cuisinier conducted the viscosity and ionic conductivity measurements for all solvent/salt combinations in this chapter and assisted in the preparation of certain figures. Drs. Erik J. Berg and Petr Novak conducted the OEMS experiments displayed in Figures 7.15 and 7.16.

7.2 Experimental Details

7.2.1 Synthesis of 2,3-dimethyl-2,3-dimethoxybutane (DMDMB)

Under an argon atmosphere, pinacol (1.5 mol) (98%, Aldrich) was added to 2 L tetrahydrofuran (>99%, Caledon) in a 3 L round-bottom flask. The tetrahydrofuran was dried over molecular sieves (4A, Sigma-Aldrich) prior to use. Sodium hydride (3.3 mol) (50 wt.% in mineral oil, J.T. Baker) was added to this mixture slowly while mechanically stirring. The mixture was heated to reflux and stirred continuously for approximately 12 hours. After cooling, the flask was placed in an icebath and iodomethane (3.3 mol) (99%, Sigma-Aldrich) was then added dropwise. Following the complete addition of iodomethane, the mixture was heated again to reflux and allowed to react for an additional 12 hours. After the reaction was complete, the solid sodium iodide precipitate was filtered off, and the THF solvent was evaporated with gentle heating. The DMDMB was then collected by fractional distillation at atmospheric pressure at a boiling point of 144-146 °C. The DMDMB was stored over 4A molecular sieves in a brown glass bottle.

7.2.2 Characterization of DMDMB and [$(DMDMB)_2Li$]TFSI

The viscosity of the solvent and electrolyte was measured using a μVISC viscometer (Rheosense, Inc.) and the ionic conductivity of the [$(DMDMB)_2Li$]TFSI electrolyte with a ORION STAR conductimeter.

7.2.3 Computational Methods

In this work, Hartree Fock (HF) calculations were carried out using the Gaussian 03 software package.[25] The 6–311G(d,p) basis set was used for all atoms. All considered systems were fully optimized and characterized through harmonic frequency analysis.

7.2.4 Nuclear Magnetic Resonance Spectroscopy (NMR)

NMR experiments were conducted in D_2O or $CDCl_3$ solution on a Bruker Advance 300 MHz instrument at room temperature. ^1H spectra in D_2O were referenced to the residual HDO peak at 4.78 ppm (DSS at 0 ppm); ^1H spectra in $CDCl_3$ were referenced to the residual $CHCl_3$ peak at 7.26 ppm (TMS at 0 ppm). The ^{13}C spectra in $CDCl_3$ were referenced to the residual $CHCl_3$ at 77.2 ppm.

7.2.5 Reactions with KO_2

All experiments were conducted in an Ar-filled glove box. 1.5 mmol KO_2 (Sigma-Aldrich) and 2.5 mmol 18-crown-6 (99%, Sigma-Aldrich) were added to 5 mL of solvent and were stirred for at least 1 hour to ensure complete chelation of the KO_2 by the crown ether. The reaction is shown below (7-1):

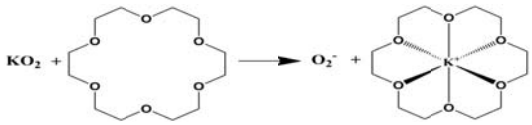

(7-1)

A solution of LiTFSI in the same solvent (3 mmol Li^+) was added to form the lithiated oxide, Li_2O_2. All reactions were stirred for 24 hours in an inert atmosphere to ensure good contact. The solid was collected by centrifugation, washed once with the reaction solvent (DME or DMDMB) and dried *in vacuo* before analysis. The solid products were analyzed

by powder X-ray diffraction and ^{1}H-NMR. For the ^{1}H-NMR analysis, a sample of the solid product was dissolved in 0.7 mL D_2O.

7.2.6 Galvanostatic Cycling

The LiTFSI (Novolyte) was dried at 150 °C *in vacuo* for 5 days prior to preparation of the electrolyte with the dried and purified DMDMB. For comparison purposes, a $[(DME)_2Li]TFSI$ electrolyte was prepared in the exact same manner with 1,2-dimethoxyethane (99.5% anhydrous, Sigma-Aldrich).

7.2.7 Fourier Transform Infrared Spectroscopy (FTIR) and Raman Spectroscopy

The FTIR spectra of DMDMB and $[(DMDMB)_2Li]TFSI$ was obtained with a Bruker Tensor 37 FTIR instrument in transmission mode between 600 and 4000 cm^{-1} by placing a portion of the liquid samples between two NaCl plates.

Raman analysis was performed on a HORIBA Jobin Yvon instrument with a laser excitation energy of 633 nm. The electrolyte was placed into a quartz cuvette and sealed under argon.

7.3 Results

7.3.1 Characterization and Properties of DMDMB and $[(DMDMB)_2Li]TFSI$

The simple concept of *backbone* ($-CH_2-$) protection of glyme (monoglyme, 1,2-dimethoxyethane, DME) is shown in (**Figure 7.1a,b**). The target material 2,3-dimethyl-2,3-dimethoxybutane (DMDMB) (**Figure 7.1c**) was prepared by a Williamson ether synthesis from pinacol, as described in the experimental methods section;[26] the NMR spectra are provided in **Figure 7.2**. In addition to the anticipated lower reactivity with

superoxide or Li_2O_2, the DMDMB molecule possesses enhanced properties as an electrolyte solvent for Li-O_2 batteries. First, the volatility of this novel solvent (b.p. = 144-146 °C) is much less than DME (b.p. = 85 °C), making it more practical for electrolyte applications.[26] The additional methyl groups also make this solvent very hydrophobic which can aid in protecting the lithium metal anode from reaction with residual water, and solubilizing O_2.

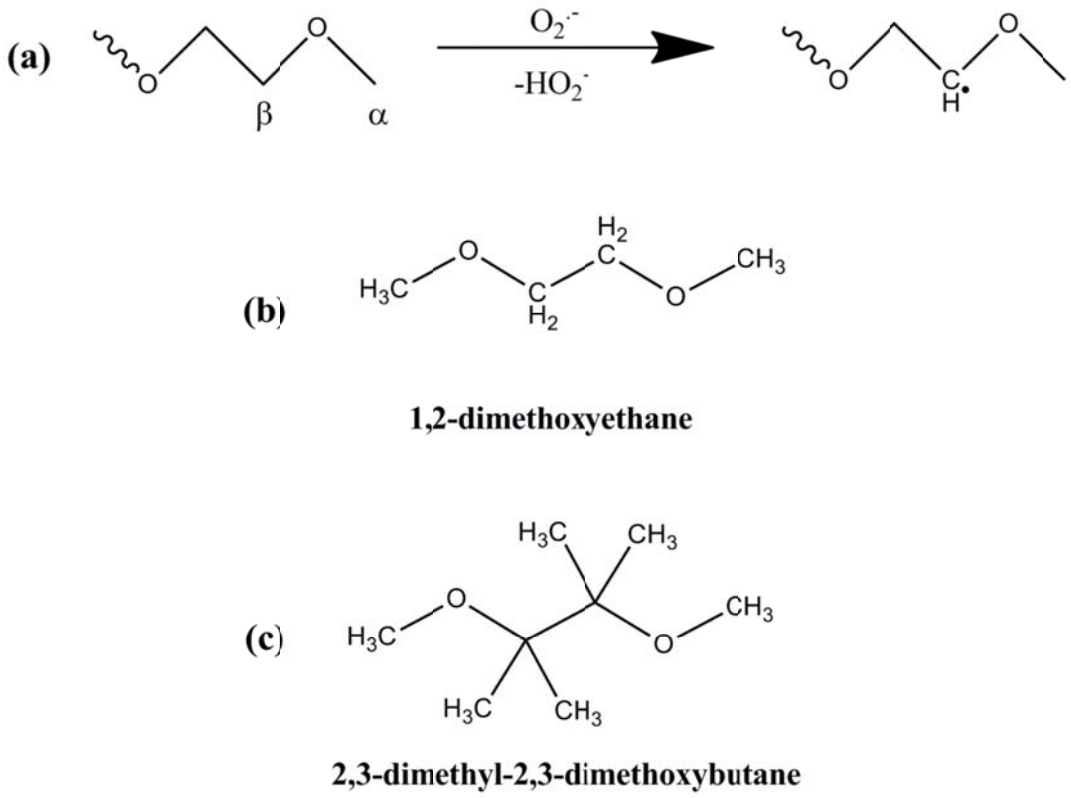

Figure 7.1 (a) Proposed initial hydrogen abstraction step of glymes by superoxide during cell discharge and the structures of (b) 1,2-dimethoxyethane (DME) and (c) 2,3-dimethyl-2,3-dimethyoxybutane (DMDMB).

After this solvent was synthesized and purified by fractional distillation, the structure was verified with ^{1}H-NMR and ^{13}C-NMR (**Figure A4.3**). To utilize this solvent as a non-

aqueous electrolyte, the solubility of various lithium salts was explored. It was found that of all the salts examined; lithium [perchlorate, hexafluorophosphate, tetrafluoroborate, triflate, bis(fluorosulfonyl) imide, and bis(trifluoromethanesulfonyl) imide (LiTFSI)], only the latter was soluble. Even this salt was only soluble in a precise molar ratio of 1:2 (LiTFSI:DMDMB), indicating formation of a single phase chelate species, denoted $[(DMDMB)_2Li]TFSI$. With lower amounts of LiTFSI, two-phase liquid separation occurred ($[(DMDMB)_2Li]TFSI$ + DMDMB) and higher amounts of LiTFSI resulted in a saturation point ($[(DMDMB)_2Li]TFSI$ + LiTFSI). The properties of both the DMDMB solvent and the $[(DMDMB)_2Li]TFSI$ electrolyte are summarized in **Table 7.1**.

Table 7.1. *Properties of the synthesized DMDMB solvent and the $[(DMDMB)_2Li]TFSI$ electrolyte.*

Property	**DMDMB**	**$[(DMDMB)_2Li]TFSI$**
Boiling Point (°C)	144-146	
Density (g/cm^3 at 25 °C)	0.875±0.004	1.235±0.026
H_2O Content (ppm)	<1	<10
Viscosity (mPa.s at 25 °C)	1.48	160.22
Ionic Conductivity (mS/cm at 25 °C)		0.615

The density of the DMDMB solvent is less than that of H_2O, whereas that of the $[(DMDMB)_2Li]TFSI$ is greater. This is seen in the photographs shown in **Figure 7.2a** and **Figure 7.2c**, respectively, where the H_2O phase remains at the bottom for the DMDMB solvent and at the top of the $[(DMDMB)_2Li]TFSI$ electrolyte. The viscosity and ionic conductivity of the latter is comparable to that of many room temperature ionic liquids.[27] This is due to the strong chelation of the Li^+ cation by two molecules of DMDMB *via* the oxygen atoms.

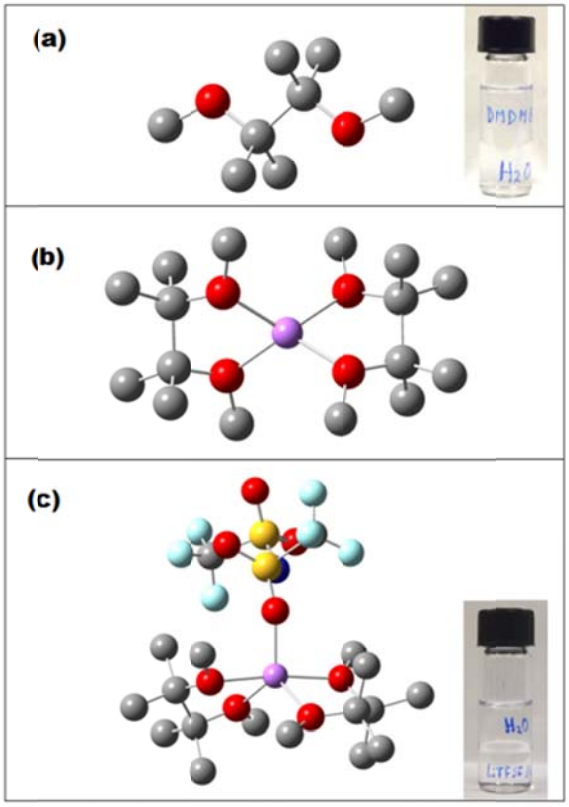

Figure 7.2 Optimized geometric structures of (a) the DMDMB molecule, (b) the chelated $(Li\text{-}DMDMB_2)^+$ cation, and (c) the $[(DMDMB)_2Li]TFSI$ complex at the HF/6-311G** level. Hydrogen atoms are excluded from all structures for clarity. Atoms are coloured as follows: carbon (grey), oxygen (red), lithium (purple), fluorine (light blue), nitrogen (dark blue, behind sulfur), and sulfur (dark yellow). The images in (a) and (c) display the phase separation between water and the DMDMB solvent and $[(DMDMB)_2Li]TFSI$ electrolyte.

To understand this complex further, we carried out *ab initio* calculations to determine its possible configurations. The optimized geometric structures of the synthesized DMDMB molecule, the $(Li\text{-}DMDMB_2)^+$ cation and the $[(DMDMB)_2Li]TFSI$ ionic liquid electrolyte are depicted in **Figure 7.2**. The $(Li\text{-}DMDMB_2)^+$ cation (**Figure 7.2b**) exhibits a

tetrahedral environment around the Li^+ ion, where the Li^+ is strongly bound by each oxygen of the two DMDMB molecules. With the addition of the $TFSI^-$ anion (**Figure 7.2c**), a distorted square pyramidal geometry (coordination number = 5) is adopted, where the lithium cation is coordinated to each of the oxygen atoms of the two DMDMB molecules and one of the oxygen atoms of the TFSI anion. To understand the effect of the $TFSI^-$ anion in this chelate-type ionic liquid, a separate calculation was carried out by replacing the $TFSI^-$ with a PF_6^- anion (**Figure 7.3**). This showed that the stable bi-chelated environment formed by DMDMB is lost, and thus PF_6^- or other "hard" anions prevent a stable coordination sphere from forming, and inhibit solubilization of the salt.

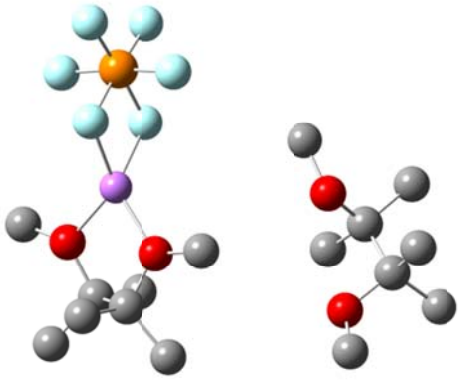

Figure 7.3 Optimized geometric structure of a $LiPF_6$-$DMDMB_2$ complex at the HF/6-311G** level. Hydrogen atoms are omitted for clarity. The colours of the atoms are: carbon (grey), oxygen (red), lithium (purple), fluorine (light blue), and phosphorous (dark yellow).

The ionic liquid nature of the LiTFSI-$DMDMB_2$ electrolyte was further examined by FTIR and Raman spectroscopy (**Figure 7.4**). The region between 800 and 900 cm^{-1} is characteristic of C-O-C stretching and CH_2 rocking modes of glymes.[28] In this region,

important changes are observed with the conformation induced by the lithium–oxygen interaction. [29] The shift from 840 cm^{-1} for DMDMB to 835 cm^{-1} for the $[(DMDMB)_2Li]TFSI$ is indicative of interaction between the oxygen atoms of the DMDMB and the Li^+ cation.

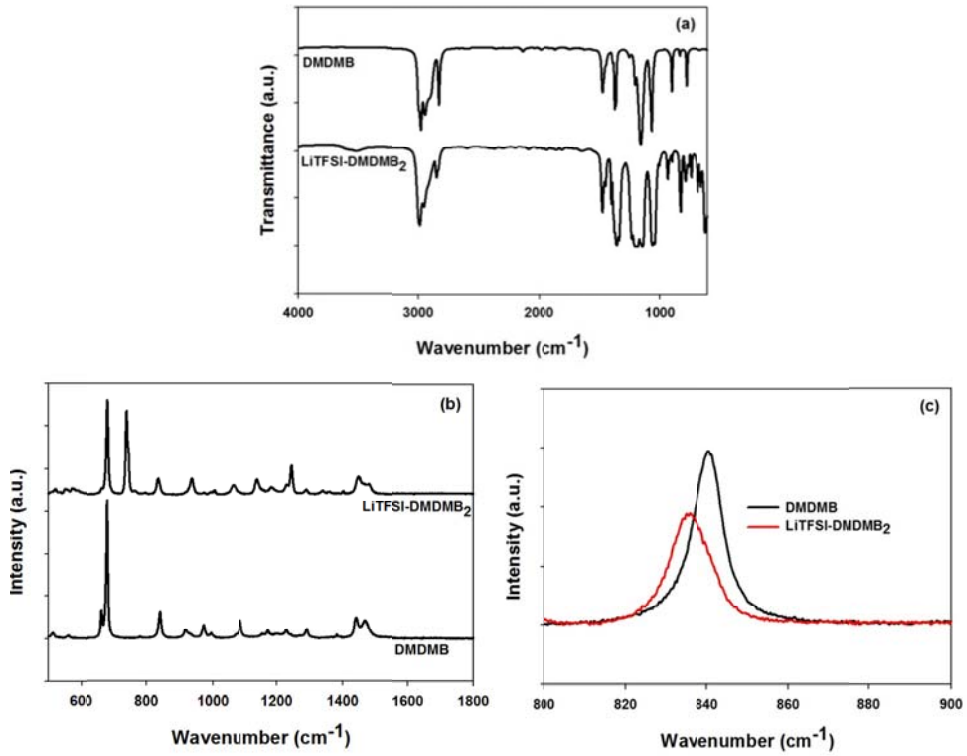

Figure 7.4 FTIR spectra (a) and Raman spectra (b,c) of the DMDMB solvent and $[(DMDMB)_2Li]TFSI$ electrolyte. (c) displays the region of C-O-C stretching in the DMDMB molecule with a shift from 840 cm^{-1} to 835 cm^{-1} for the $[(DMDMB)_2Li]TFSI$ indicative of a strong interaction between the oxygen atoms of the DMDMB and the Li^+ cation.

The low volatility of this ionic liquid enables its use at elevated temperature in Li-O_2 or other types of lithium batteries such as Li-ion. Thermal gravimetric analysis was carried

out to probe the decomposition and vaporization of the DMDMB and the $[(DMDMB)_2Li]TFSI$ electrolyte. In **Figure 7.5a**, TG analysis shows that the solvent attains an appreciable vapor pressure just above room temperature and is completely evaporated at its boiling point of ~145 °C. The ionic liquid, on the other hand, does not begin to lose mass until approximately 80 °C and slowly evaporates up to roughly 325 °C, followed by decomposition of the LiTFSI. When the temperature is held at 80 °C (**Figure 7.5b**) under open conditions, the ionic liquid is of much lower volatility compared to the DMDMB solvent, experiencing only a 3% weight loss over 2.5 hours. This promising thermal behavior is similar to that of a tetraglyme-LiTFSI equimolar complex.[30] It can be attributed to the strong chelation of Li^+ by the two DMDMB molecules, increasing the density, viscosity, and thus, vapour pressure of the ionic liquid relative to that of the DMDMB.

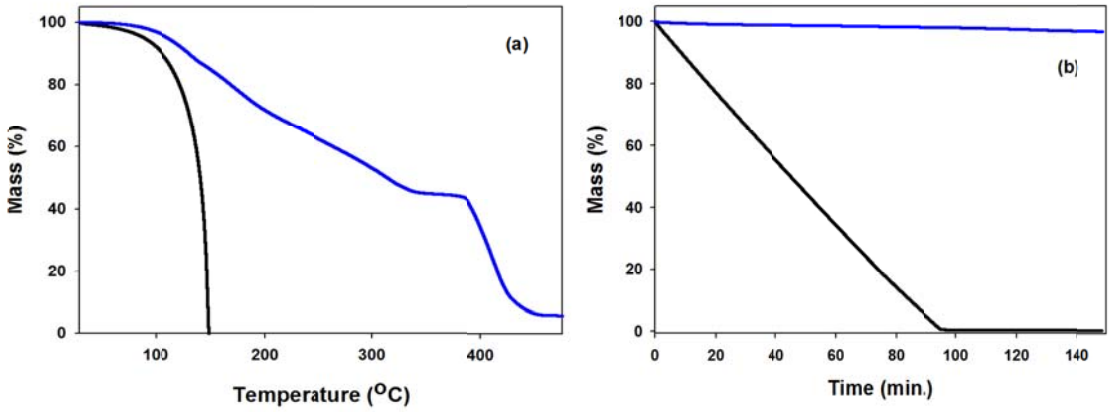

Figure 7.5 TGA curves for DMDMB (black) and $[(DMDMB)_2Li]TFSI$ (blue). (a) Temperature ramp at 10 °C/min under N_2 flow at 100 mL/min. (b) Temperature dwell at 80 °C in an N_2 atmosphere.

7.3.2 Electrochemical Properties of $[(DMDMB)_2Li]TFSI$

The stability window of the $[(DMDMB)_2Li]TFSI$ electrolyte was examined with cyclic voltammetry (CV) and found to be 0 – 4.5 V vs Li^+/Li^0. Using a Pt microelectrode as the working electrode and Li foil as the counter and reference electrodes, the CV (**Figure 7.6**) under argon exhibits typical features of a Li^+-based electrolyte. On the first cycle, the plating of Li onto the Pt surface occurs below 0 V vs. Li/Li^+ with no reduction of the solvent. The crossover of current after potential reversal is attributed to the nucleation of lithium and the increase of the working electrode surface area, possibly caused by the first layer of plated lithium and/or the formation of lithium dendrites on the surface of the platinum substrate.[31] In the anodic scan, the current begins to rise at exactly at 0 V vs. Li/Li^+ with the primary peak at 0.2 V from stripping plated Li from the surface of the Pt electrode. The additional peaks at 0.3, 0.7, and 1.4 V are due to the de-alloying of Li_xPt alloys formed during the reduction process.[31,32,33] On Pt, the electrolyte is completely stable up to 4.5 V, above which it is readily oxidized.

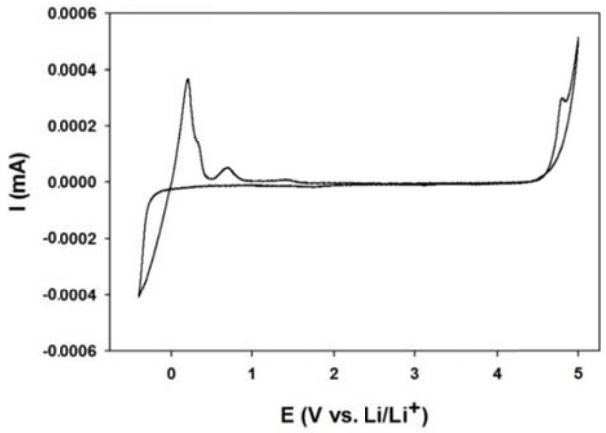

Figure 7.6 Cyclic voltammogram of the $[(DMDMB)_2Li]TFSI$ electrolyte on a Pt microelectrode at 5 mV/s under Ar (1st cycle).

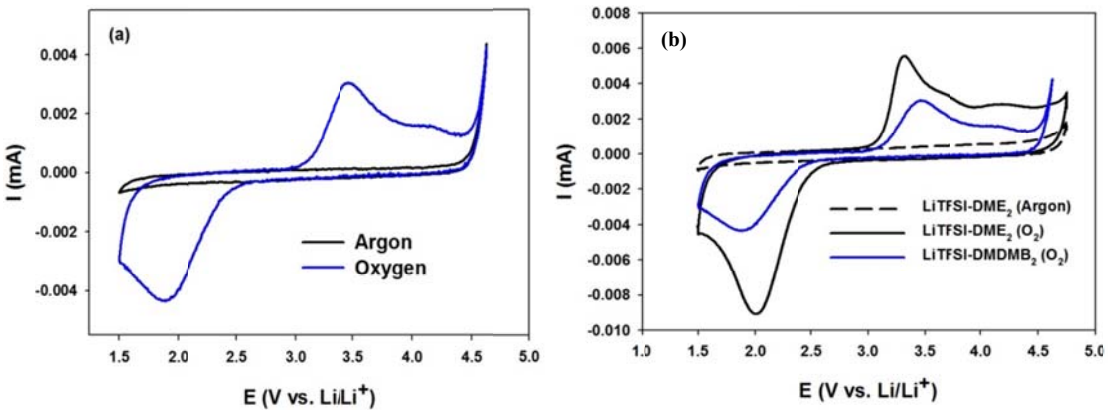

Figure 7.7 (a) Cyclic voltammograms of $[(DMDMB)_2Li]TFSI$ on glassy carbon at 100 mV/s (3rd cycle), (b) a comparison between the $[(DMDMB)_2Li]TFSI$ and $[(DME)_2Li]TFSI$ electrolytes on a glassy carbon electrode at 100 mV/s (3rd cycle).

Figure 7.7a shows the results of probing the oxygen reduction and oxygen evolution reactions (ORR and OER, respectively) on a glassy carbon electrode. The ORR is characterized by one broad peak starting at 2.5 V; OER begins at 3 V with a classic signature of two anodic peaks. A similar CV profile has been observed with DME as the electrolyte,[34] which is confirmed by our studies (**Figure 7.7b**).

The smaller current response and slight shift in the ORR and OER peaks *vis a vis* DME is due to the higher viscosity of the $[(DMDMB)_2Li]TFSI$ ionic liquid. The anodic stability of the electrolyte was also studied using Swagelok™-type Li-O_2 cells with metallic lithium negative electrodes and carbon positive electrodes (**Figure 7.8**). These studies showed that under galvanostatic control (using a high surface area electrode) the electrolyte is completely stable up to 4.2V, above which it undergoes electrochemical oxidation (**Figure 7.8a,b**) The stability window of $[(DME)_2Li]TFSI$ is slightly higher (**Figure 7.8b**), yet even at a typical cut-off of 4.5 V, DME shows some anodic

decomposition even when cycled under argon (**Figure 7.8c**), which has also previously been shown with TEGDME.[18] Thus, the voltage stability windows for DME and DMDMB are not vastly different.

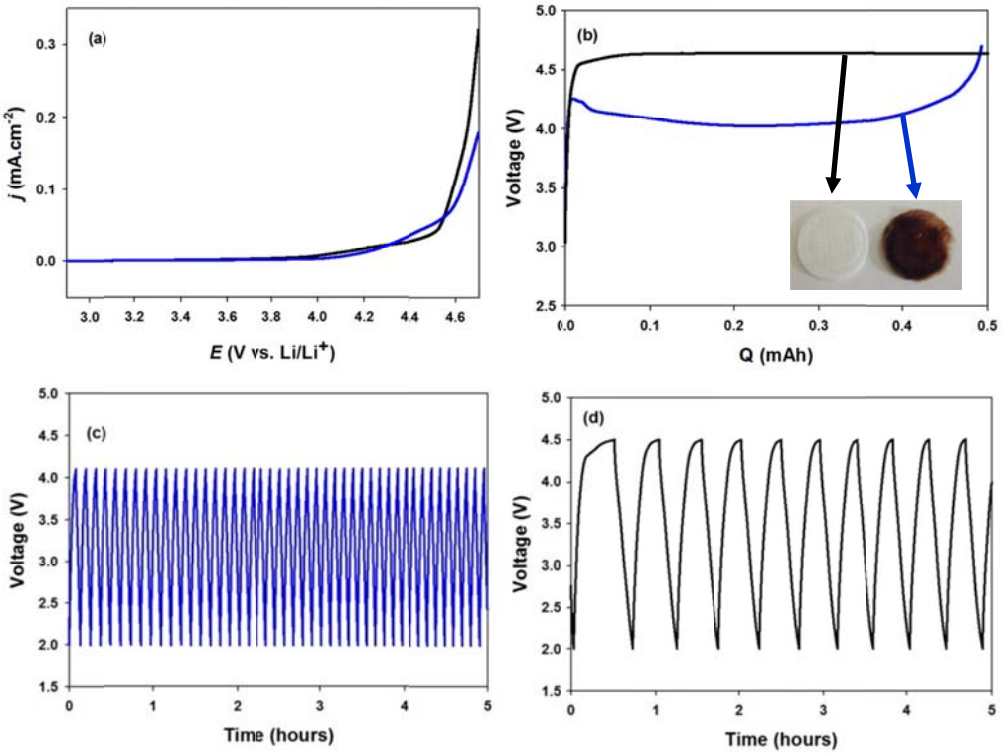

Figure 7.8 Anodic stability of the $[(DME)_2Li]TFSI$ (black) and $[(DMDMB)_2Li]TFSI$ (blue) electrolytes. (a) Anodic linear sweep voltammograms at a scan rate of 0.1 mV/s. (b) Anodic stability of the $[(DME)_2Li]TFSI$ and $[(DMDMB)_2Li]TFSI$ electrolytes at a current density of 50 $\mu A/cm^2$. The image shows the separators (white for DME and brownish-red for DMDMB) after holding the anodic current for 0.5 mAh. (c) Galvanostatic discharge-charge curves in the range of 2V to 4.1 V for the $[(DMDMB)_2Li]TFSI$ electrolyte at a current density of 50 $\mu A/cm^2$ under argon. (d) Galvanostatic discharge-charge curves in the range of 2V to 4.5 V for the $[(DME)_2Li]TFSI$ electrolyte at a current density of 50 $\mu A/cm^2$ under argon.

Although the electrolyte appears to be stable up to at least 4.4 V under potentiodynamic control (**Figure 7.6, 7.8a**), when galvanostatic control is used, the electrolyte undergoes significant decomposition just beyond ~4.2 V (**Figure 7.6b**). At this point DMDMB decomposes, as determined by NMR studies (not shown) on the electrolyte after full charge (separators in **Figure 7.8b**). The oxidation appears to be auto-catalytic in nature owing to the decrease in the voltage after the initial product is formed. When the voltage is be maintained below 4.1 V, however, it is perfectly stable **(Figure 7.8c**). The stability window of $[(DME)_2Li]TFSI$ is slightly higher (**Figure 7.8b**), yet even at a typical cut-off of 4.5 V, DME shows some anodic decomposition even when cycled under argon (**Figure 7.8d**), which has also previously been shown with TEGDME.[35] The scheme for the electrochemical oxidation of DME is displayed in **Figure 7.9**. In summary, the stability window for DME and DMDMB are not very different, yet appear to form vastly different products from electrochemical oxidation via different pathways.

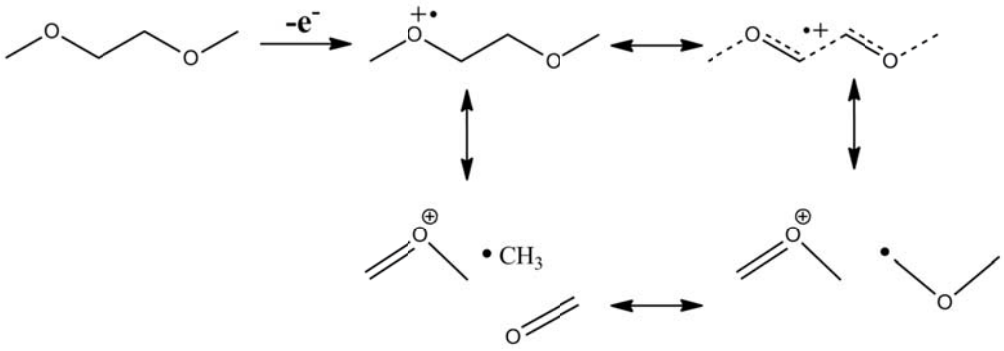

Figure 7.9 Electrochemical oxidation of DME.[36]

Figure 7.10a shows the first discharge voltage profile of electrodes conducted with $[(DMDMB)_2Li]TFSI$ at various current densities and at elevated temperature, compared to $[(DME)_2Li]TFSI$. The main limitation of $[(DMDMB)_2Li]TFSI$ is its higher viscosity and

lower ionic conductivity relative to $[(DME)_2Li]TFSI$. At room temperature, the viscosity and ionic conductivities of $[(DME)_2Li]TFSI$ are 43.53 mPa.s and 3.42 mS/cm^2, compared to 160.22 mPa.s and 0.615 mS/cm^2 for $[(DMDMB)_2Li]TFSI$ (**Table 7.1**). These transport limitations can be overcome by either running the cells at elevated temperature or by using a lower current density.

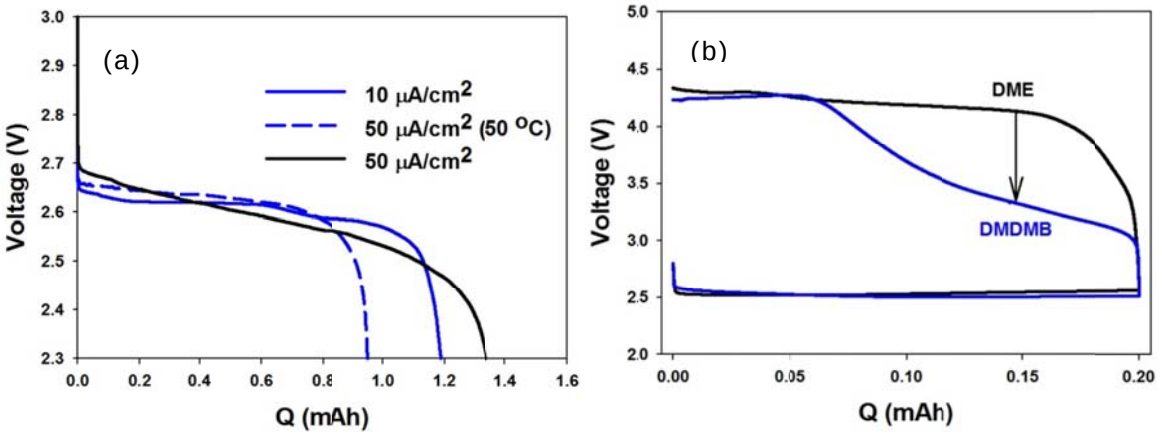

Figure 7.10 (a) Discharge curves for $[(DMDMB)_2Li]TFSI$ at various rates and temperature with a comparison to $[(DME)_2Li]TFSI$ proving that the limitation is mass transport in the $[(DMDMB)_2Li]TFSI$ electrolyte, and (b) the first galvanostatic discharge-charge cycle for the $[(DMDMB)_2Li]TFSI$ and $[(DME)_2Li]TFSI$ electrolytes at current densities of 50 μA/cm^2.

In **Figure 4.10b**, the first galvanostatic discharge-charge profiles are displayed for the two electrolytes with a capacity cut-off (0.2 mAh). On the charge process, $[(DME)_2Li]TFSI$ shows no low voltage plateau, and the high voltage plateau is reached quickly (>4 V) after approximately 15 % of the total charge. In contrast, $[(DMDMB)_2Li]TFSI$ displays a long low voltage sloping plateau starting at 3 V (the

theoretical OER voltage), lasting for about 70% of the total charge. As discussed in chapters 5 and 6, the low voltage plateau is characteristic of the charging of Li_2O_2 which lacks a passivating layer (carbonates, carboxylates, and other species formed from electrolyte decomposition on discharge and/or charge) at the Li_2O_2/electrolyte interface.3 As previously discussed in chapter 5, carbonaceous electrode materials possess larger overpotentials (high voltage plateaus) than non-carbonaceous materials,[37,38] and thus the rise to the high voltage plateau is due in part to the Li_2O_2/electrode interfacial resistance caused by the oxidation of carbon.[39,40] In contrast, TiC as an electrode support with DMDMB resulted in the charging voltage not exceeding 4.2V (see below), which is the decomposition voltage of the electrolyte under operating cell conditions. The $TFSI^-$ anion (present here in large abundance due to the 2:1 solvent-salt complex) has also been shown to give rise to LiF in the discharge product,[10,41] which can cause impedance. As presented in the Appendix (**Figure A5.1**), LiF was detected by ^{19}F-NMR in cathodes discharged in both $[(DMDMB)_2Li]TFSI$ and $[(DME)_2Li]TFSI$.

7.3.3 Analysis of Discharge Products

To evaluate $[(DMDMB)_2Li]TFSI$ as an electrolyte, full cell studies were carried out using Li as a negative electrode, and compared to those run in DME with exactly the same salt concentration (*i.e.* $[(DME)_2Li]TFSI$). **Figure 7.11** displays the powder X-ray diffraction patterns for the cathodes discharged in both electrolytes. Li_2O_2 is confirmed to be the single crystalline phase in both cases. Interestingly, the Li_2O_2 formed in the $[(DMDMB)_2Li]TFSI$ electrolyte exhibits narrower (101) and (110) reflections than that

formed in DME, indicative of differences in crystallinity or morphology owing to solvation effects.

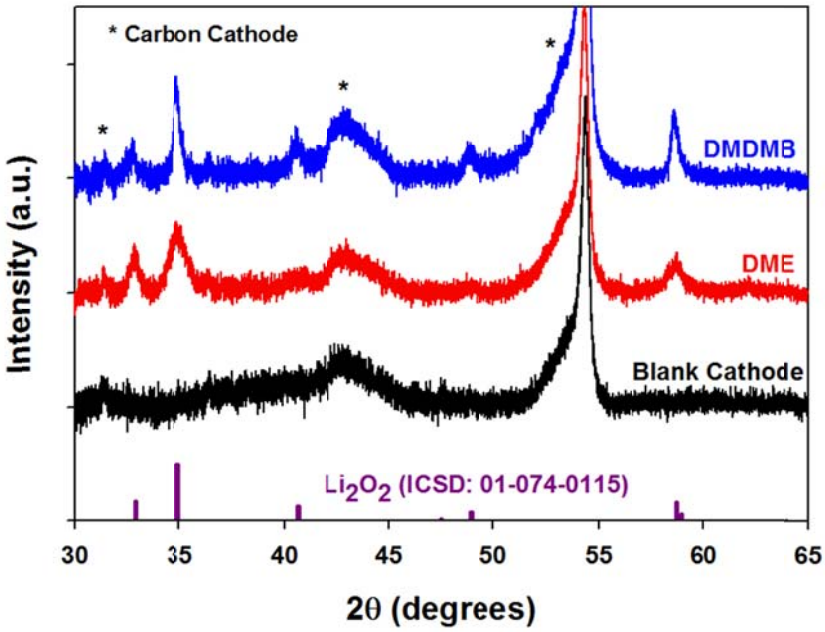

Figure 7.11 Powder X-ray diffraction patterns of cathodes discharged at 25 μA/cm^2 to a capacity cut-off of 0.5 mAh in [(DMDMB)$_2$Li]TFSI and [(DME)$_2$Li]TFSI.

Figure 7.12 shows the results of the NMR analysis of the products in cathodes discharged to a capacity of 0.5 mAh. The ^{1}H-NMR spectrum for the cathode discharged in $[(DME)_2Li]TFSI$ revealed significant fractions of lithium formate (δ = 8.46 ppm) in accordance with previous findings.[10,13] The peak at 3.87 ppm is assigned to dimethyl oxalate. We were able to detect this species by analyzing the products contained in the cathodes (by dissolution in D_2O) without washing them first with an additional solvent. This compound is formed by the addition of oxygen to the β-carbon in the DME backbone after the β-hydrogen is abstracted by superoxide (discussed in more detail below). The cathode discharged in the $[(DMDMB)_2Li]TFSI$ electrolyte, however, contains six fold less lithium formate, and *no* lithium acetate, dimethyl oxalate, or any other proton-containing decomposition products. This demonstrates that replacing the β-hydrogens on the DME backbone with methyl groups eliminates the possibility of hydrogen abstraction at those sites by O_2^-/Li_2O_2. The hydrogen atoms on those methyl groups appear to be stable, consistent with thermodynamic expectation. Thus, protection of the terminal methyl groups alone (ie with trimethyl silyl moieties) is unlikely to provide a practical solution. In fact, 2NM4 was synthesized (Appendix, A6) which was consisted of the TEGDME backbone with both end members protected with trimethylsilyl groups. ^{1}H-NMR revealed substantial decomposition products in cathodes discharged in both TEGDME and 2NM4. The decomposition pathway obviously begins via superoxide attack at the β-position (discussed in detail below).

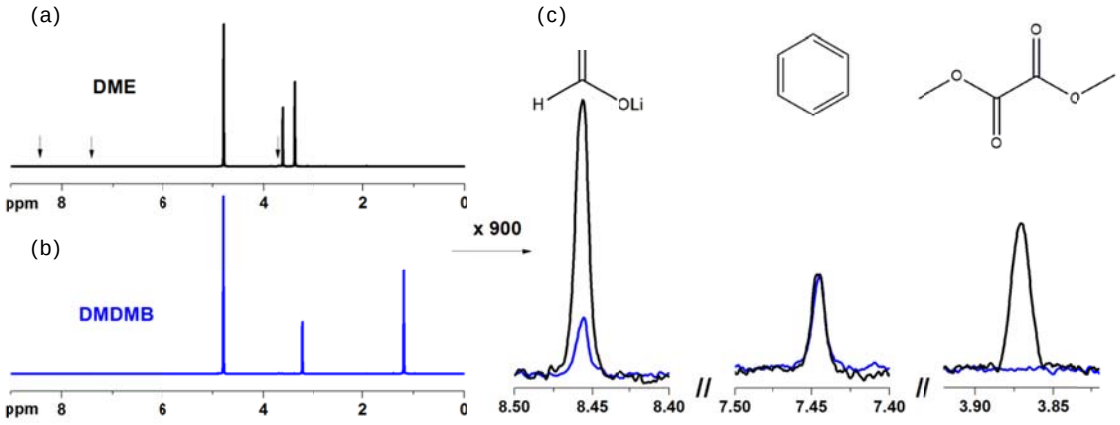

Figure 7.12 The ^{1}H-NMR spectra of side-products deposited on cathodes after 1st discharge in (a) $[(DMDMB)_2Li]TFSI$ and (b) $[(DME)_2Li]TFSI$. The cells were both discharged at 25 μA/cm^2 to a capacity cut-off of 0.5 mAh. The HDO peak (δ = 4.78 ppm) and the corresponding residual solvents are visible in the overall spectra. These spectra were normalized to an internal C_6H_6 standard (δ = 7.45 ppm) shown in (c). The expansions shown in (c) display the main observed decomposition products: lithium formate (left, δ = 8.46 ppm) and dimethyl oxalate (right, δ = 3.87 ppm).

7.3.4 Probing for Hydrogen Abstraction Susceptibility

Our early studies using KO_2 showed that TEGDME is stable with respect to superoxide attack when the contact time is quite limited.[16] This has since been confirmed, and it was further demonstrated that the reactivity of higher order glymes with KO_2 is based on their purity: non-distilled TEGDME suffered significant decomposition, whereas distilled TEGDME was quite stable.[20] We have found that the concentration of KO_2 and

the time of exposure also play major roles in the decomposition of glymes. In agreement with the work of Schwenke *et al.*,[20] we have found that adding 18-crown-6 to these reactions enhances KO_2 solubility and reactivity, though it ultimately results in decomposition of the crown ether itself. In our case, we use both 18-crown-6 and the lithium cation source LiTFSI in order to more closely mimic the Li-O_2 discharge reaction, and to produce both Li_2O_2 and possible decomposition products. The XRD patterns of the solid precipitate obtained from using DME and DMDMB in these reactions are shown in **Figure 7.13a**. In both cases, Li_2O_2 is evident along with some K_2CO_3 resulting from the aforementioned decomposition of the [K^+/18-crown-6] complex by O_2^-. The ^{1}H-NMR spectra of the same solid precipitates dissolved in D_2O are shown. For DME, a substantial amount of lithium formate is observed, but no lithium acetate, the second most-commonly detected proton-containing decomposition product of longer glymes. The dimethyl oxalate, which was observed in the discharged cathode (**Figure 7.12**), did not appear in the KO_2 reactions. As proposed by Freunberger *et al.*,[13] we also believe the oxalate forms *via* addition of molecular oxygen to the radical product of β-hydrogen abstraction (See **Figure 7.14**, Path 1). As these KO_2 reactions were carried under an argon atmosphere, we conclude that this species only forms in the presence of oxygen. In the case of DMDMB, virtually *no lithium formate* was observed under the forcing conditions of the KO_2 reactions. The supernatant liquid of each KO_2 reaction was also subjected to ^{1}H-NMR analysis but no decomposition products were detected in either case.

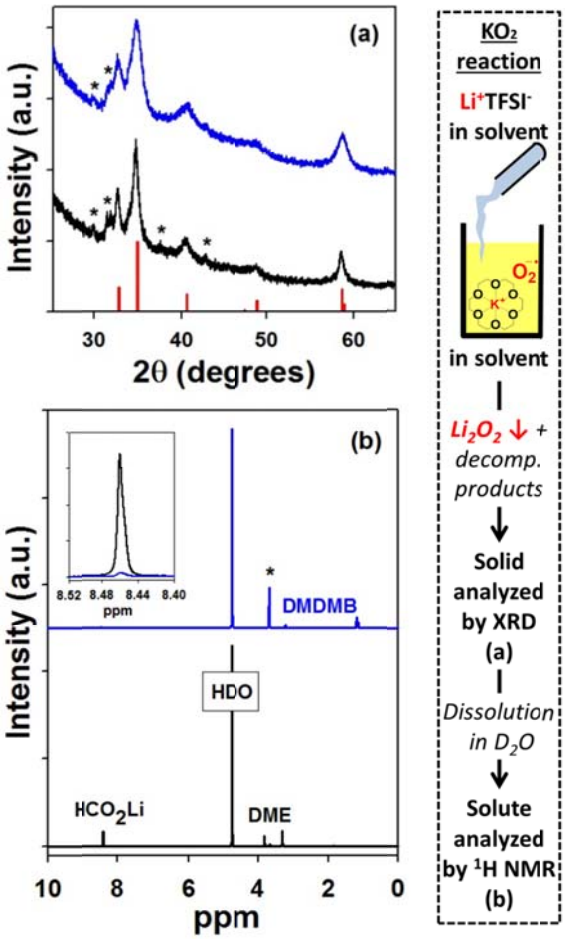

Figure 7.13 Analysis of the solid product obtained from reaction between KO_2 and the solvents DME (black) and DMDMB (blue). The scheme for these reactions is shown on the right. a) XRD patterns showing the formation of Li_2O_2. Peaks arising from K_2CO_3 are indicated with *. The pattern for Li_2O_2 (PDF# 01-074-0115) is displayed with red bars. b) ^{1}H-NMR spectra of product dissolved in D_2O (DMDMB in blue and DME in black). The inset displays an overlay of the lithium formate peaks (δ = 8.46 ppm) with the intensity normalized to that of the HDO peaks at 4.78 ppm. The peak labelled with * (δ = 3.68 ppm) in the DMDMB solid product spectrum arises from the $[K^+/18\text{-crown-6}]TFSI^-$ salt which is insoluble in the DMDMB solvent.

The breakdown of TEGDME on Li_2O_2 surfaces has previously been studied by XPS and shown to form large amounts of carboxylates.[42] In our study, DME and DMDMB were allowed to react with Li_2O_2 powder for three days. Their dried solid products were analyzed by FTIR and ^{1}H-NMR but these methods were not sensitive enough to detect such relatively small amounts of these species. Nonetheless, this indicates that the decomposition of glymes is primarily due to the superoxide intermediate on discharge of the Li-O_2 battery rather than direct contact with bulk, stoichiometric Li_2O_2 surfaces, in accord with a previous report.[23]

7.3.5 Mechanism Overview

The main products of decomposition of DME by strong oxidizing agents in aqueous solution are methanol, formaldehyde, and formic acid.[44] We believe that under aprotic conditions, the analogous oxidation byproducts are formed *via* hydrogen abstraction-initiated mechanisms, as illustrated in **Figure 7.14**. The decomposition of DME probably begins with hydrogen abstraction from the β site by the superoxide radical. Should this attack molecular oxygen, the formation of dimethyl oxalate ensues, as discussed above (**Figure 7.14**, Path 1). Should the initially-formed radical undergo β–scission, a methoxy radical and methyl vinyl ether will be created, where the latter will likely undergo polymerization. Hydrogen abstraction from the methoxy radical would lead to formaldehyde, which, in the presence of Li^+ and more O_2^- or Li_2O_2, will be oxidized to lithium carbonate *via* lithium formate (**Figure 7.14**, Path 2). Decomposition of DME may also begin with hydrogen abstraction at the α-position, giving a radical species that could

fragment to give formaldehyde, and again lead to formate and carbonate (**Figure 7.14**, Path 3).

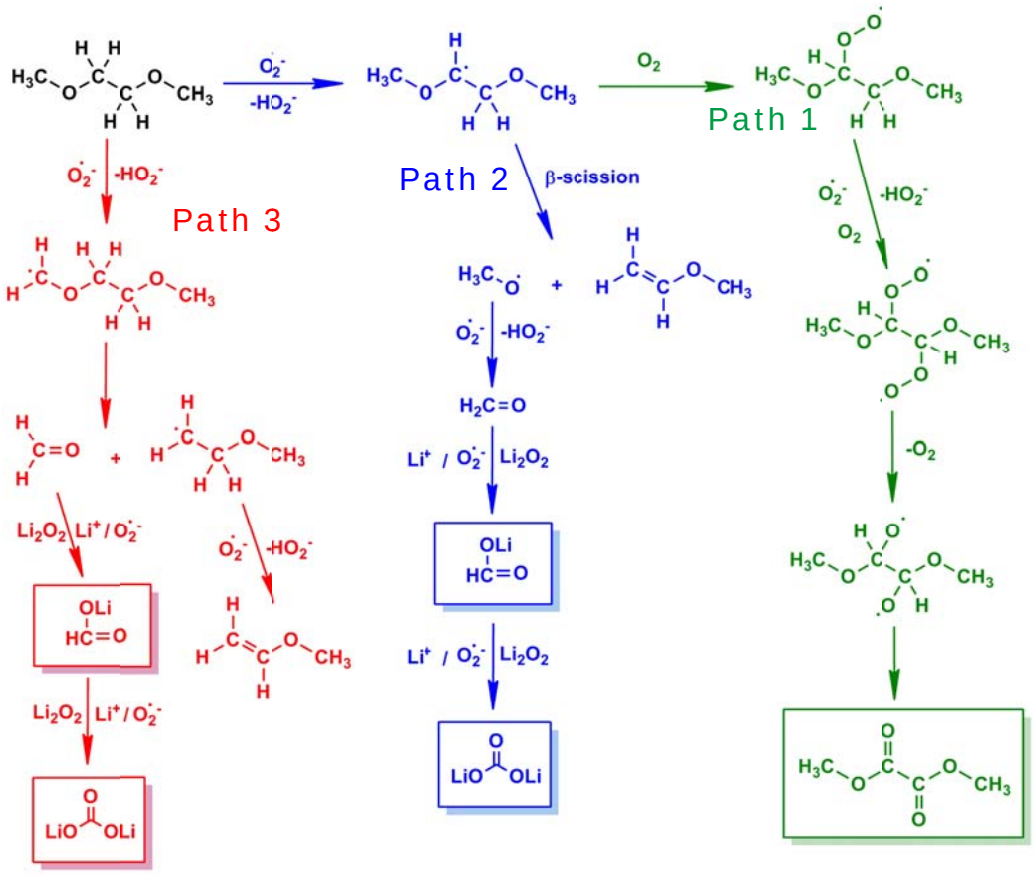

Figure 7.14 Proposed mechanism for the decomposition of DME by superoxide attack in the presence and absence of O_2.

Both mechanistic pathways can give rise to lithium formate (**Figure 7.14**, Paths 2 and 3), and if both are equally viable, no decrease in byproduct formation should be observed for DMDMB. However, when subjected to the same Li-O_2 discharge reaction, DMDMB proved to be significantly more stable, as ^{1}H NMR analysis of the precipitates showed a

dramatic decrease in the occurrence of lithium formate (**Figure 7.13b**, inset). On replacement of the β-hydrogens of DME with methyl groups, that hydrogen abstraction pathway is eliminated. It leaves only α-hydrogen abstraction as a means of formate production, accounting for the minor amounts of this side product after cell operation, and virtually zero using KO_2 reactions as a probe. Although the literature suggests that both sites are equally as susceptible to hydrogen abstraction,[43,44] based on the greatly decreased lithium formate production, our results clearly demonstrate that β-hydrogen abstraction is the dominant pathway. This is consistent with thermodynamic principles, in that formation of an oxygen-stabilized 2° radical (**Figure 7.14**, Path 2) should be more favourable than formation of an oxygen-stabilized 1° radical (**Figure 7.14**, Path 3). Furthermore, the presence of dimethyl oxalate in DME confirms the β-hydrogens are abstracted and not the α-hydrogens. We note that the added stability for DMDMB *vis a vis* DME is unlikely to arise from chelation or steric effects, since the α-methyl groups are equally accessible in both solvents.

7.3.6 Online Electrochemical Mass Spectrometry and Galvanostatic Cycling

Mass spectrometry was used to monitor the evolution of gases generated from charging cells with $[(DMDMB)_2Li]TFSI$ and $[(DME)_2Li]TFSI$ electrolytes. ^{13}C electrodes were used in this OEMS study to differentiate between CO_2 produced from electrolyte decomposition ($^{12}CO_2$) and carbon electrode oxidation ($^{13}CO_2$). The gas evolution in conjunction with the voltage profiles are displayed in **Figure 7.15a,b** for the $[(DME)_2Li]TFSI$ and $[(DMDMB)_2Li]TFSI$ electrolytes. Of the various gases (O_2, H_2, CO_2) known to evolve during the charge process of the Li-O_2 cell,[45] only O_2 and CO_2 were

prominent. No hydrogen was evolved over the course of charge. The end of charge can clearly be seen by the decrease in O_2 flux. For the DME-based electrolyte (**Figure 7.15a**), this decrease in O_2 evolution occurs well beyond the equivalent discharge capacity of 1 mAh; proving that an excess of current is required to completely oxidize the Li_2O_2 in the presence of the decomposition products which were formed during discharge. This is emphasized by the $^{12}CO_2$ signal reaching a maximum at 1.4 mAh. Complete Li_2O_2 oxidation does not occur until all discharge products (including salt decomposition, electrode and electrolyte side-products) have been oxidized. In the case of the DMDMB-based electrolyte (**Figure 7.15b**), the O_2 evolution begins to decrease as complete charge capacity is reached. The end of discharge can also be monitored by the $^{13}CO_2$ signal, which rises once the solid Li_2O_2 (and other discharge products) are removed from the surface (at ~0.9 mAh for DMDMB and ~1.2 mAh for DME). This results from the oxidation of $Li_2{}^{13}CO_2$ formed at the Li_2O_2/carbon interface.[3,40] In summary, DME requires an excess of charge to fully oxidize the various products formed on discharge. With DMDMB, the side-products are minimal, enabling improved charge reversibility.

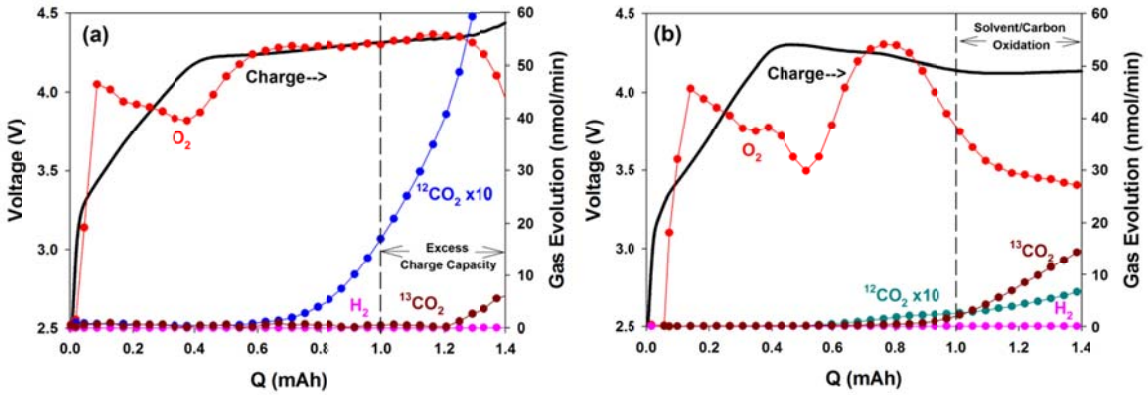

Figure 7.15 Voltage profiles (black lines) and gas evolution (O_2: red, $^{12}CO_2$:blue/teal, $^{13}CO_2$: brown, H_2: pink) during galvanostatic charge at 0.25 mA of a ^{13}C cathode in: a) DME and b) DMDMB. The cells were first discharged to 1 mAh in O_2 at 0.25mA.

The $^{12}CO_2$ evolution profiles are displayed in **Figure 7.16** along with the quantitative amounts of total $^{12}CO_2$. The $^{12}CO_2$ evolution can arise from the oxidation of various carbonates, alkyl carbonates, and carboxylates formed as side-products from the electrolyte during discharge.[3,13,40] The amount of $^{12}CO_2$ evolved from both electrolytes was negligible in the absence of Li_2O_2 (not shown here). This is in accord with the understanding that CO_2 is not a likely species formed from the simple anodic oxidation of DME (see **Figure 7.9**),[46,47] and is unlikely to arise from DMDMB electrochemical oxidation. Thus, we conclude that all the $^{12}CO_2$ shown in **Figure 7.16** (and **Figure 7.15a,b**) is a direct result of the oxidation of electrolyte decomposition products that result from hydrogen abstraction. Although some $^{12}CO_2$ is observed for both electrolytes, it is significantly less for DMDMB. Integration of the total amount of $^{12}CO_2$ evolved on charge yields total quantities of 0.872 µmol for DME and 0.101 µmol for DMDMB. These values

correlate to 4.7% and 0.5% of the discharge product, for DME and DMDMB, respectively (based on a $2e^-/Li_2O_2$ process during discharge; 18.66 μmol Li_2O_2 is expected per mAh).[10] The value for the DME carbonate/carboxylate decomposition products is in excellent agreement with McCloskey *et al*.[3] who claim ~5% of the discharge product is comprised of carbonates at the electrolyte/Li_2O_2 interface using a 1 M LiTFSI/DME electrolyte. This suggests that although decomposition via hydrogen abstraction from the DMDMB is strongly suppressed (recall that a six-fold decrease in lithium formate is detected from ^{1}H-NMR on discharged cathodes), very small amounts of CO_2-evolving side-products are still formed. The most plausible pathway for the minor decomposition observed for DMDMB is one similar to Path 3 in **Figure 7.14**. Thus we conclude that there is significantly less decomposition of the [$(DMDMB)_2$Li]TFSI electrolyte leading to carboxylates and/or carbonates during discharge or charge of the cell compared to DME.

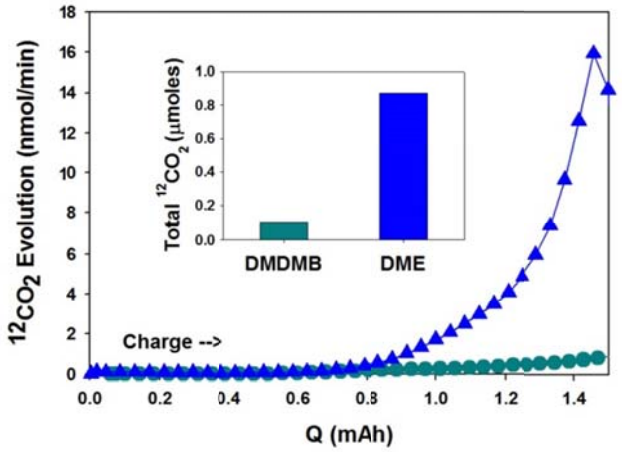

Figure 7.16 Comparison of the $^{12}CO_2$ evolution from the DME (blue triangles) and DMDMB (teal circles) electrolytes by differential electrochemical mass spectrometry during galvanostatic charge at 0.25 mA of a ^{13}C cathode. The cells were first discharged to 1 mAh in O_2 at 0.25 mA.

Due to the known instability of carbon-based cathode materials in the Li-O_2 battery, to examine the cycling performance of the [$(DMDMB)_2$Li]TFSI electrolyte, our carbon electrodes were replaced with TiC electrodes.[8] When attempting to cycle with carbon electrodes, the instability of the electrode material outweighed the positive effects of the DMDMB. In this case, the cycle life was poor for both electrolytes. The lead ruthenium pyrochlore catalyst (PRO, studied in Chapter 6), was not used here for several reasons. First, PRO is capable of oxidizing all decomposition products along with Li_2O_2, and the goal of this experiment was to compare the cycling performance of electrolytes which produce varying amounts of side-products during discharge. Also, PRO decreases the anodic stability of electrolytes, which is already substantially lower for DMDMB (~4.2 V) relative to DME (~4.6 V). However, cells utilizing the new chelate ionic liquid electrolyte and TiC electrodes were cycled for over 300 hours with little increase in polarization (**Figure 7.17**). In comparison, cells with the DME electrolyte (and TiC electrodes), had a cycle life of less than 130 hours. The rapid build-up of carbonate/carboxylate by-products in the DME cell cause the charging voltage to increase with the number of cycles. This is followed by a decrease in discharge voltage after passivation of the active surface sites for oxygen reduction. With the lower degree of discharge by-product build-up, the charging voltage remains below 4.2 V with increasing number of cycles for DMDMB and no decrease in discharge voltage is observed until about 300 hours.

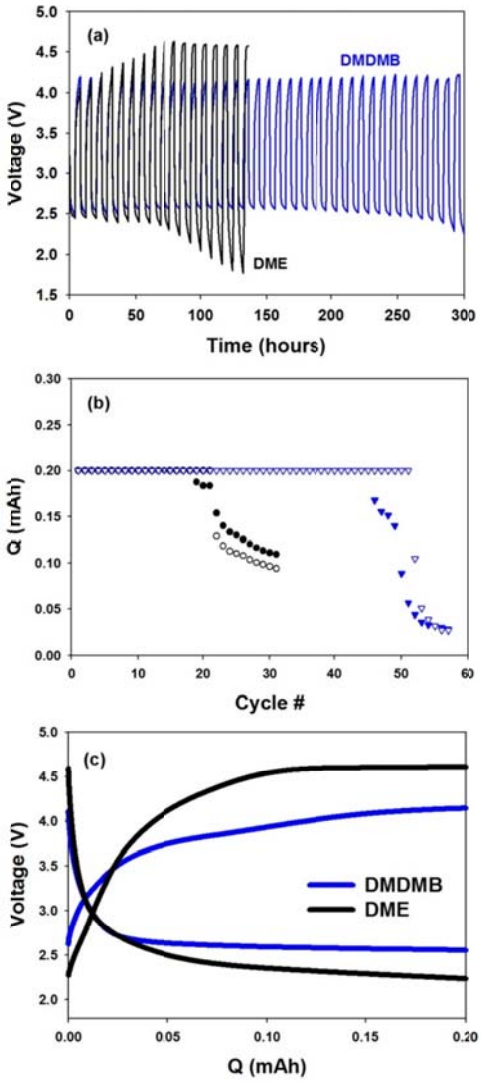

Figure 7.17 Galvanostatic cycling of Li-O_2 batteries with DME (black) and DMDMB electrolytes (blue) at 50 μA/cm^2 using lithium metal and TiC as the negative and positive electrodes, respectively. A capacity cut-off of 0.2 mAh (4 hour discharge or charge maximum), was applied, along with a lower voltage limit of 1.75 V and an upper voltage limit of 4.65 V. The overall voltage vs. time plot is displayed in (a). Capacities vs. cycle number for discharge (solid shapes) and charge (open shapes) are displayed in (b). The voltage profiles of the 10th cycle are shown in (c).

7.4 Discussion

Two major mechanisms of electrolyte decomposition are prominent in the Li-O_2 cell: nucleophilic attack and hydrogen abstraction. In this study we have shown that, in the case of glymes, hydrogen atoms on α-methyl moieties are resistant to abstraction, yet hydrogen atoms on β-methylenes are not. A significant finding of this work is that methyl moitiés can be used as "protecting" groups, thus eliminating the necessity to remove all hydrogen atoms from a potential solvent. Other possible protecting groups include fluorine atoms or trimethylsilyl groups. There are multiple challenges with creating a stable electrolyte system for the Li-O_2 battery. Not only should the solvent be stable with respect to metallic lithium and protected from the possibility of nucleophilic attack and hydrogen abstraction (via identification and replacement of acidic hydrogen atoms), but the solvent should also possess good physical properties and solvating capability. Oxygen must be highly soluble in the electrolyte system, while at the same time, the solvent must be polar enough to solvate lithium cations. The challenge with the other protecting groups mentioned above is their weak interaction with lithium cations, resulting in poor solubility of most lithium salts. A compromise between stability and solubility of both Li^+ and O_2 will be a major hurdle to overcome. When systematically designing a stable electrolyte solvent, viscosity and ionic conductivity are also key to good performance. Although viscous electrolytes aid in thermal stability, the diffusion of O_2 in solution is also hindered due to mass transport effects.

There are many conflicting reports concerning which strong nucleophilic species primarily act as the main culprit responsible for electrolyte decomposition.[13,15,17,21] Based

on our results, the solution-based superoxide (O_2^- or LiO_2) causes the most damage, while other species (ie. substoichiometric Li_2O_2 formed *in situ*) are still likely to be problematic. It should be noted that McCloskey *et al.* [10] claim that a parasitic reaction between LiO_2 (or O_2^-) and an electrolyte would lead to a 1 e^-/O_2 electrochemical formation of LiO_2/O_2^-, followed by chemical reaction. Since e^-/O_2 on discharge is always ≥ 2.00, they conclude that any chemical reaction must be between Li_2O_2 and the electrolyte. However, this does not acknowledge that the disproportionation reaction ($2LiO_2 \rightarrow Li_2O_2 + O_2$) is an equally probable pathway, especially at low current densities.[48] By reacting DME with KO_2 and 18-crown-6, the main decomposition product, lithium formate was identified here, yet, by direct reaction with solid microcrystalline Li_2O_2, no decomposition products were observed. In a greater context, the much lower charging overpotential observed for Na-O_2[49,50] and K-O_2 batteries,[51] may be related to the stability of the 1 e^- solid NaO_2 and KO_2 products *vs* the unstable LiO_2 species. The lifetime of the solution soluble intermediate (O_2^-) formed in these cases (NaO_2 and KO_2) is limited by rapid combination with the cation/crystallization, as compared to recombination by solution (or surface) disproportionation for LiO_2. Additionally, in the case of discharge in the Li-O_2 battery, the disproportionation reaction is known to form singlet oxygen,[52] which is an even more destructive reactive oxygen species.

Beyond electrolyte solvents, superoxide has been shown to react with virtually every component of the Li-O_2 battery, including binders,[16] electrolyte salt anions,[10,41] and carbon electrode surfaces.[39,40] Additionally, 100% Li_2O_2 formation is never observed, even on the first discharge. The group at IBM has shown that between 77-91% Li_2O_2 yield is typical,

depending on the cathode material, for a DME-based electrolyte.[10] In their study,[10] they show that the formation of LiF from LiTFSI salt decomposition also contributes to ~3%. Lithium formate also contributes another ~3%, and the remaining decomposition is attributed to reactions with the carbon cathode and solution soluble species. The lack of a complete flat charging plateau at low voltage (**Figure 7.10c**) in our present study for the $[(DMDMB)_2Li]TFSI$ electrolyte can also be attributed to the additional side-reactions with the LiTFSI salt and the carbon cathodes. Also, in the work of McCloskey et al,[10] the yield is decreased with decreasing current density. In the context of our previous work (Chapter 3), much better charge characteristics were observed when higher discharge current densities were applied.[48] Although we attributed this mainly to the morphological changes upon discharge (thin films vs. toroids); it could also be in part an effect of the lifetime of this superoxide species in solution. At lower discharge current densities, the superoxide remains in solution for a longer time before dismutase can occur.

7.5 Conclusions

Armed with the above knowledge of the Li-O_2 battery system, we propose that there are three possible approaches to enhancing the stability of battery: 1) increase the resistance of every component of the battery to attack by superoxide; 2) utilize a "superoxide dismutase-like" catalyst to promote faster kinetics of the dismutase reaction; 3) limit the lifetime of superoxide in the cell. Currently, approach 1) is being undertaken by many groups and is perhaps the most logical at this stage of understanding. To the best of our knowledge, approach 2) has not been examined in this light, yet it is possible that, since the role of catalysts is still unknown, certain materials could promote this dismutase

reaction in a beneficial way. Approach 3) is perhaps the simplest to test; by increasing the discharge current rate. However, selection of materials (electrolytes, electrodes, etc.) becomes important to enable such rate increases. This proof-of-concept utilized here with TiC electrodes shows that stable cycling can be obtained only when a stable electrolyte used in conjunction with an equally stable cathode material.[8] The above-mentioned physical properties of electrolytes (ionic conductivity, viscosity, and oxygen solubility) become critical in all cases.

In summary, we have clearly demonstrated that hydrogen abstraction from solvent molecules can be prevented with targeted organic chemistry design strategies, and this is critical to minimizing side reactions that lead to carbonate formation. Further work is required to obtain a completely stable system for the Li-O_2 battery to allow for extended cycling. We have shown a pathway forward in this aspect. The findings offer insights into the understanding of electrolyte stability and new opportunities in tailoring new electrolytes.

Chapter 8

Summary and Conclusions

In Chapter 3 of this thesis, a fundamental understanding of the discharge process in the battery (the oxygen reduction reaction or ORR) was presented. The effect of current density on the morphology and chemical nature of the discharge product (namely toroidal and thin-film morphologies of Li_2O_2) was discussed along with the related charging performance. Evidence from diffraction, electrochemical, FESEM and STEM measurements shows that slower current densities favor aggregation of lithium peroxide nanocrystallites nucleated *via* solution dismutase on the surface of the electrode; whereas fast rates deposit quasi-amorphous thin films. The latter provide a lower overpotential on charge due to their nature and close contact with the conductive electrode surface, albeit at the expense of lower discharge capacity.

The charge reaction (oxygen evolution or OER) was studied using *operando* X-ray diffraction, online electrochemical mass spectrometry, and scanning electron microscopy and the results were discussed in Chapter 4. Both electrochemically deposited Li_2O_2 (E-Li_2O_2) and commercial crystalline Li_2O_2 powder (C-Li_2O_2) were analyzed. For electrochemically formed Li_2O_2, a two-stage oxidation is proposed. At low potentials this involves the decay of amorphous Li_2O_2, whereas at higher potentials, crystalline Li_2O_2 is decomposed via a small actively transforming fraction that evolves oxygen via a Li deficient solid-solution reaction. This preferentially starts with the smallest crystallites. From refinement of the diffraction patterns, these crystallites possess a platelet

morphology, which stack together to form the observed toroid macrostructures. For bulk crystalline Li_2O_2 with an isotropic crystallite shape and larger crystallite dimensions, a single stage oxidation is observed. The observation of sub-stoichiometric $Li_{2-x}O_2$ at the early stage of oxidation and the gradual decreasing average crystallite size suggests that a small active fraction evolves oxygen via a Li deficient solid solution reaction. From ex situ SEM imaging throughout the charge process, the oxidation takes place at the outer (electrolyte-exposed) surface of the crystallites. However, in this case the oxidation process gradually consumes all of the C-Li_2O_2 crystallites, leading to a decrease in the average crystallite domain size. This study suggests that the conductivity of the Li_2O_2 plays a critical role in the charge efficiency and the observed overpotential. Increasing the conductivity of the formed Li_2O_2 during discharge will enhance the charge performance, as was shown in the case of the amorphous phase.

In Chapter 5, the charge reaction is isolated from the discharge by utilizing electrodes prefilled with commercial lithium peroxide with a crystallite size of about 200 - 800 nm. A combination of S/TEM, on-line mass spectrometry, XPS, and electrochemical methods was used to probe the nature of surface films on carbon and conductive Ti-based nanoparticles. It was shown that oxygen evolution from lithium peroxide is strongly dependent on their surface properties. Insulating TiO_2 surface layers on TiC and TiN - even as thin as 3 nm – can completely inhibit the charge reaction under these conditions. TiC which lacks this oxide film readily facilitates oxidation of the bulk Li_2O_2 crystallites, at a much lower overpotential relative to carbon. Since most materials are subject to some degree of oxidation, precise control of the surface chemistry at the nanoscale becomes of

upmost importance for Li-O_2 cathodes. It is expected that conductive oxides (in their highest oxidation state), or conductive materials which are thermodynamically stable with respect to oxidation will be beneficial in these systems.

The role that "electrocatalysts" play in the aprotic Li-O_2 battery and the mechanism(s) by which they function has been under much scrutiny. In Chapter 6, a lead ruthenium oxide with a pyrochlore structure proved to be a paramount catalyst for the oxygen reduction and evolution reactions (particularly OER) in alkaline aqueous media. This material was then utilized as a model catalyst for these same reactions in non-aqueous media with Li^+ cations present. It was found that, relative to carbon, the pyrochlore does have significant electrocatalytic properties, namely a lowering of the charging voltage. The main cause of this voltage shift is the ability of the metal oxide to completely oxidize side-products which are formed during discharge, by reaction between the superoxide (O_2^- /LiO_2) intermediate and the electrolyte solvent (tetraethylene glycol dimethyl ether, TEGDME). Carbon is unable to oxidize these side-products below the voltage at which electrolyte oxidation occurs. This further helps to explain the nature of "electrocatalysis" in the Li-O_2 battery.

In Chapter 7, a new lithium-ether-derived chelate ionic liquid was synthesized to serve as an electrolyte for the Li-O_2 battery. This complex is stable to metallic lithium, and its ethereal framework is much more inherently stable to superoxide-initiated hydrogen abstraction than monoglyme, 1,2-dimethoxyethane (DME). Reactions of chemically generated superoxide with this electrolyte show that virtually no decomposition products such as lithium formate are generated. When employed in a Li-O_2 battery, a ten-fold

decrease in CO_2 evolution is evident on charge by comparison to DME and greatly enhanced cycling stability was observed with TiC as a cathode support. A mechanism is proposed to account for the lowered reactivity, offering new insight into the stability of organic electrolytes in Li-O_2 batteries. This approach to electrolyte design can be extended to other organic systems to provide a platform for the design of advanced electrolyte systems.

Future work must always entail the examination of stability of all parts of the Li-O_2 battery. A practical battery will not be achievable if any of the battery components are subject to attack by superoxide or peroxide. Here, TiC was identified as a potential candidate as a positive electrode material. The synthesized electrolyte solvent, DMDMB, and the formed chelate ionic liquid electrolyte [$(DMDMB)_2$Li]TFSI shows promise, with enhanced stability towards hydrogen abstraction. However, the LiTFSI salt still poses a problem, with the formation of LiF. Synthesis of new salts should also be an avenue of future work. Tailoring the physical properties (ionic conductivity, viscosity, and oxygen solubility) of electrolytes is required.

Additionally, in attempt to increase the capacity, and thus the energy density, the solution pathway is desirable. This can be achieved with the addition of solubilising agents for O_2^- (such as TBA^+, other anion receptors or even H_2O). In this case, the lithium negative electrode will need to protected to confine the solution-phase O_2^- to the cathode side of the battery. Currently, a trade-off must be made between achieving high capacity and charge performance. Because good electrical conductivity of Li_2O_2 is crucial for lowering the charging voltage (via the surface $Li_{2-x}O_2$ pathway), amorphous or defective

Li_2O_2 is preferential for this purpose. However, the solution-mediated discharge pathway produces mainly platelet Li_2O_2 crystallites which are oxidized at a higher voltage. The use of solution phase redox mediators is another promising direction to charge the solid, insulating Li_2O_2 with ease.

Appendices

A1. Note on Current Rates and Capacities

Two units of current rate are often seen in the literature (mA/cm^2 and mA/g_{carbon}) for studies on Li-O_2 batteries. The first metric (mA/cm^2) depends on the electrochemical active surface area (EASA) of the cathode and the latter (mA/g_{carbon}) is highly dependent on the thickness of the oxygen electrode and the relative mass of other components of the electrode. The second has been adapted from other battery systems where the reactions involved are dependent on the bulk of the electrode material, such as intercalation compounds. In this thesis current rates based on the geometric surface area ($\mu A/cm^2$) have been used since the discharge and charging reactions of the Li-O_2 battery are surface reactions, yet the EASA is often very difficult to estimate. In this sense, the unit of $\mu A/cm^2_{geometric}$ is the best for reliable comparison of results with other studies. Likewise, the units of capacity in studies of the Li-O_2 cell are generally given as mAh/g_{carbon}. This again can give poor comparisons and lead to lack of reproducibility, since the electrochemical reactions occur on the surface. Many other factors such as pore size, thickness, mass and volume of all other components, diameter must all be known if units of mAh/g_{carbon} are to be used and quoted. Throughout this thesis, values of capacity based on geometric surface area (mAh/cm^2) were displayed as electrical charge transferred (mAh) since our electrodes all have a geometric surface area of 1 cm^2.

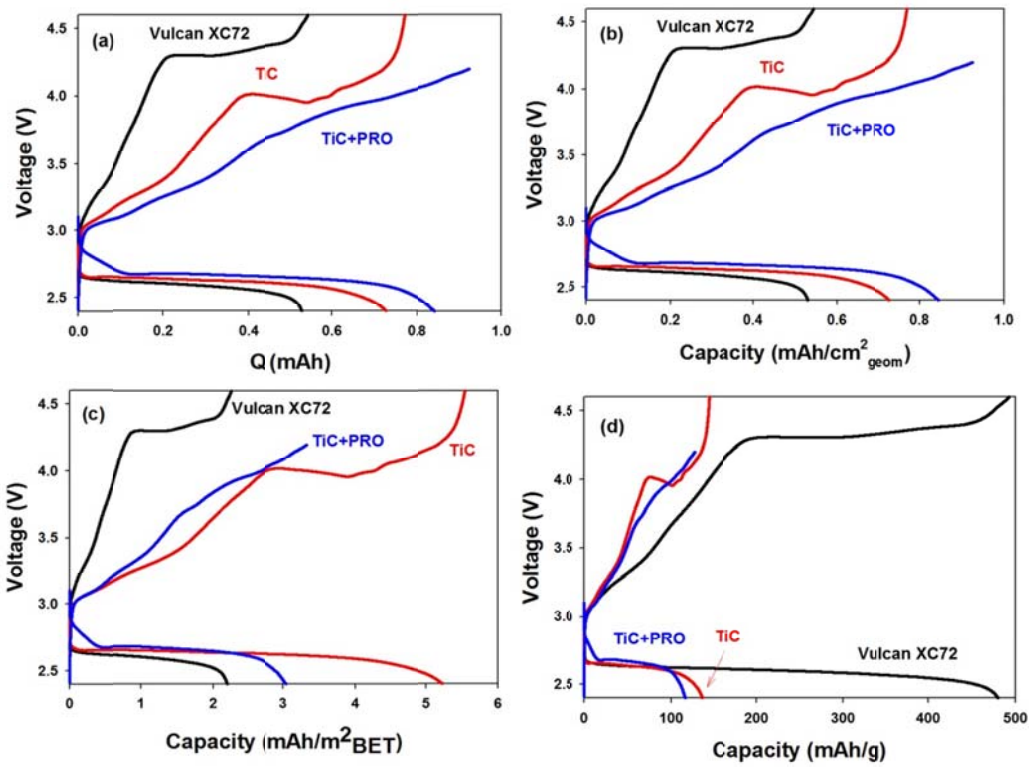

Figure A1.1 Voltage profiles for Vulcan XC72, TiC, and TiC+PRO electrodes for the first cycle in 1 M LiTFSI/TEGDME at a current density of 50 μA/$cm^2_{geometric}$. The capacities are plotted in the units of mAh (a), mAh/$cm^2_{geometric}$ (b), mAh/m^2_{BET}, and mAh/g (c).

Shown below (**Figure A1.1**) are the voltage profiles for the first cycle using three different electrode compositions. **Figure A1.1a** was previously presented in Chapter 6 as **Figure 6.9a**. As can be clearly seen, the units in (a) and (b) are identical. An estimate of the EASA was made using the calculated BET surface area of each material and its corresponding mass in the particular electrode cycled. Due to the much lower surface area of TiC (26 m^2/g) compared to Vulcan XC72 carbon (219 m^2/g), the capacity obtained in the units of mAh/m^2_{BET} in **Figure A1.1c** appear larger for TiC and TiC+PRO electrodes. It is possible that not all of the carbon surface area is accessible and electrochemically active

in the fabricated porous electrode. It should be noted, however, that the capacity for the Vulcan XC72 electrode presented here is quite similar to that in **Figure 3.2**. In the work of Peng *et al.*,[1] where nanoporous gold electrodes were used, capacities in the unit of mAh/g_{gold} were reported. Similarly, Thotiyl *et al.*[2] report capacities in the unit of mAh/g_{TiC} when TiC electrodes were used. Here, **Figure A1.1d** shows that the density of the material has a direct impact on the capacity when plotted as mAh/g. Although the mass of the electrode is important to obtain high gravimetric energy densities of Li-O_2 batteries, it is quite difficult to make direct comparisons of performance between different materials if these units are used, since the ORR and OER reactions all occur at the surface.

A2. Rotating Ring Disk Electrode Studies – Testing and Calibration of System Using Ferrocene

All potential scales in this thesis have been referenced to the Li/Li^+ couple. In most of the electrolytes used, lithium metal was used as the reference electrode. However, in studies where acetonitrile was used, the Ag/Ag^+ reference electrode was used since acetonitrile is not stable in the presence of lithium.[3] The Ag/Ag^+ scale was calibrated to Li/Li^+ using ferrocene. Ferrocene is commonly used as an internal standard, as suggested by IUPAC, because the potential of the Fc/Fc^+ redox couple is unaffected by the electrolyte and electrode material. Shown below in **Figure A2.1** are the cyclic voltammograms on a glassy carbon disk for the Fc/Fc^+ couple in 0.1 M $TBAPF_6$/MeCN (referenced to Ag/Ag^+) and 1 M $LiPF_6$/PC (referenced to Li/Li^+).

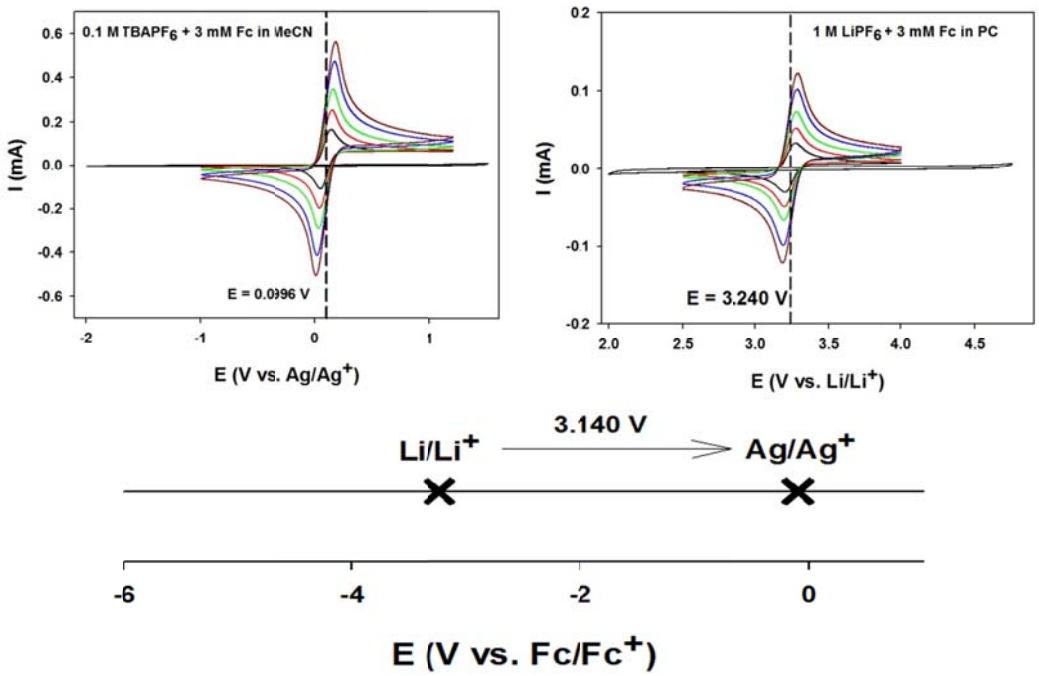

Figure A2.1 Cyclic voltammograms at various scan rates of ferrocene in 0.1 M $TBAPF_6$/MeCN using a Ag/Ag^+ reference electrode (top left) and in 1 M $LiPF_6$/PC using a Li/Li^+ reference electrode (top right). The calibration scale for the Fc/Fc^+ couple is shown at the bottom, which was used to plot all curves in this thesis with respect to the Li/Li^+ scale.

The Fc/Fc^+ couple was also used to test the rotating disk electrode (RDE) and rotating ring disk electrode (RRDE). In **Figure A2.2**, the linear voltammograms at various rotation rates are displayed for oxidation of ferrocene to the ferrocenium ion ($Fc \rightarrow Fc^+ + e^-$) along with the corresponding Levich plot. Using the Levich equation (2-1) and the kinematic viscosity of acetonitrile (4.37×10^{-3} cm^2 s^{-1})[4], the diffusion coefficient for ferrocene was calculated to be 2.8×10^{-5} cm^2 s^{-1}. This is quite close to the value of 2.4×10^{-5} cm^2 s^{-1} calculated by Kadish *et al.*[5]

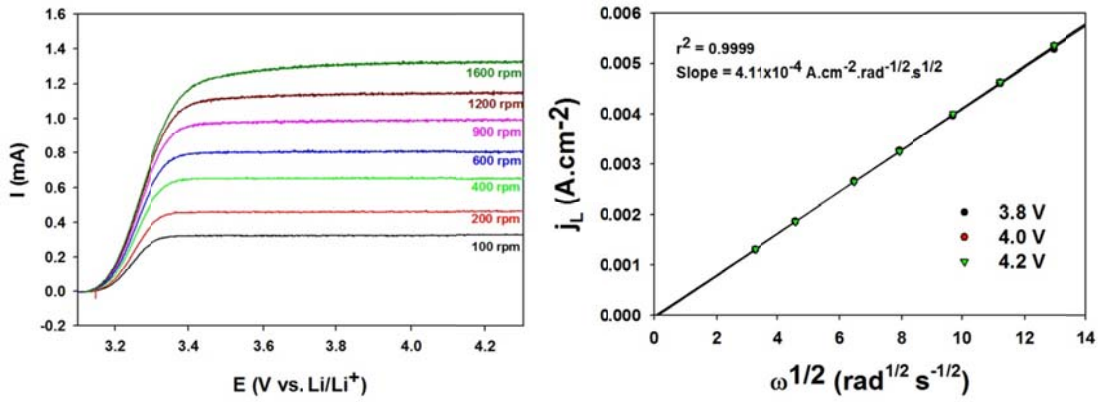

Figure A2.2 Linear sweep voltammograms at 5 mV/s for the oxidation of ferrocene in 0.1 M $TBAPF_6$/MeCN (left) on a glassy carbon rotating disk electrode. The corresponding Levich plot is displayed on the right.

The RRDE tip used in these studies has a rated collection efficiency of 37%. However, as shown in **Figure A2.3**, determined experimentally, the collection efficiency for the ferrocene/ferrocenium couple in acetonitrile was slightly higher. The average across the range of rotation rates was 42.4% and this value was used to normalize the ring current for all subsequent RRDE experiments for the detection of soluble superoxide.

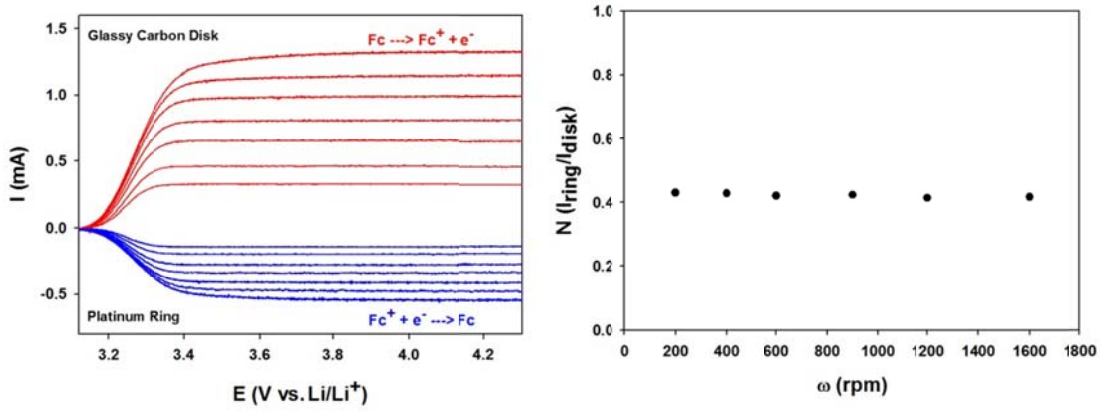

Figure A2.3 The rotating ring disk electrode analysis of the Fc/Fc^+ redox couple in 0.1 M TBAPF6/MeCN. Linear sweep voltammetry was performed at 5 mV/s on the glassy carbon disk and the platinum ring was held at a potential of 4.0 V vs. Li/Li^+. The experimental collection efficiency (I_{ring}/I_{disk}) for this redox couple is plotted on the right.

A3. Effect of Cation and Solvent on the ORR/OER Characteristics

Figure A3.1 displays the cyclic voltammograms for ORR/OER with Li^+ and TBA^+ in DME. When Li^+ is present (**Figures A3.1a,b**), the surface of glassy carbon is rapidly coated with the insoluble lithium oxides during oxygen reduction. When the upper voltage cutoff of 4.5 V is used (common for Li-O_2 batteries), a decay in the current is observed over the first 10 cycles (**Figure A3.1a**). However, when the upper voltage cutoff is increased to 4.7 V (**Figure A3.1b**), reversible cycling is obtained. This is clear evidence of passivation of the carbon surface by the discharge product(s), which are not fully oxidized by 4.5 V, yet can be fully removed by 4.7 V. Contrarily, when the cation is bulky (as TBA^+, **Figure A3.1c**), the ORR product is stabilized as soluble O_2^-. No passivation is observed even to the lower voltage cutoff of 3.75 V over ten cycles. The other distinctions

between Li^+ and TBA^+ are the much greater current densities for TBA^+ and the shift in potentials (**Figure A3.1d**). The 8-fold greater current density produced for the CVs with TBA^+ is clear evidence for a solution-based redox couple (O_2/O_2^-) vs. the surface-dominated process with Li^+. The current density can be correlated to the capacity of a battery system, which indicates that a solution-mediated process is necessary to achieve high discharge capacities in the Li-O_2 battery. The positive shift in potential for the reduction of O_2 when Li^+ is the active cation (relative to TBA^+) has been suggested to be analogous to the proton induced charge transfer in the aqueous system involving H_2O_2.[6] This suggests that LiO_2 is directly formed at the surface, rather than O_2^- and its subsequent combination with Li^+.

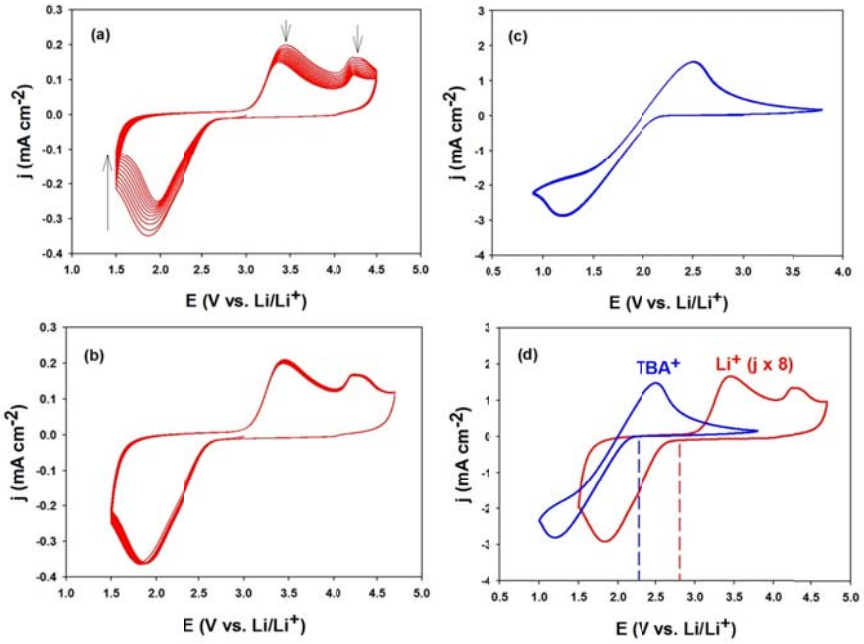

Figure A3.1 Cyclic voltammograms at a scan rate of 100 mV/s on a glassy carbon disk in 0.1 M LiTFSI/DME (a,b) and 0.1 M TBATFSI/DME (c). The first 10 cycles are displayed in (a,b,c). A comparison of the first cycle for Li^+ and TBA^+ is shown in (d).

A rotating ring disk electrode was used to probe the solubility of O_2^- or LiO_2. In **Figure A3.2a**, LiTFSI/DME was used as the electrolyte; linear sweep voltammetry was performed at the disk to reduce oxygen and the soluble LiO_2 was detected at the ring by holding the ring potential at 3.5 V vs. Li/Li^+. This potential was selected since no decomposition products are oxidized at this voltage, as shown in **Figure A3.1a/b**. Compared to the argon background, a defined reduction peak is observed at the disk (solid red voltammogram). No limiting current was observed due to the passivation of the electrode surface, as discussed above. Ring current is observed (dotted red curve), indicating a finite solubility of the LiO_2 intermediate. The I_{ring}/I_{disk} ratio is approximately 0.14, meaning that roughly 14% of the produced LiO_2 goes into solution. This fraction can undergo disproportionation in solution, as described in Chapter 3.

When TBATFSI/DME was used as the electrolyte (**Figure A3.2b**), the fraction of soluble O_2^- is roughly 48% at the initial stage of reduction, but appears to reach a limiting current. This is in accord with the work of Johnson *et al.*,[7] who recently proposed that a solution phase process occurs at higher potentials ($O_2 + e^- \rightarrow O_2^-$), followed by direct electron reduction at lower potentials ($O_2^- + e^- \rightarrow O_2^{2-}$). **Figure A3.3c** compares the relative I_{disk} and I_{ring} with Li^+ and TBA^+ on the same scale. Again, clearly the enhanced solubility of O_2^- with TBA^+ results in greater currents at both the disk and ring.

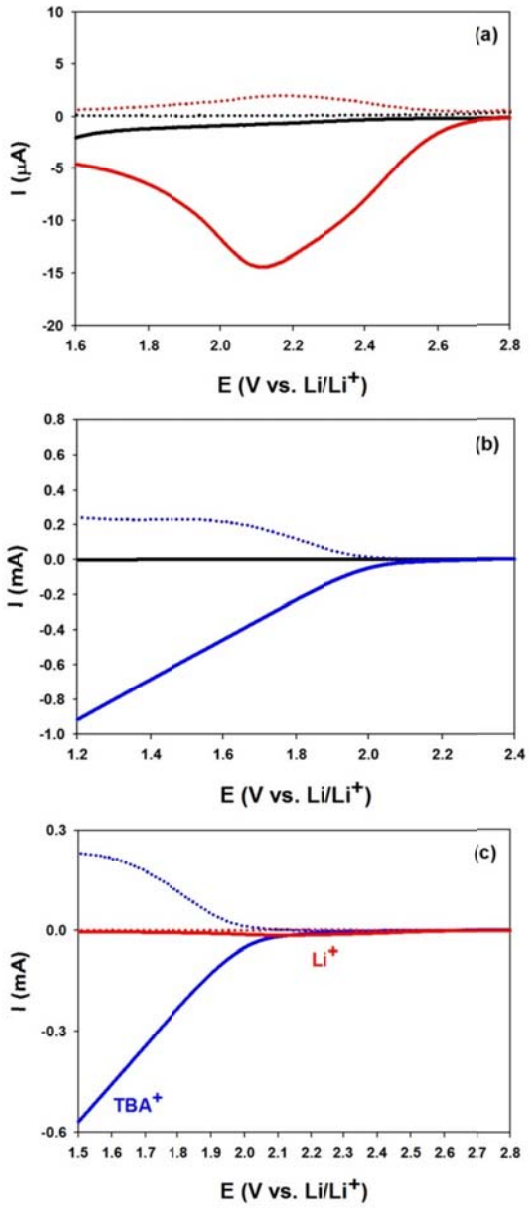

Figure A3.2 The rotating ring disk electrode analysis of superoxide solubility in 0.1 M LiTFSI/DME (a) and TBATFSI/DME (b) at 200 rpm. Linear sweep voltammetry was performed on the glassy carbon disk at 5 mV/s and the potential of the platinum ring was held at 3.5 V. A comparison of the disk/ring currents for Li^+ and TBA^+ is displayed in (c).

The solvent effect on the Li-O_2 battery system has been thoroughly examined in the past.[3,7] Here, a brief comparison between DME and MeCN has been made. In the earlier report,[3] the DME solvent, with an intermediate donor number (20.0), has a lower conductivity with Li^+ and TBA^+, but a relatively high oxygen solubility. The lower donor number MeCN solvent (14.1) possess very high ionic conductivity with both Li^+ and TBA^+ and also has a high oxygen solubility. Both solvents have a very low viscosity. MeCN has the advantage of having an extremely high anodic stability beyond 5 V vs. Li/Li^+ (**Figure A3.3a**), but unfortunately, it cannot be used directly in the Li-O_2 battery because it is reduced by metallic lithium. It can be seen from **Figure A3.3a** and **A3.3b**, with Li^+ and TBA^+ respectively, that the kinetics for ORR/OER are much greater in MeCN than DME. This is most likely due to the approximate 10-fold higher ionic conductivity in this solvent (1.42 mS cm^{-1} for DME and 10.85 mS cm^{-1} for MeCN with TBA^+).3 Also notable is the decreased decomposition in MeCN compared to DME when Li^+ is present. This is observed by the decrease in intensity of high voltage oxidation peaks in **Figure A3.3a**. The stability of MeCN with respect to nucleophillic attack by LiO_2/Li_2O_2 has also been previously suggested.[8]

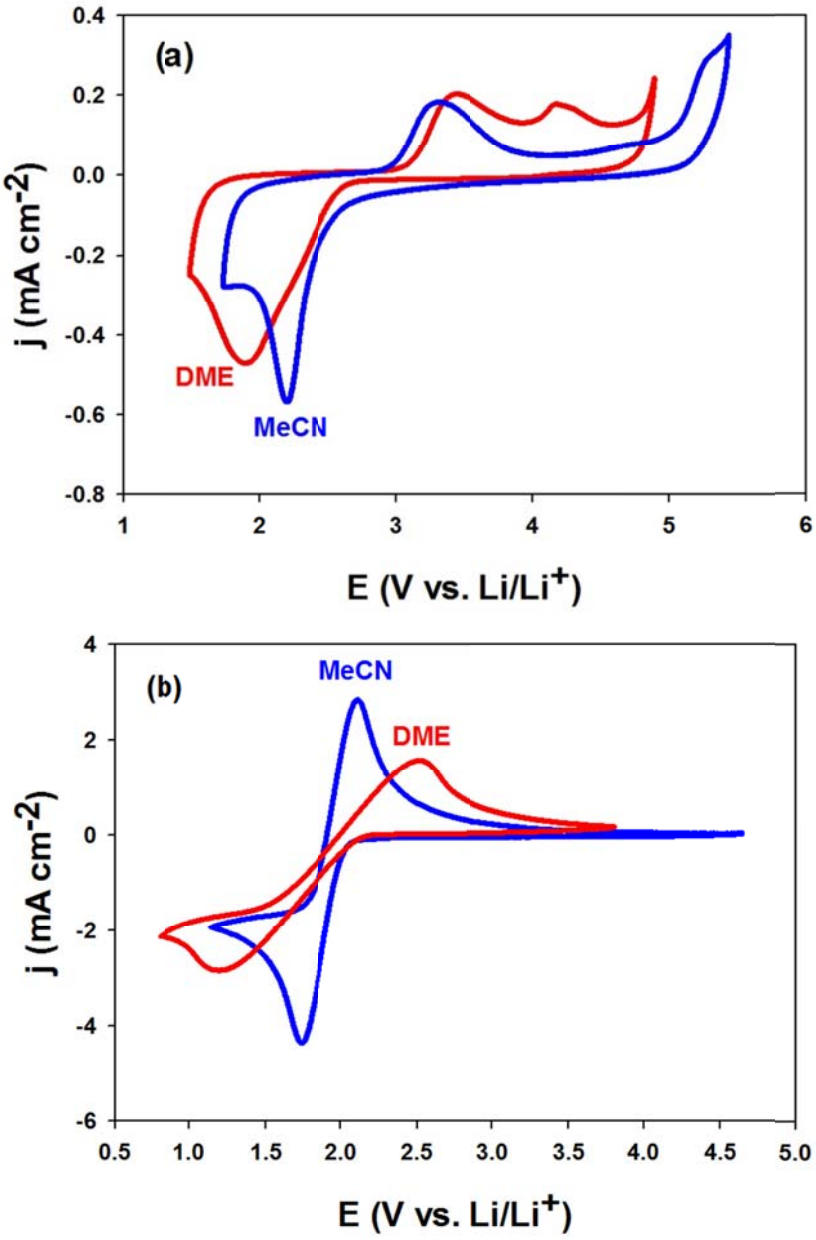

Figure A3.3 Cyclic voltammograms at a scan rate of 100 mV/s on a glassy carbon disk with 0.1 M LiTFSI in DME and 0.1 M $LiPF_6$ in MeCN (a) and 0.1 M TBATFSI in DME and 0.1 M $TBAPF_6$ in MeCN (b).

As a comparison to DME, the solubility of LiO_2 was probed in MeCN using the RRDE (**Figure A3.4**). Very different behaviour was observed. The lack of any ring current proves that LiO_2 has zero solubility in MeCN. This was also previously reported, and explained based on its low donor number.[7]

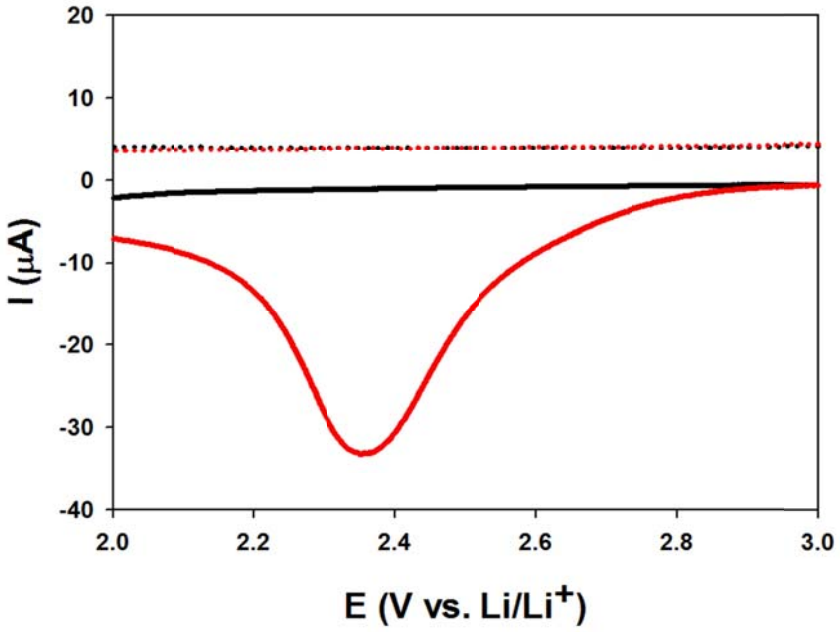

Figure A3.4 The rotating ring disk electrode analysis of superoxide solubility in 0.1 M LiTFSI/MeCN at 200 rpm. Linear sweep voltammetry was performed on the glassy carbon disk at 5 mV/s and the potential of the platinum ring was held at 3.5 V.

Due to the enhanced kinetics of ORR/OER in MeCN relative to DME (**Figure A3.3b**), these reactions were more carefully examined in the absence of Li^+, where the solution phase process allows for simplified analysis of the involved electrochemistry. **Figure A3.5** shows the CVs for ORR/OER in 0.1 M $LiPF_6$/MeCN. When the cathodic voltage cut-off is > 1V vs. Li/Li^+, the simple, reversible O_2/O_2^- couple (1 e^- process) is observed. This scenario is displayed in by the red curve. The second electron reduction of O_2^- to O_2^{2-} begins around 0.5 V vs. Li/Li^+ (blue CV). During the anodic sweep, a decrease in the area of the oxidation peak for $O_2^- \rightarrow O_2 + e^-$ is observed. This is proportional to the amount of O_2^- which was further reduced to O_2^{2-} during the cathodic sweep. The additional peaks observed above 2.5 V vs. Li/Li^+ arise from the oxidation of the O_2^{2-} species. This occurs in three steps. It is suspected that the reactions are as follows: 1) $O_2^{2-} \rightarrow O_2^- + e^-$, 2) $O_2^- \rightarrow O_2 + e^-$, and 3) is the oxidation of some decomposition product(s).[9] One thing is clear; the oxidation of the soluble peroxide species occurs in multiple steps, rather than a direct 2 e^- transfer. It is unknown; however, why step 2) doesn't happen simultaneously with step 1), since the O_2^- species is thermodynamically unstable at this potential (ie. the oxidation peak for the reversible O_2/O_2^- couple is below that of peaks for O_2^{2-}). Another possible scenario is that the observed oxidation peaks are identical to those proposed by Ernst *et al.* in the presence of weak acids.[9] Even trace amounts of water in the system can serve as the proton source. In this scenerio, upon reduction, the low voltage reduction peak is not a result of $O_2^- + e^- \rightarrow O_2^{2-}$, but rather $O_2^- + H^+ + e^- \rightarrow HO_2^-$. During oxidation, the reaction in step 1) would be $HO_2^- \rightarrow e^- + HO_2$ and step 2) would be $HO_2 \rightarrow e^- + H^+ + O_2$.

Step 3) is still anticipated to arise from the oxidation of a decomposition product, which must be a result of deprotonation of MeCN by the HO_2^- or O_2^{2-} species.[9]

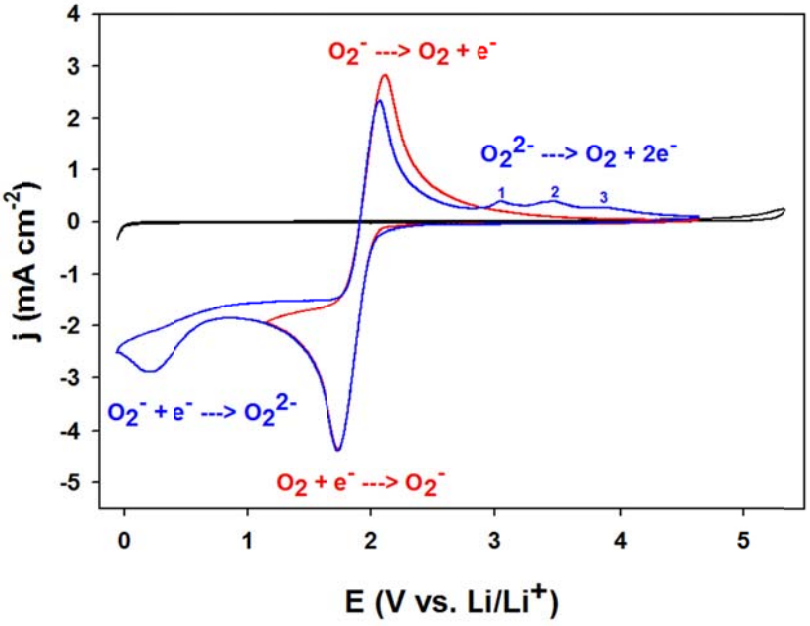

Figure A3.5 Cyclic voltammograms at a scan rate of 100 mV/s on a glassy carbon disk in 0.1 M $TBAPF_6$/MeCN. The black curve was done under an argon atmosphere and the red and blue curves were done in oxygen-saturated electrolyte.

The ORR was examined in MeCN (with TBA^+) using the rotating disk electrode (RDE). In **Figure A3.6**, the linear sweep voltammograms at various rotation rates are displayed for the reduction of oxygen along with the corresponding Levich plot. The parameters are well established for oxygen in acetonitrile. The kinematic viscosity of acetonitrile (4.37×10^{-3} cm^2 s^{-1})[4], the solubility of oxygen in acetontrile (8.1×10^{-6} mol cm^{-3}) [3], and the diffusion coefficient for oxygen in acetonitrile (4.64×10^{-5} cm^2 s^{-1})[10] were used in the Levich equation (2-1). The number of electrons transferred for the reduction of

oxygen with TBA^+ was calculated to be 1.2. This confirms the first step in the ORR process to be the 1 e^- reduction of O_2 to O_2^-.

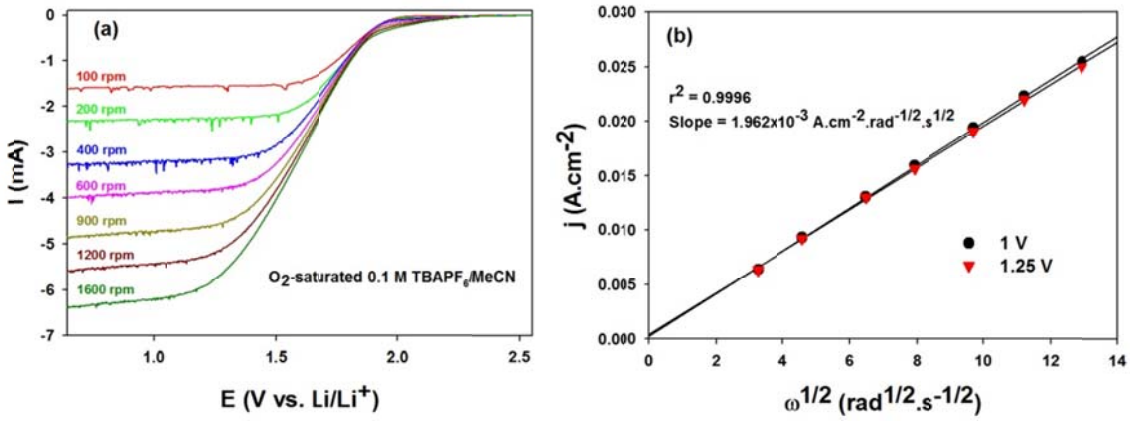

Figure A3.6 Linear sweep voltammograms at 5 mV/s for the reduction of oxygen in 0.1 M $TBAPF_6$/MeCN (left) on a glassy carbon rotating disk electrode. The corresponding Levich plot is displayed on the right.

A4. Detailed Synthesis and Characterization of DMDMB

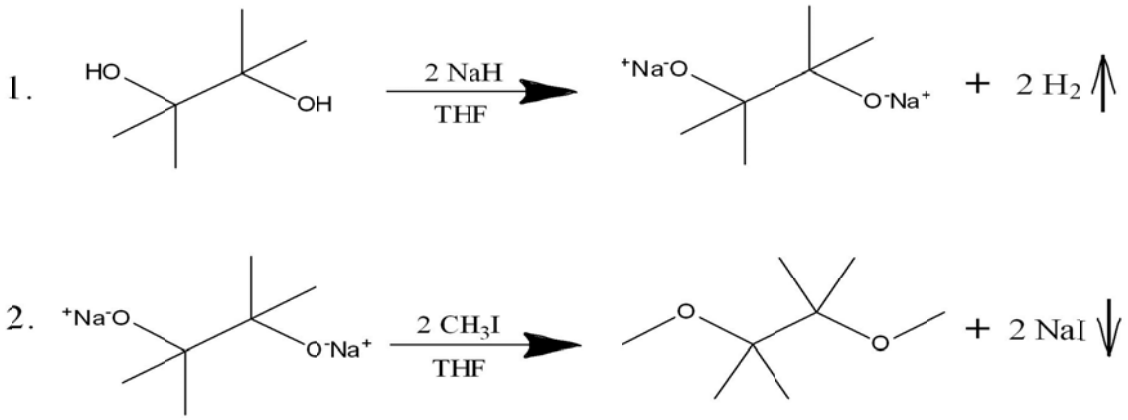

Figure A4.1 Scheme for the synthesis of DMDMB.

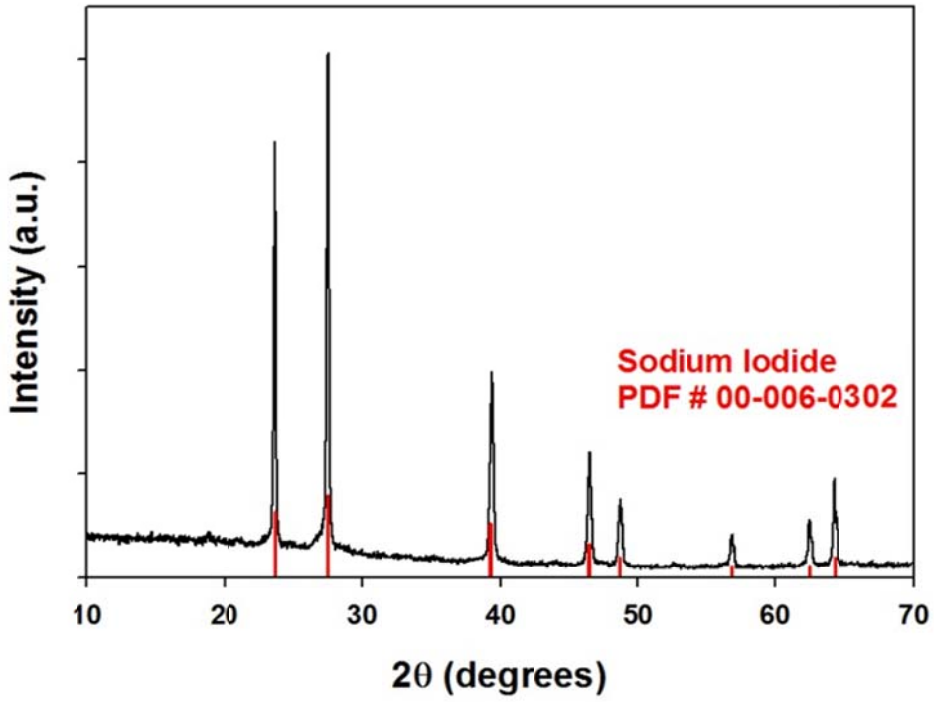

Figure A4.2 The powder X-ray diffraction pattern for the solid precipitate formed during the synthesis of DMDMB.

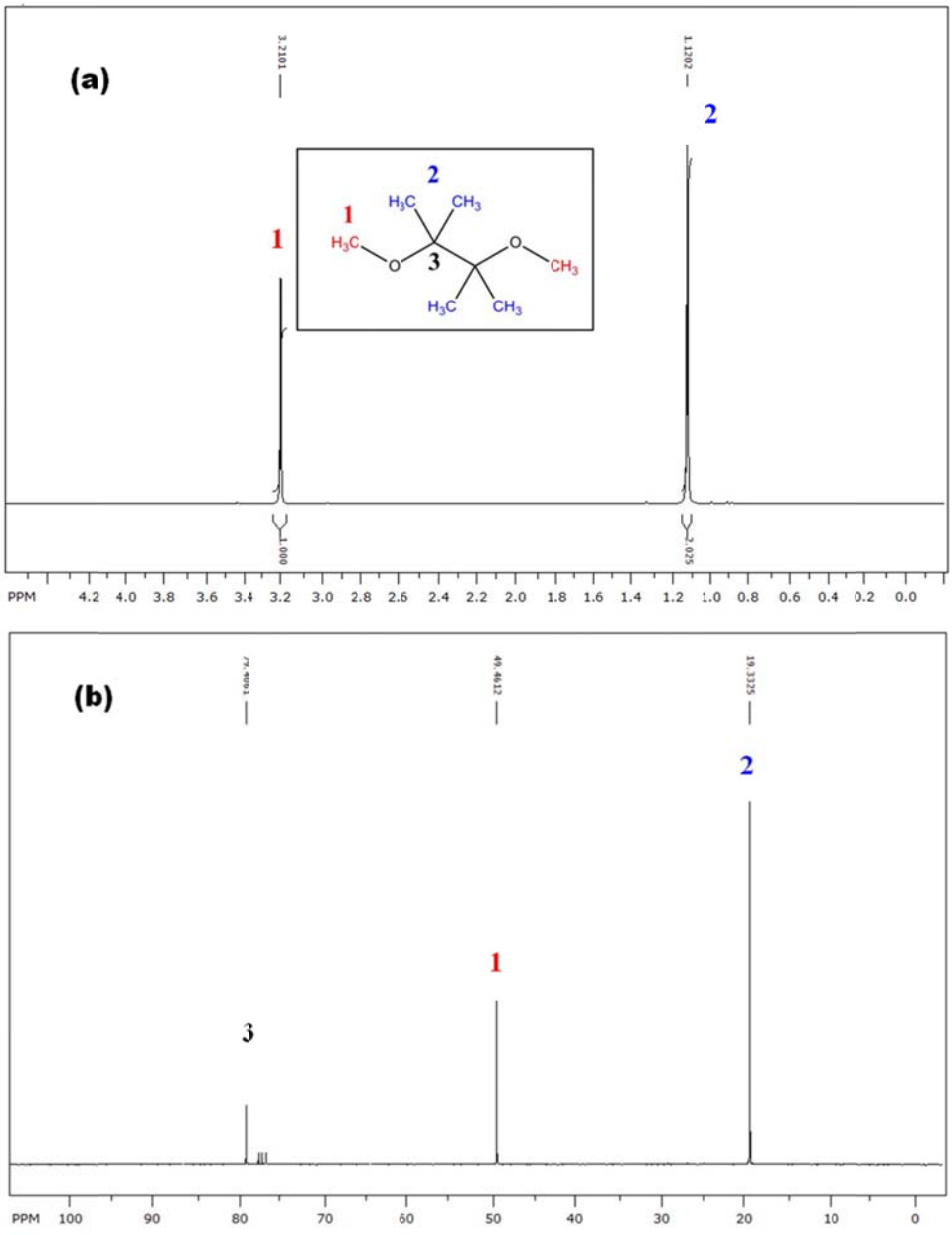

Figure A4.3 (a) ^{1}H-NMR and (b) ^{13}C-NMR spectra of purified DMDMB solvent.

The ^{1}H spectrum shows two peaks with an integrated ratio of 1:2, in full accord with the structure of DMDMB. The peak at 3.21 ppm arises from the 6 equivalent protons of the terminal methyl groups (α) which replaced the hydroxyl protons of the pinacol molecule during the synthesis. The peak at 1.12 ppm is characteristic of the 12 protons of the methyl groups on the internal carbons (β and γ) which is also present in the pinacol starting material. The ^{13}C spectrum indicates the three types of carbon atoms in the DMDMB structure. The peak at 79.40 ppm is due to the two saturated carbons on the backbone between the two oxygen atoms. The peak at 49.46 ppm is the signature of the two carbons of terminal methyl groups. The peak at 19.33 ppm arises from the four "protecting" methyl carbons.

A5. Detection of LiF in Discharged Cathodes

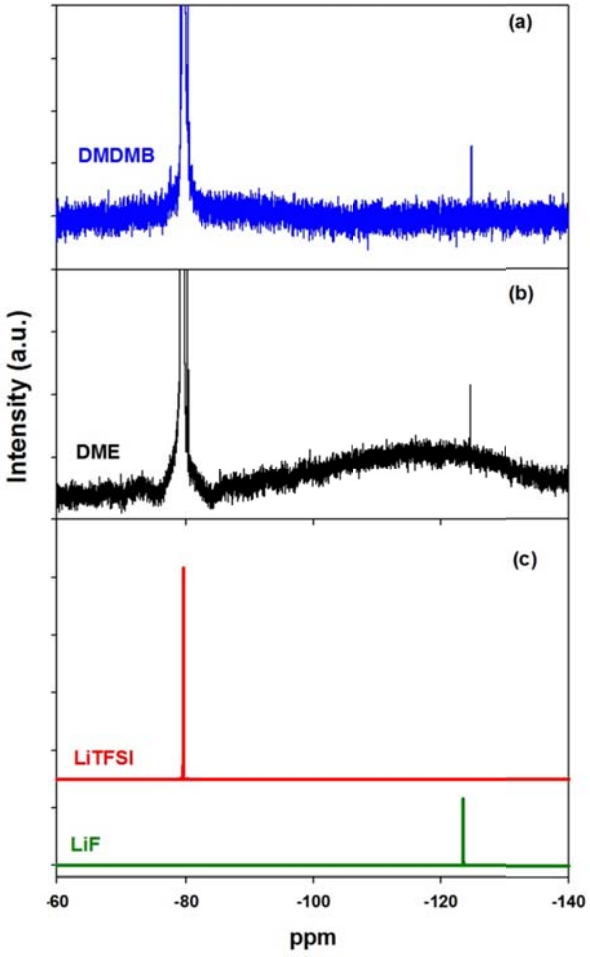

Figure A5.1 The ^{19}F-NMR spectra of side-products deposited on P50 carbon paper cathodes after 1st discharge in (a) [$(DMDMB)_2Li$]TFSI and (b) [$(DME)_2Li$]TFSI. Multiple cells were discharged at 25 μA/cm^2 such that the total discharge capacity in each electrolyte was equal to 1.5 mAh. The cathodes were soaked in D_2O to dissolve any LiF and the ^{19}F-NMR was performed on the D_2O solution. The reference spectra for LiTFSI and LiF in D_2O are displayed in (c). P50 carbon paper electrodes were used in this study to avoid the interference of fluorine from PTFE binder.

A6. Synthesis of Tetraethylene Glycol Di(trimethylsilyl) Ether and its use as an electrolyte solvent

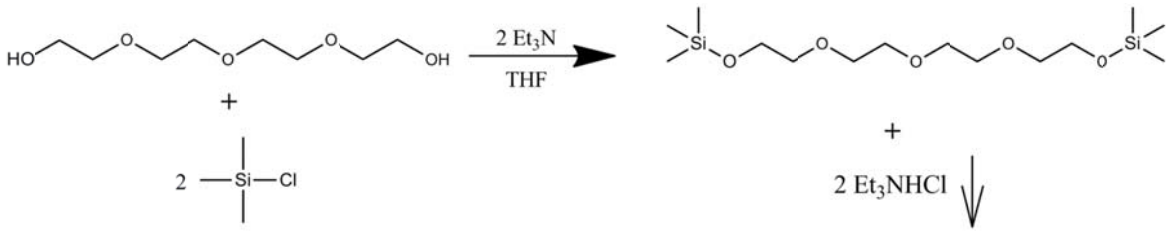

Figure A6.1 Scheme for the synthesis of 2NM4.

To examine the effect of protecting the α-hydrogen atoms of glyme molecules from abstraction by superoxide (as opposed to the protection of the β-hydrogen atoms in Chapter 7), 2NM4 was synthesized (**Figure A6.1**) and purified by vacuum distillation (**Figure A6.2**).[11] In this molecule, the terminal methyl groups of TEGDME were replaced by inert trimethyl silyl groups.

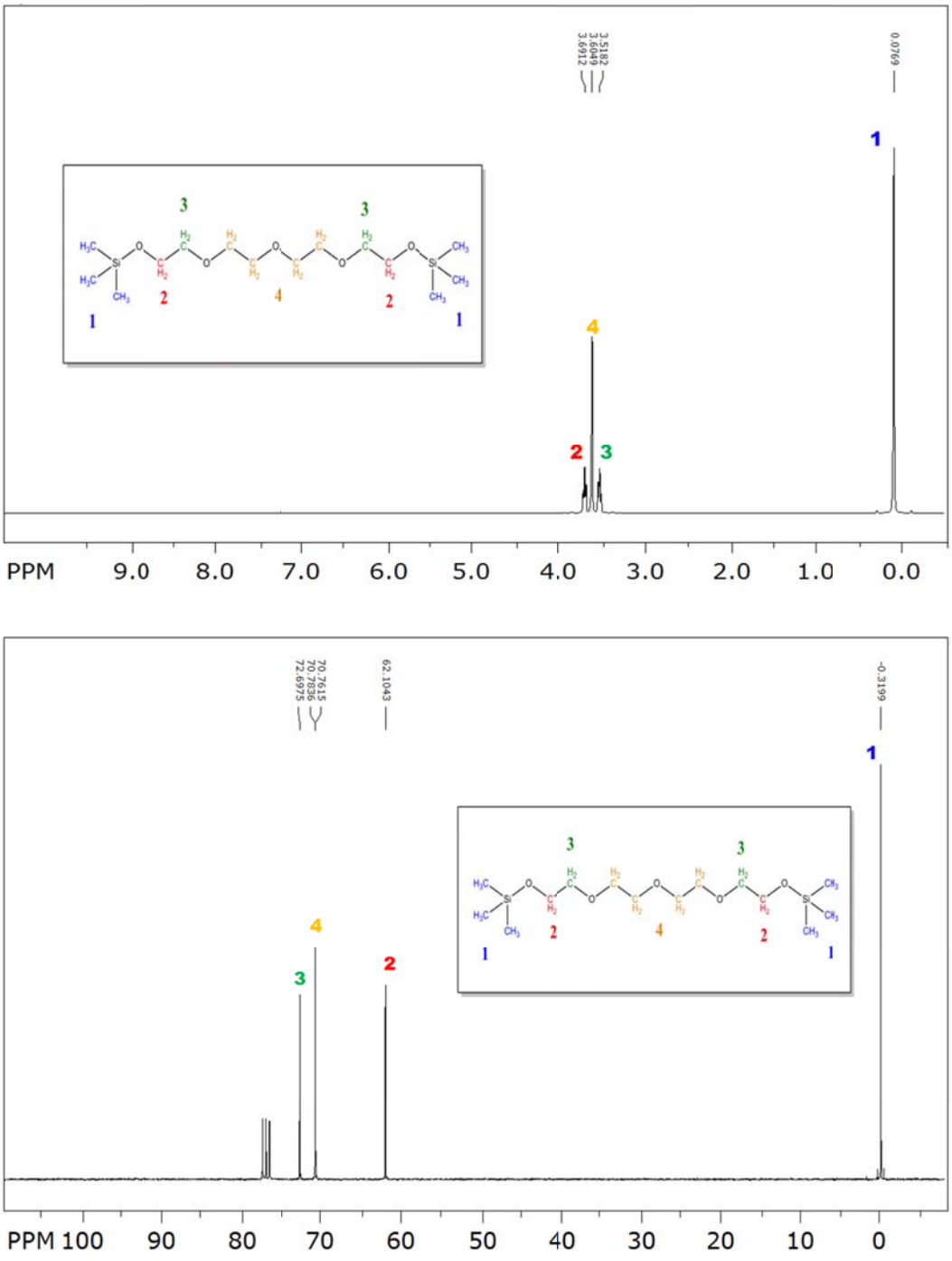

Figure A6.2 The ^{1}H-NMR (top) and ^{13}C-NMR (bottom) spectra for purified 2NM4 solvent.

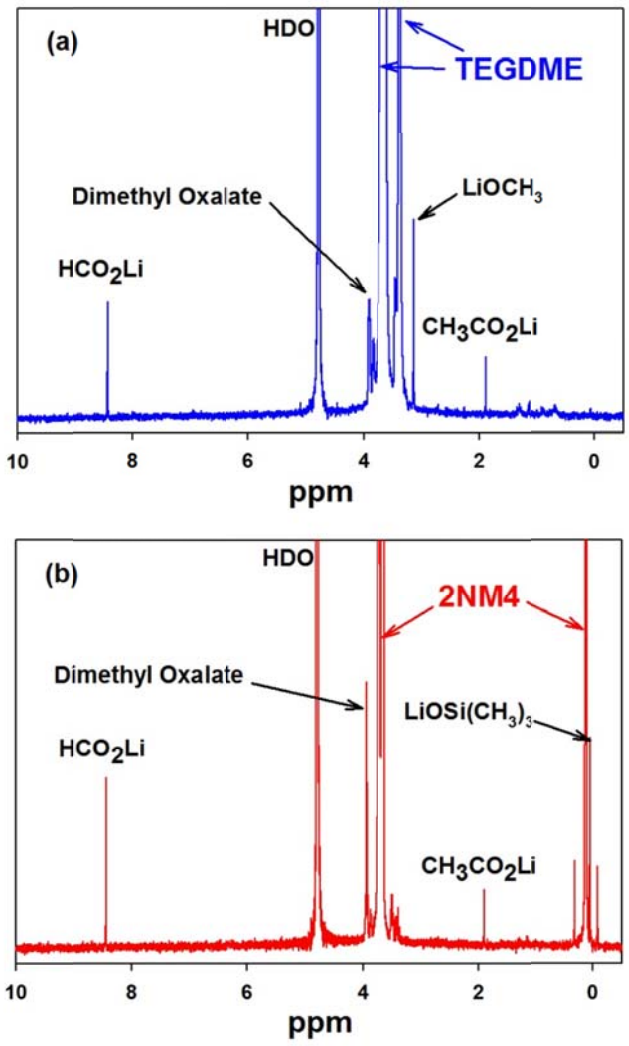

Figure A6.3 The ^{1}H-NMR spectra of side-products deposited on cathodes after 1st discharge in (a) 1 M LiTFSI/TEGDME and (b) **1** M LiTFSI/2NM4. The cells were both discharged at 25 μA/cm^2 to a capacity cut-off of 1 mAh. The HDO peak (δ = 4.78 ppm) and the corresponding residual solvents are visible in both spectra. Substantial decomposition products were detected in both cases: lithium formate (δ = 8.46 ppm),

dimethyl oxalate (δ = 3.92 ppm), lithium acetate (δ = 1.89 ppm), lithium methoxide (from TEGDME, δ = 3.33 ppm), and lithium trimethylsilanolate (from 2NM4, δ = 0.05 ppm).

In **Figure A6.3**, the ^{1}H-NMR spectra for the side-products contained in carbon cathodes discharged in TEGDME (**Figure A6.3a)** and 2NM4 (**Figure A6.3b)** are displayed. The cathodes were soaked in 0.7 mL of D_2O for 24 hours to dissolve the decomposition side-products and the ^{1}H-NMR was performed on this liquid. Clearly, the terminal protecting groups had minimal effect, as substantial amounts of lithium formate, lithium acetate, dimethyl oxalate were identified from both solvents. Noteworthy, is that lithium acetate was never observed for DME (in Chapter 7), so this product obviously only forms from cleavage of the glyme backbone chain when n>1 in $CH_3O(CH_2CH_2O)_nCH_3$. The structure of TEGDME is $CH_3O(CH_2CH_2O)_4CH_3$ and the structure of 2NM4 is $(CH_3)_3SiO(CH_2CH_2O)_4Si(CH_3)_3$. Lithium methoxide and lithium trimethylsilanolate also form in TEGDME and 2NM4, respectively, as a result of the longer chain lengths (n=4). Overall, protection of the terminal methyl groups in glyme molecules is deemed to be unsuitable for enhancing their stability with respect to superoxide attack. The decomposition pathways 1 and 2, as presented in **Figure 7.14** were confirmed to be dominant for both TEGDME and 2NM4, in contrast to pathway 3. This study presents further proof that the terminal methyl groups in glyme molecules are much more resistant than the backbone methylene groups to hydrogen abstraction by superoxide.

References

Chapter 1 References

[1] R. Black, B. Adams, L. F. Nazar, *Adv. Energy Mater*. **2012**, *2*, 801.

[2] J. Lu, L. Li, J.-B. Park, Y.-K. Sun, F. Wu, K. Amine, *Chem. Rev.* **2014**, *114*, 5611.

[3] Y.-C. Lu, B. M. Gallant, D. G. Kwabi, J. R. Harding, R. R. Mitchell, M. S. Whittingham, Y. Shao-Horn, *Energy Environ. Sci.* **2013**, *6*, 750.

[4] H.-G. Jung, Y. S. Jeong, J.-B. Park, Y.-K. Sun, B. Scrosati, Y.-J. Lee, *ACS Nano*, **2013**, *7*, 3532.

[5] J. Read, K. Mutolo, M. Ervin, W. Behl, J. Wolfenstine, A. Driedger, D. Foster, *J. Electrochem. Soc.* **2003**, *150*, A1351.

[6] A. Debart, A. J. Paterson, J. Bao, P.G. Bruce, *Angew. Chem. Int. Ed,* **2008**, *47*, 4521.

[7] C. O Laoire, S. Mukerjee, K. M. Abraham, *J. Phys. Chem. C* **2009**, *113*, 20127.

[8] Y. C. Lu, H. Gasteiger, M. Parent, V. Chiloyan, Y. Shao-Horn, *Electrochem Solid State Lett.* **2010**, *13*, A69.

[9] J. Zhang, W. Xu, X. Li, W. Liu, *J. Electrochem. Soc.* **2010**, *157*, A940.

[10] L. Trahey, C. S. Johnson, J. T. Vaughey, S.-H. Kang, L. J. Hardwick, S. A. Freunberger, P. G. Bruce, M. M. Thackeray, *Electrochem. Solid-St. Lett*. **2011**, *14*, A64.

[11] J.-S. Lee, S. T. Kim, R. Cao, N.-S. Choi, M. Liu, K. T. Lee, J. Cho, *Adv. Energy Mater.* **2011**, *1*, 34.

[12] G. Girishkumar, B. McCloskey, A. C. Luntz, S. Swanson, W. Wilcke, *J. Phys. Chem. Lett*. **2010**, *1*, 2193.

[13] K. M. Abraham, Z. Jiang, *J. Electrochem. Soc.* **1996**, *143*, 1.

[14] T. Ogasawara, A. Debart, M. Holzapfel, P. Novak, P. G. Bruce, *J. Am. Chem. Soc.* **2006**, *128*, 1390.

[15] B. D. McCloskey, D. S. Bethune, R. M. Shelby, G. Girishkumar, A. C. Luntz, *J. Phys. Chem. Lett.* **2011**, *2*, 1161.

[16] S. D. Beattie, D. M. Manolescu, S. L. Blair, *J. Electrochem. Soc.* **2009**, *156*, A44.

[17] C. O. Laoire, S. Mukerjee, E. Plichta, M. A. Hendrickson, K. M. Abraham, *J. Electrochem. Soc.* **2011**, *158*, A302.

[18] B. D. McCloskey, R. Scheffler, A. Speidel, D. S. Bethune, R. M. Shelby, A. C. Luntz, *J. Am. Chem. Soc*. **2011**, *133*, 18038.

[19] C. O. Laoire, S. Mukerjee, E. Plichta, M. A. Hendrickson, K. M. Abraham, *J. Phys. Chem. C*, **2010**, *114*, 9178.

[20] F. Mizuno, S. Nakanishi, Y. Kotani, S. Yokoishi, H. Iba, *Electrochemistry* **2010**, *78*, 403.

[21] S. Freunberger, Y. Chen, Z. Peng, J. Griffin, L. Hardwick, F. Barde, P. Novak, P.G. Bruce, *J. Am. Chem. Soc.* **2011**, *133*, 8040.

[22] G. Y. Aleshin, D. A. Semenenko, A. I. Belova, T. K. Zakharchenko, D. M. Itkis, E. A. Goodilin, Y. D. Tretyakov, *Solid State Ionics* **2011**, *184*, 62.

[23] R. Mitchell, B. Gallant, C. Thompson, Y. Shao-Horn, *Energy Environ. Sci.* **2011**, *4*, 2952.

[24] J. Xiao, D. Mei, X. Li, W. Xu, D. Wang, G. Graff, W. Bennett, Z. Nie, L. Saraf, I. Aksay, J. Liu, J. G. Zhang, *Nano Lett.* **2011**, *11*, 5071.

[25] Z. Peng, S. A. Freunberger, L. J. Hardwick, Y. Chen, V. Giordani, F. Bardé, P. Novák, D. Graham, J.-M. Tarascon, P. G. Bruce, *Angew. Chem. Int. Ed.* **2011**, *50*, 6351.

[26] Y. Mo, S. P. Ong, and G. Ceder, *Phys. Rev. B,* **2011**, *84*, 205446.

[27] R. Padbury, X. Zhang, *J. Power Sources*, **2011**, *196*, 4436.

[28] S. Zhang, D. Foster, J. Read, *J. Power Sources*, **2010**, *195*, 1235.

[29] P. Albertus, G. Girishkumar, B. McCloskey, R. S. Sanchez-Carrera, B. Kozinsky, J. Christiansen, A. C. Luntz, *J. Electrochem. Soc.* **2011**, *158*, A343.

[30] V. Viswanathan, K. S. Thygesen, J. S. Hummelshøj, J. K. Nørskov, G. Girishkumar, B. D. McCloskey, A. C. Luntz, *J. Chem. Phys.* **2011**, *135*, 214704.

[31] J. Højberg, B. D. McCloskey, J. Hjelm, T. Vegge, K. Johansen, P. Norby, A. C. Luntz, *ACS Appl. Mat. Interfaces*. **2015**, *7*, 4039.

[32] X. H. Yang, Y. Y. Xia, *Solid State Electrochem*, **2010**, *14*, 109.

[33] B. Viswanathan, C. V. Rao, U. V. Varadaraju, in *Photo/Electrochemistry & Photobiology in the Environment, Energy and Fuel*, 1st Edition (Eds.: S. Kaneco, K. Funasaka, B. Viswanathan), Research Signpost **2006**, Ch. 2, 43-101.

[34] F. Cheng, Y. Su, J. Liang, Z. Tao, J. Chen, *Chem. Mater.* **2010**, *22*, 898.

[35] R. Bashyam, P. Zelenay, *Nature* **2006**, *443*, 63.

[36] S. Maldonado, K. J. Stevenson, *J. Phys. Chem. B* **2005,** *109*, 4707.

[37] D. Geng, Y. Chen, Y. Chen, Y. Li, R. Li, X. Sun, S. Yeb, S. Knights, *Energy Environ. Sci.* **2011**, *4*, 760.

[38] J. D. Wiggins-Camacho, K. J. Stevenson, *J. Phys. Chem. C* **2011**, *115*, 20002.

[39] D. Vasudevan, H. Wendt, *J. Electroanal. Chem.* **1995**, *192*, 69.

[40] D. T. Sawyer, G. Chlerlcato, Jr., C. T. Angells, E. J. Nannl, Jr., T. Tsuchlya, *Anal. Chem.* **1982**, *54,* 1720.

[41] H. Cheng, K. Scott, *J. Power Sources*, **2010**, *195*, 1370.

[42] H. Cheng, K. Scott, *App. Cat. B*, **2011**, *108-109*, 140.

[43] Y. C. Lu, Z. C. Xu, H. Gasteiger, S. Chen, K. Hamad-Schifferli, Y. Shao-Horn, *J. Amer. Chem. Soc.* **2010**, *132*, 12170.

[44] D. Aurbach, M. Daroux, P. Faguy, E. Yeager, *J. Electroanal. Chem.* **1991**, *297*, 225.

[45] R. Black, J. H. Lee, B. Adams, C. Mims, L. F. Nazar, *Angew. Chemie - Int. Ed.* **2013**, *52*, 392.

[46] S. W. Lee, B. M. Gallant, Y. Lee, N. Yoshida, D. Y. Kim, Y. Yamada, S. Noda, A. Yamada, Y. Shao-Horn, Y. *Energy Environ. Sci.* **2012**, *5*, 5437.

[47] G. Q. Zhang, J. P. Zheng, R. Liang, C. Zhang, B. Wang, M. Hendrickson, E. J. Plichta, *J. Electrochem. Soc.* **2010**, *157*, A953.

[48] E. Yoo, H. Zhou, *ACS Nano*, **2011**, *5*, 3020.

[49] M. Radin, J. Rodriguez, F. Tian, D. Siegel, *J. Amer. Chem. Soc*, **2012**, 134, 1093.

[50] M. M. O. Thotiyl, S. Freunberger, Z. Peng, P. G. Bruce, *J. Am. Chem. Soc.* **2013**, *135*, 494.

[51] D. M. Itkis, D. Semenenko, E. Y. Kataev, A. I. Belova, V. S. Neudachina, A. P. Sirotina, M. Hävecker, D. Teschner, A. Knop-Gericke, P. Dudin, A. Barinov, E. A. Goodilin, Y. Shao-Horn, L. V. Yashina, *Nano Lett.* **2013**, *13*, 4697.

[52] H. Kim, J. Park, *J. Mater. Chem. A* **2014**, *2*, 11891.

[53] A. Riaz, K.-N. Jung, W. Chang, K.-H. Shin, J.-W. Lee, *ACS Appl. Mater. Interfaces* **2014**, *6*,17815.

[54] Y. Cui, Z. Wen, Y. Liu, *Energy Environ. Sci.* **2011**, *4*, 4727.

[55] J. Cao, S. Liu, J. Xie, S. Zhang, G. Cao, X. Zhao, *ACS Catal.* **2015**, *5*, 241.

[56] M. M. O. Thotiyl, S. A. Freunberger, Z. Peng, Y. Chen, Z. Liu, P. G. Bruce, *Nat. Mater.* **2013**, *12*, 1050.

[57] J. Lu, Y. Lei, K. C. Lau, X. Luo, P. Du, J. Wen, R. S. Assary, U. Das, D. J. Miller, J. W. Elam, H. M. Albishri, D. A. El-Hady, Y.-K. Sun, L. A. Curtiss, K. Amine, *Nat. Commun.* **2013**, *4*, 2383.

[58] Z. Peng, S. A. Freunberger, Y. Chen, P. G. Bruce, *Science* **2012**, *337*, 563.

[59] D. T. Sawyer, J. S. Valentine, *Acc. Chem. Res.* **1981**, *14*, 393.

[60] R. Black, S. Oh, T. Yim, J.H. Lee, B. Adams, L. F. Nazar, *J. Am. Chem. Soc*. **2012**, *134*, 2902.

[61] V. S. Bryantsev and M. Blanco, *J. Phys. Chem. Lett.*, **2011**, *2*, 379.

[62] R. S. Assary, L. A. Curtiss, P. C. Redfern, Z. Zhang, and K. Amine, *J. Phys. Chem. C*, **2011**, *115*, 12216.

[63] S. A. Freunberger, Y. Chen, N. E. Drewett, L. J. Hardwick, F. Bardé, P. G. Bruce, *Angew. Chem. Int. Ed.* **2011**, *50*, 1.

[64] J. Read, *J. Electrochem. Soc.* **2002**, *9*, A1190.

[65] A. Kraytsberg, Y. Ein-Eli, *J. Power Sources*, **2011**, *196*, 886.

[66] T. Kuboki, T. Okuyama, T. Ohsaki, N. Takami, *J. Power Sources*, **2005**, *146*, 766.

[67] F. Mizuno, S. Nakanishi, A. Shirasawa, K. Takechi, T. Shiga, H. Nishikoori, H. Iba, *Electrochemistry*, **2011**, 876.

[68] R. G. Pearson, *J. Am. Chem. Soc.* **1963**, *85*, 3533.

[69] N. B. Aetukuri, B. D. McCloskey, J. M. García, L. E. Krupp, V. Viswanathan, A. C. Luntz, *Nat. Chem.* **2014**, *7*, 50.

[70] L. Johnson, C. Li, Z. Liu, Y. Chen, S. A. Freunberger, J. Tarascon, P. C. Ashok, B. B. Praveen, K. Dholakia, P. G. Bruce, *Nat. Chem.* **2014**, *6*, 1091.

[71] K. U. Schwenke, M. Metzger, T. Restle, M. Piana, H. A. Gasteiger, *J. Electrochem. Soc.* **2015**, *162*, A573.

[72] S. Meini, S. Solchenbach, M. Piana, H. A. Gasteiger, *J. Electrochem. Soc.* **2014**, *161*, A1306.

[73] V. Giordani, V. S. Bryantsev, J. Uddin, W. Walker, G. V. Chase, D. Addison, *ECS Electrochem. Lett.* **2013**, *3*, A11.

[74] J. Uddin, V. S. Bryantsev, V. Giordani, W. Walker, G. V. Chase, D. Addison, *J. Phys. Chem. Lett.* **2013**, *4*, 3760−3765.

[75] V. Giordani, W. Walker, V. S. Bryantsev, J. Uddin, G. V. Chase, D. Addison, *J. Electrochem. Soc.* **2013**, *160*, A1544.

[76] Y. Chen, S. A. Freunberger, Z. Peng, F. Bardé, P. G. Bruce, *J. Am. Chem. Soc.* **2012**, *134*, 7952.

[77] Y. Chen, S. A. Freunberger, Z. Peng, O. Fontaine, P. G. Bruce, *Nat. Chem.* **2013**, *5*, 489.

[78] D. Xu, Z. Wang, J. Xu, L. Zhang, X. Zhang, *Chem. Commun.* **2012**, *48*, 6948.

[79] M. J. Trahan, S. Mukerjee, E. J. Plichta, M. A. Hendrickson, K. M. Abraham, *J. Electrochem. Soc.* **2012**, *160*, A259.

[80] D. G. Kwabi, T. P. Batcho, C. V. Amanchukwu, N. Ortiz-Vitoriano, P. Hammond, C. V. Thompson, Y. Shao-Horn, *J. Phys. Chem. Lett.* **2014**, *5*, 2850.

[81] D. Sharon, M. Afri, M. Noked, A. Garsuch, A. A. Frimer, D. Aurbach, *J. Phys. Chem. Lett.* **2013**, *4*, 3115.

[82] A. K. Thapa, K. Saimen, T. Ishihara, *Electrochem. Solid-St. Lett.* **2010**, *13*, A165.

Chapter 2 References

[1] R. R. Garsuch, D.-B. Le, A. Garsuch, J. Li, S. Wang, A. Farooq, J. R. Dahn, *J. Electrochem. Soc.* 2008, **155**, A721.

[2] B. D. Adams, R. Black, Z. Williams, R. Fernandes, M. Cuisinier, E. Jaemstorp Berg, P. Novak, G. K. Murphy, L. F. Nazar, *Adv. Energ. Mater.* **2014**, 1400867.

[3] C. V. Amanchukwu, J. R. Harding, Y. Shao-Horn, P. T. Hammond, *Chem. Mater.* **2015**, *27*, 550.

[4] R. Black, S. H. Oh, J. H. Lee, T. Yim, B. Adams, L. F. Nazar, *J. Am. Chem. Soc.*, **2012**, *134*, 2902.

[5] B. D. McCloskey, A. Valery, A. C. Luntz, S. R. Gowda, G. M. Wallraff, J. M. Garcia, T. Mori, L. E. Krupp, *J. Phys. Chem. Lett.* **2013**, *4*, 2989.

[6] C. M. A. Brett, A. M. O. C. Brett, Chapter 8 in *Electrochemistry: Principles, Methods, and Applications*, Oxford University Press Inc., New York, **1994**.

[7] C. Suryanarayana, M. Grant Norton, *X-Ray Diffraction A Practical Approach*, Plenum Press, New York, **1998**.

[8] B. E. Warren, *X-Ray Diffraction*, General Publishing Company Ltd., North York, ON, **1990**.

[9] S. Brunauer, P. H. Emmett and E. Teller, *J. Am. Chem. Soc.*, **1938**, *60*, 309.

[10] N. Tsiouvaras, S. Meini, I. Buchberger, H. A. Gasteiger, *J. Electrochem. Soc.* **2013**, *160*, A471.

[11] E.J. Berg, P. Novak, ECL Annual Report, **2012**, *Paul Scherrer Institut*, p. 47 (http://www.psi.ch/lec/AnnualReportsUebersichtsTabelle/ECL-Annual-Report_2012.pdf).

[12] P. Hartmann, C. L. Bender, J. Sann, A. K. Dürr, M. Jansen, J. Janek, P. Adelhelm, *Phys. Chem. Chem. Phys.* **2013**, *15*, 11661.

Chapter 3 References

[1] R. R. Mitchell, B. M. Gallant, C. V. Thompson, Y. Shao-Horn, *Energy Environ. Sci.*, **2011**, *4*, 2952.

[2] R. Black, S. H. Oh, J.-H. Lee, T. Yim, B. Adams, L. F. Nazar, *J. Am. Chem. Soc.,* **2012**, *134*, 2902.

[3] S. H. Oh, R. Black, E. Pomerantseva, J.-H. Lee, L. F. Nazar, *Nature Chem.,* **2012**, *4*, 1004.

[4] J. Yang, D. Zhai, H.H. Wang, K. C. Lau, J. A. Schlueter, P. Du, D. J. Myers, Y.-K. Sun, L. A. Curtiss, K. Amine, *Phys. Chem. Chem. Phys.*, **2013**, *15*, 3764.

[5] B. D. McCloskey, R. Scheffler, A. Speidel, G. Girishkumar, A. C. Luntz, *J. Phys. Chem. C,* **2012***, 116*, 23897.

[6] C. Ó. Laoire, S. Mukerjee, E. J. Plichta, M. A. Hendrickson, K. M. Abraham, *J. Electrochem. Soc.,* **2011**, *158*, A302.

[7] H.-G. Jung, J. Hassoun, J.-B. Park, Y.-K. Sun, B. Scrosati, *Nature Chem.,* **2012**, *4*, 579.

[8] B. D. McCloskey, D. S. Bethune, R.M. Shelby, T. Mori, R. Scheffler, A. Speidel, M. Sherwood, A. C. Luntz, *J. Phys. Chem. Lett.,* **2012**, *3*, 3043.

[9] R. Black, J.-H. Lee, B. Adams, C.A. Mims, L.F. Nazar, *Angew. Chem. Int. Ed.,* **2013**, *52*, 392.

[10] Y.-C. Lu, H. A. Gasteiger, E. Crumlin, R. Jr. McGuire, Y. Shao-Horn, *J. Electrochem. Soc.,* **2010**, *157*, A1016.

[11] Z. Peng, S. A. Freunberger, Y. Chen, P. G. Bruce, *Science*, **2012**, *337*, 563.

[12] Z. Peng, S. A. Freunberger, L. J. Hardwick, Y. Chen, V. Giordani, F. Bard, P. Novak, D. Graham, J.-M. Tarascon, P. Bruce, *Angew. Chem. Int. Ed.,* **2011**, *50*, 6351.

[13] Y. C. Lu, D. G. Kwabi, K.P.C. Yao, J.R. Harding, J. Zhou, L. Zuin, Y. Shao-Horn, *Energ. Environ. Sci.,* **2011**, *4*, 2999.

[14] K. C. Lau, R. S. Assary, P. C. Redfern, J. P. Greeley, L. A. Curtiss, J. *Phys. Chem. C*, **2012**, *116*, 23890.

[15] D. T. Sawyer, G. Jr. Chlerlcato, C. T. Angells, E. J. Jr. Nannl, T. Tsuchlya, *Anal. Chem.,* **1982**, *54,* 1720.

[16] J. Herranz, A. Garsuch, H. A. Gasteiger, *J. Phys. Chem. C,* **2012**, *116*, 19084.

[17] C. O. Laoire, S. Mukerjee, K. M. Abraham, E. J. Plichta, M. A. Hendrickson, *J. Phys. Chem. C,* **2010**, *114*, 9178.

[18] C.O. Laoire, S. Mukerjee, K. M. Abraham, E. J. Plichta, M. A. Hendrickson, *J. Phys. Chem. C,* **2009**, *113,* 20127.

[19] Y.-C. Lu, H. A. Gasteiger, E. Crumlin, R. Jr. McGuire, Y. Shao-Horn, *Electrochem. Solid-St. Lett*., **2010**, *13*, A69.

[20] M.W. Chase, Jr., NIST-JANAF Thermochemical Tables, Fourth Edition, *J. Phys. Chem. Ref. Data*, Monograph 9, **1998**, 1510.

[21] R. H. Snow, R. H. Thermodynamic Evaluation of the Possibility of Lithium Superoxide Production Technical Report, *Aerospace Medical Research Laboratories,* **1965**.

[22] D. Sawyer, J.L. Roberts, Jr. *J. Electroanal. Chem*., **1966**, *12*, 90.

[23] D. Aurbach, M. Daroux, P. Faguy, E. Yeager, *J. Electroanal. Chem.,* **1991**, *297*, 225.

[24] S. Nakanishi, F. Mizuno, T. Abe, H. Iba, *Electrochemistry*, **2012**, *80*, 783.

[25] Y.-C. Lu, B. M. Gallant, D. G. Kwabi, J.R. Harding, R. R. Mitchell, M. S. Whittingham, Y. Shao-Horn, *Energ. Enviro. Sci.,* **2013**, *6*, 750.

[26] J. H. Lee, R. Black, G. Popov, E. Pomeransteva, F. Nan, G. A. Botton, L. F. Nazar, *Energ. Environ. Sci*., **2012**, *5*, 9558.

[27] V. Viswanathan, K. S. Thygesen, J. S. Hummelshøj, J. K. Nørskov, G. Girishkumar, B. D. McCloskey, A. C. Luntz *J. Chem. Phys.* **2011**, *135*, 214704.

[28] Y.-C. Lu and Y. Shao-Horn, *J. Phys. Chem. Lett.,* **2013**, *4*, 93.

[29] D. Sharon, V. Etacheri, A. Garsuch, M. Afri, A. A. Frimer, D. Aurbach, *J. Phys. Chem. Lett.,* **2013**, *4*, 127.

[30] Y.-C. Lu, H. A. Gasteiger, Y. Shao-Horn, *J. Am. Chem. Soc.,* **2011**, *133*, 19048.

[31] B. D. McCloskey, A. Speidel, R. Scheffler, D. C. Miller, V. Viswanathan, J. S. Hummelshøj, J. K. Nørskov, A. C. Luntz, *J. Phys. Chem. Lett.,* **2012**, *3*, 997.

[32] Y. Mo, S. P. Ong, G. Ceder, *Phys. Rev. B,* **2011**, *84*, 205446.

[33] C. Tran, J. Kafle, X.-Q. Yang, D. Qu, *Carbon*, **2011**, *49*, 1266.

[34] I. Kowalczk, J. Read, M. Salomon, *Pure Appl. Chem.,* **2007**, *79*, 851.

[35] Y.-G. Ryu, D.-M. Im, M.-J. Lee, D.-J. Lee, S.-B. Ma, *US Patent Application Publication*, **2012**, *US 2012/0107728A1*.

[36] M. Safari, B. D. Adams, L. F. Nazar, *J. Phys. Chem. Lett.* **2014**, *5*, 3486.

Chapter 4 References

[1] Y. C. Lu, B. M. Gallant, D. G. Kwabi, J. R. Harding, R. R. Mitchell, M. S. Whittingham, Y. Shao-Horn, *Energy Environ. Sci.* **2013**, *6*, 750.

[2] J. H. Lee, R. Black, G. Popov, E. Pomerantseva, F. Nan, G. A. Botton, L. F. Nazar, *Energy Environ. Sci.* **2012**, *5*, 9558.

[3] B. D. McCloskey, D. S. Bethune, R. M. Shelby, G. Girishkumar, A. C. Luntz, *J. Phys. Chem. Lett.* **2011**, *2*, 1161.

[4] B. D. McCloskey, R. Scheffler, A. Speidel, G. Girishkumar, A. C. Luntz, *J. Phys. Chem. C* **2012**, *116*, 23897.

[5] B. D. McCloskey, A. Speidel, R. Scheffler, D. C. Miller, V. Viswanathan, J. S. Hummelshøj, J. K. Nørskov, A. C. Luntz, *J. Phys. Chem. Lett.* **2012**, *3*, 997.

[6] S. R. Gowda, A. Brunet, G. M. Wallraff, B. D. McCloskey, *J. Phys. Chem. Lett.* **2013**, *4*, 276.

[7] C. O. Laoire, S. Mukerjee, K. M. Abraham, E. J. Plichta, M. A. Hendrickson, *J. Phys. Chem. C* **2010**, *114*, 9178.

[8] B. D. Adams, C. Radtke, R. Black, M. L. Trudeau, K. Zaghib, L. F. Nazar, *Energy Environ. Sci.* **2013**, *6*, 1772.

[9] B. M. Gallant, D. G. Kwabi, R. R. Mitchell, J. Zhou, C. V. Thompson, Y. Shao-Horn, *Energy Environ. Sci.* **2013**, *6*, 2518.

[10] J. Yang, D. Zhai, H. H. Wang, K. C. Lau, J. A. Schlueter, P. Du, D. J. Myers, Y. K. Sun, L. A. Curtiss, K. Amine, *Phys. Chem. Chem. Phys.* **2013**, *15*, 3764.

[11] D. Zhai, H. H. Wang, J. Yang, K. C. Lau, K. Li, K. Amine, L. A. Curtiss, *J. Am. Chem. Soc.* **2013**, *135*, 15364.

[12] S. Kang, Y. Mo, S. P. Ong, G. Ceder, *Chem. Mater.* **2013**, *25*, 3328.

[13] M. D. Radin, D. J. Siegel, *Energy Environ. Sci.* **2013**, *6*, 2370.

[14] J. Lu, Y. Lei, K. C. Lau, X. Luo, P. Du, J. Wen, R. S. Assary, U. Das, D. J. Miller, J. W. Elam, H. M. Albishri, D. A. El-Hady, Y.-K. Sun, L. A. Curtiss, K. Amine, *Nat. Commun.* **2013**, *4*.

[15] R. R. Garsuch, D. B. Le, A. Garsuch, J. Li, S. Wang, A. Farooq, J. R. Dahn, *J. Electrochem. Soc.* **2008**, *155*, A721.

[16] A. C. Larson, R. B. Von Dreele, *General Structure Analysis System (GSAS)*, Los Alamos National Laboratory, **2004**.

[17] F. Fehér, I. von Wilucki, G. Dost, G. *Chem. Ber.* **1953**, *86*, 1429.

[18] H. Föppl, *Zeitschrift fuer Anorganische und Allgemeine Chemie*, **1957**, *291*, 12.

[19] L. G. Cota, P. de la Mora, *Acta Cryst. B.* **2005**, *B61*, 133.

[20] M. K. Y. Chan, E. L. Shirley, N. K. Karan, M. Balasubramanian, Y. Ren, J. P. Greeley, T. T. Fister, *J. Phys. Chem. Lett.* **2011**, *2*, 2483.

[21] J. Heyd, G. E. Scuseria, M. Ernzerhof, *J. Chem. Phys.* **2003**, *118*, 8207.

[22] J. Heyd, G. E. Scuseria, M. Ernzerhof, *J. Chem. Phys.* **2006**, *124*.

[23] G. Kresse, J. Furthmuller, *Comput. Mater. Sci.* **1996**, *6*, 15.

[24] G. Kresse, D. Joubert, *Phys. Rev. B* **1999**, *59*, 1758.

[25] S. P. Ong, Y. Mo, G. Ceder, *Phys. Rev. B: Condens. Matter Mater. Phys.* **2012**, *85*.

[26] J. Rodríguez-Carvajal, *Phys. B (Amsterdam, Neth.)* **1993**, *192*, 55.

[27] T. Roisnel, J. Rodríguez-Carvajal, In *7th European Powder Diffraction Conference*; Delguez, R., Mittemeijer, E. J., Eds. Barcelona, **2001**; vol. 378-381, pg. 118.

[28] P. W. Stephens, *J. Appl. Crystallogr.* **1999**, *32*, 281.

[29] R. Black, S. H. Oh, J. H. Lee, T. Yim, B. Adams, L. F. Nazar, *J. Am. Chem. Soc.* **2012**, *134*, 2902.

[30] R. R. Mitchell, B. M. Gallant, C. V. Thompson, Y. Shao-Horn, Y. *Energy Environ. Sci.* **2011**, *4*, 2952.

[31] R. R. Mitchell, B. M. Gallant, Y. Shao-Horn, C. V. Thompson, *J. Phys. Chem. Lett.* **2013**, *4*, 1060.

[32] N. C. Popa, *J. Appl. Crystallogr.* **1998**, *31*, 176.

[33] H. Lim, E. Yilmaz, H. R. Byon, *J. Phys. Chem. Lett.* **2012**, *3*, 3210.

[34] J. S. Hummelshøj, J. Blomqvist, S. Datta, T. Vegge, J. Rossmeisl, K. S. Thygesen, A. C. Luntz, K. W. Jacobsen, J. K. Nørskov, *J. Chem. Phys.* **2010**, *132*.

[35] R. Black, J. H. Lee, B. Adams, C. A. Mims, L. F. Nazar, *Angew. Chem., Int. Ed.* **2013**, *52*, 392.

[36] F. Tian, M. D. Radin, D. J. Siegel, *Chem. Mater.* **2014**, *26*, 2952.

[37] P. Hohenberg, W. Kohn, *Phys. Rev.* **1964**, *136*, B864.

[38] J. B. Varley, V. Viswanathan, J. K. Nørskov, A. C. Luntz, *Energy Environ. Sci.* **2014**, *7*, 720.

[39] P. M. Diehm, P. Ágoston, K. Albe, *ChemPhysChem* **2012**, *13*, 2443.

[40] J. Xu, J. Harmer, G. Li, T. Chapman, P. Collier, S. Longworth, S. C. Tsang, *Chem. Commun.* **2010**, *46*, 1887.

[41] S. Meini, S. Solchenbach, M. Piana, H. A. Gasteiger, *J. Electrochem. Soc.* **2014**, *161*, A1306.

[42] S. Meini, N. Tsiouvaras, K. U. Schwenke, M. Piana, H. Beyer, L. Lange, H. A. Gasteiger, *Phys. Chem. Chem. Phys.* **2013**, *15*, 11478.

[43] B. D. McCloskey, A. Valery, A. C. Luntz, S. R. Gowda, G. M. Wallraff, J. M. Garcia, T. Mori, L. E. Krupp, *J. Phys. Chem. Lett.* **2013**, *4*, 2989.

[44] B. D. Adams, R. Black, Z. Williams, R. Fernandes, M. Cuisinier, E. Jaemstorp Berg, P. Novak, G. K. Murphy, L. F. Nazar, *Adv. Energ. Mater.* **2015**, *5*, 1400867.

[45] S. A. Freunberger, Y. Chen, Z. Peng, J. M. Griffin, L. J. Hardwick, F. Bardé, P. Novák, P. G. Bruce, *J. Am. Chem. Soc.* **2011**, *133*, 8040.

[46] W. Xu, V. V. Viswanathan, D. Wang, S. A. Towne, J. Xiao, Z. Nie, D. Hu, J. G. Zhang, *J. Power Sources* **2011**, *196*, 3894.

[47] H. Beyer, S. Meini, N. Tsiouvaras, M. Piana, H. A. Gasteiger, *Phys. Chem. Chem. Phys.* **2013**, *15*, 11025.

Chapter 5 References

[1] B. D. Adams, C. Radtke, R. Black, M. L. Trudeau, K. Zaghib, L. F. Nazar, *Energy Environ. Sci.* **2013**, *6*, 1772.

[2] Z. Peng, S. Freunberger, L. J. Hardwick, Y. Chen, V. Giordani, F. Bardé, P. Novák, D. Graham, J.-M. Tarascon, P. G. Bruce, *Angew. Chem. Int. Ed. Engl.* **2011**, *50*, 6351.

[3] B. D. McCloskey, R. Scheffler, A. Speidel, D. S. Bethune, R. M. Shelby, A. C. Luntz, *J. Am. Chem. Soc.* **2011**, *133*, 18038.

[4] S. A. Freunberger, Y. Chen, N. E. Drewett, L. J. Hardwick, F. Bardé, P. G. Bruce, *Angew. Chem. Int. Ed. Engl.* **2011**, *50*, 8609.

[5] S. A. Freunberger, Y. Chen, Z. Peng, J. M. Griffin, L. J. Hardwick, F. Bardé, P. Novák, P. G. Bruce, *J. Am. Chem. Soc.* **2011**, *133*, 8040.

[6] V. S. Bryantsev, V. Giordani, W. Walker, M. Blanco, S. Zecevic, K. Sasaki, J. Uddin, D. Addison, G. V. Chase, *J. Phys. Chem. A* **2011**, *115*, 12399.

[7] B. D. Mccloskey, D. S. Bethune, R. M. Shelby, G. Girishkumar, A. C. Luntz, *J. Phys. Chem. Lett.* **2011**, 1161.

[8] Y. Chen, S. A. Freunberger, Z. Peng, F. Bardé, P. G. Bruce, *J. Am. Chem. Soc.* **2012**, *134*, 7952.

[9] M. M. O. Thotiyl, S. A. Freunberger, Z. Peng, P. G. Bruce, *J. Am. Chem. Soc.* **2013**, *135*, 494.

[10] D. M. Itkis, D. Semenenko, E. Y. Kataev, A. I. Belova, V. S. Neudachina, A. P. Sirotina, M. Hävecker, D. Teschner, A. Knop-Gericke, P. Dudin, A. Barinov, E. Goodilin, Y. Shao-Horn, L. V. Yashina, *Nano Lett.* **2013**, *13*, 4697.

[11] J. Lu, Y. Lei, K. C. Lau, X. Luo, P. Du, J. Wen, R. S. Assary, U. Das, D. J. Miller, J. W. Elam, H. M. Albishri, D. A. El-Hady, Y.-K. Sun, L. A. Curtiss, K. Amine, *Nat.Commun.* **2013**, *4*, 2383.

[12] Z. Peng, S. A. Freunberger, Y. Chen, P. G. Bruce, *Science* **2012**, *337*, 563.

[13] Y. Chen, S. A. Freunberger, Z. Peng, O. Fontaine, P. G. Bruce, *Nature Chem.* **2013**, *5*, 489.

[14] M. M. O. Thotiyl, S. A. Freunberger, Z. Peng, Y. Chen, Z. Liu, P. G. Bruce, *Nat. Mater.* **2013**, *12*, 1050.

[15] G. Zhao, R. Mo, B. Wang, L. Zhang, K. Sun, *Chem. Mater.*, **2014**, *26*, 2551.

[16] B. Avasarala, P. Haldar, *Electrochim. Acta* **2010**, *55*, 9024.

[17] D. J. Ham, J. S. Lee, *Energies* **2009**, *2*, 873.

[18] P. He, Y. Wang, H. Zhou, *Chem. Commun.* **2011**, *47*, 10701.

[19] J. Park, Y.-S. Jun, W.-R. Lee, J. A. Gerbec, K. A. See, G. D. Stucky, *Chem. Mater.* **2013**, *25*, 3779.

[20] F. Li, R. Ohnishi, Y. Yamada, J. Kubota, K. Domen, A. Yamada, H. Zhou, *Chem. Commun.* **2013**, *49*, 1175.

[21] M. J. Kenney, M. Gong, Y. Li, J. Z. Wu, J. Feng, M. Lanza, H. Dai, *Science*, **2013**, *342*, 836.

[22] R. R. Garsuch, D.-B. Le, A. Garsuch, J. Li, S. Wang, A. Farooq, J. R. Dahn, *J. Electrochem. Soc.* **2008**, *155*, A721.

[23] E. Nasybulin, W. Xu, M. H. Engelhard, Z. Nie, S. D. Burton, L. Cosimbescu, M. E. Gross, J. Zhang, *J. Phys. Chem. C* **2013**, *117*, 2635.

[24] Y.-C. Lu, H. A. Gasteiger, M. C. Parent, V. Chiloyan, Y. Shao-Horn, *Electrochem. Solid-State Lett.* **2010**, *13*, A69.

[25] J. R. Harding, Y.-C. Lu, Y. Tsukada, Y. Shao-Horn, *Phys. Chem. Chem. Phys.* **2012**, *14*, 10540.

[26] S. Meini, N. Tsiouvaras, K. U. Schwenke, M. Piana, H. Beyer, L. Lange, H. A. Gasteiger, *Phys. Chem. Chem. Phys.* **2013**, *15*, 11478.

[27] H. Beyer, S. Meini, N. Tsiouvaras, M. Piana, H. A. Gasteiger, *Phys. Chem. Chem. Phys.* **2013**, *15*, 11025.

[28] S. Ganapathy, B. D. Adams, G. Stenou, M. S. Anastasaki, K. Goubitz, X.-F. Miao, L. F. Nazar, M. Wagemaker, *J. Am. Chem. Soc.* **2014**, *136*, 16335.

[29] S. Meini, S. Solchenbach, M. Piana, H. A. Gasteiger, *J. Electrochem. Soc.* **2014**, *161*, A1306.

[30] B. D. McCloskey, A. Speidel, R. Scheffler, D. C. Miller, V. Viswanathan, J. S. Hummelshøj, J. K. Nørskov, A. C. Luntz, *J. Phys. Chem. Lett.* **2012**, *3*, 997.

[31] J. Yang, D. Zhai, H. H. Wang, K. C. Lau, J. A. Schlueter, P. Du, D. J. Myers, Y.-K. Sun, L. A. Curtiss, K. Amine, *Phys. Chem. Chem. Phys*., **2013**, *15*, 3764.

[32] B. Avasarala, P. Haldar, *Int. J. Hydrogen Energ.* **2011**, *36*, 3965.

[33] B. D. McCloskey, A. Valery, A. C. Luntz, S. R. Gowda, G. M. Wallraff, J. M. Garcia, T. Mori, L. E. Krupp, *J. Phys. Chem. Lett.* **2013**, *4*, 2989.

[34] A. C. Luntz, B. D. McCloskey, *Chem. Rev.* **2014**, *114*, 11721.

[35] S. Gavarini, R. Bes, N. Millard-Pinard, S. Cardinal, C. Peaucelle, A. Perrat-Mabilon, V. Garnier, C. Gaillard, *J. Appl. Phys.* **2011**, *109*, 014906.

[36] R. Wasche, D. Klaffke, *Tribol. Int.* **1999**, *32*, 197.

[37] G. N. Komratov, *Powder Metall. Met. C+* **1997**, *36*, 510.

Chapter 6 References

[1] E. Coronado, E. Palomares, *J. Mater. Chem.* **2005**, *15*, 3593.

[2] B. J. Scott, G. Wirnsberger, G. D. Stucky, *Chem. Mater.* **2001**, *13*, 3140.

[3] C. Aprile, L. Teruel, M. Alvaro, H. Garcia, *J. Am. Chem. Soc.* **2009**, *131*, 1342.

[4] T. T. Emons, J. Li, L. F. Nazar, *J. Am. Chem. Soc.* **2002**, *124*, 8516.

[5] Y. Shi, B. Guo, S. A. Corr, Q. Shi, Y.-S. Hu, K. R. Heier, L. Chen, R. Seshadri, G. D. Stucky, *Nano Lett.* **2009**, *9*, 4215.

[6] T. Brezesinski, J. Wang, S. H. Tolbert, B. Dunn, *Nature Mater.* **2010**, *9*, 146.

[7] Q. Pang, D. Kundu, M. Cuisinier, L. Nazar, *Nature Comm,* **2014**, *5*, 4759.

[8] S. H. Oh, R. Black, E. Pomerantseva, J.-H. Lee, L. F. Nazar, *Nature Chem.* **2012**, *4*, 1004.

[9] T. Akazawa, Y. Inaguma, T. Katsumata, K. Hiraki, T. Takahashi, *J. Cryst. Growth* **2004**, *271*, 445.

[10] H. S. Horowitz, L. J. Longo, J. T. Lewandowski, *Mat. Res. Bull.* **1981**, *16*, 489.

[11] R. A. Beyerlein, H. S. Horowitz, J. M. Longo, M. E. Leonowicz, *J. Solid State Chem.* **1984**, *51*, 253.

[12] R. A. Beyerlein, H. S. Horowitz, J. M. Longo, *J. Solid State Chem.* **1988**, *72*, 2.

[13] H. S. Horowitz, J. M. Longo, H. H. Horowitz, *J. Electrochem. Soc.* **1983**, *130*, 1851.

[14] M. A. Subramanian, G. Aravamudan, G. v. S. Rao, *Prog. Solid St. Chem.* **1983**, *15*, 55.

[15] J. Prakash, D. Tryk, E. Yeager, *J. Power Sources* **1990**, *29*, 413.

[16] V. Raghuveer, K. Kumar, B. Viswanathan, *Int. J. Eng. Mat. Sci.* **2002**, *9*, 137.

[17] J.-M. Zen, A. S. Kumar, J.-C. Chen, *J. Mol. Catal. A: Chem.* **2001**, *165*, 177.

[18] R. G. Egdell, J. B. Goodenough, A. Hamnett, C. C. Naish, *J. Chem. Soc., Faraday Trans. I,* **1983**, *79*, 893.

[19] J. B. Goodenough, R. Manoharan, M. Paranthaman, *J. Am. Chem. Soc.* **1990**, *112*, 2076.

[20] T. Takeda, R. Kanno, Y. Kawamoto, Y. Takeda, *J. Electrochem. Soc.* **2000**, *147*, 1730.

[21] V. Esposito, E. Traversa, E. D. Wachsman, *J. Electrochem. Soc.* **2005**, *152*, A2300.

[22] V. Raghuveer, B. Viswanathan, *J. Mater. Sci.* **2005**, *40*, 6249.

[23] S. H. Oh, B. D. Adams, B. Lee, and L. F. Nazar, *Chem. Mater.* **2015**, *27*, 2322.

[24] S. Verma, H. M. Joshi, T. Jagadale, A. Chawla, R. Chandra, S. Ogale, *J. Phys. Chem. C* **2008,** *112,* 15106.

[25] A. C. C. Tseung, S. Jasem, *Electrochim. Acta* **1977**, *22*, 31.

[26] D. U. Lee, B. J. Kim, Z. Chen, *J. Mater. Chem. A*, **2013**, *1*, 4754.

[27] G. Wu, G. Cui, D. Li, P.-K. Shen, N. Li, *J. Mater. Chem.*, **2009**, *19*, 6581.

[28] F. Cheng, Y. Su, J. Liang, Z. Tao, J. Chen, *Chem. Mater.,* **2010**, *22*, 898.

[29] S. H. Oh, L. F. Nazar, *Adv. Energy Mater.* **2012**, *2*, 903.

[30] R. Black, J.-H. Lee, B. Adams, C. A. Mims, L. F. Nazar, *Angew. Chem. Int. Ed.* **2013**, *52*, 392.

[31] Z. Peng, S. A. Freunberger, L. J. Hardwick, Y. Chen, V. Giordani, F. Barde, P. Novak, D. Graham, J.-M. Tarascon, P. G. Bruce, *Angew. Chem. Int. Ed.* **2011**, *50*, 6351.

[32] B. D. McCloskey, A. Speidel, R. Scheffler, D. C. Miller, V. Viswanathan, J. S. Hummelshøj, J. K. Nørskov, A. C. Luntz, *J. Phys. Chem. Lett.* **2012**, *3*, 997.

[33] Y.-C. Lu, B. M. Gallant, D. G. Kwabi, J. R. Harding, R. R. Mitchell, M. S. Whittingham, Y. Shao-Horn, *Energy Environ. Sci.* **2013**, *6*, 750.

[34] S. A. Freunberger, Y. Chen, Z. Peng, J. M. Griffin, L. J. Hardwick, F. Barde, P. Novak, P. G. Bruce, *J. Am. Chem. Soc.*, **2011**, *133*, 8040.

[35] M. M. O. Thotiyl, S. A. Freunberger, Z. Peng, Y. Chen, Z. Liu,P. G. Bruce, *Nature Mat.* **2013***, 12,* 1050.

Chapter 7 References

[1] W. Walker, V. Giordani, J. Uddin, V. S. Bryantsev, G. V. Chase, D. Addison, *J. Am. Chem. Soc.* **2013**, *135*, 2076.

[2] Y. Chen, S. A. Freunberger, Z. Peng, F. Bardé, P. G. Bruce, *J. Am. Chem. Soc.* **2012**, *134*, 7952.

[3] B. D. McCloskey, A. Speidel, R. Scheffler, D. C. Miller, V. Viswanathan, J. S. Hummelshoj, J. K. Norskov, A. C. Luntz, *J. Phys. Chem. Lett.* **2012**, *3*, 997.

[4] Y.-C. Lu,Y. Shao-Horn, *J. Phys. Chem. Lett*. **2013**, *4*, 93.

[5] R. Black, J.-H. Lee, B. Adams, C. A. Mims, L. F. Nazar, *Angew. Chem. Int. Ed*. **2013**, *125*, 410.

[6] F. Mizuno, S. Nakanishi, Y. Kotani, S. Yokoishi, H. Iba, *Electrochemistry.* **2010**, *78*, 403.

[7] Z. Peng, S. A. Freunberger, Y. Chen, P. G. Bruce, *Science* **2012**, *337*, 563.

[8] M. M. O. Thotiyl, S. A. Freunberger, Z. Peng, Y. Chen, Z. Liu,P. G. Bruce, *Nature Mat.* **2013***, 12,* 1050.

[9] D. Sharon, M. Afri, M. Noked, A. Garsuch, A. A. Frimer, D. Aurbach, *J. Phys. Chem. Lett.* **2013**, *4*, 3115.

[10] B. D. McCloskey, A. Valery, A. C. Luntz, S. R. Gowda, G. M. Wallraff, J. M. Garcia, T. Mori, L. E. Krupp, *J. Phys. Chem. Lett.* **2013**, *4*, 2989.

[11] N. Mozhzhukhina, L. P. M. De Leo, E. J. Calvo, *J. Phys. Chem. C*, **2013**, *117*, 18375.

[12] J.-B. Park, J. Hassoun, H.-G. Jung, H.-S. Kim, C. S. Yoon, I.-H. Oh, B. Scrosati,Y.-K. Sun, *Nano Lett.* **2013**, *13*, 2971.

[13] B. D. McCloskey, D. S. Bethune, R. M. Shelby, G. Girishkumar, A. C. Luntz, *J. Phys. Chem. Lett*. **2011**, *2*, 1161.

[14] Y.-C. Lu, E. J. Crumlin, G. M. Veith, J. R. Harding, E. Mutoro, L. Baggetto, N. J. Dudney, Z. Liu, Y. Shao-Horn, *Sci. Rep.* **2012**, *2*, 715.

[15] V. S. Bryantsev, V. Giordani, W. Walker, M. Blanco, S. Zecevic, K. Sasaki, J. Uddin, D. Addison, G. V. Chase, *J. Phys. Chem. A*. **2011**, *115*, 12399.

[16] R. Black, S. H. Oh, J.-H. Lee, T. Yim, B. Adams, L. F. Nazar, *J. Am. Chem. Soc.* **2012**, *134*, 2902.

[17] S. A. Freunberger, Y. Chen, N. E. Drewett, L. J. Hardwick, F. Bardé, P. G. Bruce, *Angew. Chem. Int. Ed.* **2011**, *50*, 8609.

[18] K. R. Ryan, L. Trahey, B. J. Ingram, A. K. Burrell, *J. Phys. Chem. C.* **2012**, *116*, 19724.

[19] C. J. Barile, A. A. Gewirth, *J. Electrochem. Soc*. **2013**, *160*, A549.

[20] K. U. Schwenke, S. Meini, X. Wu, H. A. Gasteiger, M. Pianaa, *Phys. Chem. Chem. Phys.* **2013**, *15*, 11830.

[21] R. S. Assary, K. C. Lau, K. Amine, Y.-K. Sun, L. A. Curtiss, *J. Phys. Chem. C*. **2013**, *117*, 8041.

[22] H. Wang, K. Xie, *Electrochim. Acta* **2012**, *64*, 29.

[23] D. Sharon, V. Etacheri, A. Garsuch, M. Afri, A. A. Frimer, D. Aurbach, *J. Phys. Chem. Lett*. **2013**, *4*, 127.

[24] Z. Zhang, J. Lu, R. S. Assary, P. Du, H.-H. Wang, Y.-K. Sun, Y. Qin, K. C. Lau, J. P. Greeley, P. C. Redfern, H. Iddir, L. A. Curtiss, K. Amine, K. *J. Phys. Chem. C.* **2011**, *115*, 25535.

[25] M. J. Frisch, G. W. Trucks, H. B. Schlegel, G. E. Scuseria, M. A. Robb, J. R. Cheeseman, J. A. Montgomery Jr., T. Vreven, K. N. Kudin, J. C. Burant, J. M. Millam, S. S. Iyengar, J. Tomasi, V. Barone, B. Mennucci, M. Cossi, G. Scalmani, N. Rega, G. A. Petersson, H. Nakatsuji, M. Hada, M. Ehara, K. Toyota, R. Fukuda, J. Hasegawa, M. Ishida, T. Nakajima, Y. Honda, O. Kitao, H. Nakai, M. Klene, X. Li, J. E. Knox, H. P. Hratchian, J. B. Cross, V. Bakken, C. Adamo, J. Jaramillo, R. Gomperts, R. E. Stratmann, O. Yazyev, A. J. Austin, R. Cammi, C. Pomelli, J. W. Ochterski, P. Y. Ayala, K. Morokuma, G. A. Voth, P. Salvador, J. J. Dannenberg, V. G. Zakrzewski, S. Dapprich, A. D. Daniels, M. C. Strain, O. Farkas, D. K. Malick, A. D. Rabuck, K. Raghavachari, J. B. Foresman, J. V. Ortiz, Q. Cui, A. G. Baboul, S. Clifford, J. Cioslowski, B. B. Stefanov, G. Liu, A. Liashenko, P. Piskorz, I. Komaromi, R. L. Martin, D. J. Fox, T. Keith, M. A. Al-Laham, C. Y. Peng, A. Nanayakkara, M. Challacombe, P. M. W. Gill, B. Johnson, W. Chen, M. W. Wong, C. Gonzalez, J. A. Pople, Gaussian 03, revision D.01; Gaussian, Inc.: Wallingford, CT, **2004**.

[26] J. Lindner, *Monatshefte Für Chemie*. **1911**, *32*, 403.

[27] J. Reiter, E. Paillard, L. Grande, M. Winter, S. Passerini, *Electrochimica*. **2013**, *91*, 101.

[28] C. Capiglia, N. Imanishi, Y. Takeda, W. A. Henderson, S. Passerini, *J. Electrochem. Soc.* **2003**, *150*, A525.

[29] D. Brouillette, D. E. Irish, N. J. Taylor, G. Perron, M. Odziemkowskic, J. E. Desnoyers, *Phys. Chem. Chem. Phys.* **2002**, *4*, 6063.

[30] T. Tamura, T. Hachida, K. Yoshida, N. Tachikawa, K. Dokko, M. Watanabe, *J. Power Sources* **2010**, *195*, 6095.

[31] S. H. Park, J. Winnick, P. A. Kohl, *J. Electrochem. Soc.* **2002**, *149*, A1196.

[32] P.-Y. Chen, *J. Chin. Chem. Soc.* **2006**, *53*, 1017.

[33] R. Wibowo, S. E. W. Jones, R. G. Compton, *J. Phys. Chem. B.* **2009**, *113*, 12293.

[34] B. D. McCloskey, R. Scheffler, A. Speidel, G. Girishkumar, A. C. Luntz, *J. Phys. Chem. C.* **2012**, *116*, 23897.

[35] K. R. Ryan, L. Trahey, B. J. Ingram, A. K. Burrell, *J. Phys. Chem. C.* **2012**, *116*, 19724.

[36] X. Zhang, J. K. Pugh, P. N. Ross, *J. Electrochem. Soc.* **2001**, *148*, E183.

[37] F. Li, D.-M. Tang, Y. Chen, D. Golberg, H. Kitaura, T. Zhang, A. Yamada, H. Zhou, *Nano Lett.*, **2013**, *13*, 4702.

[38] J. Lu, Y. Lei, K. C. Lau, X. Luo, P. Du, J. Wen, R. S. Assary, U. Das, D. J. Miller, J. W. Elam, H. M. Albishri, D. A. El-Hady, Y.-K. Sun, L. A. Curtiss, K. Amine, *Nat. Comm.*, **2013**, *4*, 2383.

[39] D. M. Itkis, D. A. Semenenko, E. Y. Kataev, A. I. Belova, V. S. Neudachina, A. P. Sirotina, M. Hävecker, D. Teschner, A. Knop-Gericke, P. Dudin, A. Barinov, E. A. Goodilin, Y. Shao-Horn, L. V. Yashina, *Nano Lett.*, **2013**, *13*, 4697.

[40] M. M. O. Thotiyl, S. A. Freunberger, Z. Peng, P. G. Bruce, *J. Am. Chem. Soc.*, **2013**, *135*, 494.

[41] E. Nasybulin, W. Xu, M. H. Engelhard, Z. Nie, S. D. Burton, L. Cosimbescu, M. E. Gross, J.-G. Zhang, *J. Phys. Chem. C* **2013**, *117*, 2635.

[42] R. Younesi, M. Hahlin, F. Björefors, P. Johansson, K. Edström, *Chem. Mater.*, **2013**, *25*, 77.

[43] Z. K. Lin, D. L. Han, S. F. Li, Y. Y. Li, T. Yuan, *J. Chem. Phys.* **2009**, *130*, 154306.

[44] Y. Ogata, K. Takagi, T. Suzuki, *J. Chem. Soc.* **1978**, 2, 562.

[45] B. D. McCloskey , D. S. Bethune , R. M. Shelby , T. Mori , R. Scheffler, A. Speidel , M. Sherwood , A. C. Luntz , *J. Phys. Chem. Lett.* **2012**, *3*, 3043.

[46] H. Beyer, S. Meini, N. Tsiouvaras, M. Piana, H. A. Gasteiger, *Phys.Chem. Chem. Phys.,* **2013**, *15*, 11025.

[47] X. Zhang, J. K. Pugh, P. N. Ross, *J. Electrochem. Soc.* **2001**, *148*, E183.

[48] B. D. Adams, C. Radtke, R. Black, M. L. Trudeau, K. Zaghib, L. F. Nazar, *Energy Environ. Sci.* **2013**, *6*, 1772.

[49] P. Hartmann, C. L. Bender, M. Vračar, A. K. Dürr, A. Garsuch, J. Janek, P. Adelhelm, *Nature Mat.* **2013**, *12*, 228.

[50] P. Hartmann, C. L. Bender, J. Sann, A. K. Dürr, M. Jansen, J. Janek, P. Adelhelm, *Phys. Chem. Chem. Phys.* **2013**, *15*, 11661.

[51] X. Ren, Y. Wu, *J. Am. Chem. Soc.*, **2013**, *135*, 2923.

[52] A. P. Schaap, A. L. Thayer, G. R. Faler, K. Goda, T. Kimura, *J. Am. Chem. Soc.* **1974**, *96*, 4025.

Appendix References

[1] Z. Peng, S. A. Freunberger, Y. Chen, P. G. Bruce, *Science* **2012**, *337*, 563.

[2] M. M. O. Thotiyl, S. A. Freunberger, Z. Peng, Y. Chen, Z. Liu, P. G. Bruce, *Nat. Mater.* **2013**, *12*, 1050.

[3] C. O. Laoire, S. Mukerjee, K. M. Abraham, E. J. Plichta, M. A. Hendrickson, *J. Phys. Chem. C* **2010**, *114*, 9178.

[4] J. Huangxian, C. Hongyuan, G. Hong, *J. Electroanal. Chem.* **1993**, *361*, 251.

[5] K. M. Kadish, J. Q. Ding, T. Mallinski, *Anal. Chem.* **1984**, *56*, 1741.

[6] B. D. McCloskey, R. Scheffler, A. Speidel, G. Girishkumar, A. C. Luntz, *J. Phys. Chem. C* **2012**, *116*, 23897.

[7] L. Johnson, C. Li, Z. Liu, Y. Chen, S. A. Freunberger, P. C. Ashok, B. B. Praveen, K. Dholakia, J.-M. Tarascon, P. G. Bruce, *Nature Chem.* **2014**, *6*, 1091.

[8] Z. Peng, S. A. Freunberger, L. J. Hardwick, Y. Chen, V. Giordani, F. Barde, P. Novak, D. Graham, J.-M. Tarascon, P. G. Bruce, *Angew. Chem. Int. Ed.* **2011**, *50*, 6351.

[9] S. Ernst, L. Aldous, R. G. Compton, *J. Electroanal. Chem.* **2011**, *663*, 108.

[10] E. J. Calvo, N. Mozhzhukhina, *Electrochem. Commun.* **2013**, *31*, 56.

[11] L. Zhang, Z. Zhang, S. Harring, M. Straughan, R. Butorac, Z. Chen, L. Lyons, K. Amine, R. West, *J. Mater. Chem.* **2008**, *18*, 3713.